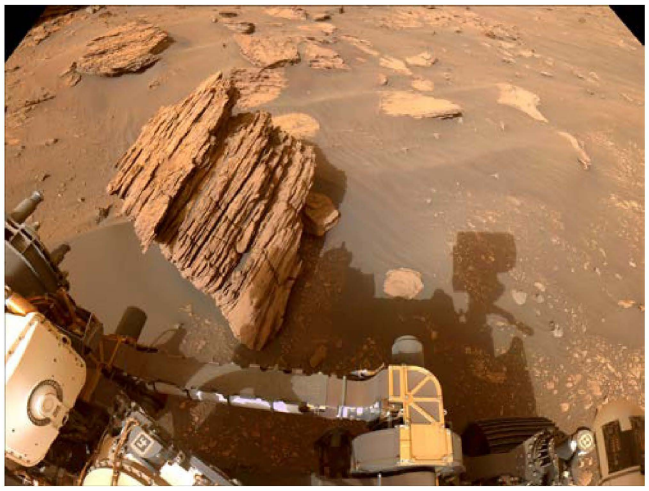

MARS 2020 INITIAL REPORTS

Volume 2

Delta Front Campaign February 15, 2023

KEN FARLEY, MARS 2020 PROJECT SCIENTIST
CALIFORNIA INSTITUTE OF TECHNOLOGY

KATIE STACK, MARS 2020 DEPUTY PROJECT SCIENTIST
JET PROPULSION LABORATORY
CALIFORNIA INSTITUTE OF TECHNOLOGY

Frontispiece: Mars 2020 Sample Collection Map

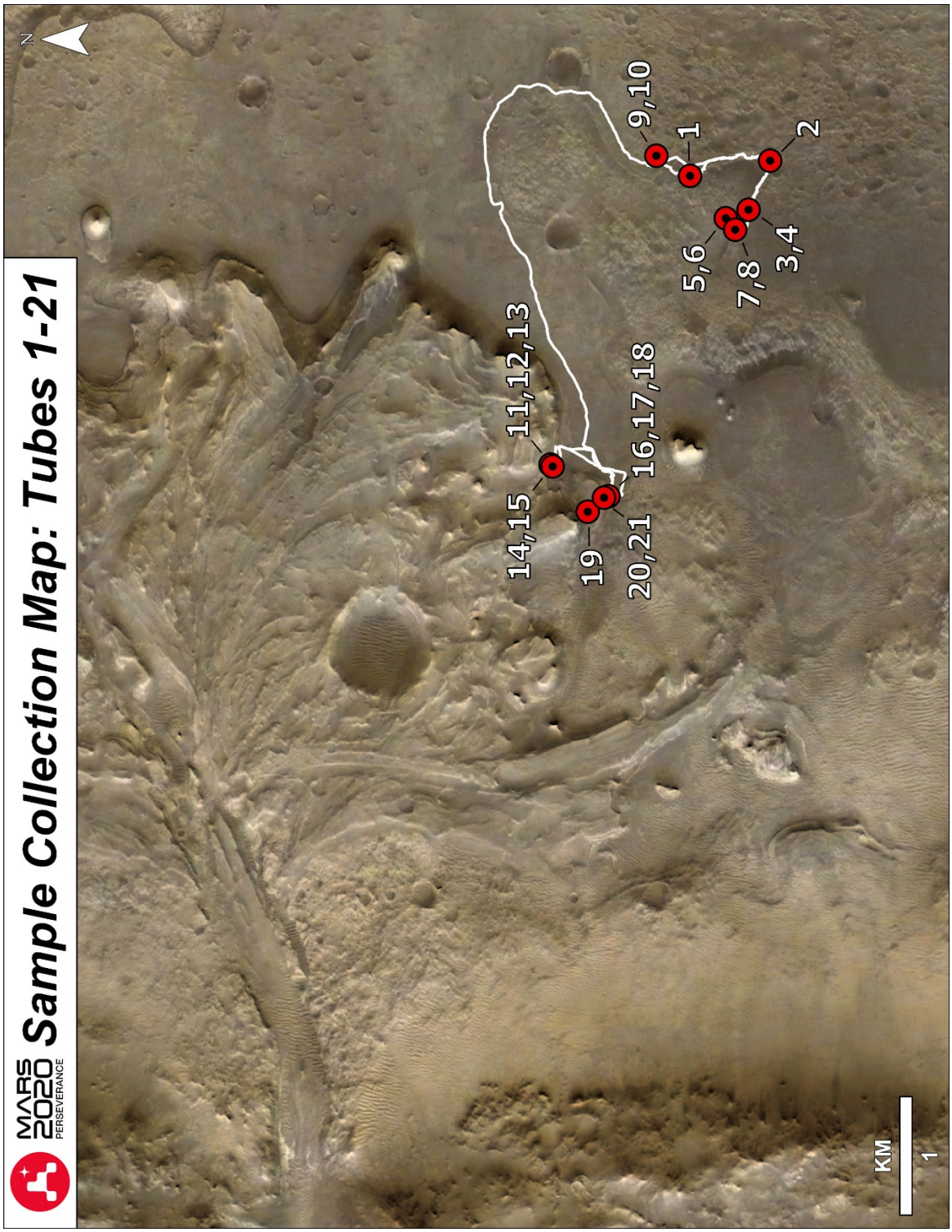

Contents

Preface

After completing the Crater Floor Campaign in early 2022, the Mars 2020 mission began investigation of the rocks exposed on the steep escarpment at the front of the Jezero western delta. The Delta Front Campaign was completed late in 2022 and was immediately followed by construction of a first sample depot, in the Three Forks area on the crater floor below the escarpment. This volume documents the 11 sample tubes collected during the Delta Front Campaign, including samples of four unique rock outcrops, paired regolith samples, and two witness tubes.

K.A. Farley, Project Scientist

K.M. Stack, Deputy Project Scientist

Mars 2020 Returned Sample Science Participating Scientists

The Mars 2020 Science Team includes individuals selected by NASA to guide sample selection, interpretation, and documentation, including preparation of these Initial Reports. For the Prime Mission these individuals are:

Kathleen Benison, West Virginia University

Tanja Bosak, Massachusetts Institute of Technology

Barbara Cohen, NASA Goddard Space Flight Center

Andy Czaja, University of Cincinnati

Vinciane Debaille, FNRS-Université Libre de Bruxelles

Libby Hausrath, University of Nevada Las Vegas

Chris Herd, University of Alberta

Keyron Hickman-Lewis, Natural History Museum London

Lisa Mayhew, University of Colorado Boulder

Mark Sephton, Imperial College London

David Shuster, University of California Berkeley

Sandra Siljeström, RISE Research Institutes of Sweden

Justin Simon, NASA Johnson Space Center

Ben Weiss, Massachusetts Institute of Technology

Maria-Paz Zorzano, Centro de Astrobiología, Spain

Explanatory Notes for Mars 2020 Initial Reports

Sample Designation

The standardized format for sample designations is **M2020-sol-N *name*. M2020** refers to the mission that collected the sample, **sol** indicates the mission sol of sample coring (sealing for witness tubes), **N** refers to the sequential number of the sample (or witness blank) acquisition, and *name* is the informal name applied to that sample and derived from the quadrangle in which the core was acquired. In the case of a witness blank acquisition, ***name*** is simply "WB" followed by the sequential number of the witness blank, starting with 1 and incrementing (e.g. WB1).

The same naming scheme is used for paired samples (i.e., two cores acquired with one associated STOP list execution; see below for definition of STOP list), except sol, N, and name all refer to the second member of the pair.

In typical usage the sample ***name*** alone is sufficient to uniquely identify a specific core. Because paired samples share a STOP list data set, when describing characteristics that refer to both members of paired samples, hyphenation of sample names will provide clarity: e.g., ***name1-name2.***

Date of Coring (or Exposure-Activation-Sealing)

This is the calendar date on which the corer was placed on the rock surface to begin acquisition. Ordinarily, coring is completed in one sol. In the case of a witness blank, the dates of initial exposure, activation (inner seal puncture), and sealing are indicated.

Estimated Volume Recovered

The rock volume (V_{rock}) estimate is derived from the penetration depth of the volume probe, a rod inserted into the tube after sample acquisition (in practice the tube is manipulated while the rod is fixed in place). Volume is computed from the implied length of sample multiplied by an assumed cylindrical cross section corresponding to the coring bit inner diameter d=13.4 mm. The core itself has d=13 mm; the 0.4 mm difference in diameter between the bit and the core is assumed to be filled by cuttings and so contributes to acquired rock volume. A full length core is typically 6 cm long, though shorter lengths can be commanded and will sometimes be all that is acquired. Note that void spaces between core fragments may exist, such that the true sample volume may be less than this estimate.

Coring Bit Number

Perseverance carries 6 rock coring bits and 2 regolith bits. The bit number used here provides insight to usage history that may be relevant for contamination and cross-contamination assessment.

Core Orientation

Three pieces of information are needed to orient the core in the Martian geographic frame (also known as the SITE frame) (Fig. 1). First, *two angles orient the core's pointing vector*. Second, the *core's roll* is noted by marking the pre-drilling WATSON image of the core face. The core orientation pointing vector is estimated as equal to the orientation of the coring drill after pre-loading on the core target.

The core pointing vector is quantified by the *azimuth* and *hade*. The azimuth is defined as the clockwise angle of the horizontal projection of the core y-axis, **cy**, from geographic north, **sx**, where the **cy**-axis lies in the martian geographic vertical plane. The hade is defined as the angle of the core face from martian geographic horizontal (**sx**-**sy** plane). These angles are obtained from coring drill and rover body ancillary orientation data at the time of pre-loading of the coring drill.

The core roll is quantified by an angle **α**, defined as the clockwise angle from the WATSON y-axis (**wy**) to **cy** as viewed in the pre-coring WATSON images. WATSON 6-7-cm standoff images are typically used for this purpose.

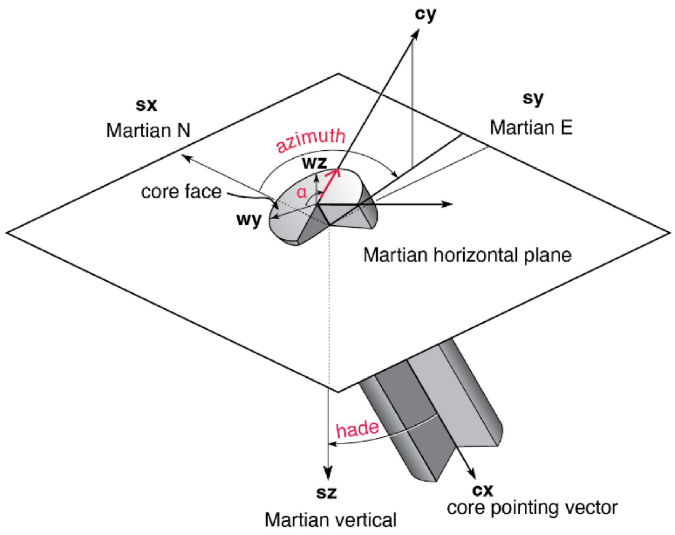

Fig. 1. Orientation system for cores collected by the Perseverance rover. Shaded cylinder is core with cutaway view in lower right quadrant. Martian geographic east, north, and down are the SITE axes, **sx**, **sy** and **sz**, respectively. The pointing vector, **cx**, points into outcrop and is normal to the core face and the **cy** axis lies in the vertical plane. The azimuth is the clockwise angle from geographic north of the projection of the **cy**-axis onto the Martian horizontal (**sx**-**sy**) plane. The hade is the angle of **cx** from vertical. The core roll, **α**, is defined as the clockwise angle from the WATSON pre-coring image y-axis, **wy**, to **cy**; this direction is marked with an arrow on the WATSON image. Adapted from Butler (1992) *Paleomagnetism: Magnetic Domains to Geologic Terranes*, Blackwell Scientific, 319 pp.

Sample Tube, Seal, and Ferrule Serial Numbers

Every sample tube carries a set of serial numbers that will allow downstream identification (Figure 2). Sample Tube serial numbers are inscribed on the side of the tube and on the top of the bearing race (left). The number on the bearing race is partially covered by the seal once it is inserted. Each tube has a unique serial number and this number should be considered the primary identifier for a sample tube. Secondary identifiers are visible in Cachecam images (Figure 2B,C), including the Seal Assembly number and the Seal Ferrule serial number. The latter is non-unique and should not be used to identify a tube.

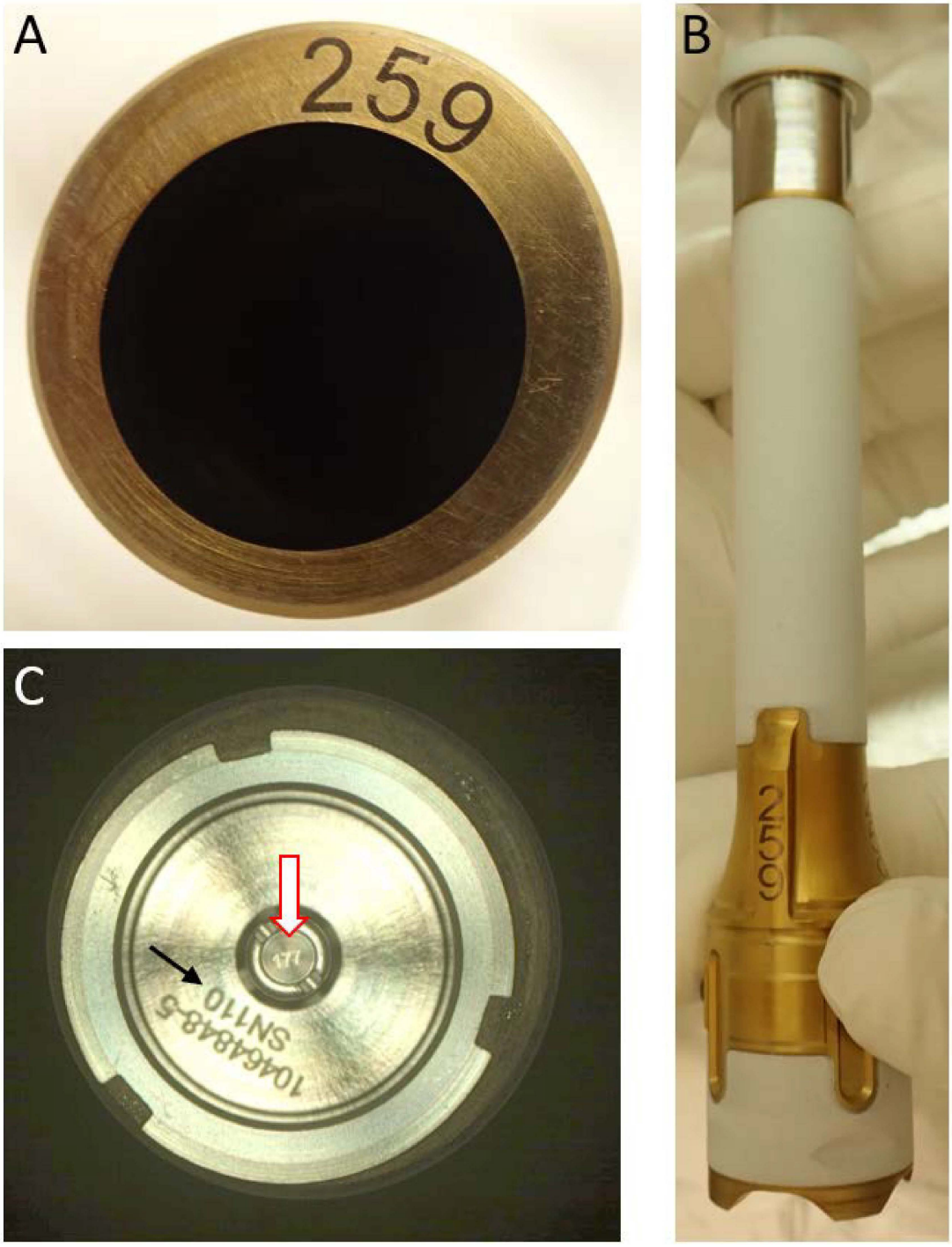

Fig. 2. Sample tube identifiers include the Sample Tube serial number inscribed on the top of the bearing race (A) and the side of the tube (B). Looking at the end of a sealed tube with Cachecam, the Seal Assembly number (red arrow) and the Seal Ferrule serial number (black arrow) are visible.

ACA Temperature at Time of Sealing

Sample tubes are sealed in the Adaptive Caching Assembly (ACA). Mechanisms in this subsystem are actively heated, so sealing occurs at temperatures higher than ambient conditions around the rover. The temperature recorded here is the average of the temperatures recorded on the Sealing Station and the Sample Handling Arm end effector. These temperatures are likely warmer than the sample and the associated head space gas.

Estimated Rover-Ambient Pressure and Temperature at Time of Sealing

Atmospheric temperature and pressure are obtained from MEDA. When MEDA data was not acquired on the same sol as sample sealing (often the case given energy limitations), the average values of pressure and temperature are estimated from the closest sol or sols. The reported temperature is the minimum of MEDA ATS 4 and 5, the sensors located 0.84 m above the surface.

Estimated Amount of Martian Atmosphere Headspace Gas

The estimated amount of headspace gas in moles (n_h) is computed from the ideal gas law and assuming the rover ambient temperature (T) and pressure (P) described above.

$n_h = P\,(V_{tube} - V_{rock})/\,RT$

where R is the gas constant. V_T is assumed to be 12 cm^3. The actual temperature of the gas upon sealing is difficult to estimate because the Adaptive Caching Assembly (ACA) is substantially warmer than rover surroundings, typically by almost 100 K. For consistency we assume rover ambient temperature in this calculation, recognizing that it is an upper limit. A lower limit would be obtained by using the reported ACA temperature in the above equation.

Abrasion Patch Name and Depth

To minimize possible degradation of the sample, much of the data associated with a given sample is acquired on a 5 cm diameter abrasion patch acquired within a few tens of cm of the coring site, and in the same lithology. This IR entry gives the name of that patch and its depth relative to the highest topographic feature in the 5 cm diameter circle that was abraded.

Anomalous Behavior

This entry highlights noteworthy deviations from the standard sampling activities or their expected results.

Additional Notes:

STOP List

To expedite the sample collection and acquisition process, the Mars 2020 Team developed a minimum set of observations to be performed in association with each sample. This Standardized Observation Protocol, or STOP list, was encoded into an optimized sample sol path for efficient and repeatable execution. STOP list observations form the main data set for each sample's Initial Report. A standardized set of observations on each sample permits a templatized Initial Report format. Although the STOP list is likely to evolve as the team learns what observations provide highest science value, it is the intention that the overall format be retained.

Instrument and Mission References

Allwood, Abigail C., Lawrence A. Wade, Marc C. Foote, William Timothy Elam, Joel A. Hurowitz, Steven Battel, Douglas E. Dawson, et al. "PIXL: Planetary Instrument for X-Ray Lithochemistry." *Space Science Reviews* 216, 134. https://doi.org/10.1007/s11214-020-00767-7.

Balaram, J., MiMi Aung, and Matthew P. Golombek. "The Ingenuity Helicopter on the Perseverance Rover." *Space Science Reviews* 217, 56. https://doi.org/10.1007/s11214-021-00815-w.

Bell, J. F., J. N. Maki, G. L. Mehall, M. A. Ravine, M. A. Caplinger, Z. J. Bailey, S. Brylow, et al. "The Mars 2020 Perseverance Rover Mast Camera Zoom (Mastcam-Z) Multispectral, Stereoscopic Imaging Investigation." *Space Science Reviews* 217, 24. https://doi.org/10.1007/s11214-020-00755-x.

Bhartia, Rohit, Luther W. Beegle, Lauren DeFlores, William Abbey, Joseph Razzell Hollis, Kyle Uckert, Brian Monacelli, et al. "Perseverance's Scanning Habitable Environments with Raman and Luminescence for Organics and Chemicals (SHERLOC) Investigation." *Space Science Reviews* 217, 58. https://doi.org/10.1007/s11214-021-00812-z.

Farley, Kenneth A., Kenneth H. Williford, Kathryn M. Stack, Rohit Bhartia, Al Chen, Manuel de la Torre, Kevin Hand, et al. "Mars 2020 Mission Overview." *Space Science Reviews* 216, 142. https://doi.org/10.1007/s11214-020-00762-y.

Hamran, Svein-Erik, David A. Paige, Hans E. F. Amundsen, Tor Berger, Sverre Brovoll, Lynn Carter, Leif Damsgård, et al. "Radar Imager for Mars' Subsurface Experiment—RIMFAX." *Space Science Reviews* 216, 128. https://doi.org/10.1007/s11214-020-00740-4.

Hayes, Alexander G., P. Corlies, C. Tate, M. Barrington, J. F. Bell, J. N. Maki, M. Caplinger, et al. "Pre-Flight Calibration of the Mars 2020 Rover Mastcam Zoom (Mastcam-Z) Multispectral, Stereoscopic Imager." *Space Science Reviews* 217, 29. https://doi.org/10.1007/s11214-021-00795-x.

Hecht, M., J. Hoffman, D. Rapp, J. McClean, J. SooHoo, R. Schaefer, A. Aboobaker, et al. "Mars Oxygen ISRU Experiment (MOXIE)." *Space Science Reviews* 217, 9. https://doi.org/10.1007/s11214-020-00782-8.

Kinch, K. M., M. B. Madsen, J. F. Bell, J. N. Maki, Z. J. Bailey, A. G. Hayes, O. B. Jensen, et al. "Radiometric Calibration Targets for the Mastcam-Z Camera on the Mars 2020 Rover Mission." *Space Science Reviews* 216, 141. https://doi.org/10.1007/s11214-020-00774-8.

Maki, J. N., D. Gruel, C. McKinney, M. A. Ravine, M. Morales, D. Lee, R. Willson, et al. "The Mars 2020 Engineering Cameras and Microphone on the Perseverance Rover: A Next-Generation Imaging System for Mars Exploration." *Space Science Reviews* 216, 137. https://doi.org/10.1007/s11214-020-00765-9.

Manrique, J. A., G. Lopez-Reyes, A. Cousin, F. Rull, S. Maurice, R. C. Wiens, M. B. Madsen, et al. "SuperCam Calibration Targets: Design and Development." *Space Science Reviews* 216, 138. https://doi.org/10.1007/s11214-020-00764-w.

Maurice, S., R. C. Wiens, P. Bernardi, P. Caïs, S. Robinson, T. Nelson, O. Gasnault, et al. "The SuperCam Instrument Suite on the Mars 2020 Rover: Science Objectives and Mast-Unit Description." *Space Science Reviews* 217, 47. https://doi.org/10.1007/s11214-021-00807-w.

Moeller, Robert C., Louise Jandura, Keith Rosette, Matt Robinson, Jessica Samuels, Milo Silverman, Kyle Brown, et al. "The Sampling and Caching Subsystem (SCS) for the Scientific Exploration of Jezero Crater by the Mars 2020 Perseverance Rover." *Space Science Reviews* 217, 5. https://doi.org/10.1007/s11214-020-00783-7.

Newman, C. E., M. de la Torre Juárez, J. Pla-García, R. J. Wilson, S. R. Lewis, L. Neary, M. A. Kahre, et al. “Multi-Model Meteorological and Aeolian Predictions for Mars 2020 and the Jezero Crater Region.” *Space Science Reviews* 217, 20. https://doi.org/10.1007/s11214-020-00788-2.

Pla-García, Jorge, S. C. R. Rafkin, G. M. Martinez, Á. Vicente-Retortillo, C. E. Newman, H. Savijärvi, M. de la Torre, et al. “Meteorological Predictions for Mars 2020 Perseverance Rover Landing Site at Jezero Crater.” *Space Science Reviews* 216, 148. https://doi.org/10.1007/s11214-020-00763-x.

Rodriguez-Manfredi, J. A., M. de la Torre Juárez, A. Alonso, V. Apéstigue, I. Arruego, T. Atienza, D. Banfield, et al. “The Mars Environmental Dynamics Analyzer, MEDA. A Suite of Environmental Sensors for the Mars 2020 Mission.” *Space Science Reviews* 217, 48. https://doi.org/10.1007/s11214-021-00816-9.

Stack, Kathryn M., Nathan R. Williams, Fred Calef, Vivian Z. Sun, Kenneth H. Williford, Kenneth A. Farley, Sigurd Eide, et al. “Photogeologic Map of the Perseverance Rover Field Site in Jezero Crater Constructed by the Mars 2020 Science Team.” *Space Science Reviews* 216, 127. https://doi.org/10.1007/s11214-020-00739-x.

Wiens, Roger C., Sylvestre Maurice, Scott H. Robinson, Anthony E. Nelson, Philippe Cais, Pernelle Bernardi, Raymond T. Newell, et al. “The SuperCam Instrument Suite on the NASA Mars 2020 Rover: Body Unit and Combined System Tests.” *Space Science Reviews* 217, 4. https://doi.org/10.1007/s11214-020-00777-5.

Cite as:

K.A. Farley and K.M. Stack, Mars 2020 Initial Reports – Volume 2 Delta Front Campaign, 2023. Include Digital Object Identifier (DOI) associated with this document on the NASA Planetary Data System.

Revision History:

This is release 3.1 of Volume 2 Delta Front Campaign Initial Reports. Release 2 differs from release 1 in that it replaces an erroneous Figure 17 in the Kukaklek IR with the correct figure. Release 3 differs from release 2 in that the scale bars in all figures in the core orientation section have been corrected. Core orientations were revised in Release 3.1.

Acknowledgement:

This research was carried out at the Jet Propulsion Laboratory, California Institute of Technology, under a contract with the National Aeronautics and Space Administration (80NM0018D0004).

INITIAL REPORT

M2020-490-11 *Swift Run*

Sample Designation: M2020-490-11 *Swift Run*

Date of Coring: 6-July-2022

Mars Time of Sample Core Sealing: 21:23 LMST, Sol 490, Ls 261.4

Latitude (N), Longitude (E), Elevation: 18.458931˚, 77.40617078˚, –2520.185m

Campaign: Delta Front

Region of Interest: *Hawksbill Gap*

Lithology: Fine to medium-grained sandstone deposited in a prodelta setting. Poorly-sorted subrounded to subangular grains range from <0.03 to 2 mm in diameter. Detrital fragments have diverse compositions, including olivine and pyroxene grains, possible alteration minerals rich in Si and Al (phyllosilicates), and lithic fragments. A fine-grained matrix or cement appears depleted in Si and Al and enriched in Fe and Mg, much of which is interpreted to be Fe-Mg carbonate. Evidence of hydration, Na and Cl salts, and oxidation (ferric Fe) were also detected.

Estimated Volume Recovered: 9.4 cm^3

Coring Bit Number: 1

Core Orientation: hade = 16.63°; azimuth = 355.94°; core roll = 220.71°

Sample Serial Numbers: Tube SN186; Seal SN188; Ferrule SN101

ACA Temperature at Time of Sealing: 40°C

Estimated Rover-Ambient Pressure and Temperature at Time of Sealing: 817 Pa, 208 K

Estimated Amount of Martian Atmosphere Headspace Gas: 1.23×10^{-6} mol

Anomalous Behavior: None

Abrasion Patch Name and Depth: *Thornton Gap*, 7 mm

August 29, 2022

D. L. Shuster, K. A. Farley, T. Bosak, B. A. Cohen, A. D. Czaja, E. M. Hausrath, L. E. Mayhew, S. Siljeström, J. I. Simon, K. M. Stack, A. Treiman, B. P. Weiss, B. V. Wogsland, M.-P. Zorzano, H.E.F. Amundsen, F. J. Calef III, D. Flannery, J. Hurowitz, T. Kizovski, L. Mandon, E. N. Mansbach, D.A.K. Pedersen, M.M. Tice, A. Udry, S. Van Bommel, K. Williford, and the Mars 2020 Team

Summary Description

Swift Run and Skyland, the pair of cores representing the fifth sample target of the Mars 2020 mission, were collected from *Skinner Ridge*, an outcrop of the *Lower Rockytop* member of the *Hawksbill Gap* region of the western Jezero delta front. *Skinner Ridge* lies at the base of ~6.5 vertical meters of exposed sedimentary rock layers of *Rockytop* (**Figures 1 - 4**) and is likely to be in place. The outcrop is a horizontally layered, medium-grained clastic sedimentary rock and has a similar sandstone lithology as *Betty's Rock*, a float block of the *Upper Rockytop* member; its upper surface has low relief (**Figures 3, 5**). We sampled this sedimentary rock because it is from a low stratigraphic position within the western Jezero delta and contains a heterogeneous population of detrital materials deposited into the delta when a lake was present. At least some of these materials most likely derived from outside Jezero crater in the Neretva Vallis watershed. The *Swift Run* and *Skyland* cores were collected from a stratigraphic position that is ~3 vertical meters above the *Hazeltop* and *Bearwallow* cores collected from the *Hogwallow Flats* member, only ~20 m to the southwest (**Figures 2, 4**).

The *Thornton Gap* abrasion patch, acquired on *Skinner Ridge*, is heterogeneous in its color, composition, and grain size, with detrital clasts ranging from <0.03 to ~2 mm, and a fine-grained cement and/or chemical weathering phases. The detrital fragments have diverse mineralogy and lithology, including igneous grains (olivine, pyroxene), lithic fragments, and alteration products rich in Al and Si (possibly chlorite). The fine-grained matrix is depleted in Si and Al and enriched in Fe and Mg, much of which is interpreted to be Fe-Mg carbonate. Evidence of hydration, and potentially Na and Cl salts and oxidation (ferric Fe) were also detected. The presence of thin horizontal layers and mm-scale grains as well as the absence of interlocking igneous grains support the interpretation that the *Swift Run* and *Skyland* cores are samples of a sandstone.

The returned sample science objectives of the *Swift Run* and *Skyland* cores include geochronology (both of detrital fragments and secondary cements/alteration), paleomagnetism, geochemistry, provenance lithology, thermochronology and the history of water and water–rock interactions both in the catchment prior to and during sedimentary deposition, and in the delta sediments after deposition. The heterogeneous detrital clast distribution, including clast sizes up to mm scale, would enable a wide variety of investigations to be performed on the sample upon its return. Mechanically-separable detrital components (i.e., >250 μm) in the delta sediments can be used to study the source rocks in the watershed feeding the crater, and to constrain the timing of delta deposition. For example, geochronology of detrital clasts will place an *upper* bound on delta deposition timing. In addition, geochronology of cements that precipitated after deposition may place a *lower* bound on delta deposition timing.

The *Swift Run* core was collected on Sol 490, has a core length of 67 mm, and based on Cachecam and ZCAM images appears to be a coherent piece of rock. The *Skyland* core was collected on Sol 495, has a core length of 58.5 mm, and based on Cachecam and ZCAM images also appears to be a coherent piece of rock.

Stratigraphic and Geologic Context

The *Lower Rockytop* member, which contains *Skinner Ridge*, is stratigraphically above the *Hogwallow Flats* member and below the *Upper Rockytop* member cropping out in the *Hawksbill Gap* region of the western Jezero delta front (**Figures 1 - 4**). *Skinner Ridge* is stratigraphically ~17 meters above the lowest exposed delta member, *Devils Tanyard*, which defines the base of the *Shenandoah* formation (**Figure 4**). Based on orbital mapping, *Devils Tanyard* lies at the contact between the Crater floor fractured rough (*Cf-fr*) and the Delta thinly layered (*D-tnl*) photogeologic units mapped in orbiter images (Stack et al., 2020). *Skinner Ridge* is ~44 vertical meters below the nearby *Franklin Cliffs* ~0.16 km to the northeast, and ~126 vertical meters below the highest exposed delta surfaces ~3.2 km to the northwest. Thus, *Skinner Ridge* is from a relatively low stratigraphic position within the exposed delta.

The *Lower* and *Upper Rockytop* members are expressed as a south facing, roughly east-west trending ~7 m vertical scarp. The scarp has continuous planar layering clearly exposed in the upper ~3 m (*Upper Rockytop* member), and less continuous layers (*Lower Rockytop* member including *Skinner Ridge* itself) more poorly exposed in the lower ~3 m (**Figure 3**). Based on ZCAM and SCAM RMI images of the scarp and *Betty's Rock*, the *Upper Rockytop* member contains pebbles and cobbles (up to 20 mm), many of which are clearly rounded. Below the cliff-forming *Lower and Upper Rockytop* members, there are several visibly distinct rock horizons at the base of the delta, e.g., *Hogwallow Flats*, an interval consisting of light-toned strata cropping out above and below thin, platy-bedrock that appears darker-toned in orbiter images. This interval can be traced laterally in orbiter images at least ~1.5 km along the delta front. Some of the lower units form subtle benches, e.g., the *Boston Knob* member (**Figure 2**), while others weather recessively (e.g., *Hughes River Gap* and *Devils Tanyard* members). Overall, these different horizontal layers indicate that the explored stratigraphy of the delta front is comprised of several distinct units and facies, that are largely, if not entirely, sedimentary in origin. This stratigraphy appears to be representative of the base of the exposed delta. However, because the contact between this stratigraphy and the crater floor basement rocks is covered by regolith, the oldest units deposited on the crater floor basement rocks may not be exposed.

Operations

Sampling objectives of the *Delta Front Campaign* included the collection of both fine-grained (< 0.06 mm) sedimentary rocks, ideally rich in clay minerals, and coarse-grained sedimentary rocks containing lithologically diverse clasts. The *Swift Run* and *Skyland* cores were collected to fulfill the coarse-grained sedimentary rock sampling objective of the campaign.

The Delta Front Campaign planning process occurred during February and March of 2022 and identified four paired samples to be collected from relatively low stratigraphic positions within the western Jezero delta, and prior to depositing the initial cache: (1 & 2) two different samples of lacustrine sediments with potential for biosignature preservation (ideally fine-grained mudstone and/or fine sandstone containing clay minerals and reduced phases indicative of anoxic preservation conditions), (3) one relatively coarse-grained sedimentary sample (ideally containing medium sand size particles, >250 μm, with a lithologic diversity of detrital material) for delta deposition geochronology and Jezero catchment provenance studies, and (4) one regolith sample.

On Sol 424, Perseverance encountered the first delta rock outcrops of the mission at a site called *Enchanted Lake* at the base of *Cape Nukshak* (**Figure 1**). *Enchanted Lake* contained the *Kaguyak* sandstone and overlying *Amalik* fine-grained, gray rocks. SCAM RMI observations at *Cape Gull* (on *Kaguyak*) and *Hook Glacier* (on *Amalik*) revealed sedimentary facies consistent with distal subaqueous deposition. The team then decided to explore a laterally equivalent section of the lower delta exposed in the *Hawksbill Gap* region with the intention to execute proximity science and sampling activities (**Figure 1**). From Sols 426-441, Perseverance drove over 700 m from *Cape Nukshak* to *Hawksbill Gap*, arriving at the lowest exposed delta deposits of *Devils Tanyard* on Sol 441. Between Sols 441 and 474, Perseverance drove up-section through the following delta members while collecting remote sensing data and seeking outcrops suitable for potential proximity science and sampling: *Devils Tanyard*, *Hughes River Gap, Boston Knob*, *Hogwallow Flats*, and *Rockytop* (**Figure 2, 4**).

Although remote sensing observations of *Devils Tanyard* and *Sunset Hill* (*Hughes River Gap* member*)* outcrops were consistent with fine- to medium-grained sandstones, throughout this interval the science and engineering teams struggled to locate outcrops suitable for proximity science. An abrasion of *Rose River Falls* within the *Hughes River Gap* member at *Sunset Hill* was conducted on Sol 452 but resulted in displacement of the rock into unconsolidated fine-grained regolith, precluding PIXL placement and other proximity science activities. On Sol 463, Perseverance arrived at *Hogwallow Flats*. Natural surface SCAM observations of *Smith Mountain* revealed a fine-grained sedimentary rock with indications of sulfate, phyllosilicates, and hydration. An abrasion of *Elkwallow Flats* within *Hogwallow Flats* was conducted on Sol 471. However, due to the rock breaking during abrasion, neither PIXL nor SHERLOC could be placed for proximity science observations. Thus, the science team decided to move Perseverance to *Betty's Rock* on Sol 474, while the science and engineering teams studied existing images to identify other *Hogwallow Flats* outcrops more likely to yield success for proximity science and sampling.

Natural surface WATSON (*Blackrock*) and SCAM (*Fourway*) images of *Betty's Rock* revealed a sedimentary rock with rounded, mm-scale pebbles of a range of apparent lithologies, although the rock was unsuitable for abrasion or sampling. Thus, the team moved Perseverance to a comparable, but in-place, outcrop of the *Lower Rockytop* member.

On Sol 477, Perseverance arrived at the *Skinner Ridge* outcrop. On Sol 480, we selected four potential targets for abrasion and sampling (*Skyland, Swift Run, Stony Man, and Thornton Gap*) and acquired WATSON images of each. *Thornton Gap* was selected as the abrasion target; the abrasion was successfully conducted on Sol 482. Initial images of the abrasion patch revealed sand-sized clasts displaying a range of colors and degrees of rounding indicative of diverse lithology and sediment transport, like that observed in *Betty's Rock*. PIXL and SHERLOC data were acquired on *Thornton Gap* on Sol 489. Remote-sensing and abraded proximity science observations revealed that *Skinner Ridge* possessed multiple desired characteristics for a coarse sedimentary rock sample including: (1) sand-sized grains or clasts >250 μm; (2) lithologically diverse detrital grains; (3) pebble-sized clasts; (4) sediment associated with delta deposition; (5) a relatively low stratigraphic position in the delta (see above); (6) the presence of secondary cements; and (7) some detrital grains that express minimal aqueous alteration. Thus, the team decided to move forward with sampling and began executing the STOP list activities. We acquired the *Swift Run* core on Sol 490 and, after a brief nuisance fault on Sol 494, we acquired the *Skyland* core on Sol 495. The *Swift Run* and *Skyland* cores are the first sedimentary rock samples collected by the Perseverance Rover. Interpreted to be medium grained sandstones, these

samples fulfill the desired characteristics for the delta front coarse-grained sediment sample and satisfy the campaign objective of collecting a single pair of such cores prior to the initial cache placement.

Perseverance processed a Witness Tube on Sols 499-500, then drove away from the *Skinner Ridge* workspace towards *Wildcat Ridge* on Sol 501.

Figure 1 | Regional context of Perseverance rover operations. (a) Geologic map with topography showing Jezero crater floor and western delta units, as defined by Stack et al. 2020. (b) Inset map showing the Delta Front Campaign regions of interest, *Cape Nukshak* and *Hawksbill Gap*, the *Swift Run (*and paired core *Skyland)* core location (red point), and rover drive route (white lines). Elevation contours are meters relative to the Mars aeroid.

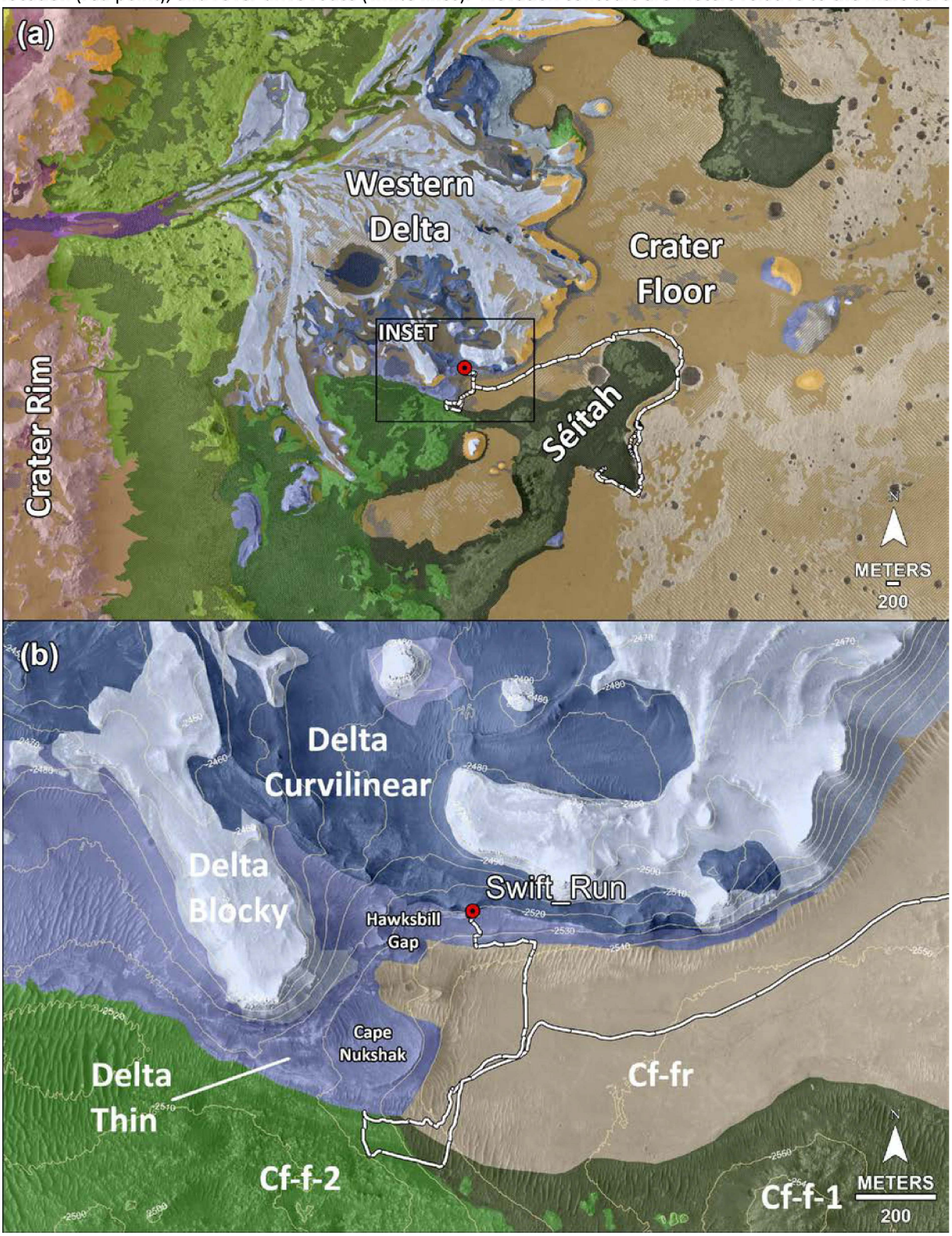

Figure 2 | Local context of Perseverance rover operations during *Swift Run* and *Skyland* sampling. HIRISE map showing the locations of sample collection together with other notable outcrops investigated during the sol path leading to *Skinner Ridge*. Location of the *Swift Run* (and *Skyland*) core indicated with a red circle.

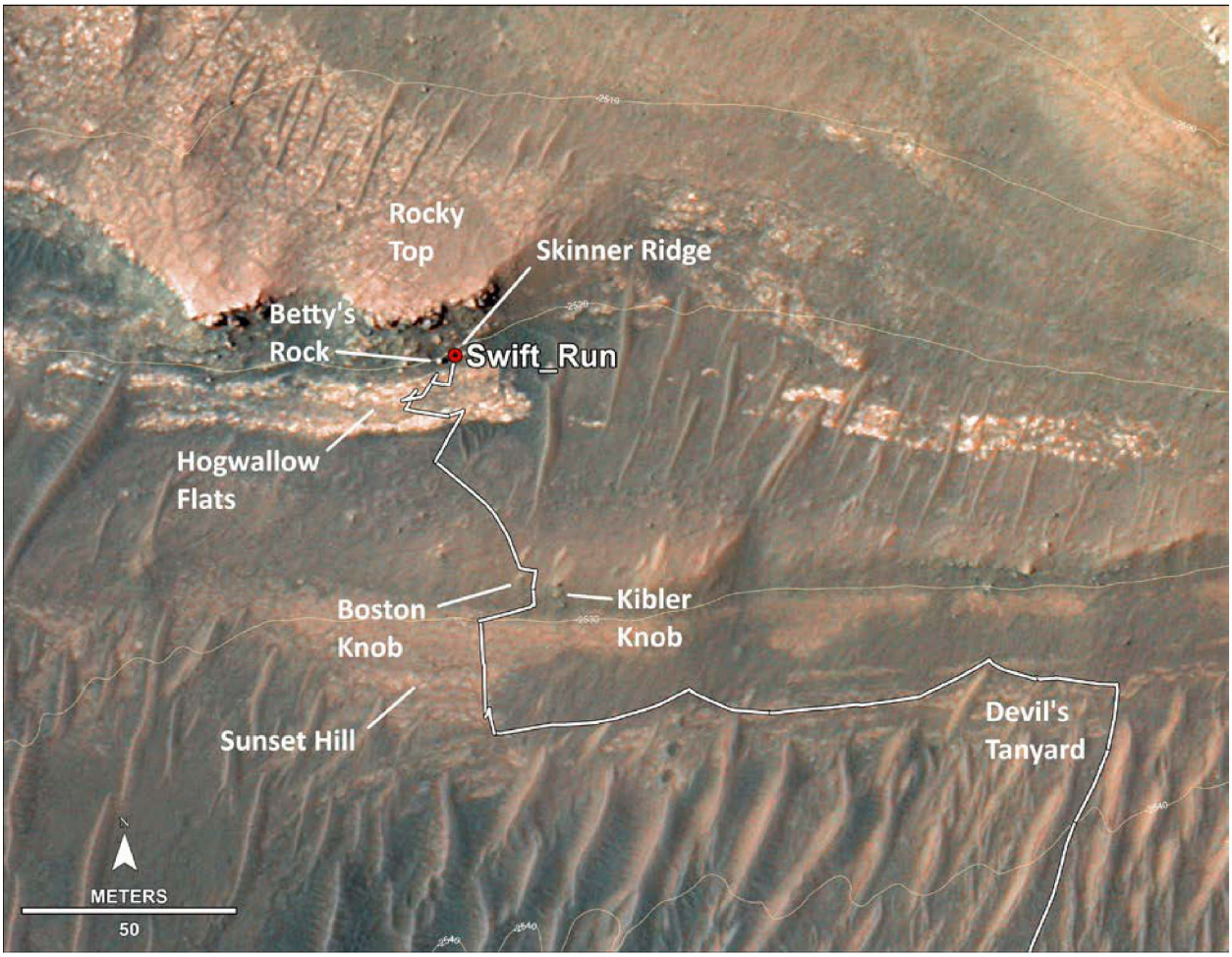

Figure 3 | View of the layered *Rockytop* ridge within the Hawksbill Gap delta front stratigraphy. The *Skinner Ridge* outcrop is located at the base of the *Lower Rockytop* unit and overlies *Hogwallow Flats*. The *Franklin Cliffs* in the distance (upper right) are comprised of stratigraphically higher delta units. Lower stratigraphic units and crater floor lie below the bottom of the image. The *Skinner Ridge* block is ~1 m across; the vertical distance from *Skinner Ridge* to the highest point of *Upper Rockytop* seen in this image is ~6.5 m. View is to the NW; Sol 459, zcam08479, Z110 enhanced color.

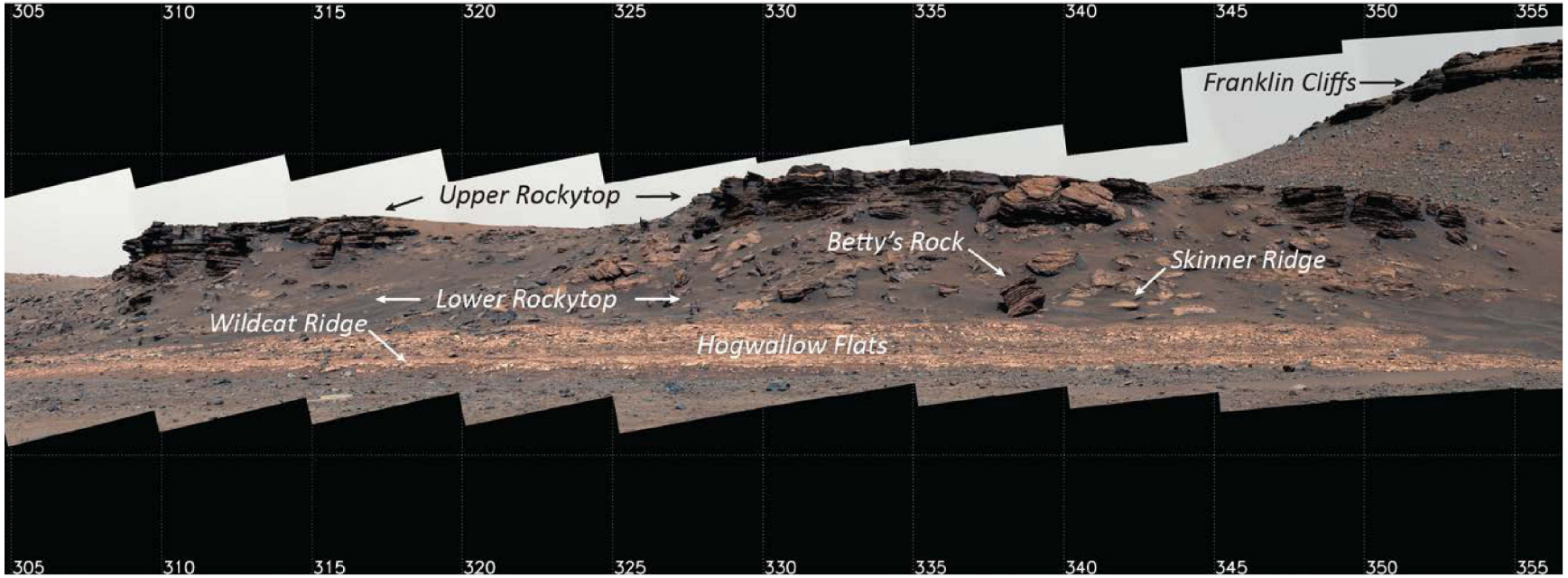

Figure 4 | Stratigraphic column of the *Shenandoah* formation explored at *Hawksbill Gap* between sols 439-538. c/si/vf = clay/siltstone/very fine sandstone; f = fine sandstone; m = medium sandstone; C = coarse sandstone; vC = very coarse sandstone.

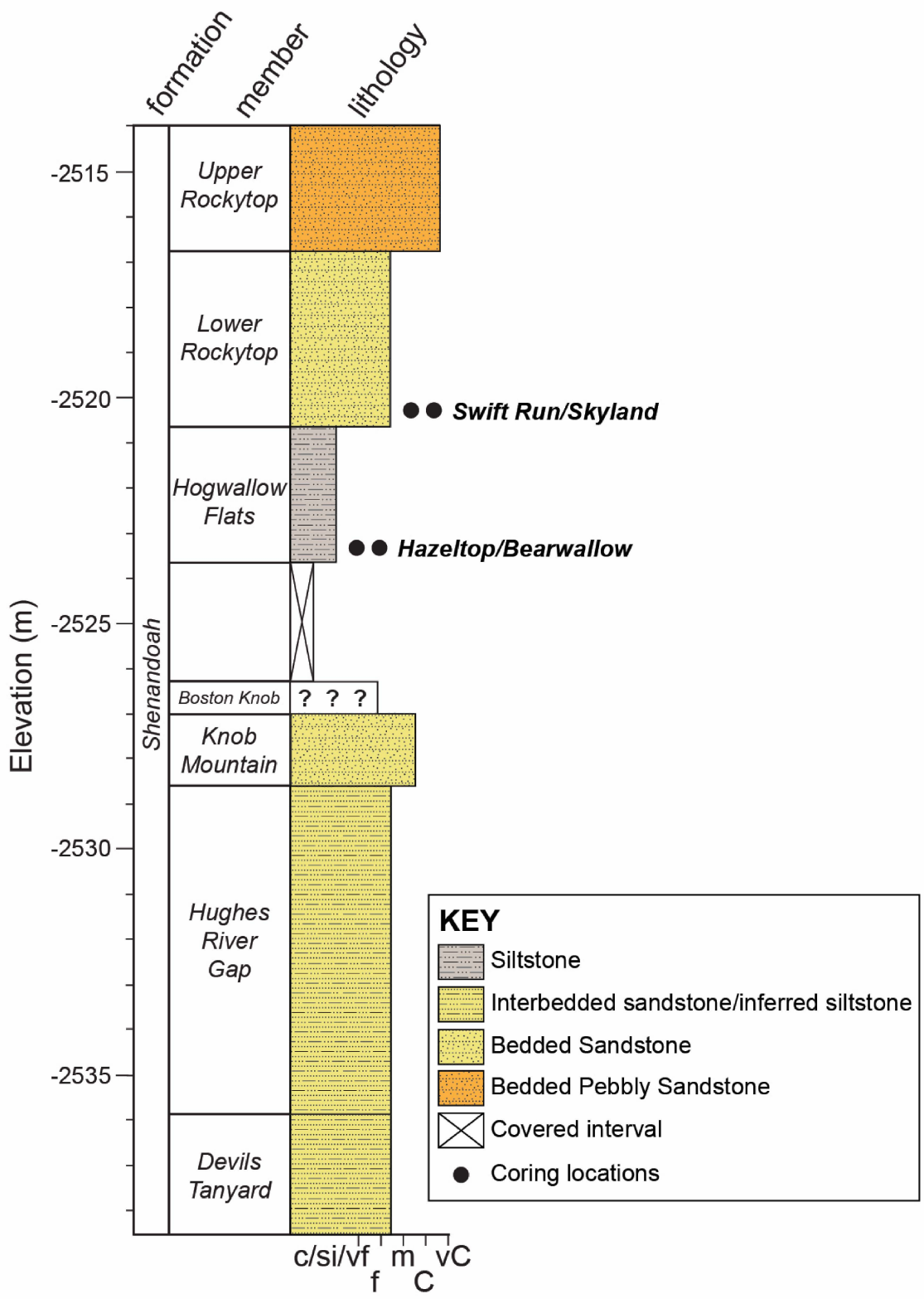

Sample-Related Observations

Workspace Images

Figures 3 and 5a show Mastcam-Z mosaics of the *Skinner Ridge* outcrop within its local context of *Lower Rockytop*. **Figure 5b** shows a Mastcam-Z workspace mosaic with the *Thornton Gap* abrasion patch and *Swift Run* core tailings pile. The *Skyland* sample was collected after this image was taken. The surface of the *Skinner Ridge* outcrop is parallel to bedding and very dusty. Bedding is visible on the downhill side of the block. Bedding within *Skinner Ridge* is around 1 cm or less in thickness. Layers alternate from more to less recessive, like *Betty's Rock* (**Figure 3**), but all layers appear to be coherent. Grains (<1 mm) are visible in some layers whereas other layers are completely covered by a dark coating. Some coatings appear to be localized to a specific bed, similar to other observations on *Rockytop* (e.g., RMI of *Buck Ridge*).

Although visibility is limited by sandy regolith surrounding the block, Skinner Ridge bedding appears parallel to the majority of bedding on *Rockytop*. This suggests that the *Skinner Ridge* block is in place. Additionally, no significant changes were observed in rock position during abrasion and sampling.

SuperCam RMI images of natural surfaces on *Skinner Ridge* (**Figure 6**) show sand size (mm-scale) grains within a dust covered surface. *Shop Hollow*, **Figure 6a**, is from the bedding-parallel surface and documents the dust coverage of the rock. *Sawlog Ridge* (**Figure 6b)** is an RMI of the raised upslope edge of *Skinner Ridge*. *Oventop Mountain* (**Figure 6c**) shows mm-thick horizontal layering with scalloped edges and some recessive layers. Grains and grain casts (0.1-0.7 mm) are visible, along with a patchy reddish coating like that on the bedding planes of the block. The visible grains in both Mastcam-Z and RMI images are similar in color and size to those observed within the *Thornton Gap* abrasion patch (see below).

Figure 5 | Mastcam-Z context images for *Skinner Ridge*. (a) Mastcam-Z image of the *Rockytop* outcrop with the *Skinner Ridge* outcrop noted by the red arrow; *Betty's Rock* is the large boulder to its left. View is to the NE; Sol 466, zcam08486, Z110 enhanced color. (b) Workspace image after abrading *Thornton Gap* and sampling *Swift Run*. Boxes show approximate locations of the RMIs shown in **Figure 6**. The abrasion patch is 5 cm across; the *Skinner Ridge* block is around 1 m across. Sol 492, zcam08517, Z034 enhanced color.

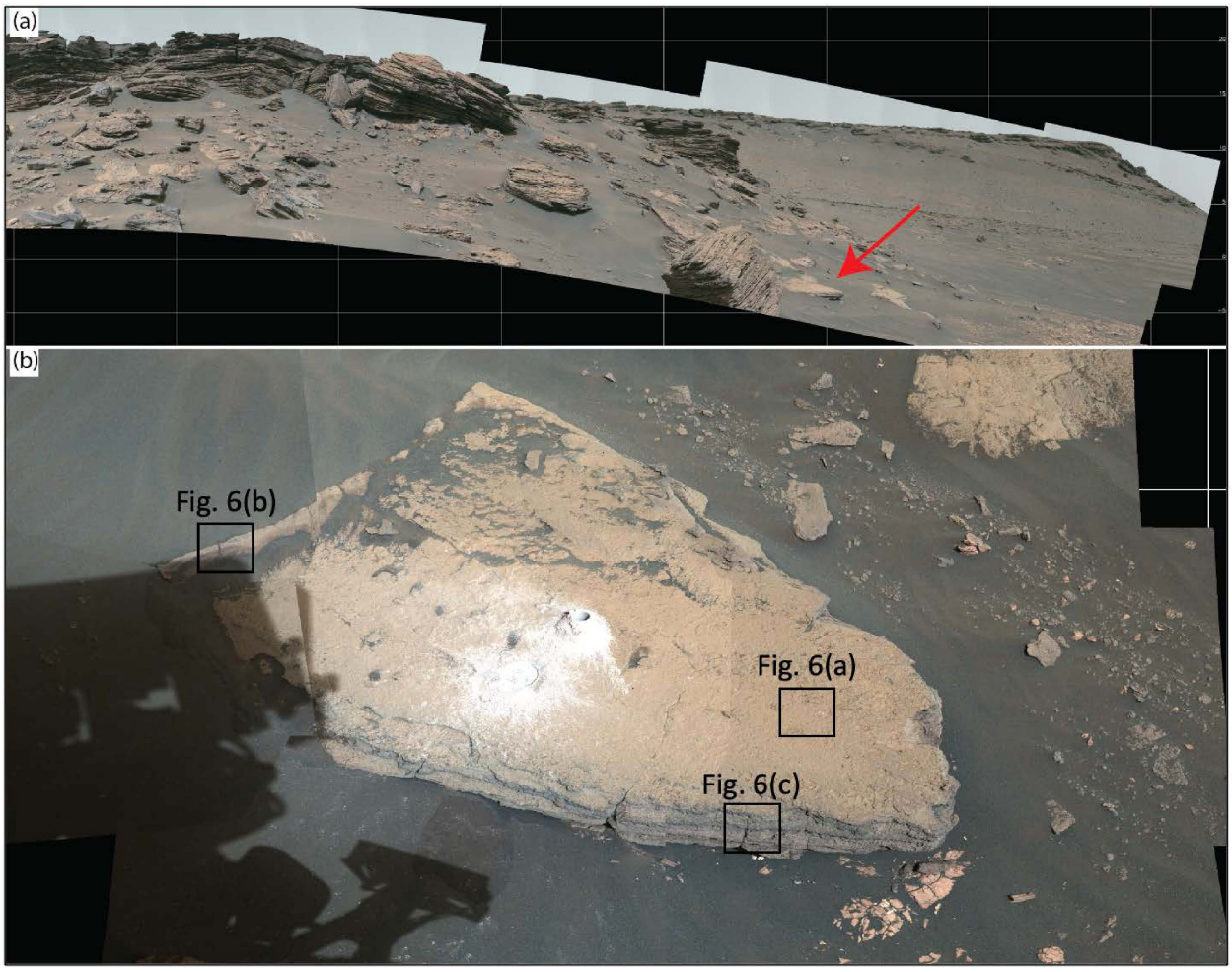

Figure 6 | SCAM RMIs of *Skinner Ridge* natural surfaces. (a) Gaussian stretch of *Shop Hollow* demonstrates a dusty surface. (b) Gaussian stretch of *Sawlog Ridge*, from a higher-standing part of the outcrop; grain boundaries can be discerned in addition to a patchy, reddish-brown coating. (c) Natural color RMI of *Oventop Mountain* shows multiple mm-thick layers with scalloped edges and alternating resistant and recessive layers.

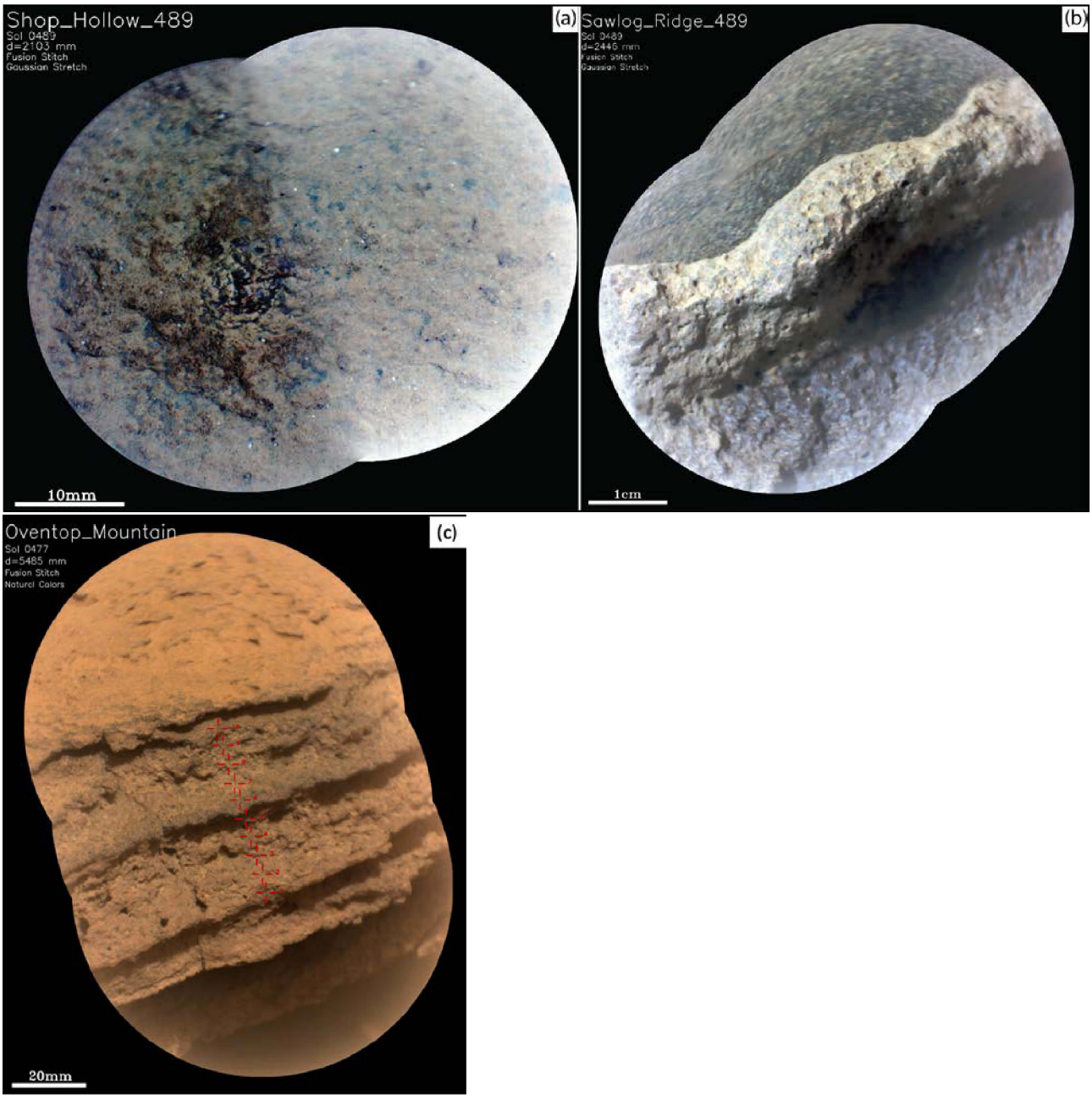

Pre and Post Coring/Abrasion Images

The *Skinner Ridge* outcrop is a light-toned, medium/fine-grained rock (observed grains are <0.03 – 2 mm). The vertical face of *Skinner Ridge* (e.g., **Figure 6c**) exhibits alternations between more prominent and more recessive (and finer-grained) bedding comparable to those seen in *Betty's Rock* and

throughout upper *Hogwallow Flats*. The eastern side of the *Skinner Ridge* rock has a crack and overhang, so the western side was favored for proximity science. The natural surface of *Skinner Ridge* (**Figure 7**) exhibits little relief. Surface fractures are common as are chips that may be flaking off. Dust and regolith are trapped along these fractures and flakes. Wind fluting or polishing is not observed. Individual grains are rarely visible in the planar surfaces, but they are sometimes observable in broken vertical faces.

Figure 7 | WATSON Sol 480 40 cm standoff mosaic with 7 cm insets of the *Swift Run* (core) and *Thornton Gap* (abrasion) locations on the *Skinner Ridge* outcrop.

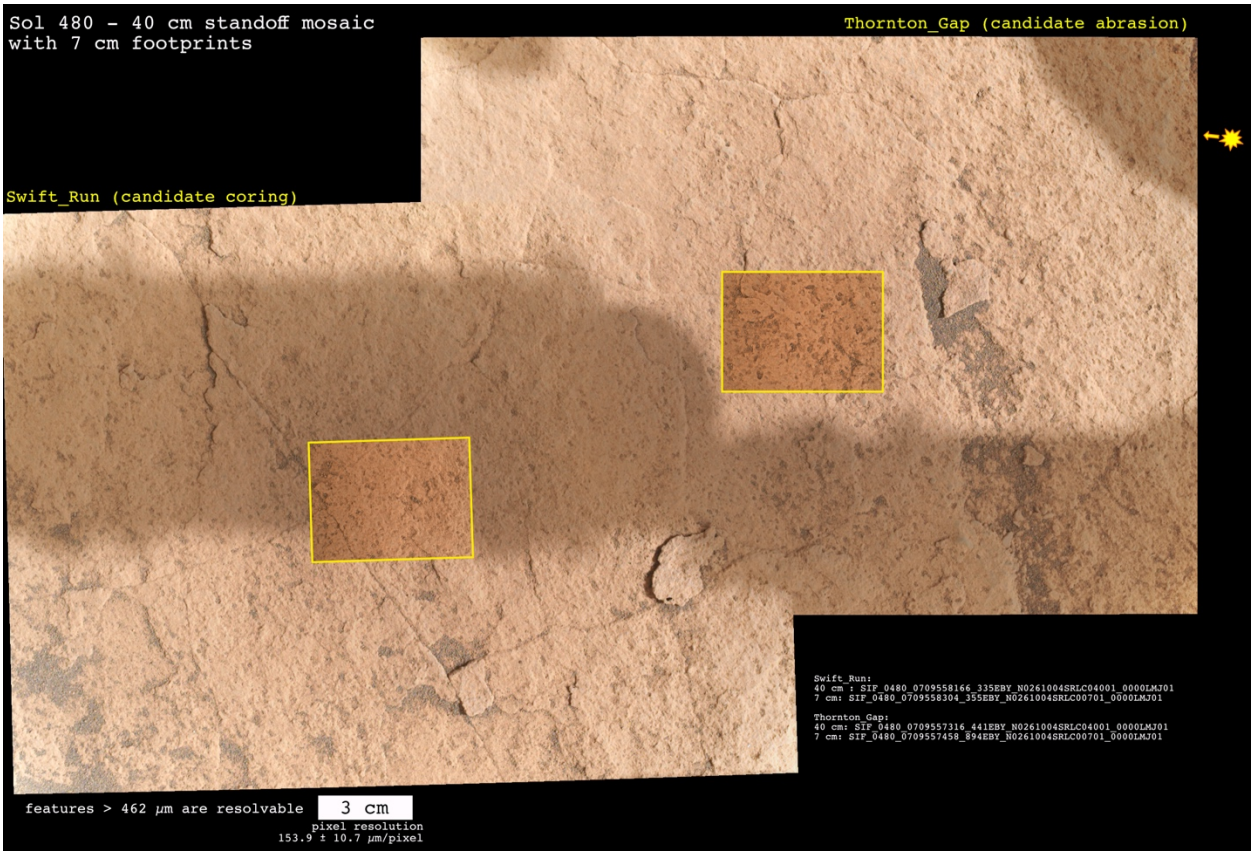

The *Thornton Gap* abrasion patch (to depth ~7 mm; **Figure 8**) shows that the underlying rock is composed of individual grains with a variety of colors and tones. Some parts of the rock appear to be grain-supported, with grains in contact with each other. Other parts of the patch appear to have substantial matrix support between grains. The rock appears to be an immature sandstone containing poorly sorted, detrital minerals from diverse lithologies. The textures observed in *Thornton Gap* differ from the abraded patches of the igneous rocks from the crater floor and indicate sediment transport and cementation of sand-sized grains into the rocks at *Skinner Ridge*. The presence of thin horizontal layers (e.g., **Figure 6c**) and mm-scale grains (**Figures 5 and 7**) as well as the absence of interlocking igneous grains support the interpretation that *Skinner Ridge* is a sandstone.

Figure 8 | WATSON image of *Thornton Gap* abrasion patch.

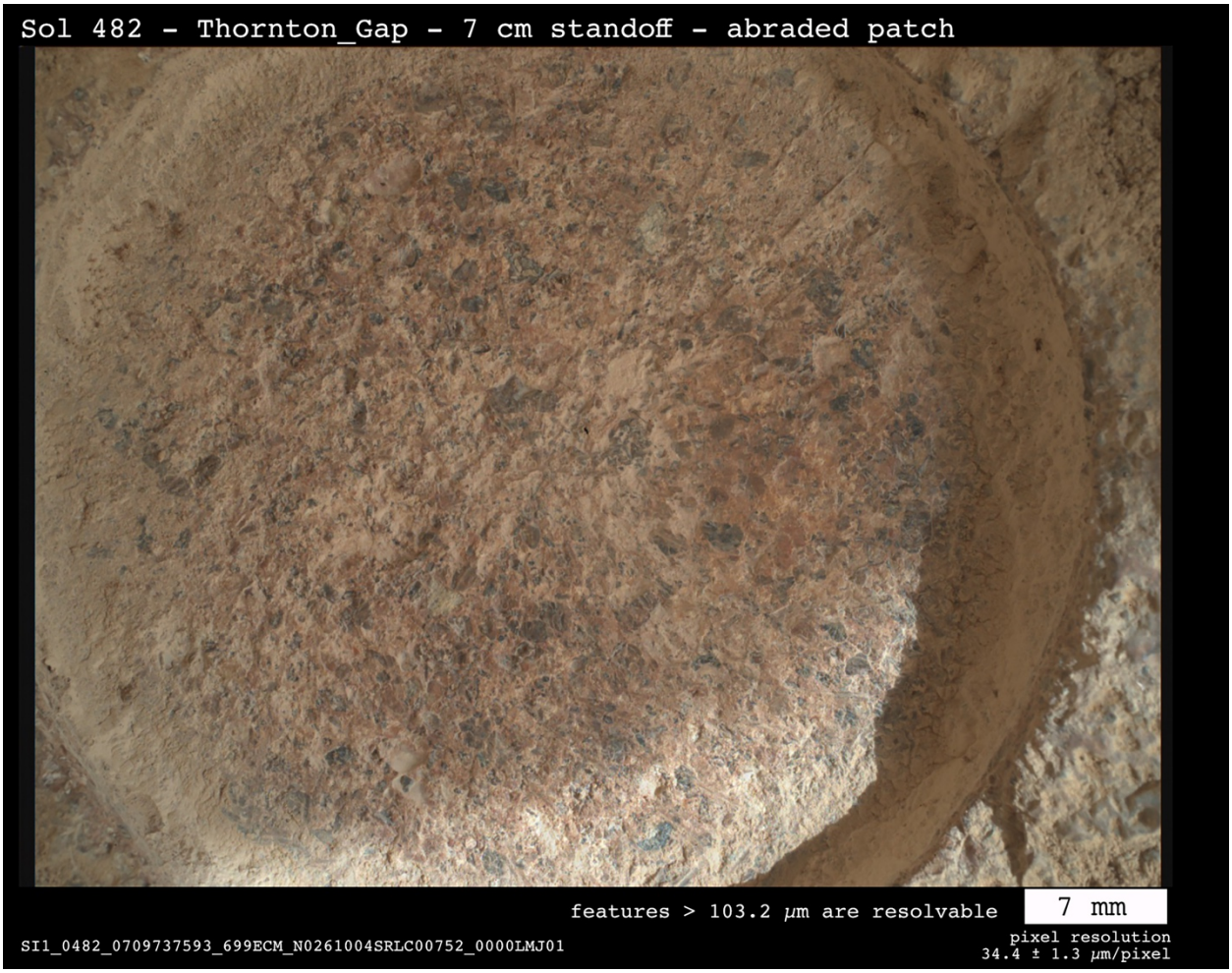

Figure 9 shows the distribution of grain sizes in *Thornton Gap* for grains (n=260) measured at intersection points of a grid with 1 mm spacing projected on a mosaic of SHERLOC ACI images of the abrasion patch. Measured grains range in size from 2 mm down to the limit of ACI resolution (10.1 μm/pixel, enabling objects of >30 μm to be resolved), with an average grain size of 396 μm. This range is consistent with being poorly sorted. The observed grain population has a bimodal distribution, with modes at φ=2 (medium sand) and φ=4 (fine sand), average grain size of φ=2.1 (medium sand) and standard deviation of φ=1.6 (poorly sorted). [$\varphi = -\log_2(D)$, where D is the diameter of a grain in millimeters.] Some of the smaller grains may be components of larger composite grains (e.g., individual mineral grains in a lithic clast). Grains are typically subrounded to subangular (**Figure 8**), with shapes ranging from rounded to angular. A range of grain-scale textures suggest both post-depositional processing (pressure-solution and/or dissolution/replacement) of this rock as well as erosion and deposition of previously aqueously altered materials as clasts within this rock.

Figure 9 | **Grain size distribution for clastic fragments in *Thornton Gap*.** Distribution based on 1 x 1 mm-spacing grid analysis of a mosaic of SHERLOC ACI images of the abrasion. Grain size in φ units: $\varphi = -\log_2(D)$, where D is the diameter of a grain in millimeters.

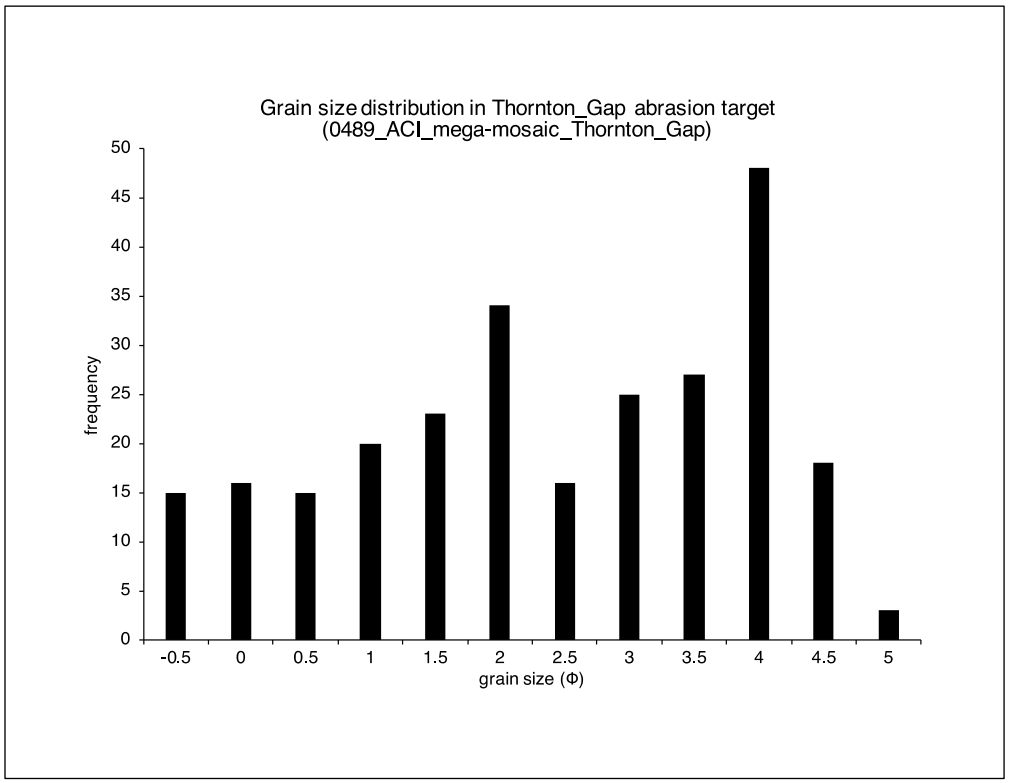

ZCAM observations of the *Skinner Ridge* natural surface, abrasion patch, and tailings are shown in **Figure 10**. The ZCAM multispectral data highlight a diversity of compositions. We observe dark (black) grains, pinkish grains that exhibit spectral signatures of ferric iron, and bright (white) grains that show evidence of hydration, a strong ferric iron signature at 528 nm, and a weaker ferric-iron absorption at 866 nm. A negative slope observed in the intensity spectrum at the longest wavelengths (between 978 and 1022 nm) indicates possible hydration. The abraded surface and tailings have a strong ferric iron signature.

The *Swift Run* and *Skyland* core-end images (**Figure 11**) show the coarse-grained nature of the rock and confirm that the reddish staining/oxidation seen in the abrasion patch is pervasive throughout the rock.

Figure 10 | (left) Mastcam-Z L0 natural color image of the *Thornton Gap* abrasion patch; (right) Mastcam-Z 528 nm band depth map, where the color scale corresponds to the strength of the 528 nm absorption band due to ferric iron, an indication of oxidation. The abrasion patch is approximately 5 cm in diameter, for scale.

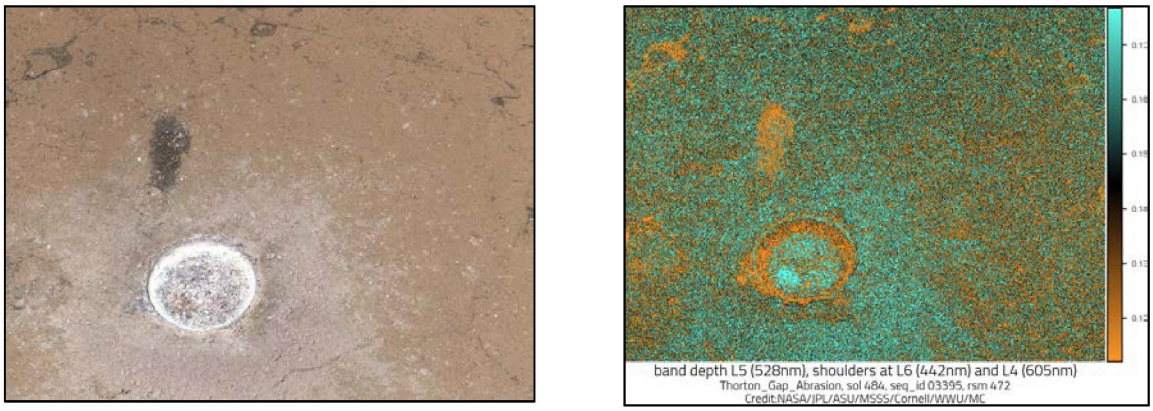

Figure 11 | (**a-b**) Cachecam images and (**c-d**) ZCAM images of the *Swift Run* (left) and *Skyland* (right) core samples The core diameters are 13 mm, for scale.

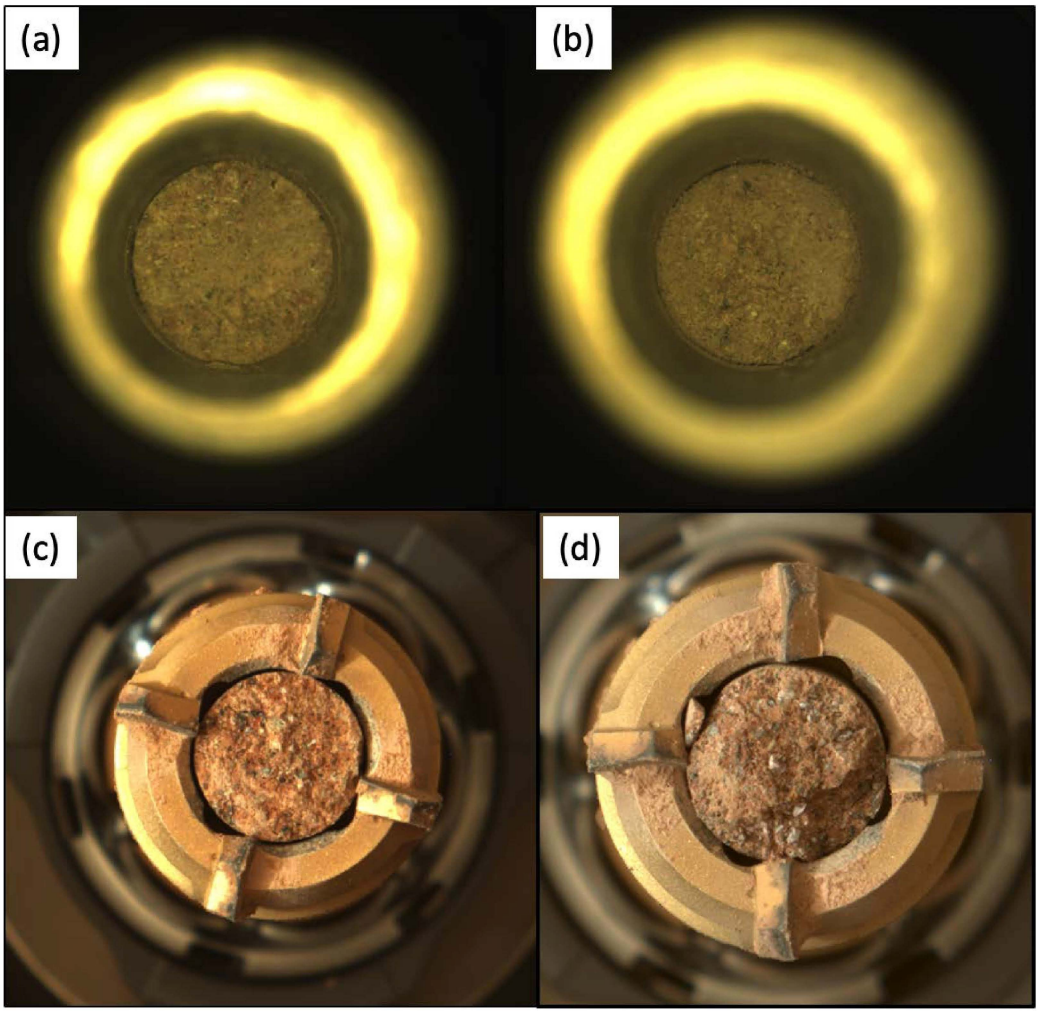

Elemental Geochemistry - PIXL

Elemental geochemistry for the *Skinner Ridge* rock is from X-ray fluorescence (XRF) mapping by the PIXL instrument of the *Thornton Gap* abrasion patch on Sol 484, and a three-line scan on Sol 489 (**Figure 12**). The Sol 484 scan was 12.5 x 4 mm in extent, with points spaced 0.1 mm apart. The Sol 489 scan was three lines 15 mm long, and 1 mm apart, with points spaced 0.1 mm apart. Unless noted, data here are from the Sol 484 scan. *Skinner Ridge* / *Thornton Gap* is inferred to be a clastic sedimentary rock, with clasts consisting of a variety of igneous and altered materials. Matrix material, i.e., existing between the clasts, in *Thornton Gap* is interpreted to include Fe-Mg carbonate.

Figure 12 |**PIXL raster scans on the *Thornton Gap* abrasion patch, Sols 484 and 489.** Opaque cyan areas indicate PIXL analyses; semi-transparent green areas indicate footprints of MCC images (**Figure 18**); these locations are overlain on WATSON image SIF_0482_0709737248_976RAS_N02621004SRLC01034_0000LMJ01. Note the area is mostly in shadow; image has been adjusted to decrease contrast across different lighting. Abrasion patch is ~5 cm diameter.

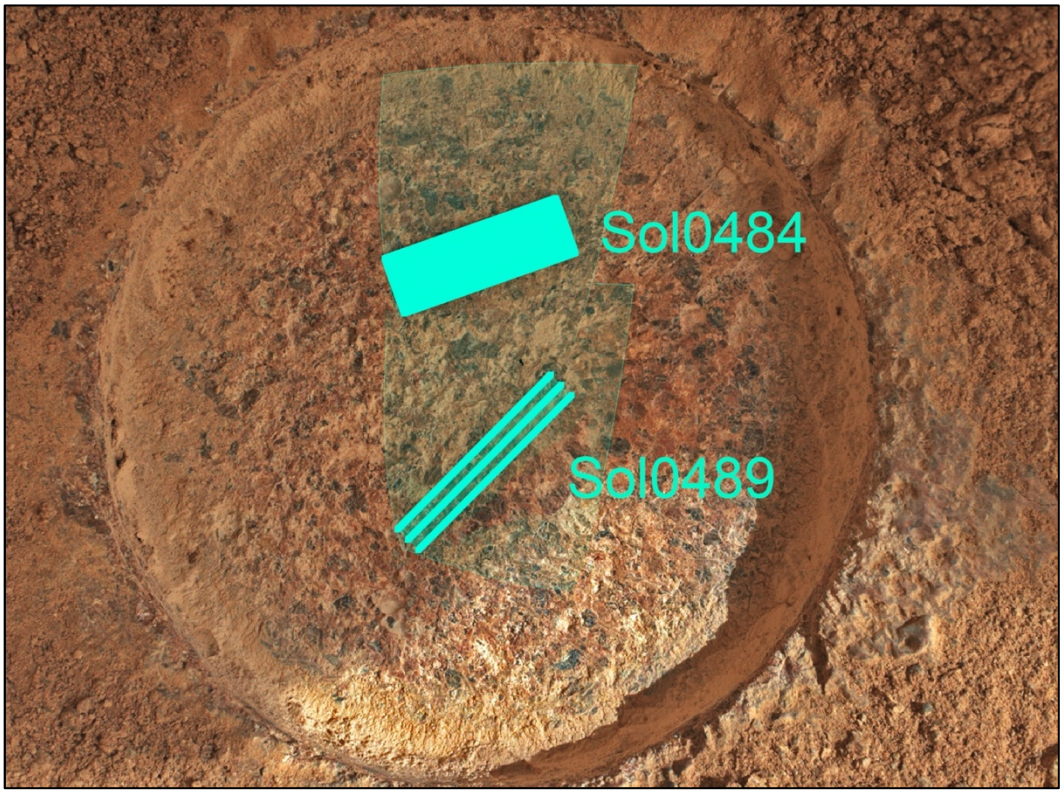

The bulk sum analysis, the average chemical composition, for the Sol 484 raster is given in **Table 1.** Beyond what is in the Table, the *Thornton Gap* bulk contains no potentially detectable elements (e.g., Ni, Sr) at levels above their detection limits. Chemically, *Thornton Gap* is mixed silicate-carbonate rock, as shown by the moderate silica content, high FeO and MgO, and the distinctly low analytical total. By the chemical classification of martian sediments in **Figure 13** (Mangold et al. 2017), the average *Thornton Gap* composition would be classified as Si-poor and nearly Fe-rich (**Figure 13a**), and neither sodic nor potassic, although it is near the boundary between normal potassium and potassic. However, the bulk analysis and most of the spot analyses fall outside the range of compositions that Mangold et

al. (2017) encountered in Gale Crater. Notably, many spot analyses from *Thornton Gap* contain < 20% SiO_2 and >30% FeO_T, unlike any Gale Crater samples. Similarly, some *Thornton Gap* spot analyses are enriched in Na or K beyond what Mangold et al. (2017) reported for Gale Crater.

Table 1 | **Chemical Compositions by PIXL XRF.**

	Bulk Raster 0484		Fe-Mg Carbonate†		Dark Clasts*		Greenish Clast**	
Wt %	N=3335	Err 1σ	N=335	1 SD	N=46	Err 1σ	N=11	Err 1σ
Na_2O	1.8	1.0	0.2	0.5	1.3	1.0	2.3	1.0
MgO	22.7	1.3	†48.7	4.4	21.6	1.2	11.6	0.7
Al_2O_3	1.7	0.4	0.6	0.2	3.0	0.4	14.6	0.7
SiO_2	22.6	1.2	5.5	1.8	27.2	1.4	35.4	1.8
P_2O_5	0.1	0.1	0.01	0.04	0.3	0.1	0.0	0.1
SO_3	2.6	0.4	2.3	4.6	2.1	0.4	1.0	0.3
Cl	4.5	0.5	2.2	1.9	4.9	0.4	1.6	0.4
K_2O	0.3	0.04	0.3	1.4	0.2	0.1	0.1	0.1
CaO	1.8	0.4	†2.9	3.5	0.3	0.1	8.5	0.4
TiO_2	0.2	0.1	0.02	0.04	0.3	0.1	0.0	0.0
Cr_2O_3	0.2	0.05	0.0	0.00	0.0	0.0	0.0	0.0
MnO	0.4	0.2	†0.7	0.1	0.3	0.2	0.1	0.1
FeO-T	24.5	1.2	†35.9	3.6	20.4	1.0	2.7	0.5
Sum %	83.5		99.2		83.3		77.9	
Mg#	62		65		65		88	

N are number of analyses averaged. Err is uncertainty (1σ) from calibration and counting statistics**.**

Mg# is molar Mg/(Mg+Fe), in percent.

†For regions in the scan area which appear to be dominated by carbonate, these tabulated values were derived from a quantification of the X-ray spectra that assumed Mg^{2+}, Ca^{2+}, Fe^{2+}, and Mn^{2+} are charge-balanced by $(CO_3)^{2-}$ for carbonates: $MgCO_3$, $CaCO_3$, $FeCO_3$, $MnCO_3$. The carbonate-dominated (nearly endmember) region was identified by selecting points with the highest backscattered X-ray intensities in the 2.9-3.1 keV range. 1 SD is standard deviation for this region.

* Combined analyses of five dark-toned clasts in scan 484.

** Clast is in PIXL scan 0489.

Figure 13 | Chemical classification of *Thornton Gap*, Sol 484 scan: individual points (dark gray) and average (dark blue point, See Table 1). Abundances are overlain on classification boundaries for Gale Crater rock analyses by ChemCam (Mangold et al. 2017). Individual data points may represent mixtures of minerals. Notable features include the range from Fe-rich (likely Fe-Mg carbonate or Fe-oxides) to Si-rich (possibly feldspar), (**Figure 13a)**; the significantly lower silica content in *Thornton Gap* compared to Gale Crater rocks (**Figure 13a**); the extreme ranges in Na and K contents compared to Gale Crater (**Figure 13b**); and the lack of correlation between abundances of Na and K (**Figure 13b**).

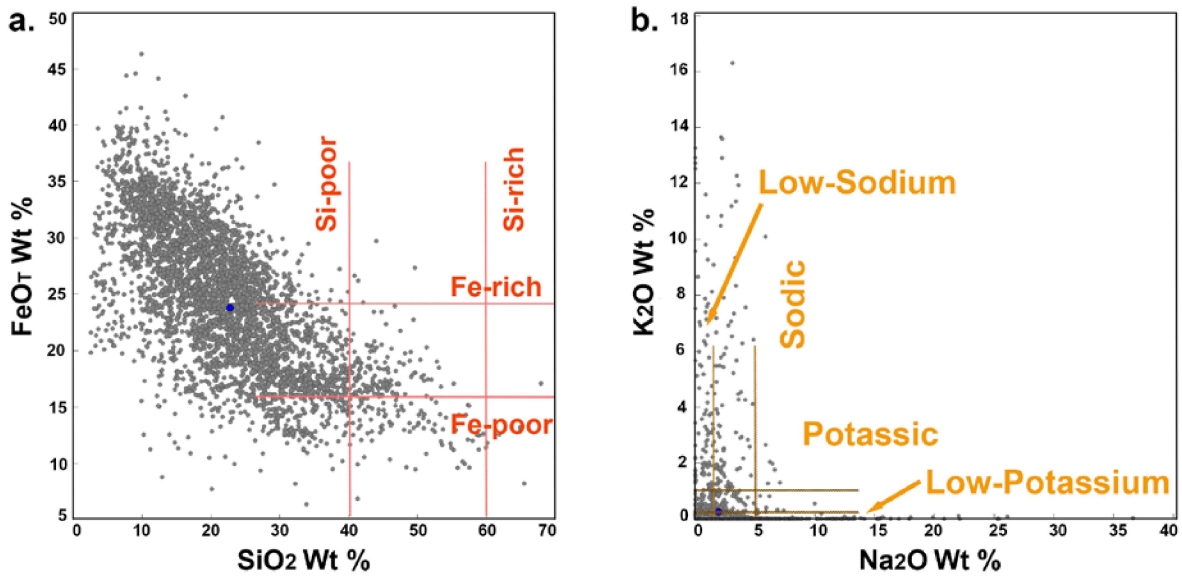

Figure 14 shows a ternary diagram of molar compositions Al_2O_3 – (CaO+Na_2O+K_2O) – (FeO_T+MgO) for each individual PIXL spot analysis in the Sol 484 raster. The majority of spot analyses and the bulk composition plot near the FeO_T+MgO apex, suggesting that the bulk of *Thornton Gap* consists of ferromagnesian silicates and/or carbonates (from the low bulk total, as above). A few spot analyses approach the composition of augite pyroxene, and a small cloud of points approach the composition of chlorite, suggesting the presence of Al-bearing phyllosilicate minerals (e.g., clinochlore, or amesite).

Figure 14 | **Mineralogical interpretation for the *Thornton Gap* abrasion, PIXL raster of Sol 484.** Data are plotted by pixel and as bulk sum composition (blue circle, **Table 1**). Common pure mineral compositions are shown for reference (opx = Ca-poor pyroxene, i.e, orthopyroxene; cpx = calcic pyroxene, i.e., augite). Aluminous alteration minerals, like clays, fall above the upper red dashed line.

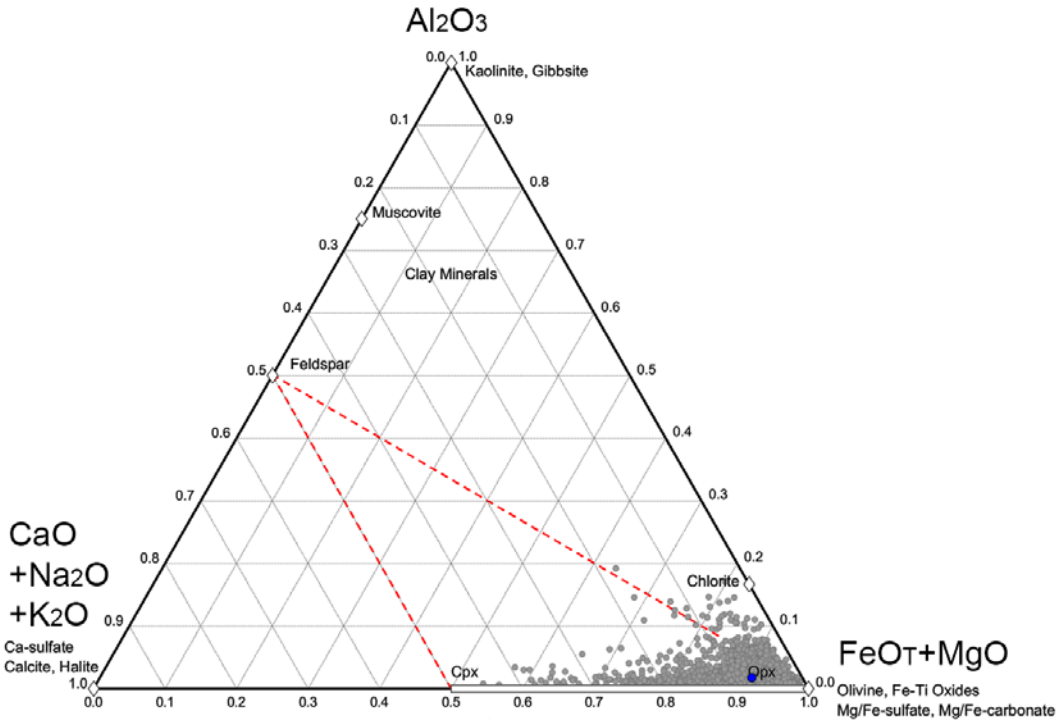

Thornton Gap is unique among the rocks observed by Perseverance to Sol 490 in its high Cl content (**Table 1**), which on a point by point basis is commonly associated with high alkalis. Among these points, there is a set with a very strong correlation between K and Cl (**Figure 15a**), and a set with a moderate correlation between Na and Cl (**Figure 15b**). It is possible that these correlations represent discrete grains of chloride or oxychlorine salts.

Figure 15 | Alkali and chlorine abundances in *Thornton Gap*, Sol 484 PIXL scan. The correlation between K and Cl (**Figure 15a**) and between Na and Cl (**Figure 15b**) suggest the presence of K and Na chloride or oxychlorine salts.

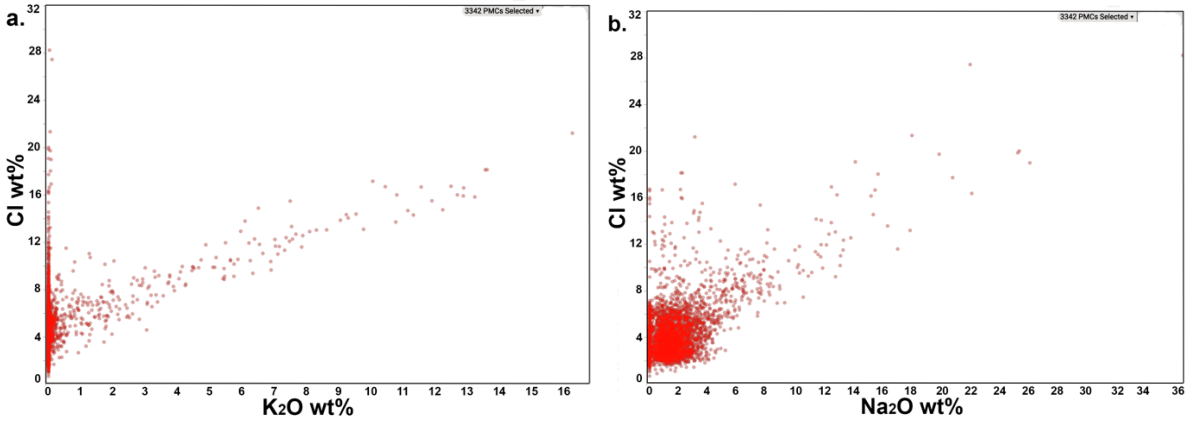

Figure 16 shows PIXL multi-element maps of the *Thornton Gap* scan of 484. **Figures 15a** and **15b** highlight the variety of sedimentary clasts in the rock. Most of them contain significant and variable SiO_2 (**Figure 16b**) and Al_2O_3 (**Figure 15a**) compared to the matrix and have MgO/FeO_T greater than that of the matrix (**Figure 16b**). A few clasts are rich in Ca (**Figure 16a**) and SO_3 (**Figure 16c**) and are likely calcium sulfate. The matrix in *Thornton Gap*, i.e., between the clasts, consists of at least two distinct materials. Part of the matrix is SiO_2-rich, up to ~65%, and appears red in **Figure 16.** Another matrix component is rich in MgO and FeO_T with little SiO_2. It is interpreted as mostly composed of Fe-Mg carbonate (**Table 1**). Minor minerals include Ca-phosphate (yellow, **Figure 16c**), Ca-sulfate (purple, **Figure 16c**), Fe-Ti oxides (green and orange, **Figure 16d**), and Fe-Cr oxide (violet, **Figure 16d**).

Figure 16 | **PIXL X-ray multi-element maps for the *Thornton Gap* abrasion patch on Sol 484**. (a) Red=FeO_T, Green=Al_2O_3, Blue=CaO. (b) Red=SiO_2, Green=FeO_T, Blue=MgO. (c) Red=CaO, Green=P_2O_5, Blue=SO_3. (d) Red=FeO_T, Green=TiO_2, Blue=Cr_2O_3.

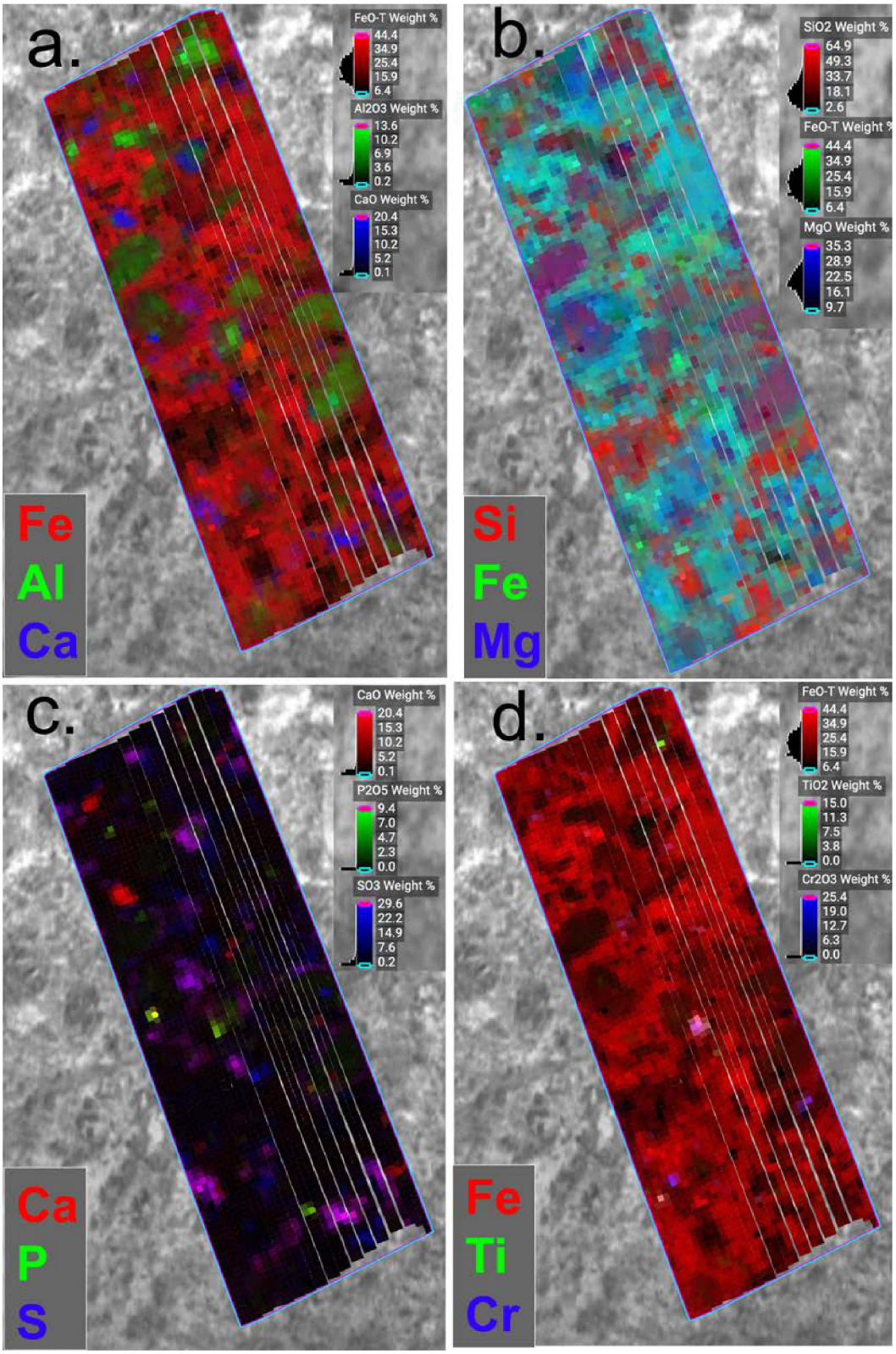

PIXL's Micro-Context Camera (MCC) images of the *Thornton Gap* abrasion patch (**Figure 17**) show more of the abrasion area than the XRF scans (**Fig. 11**) and are used to extrapolate phase proportions from those of the XRF scan areas to nearly the whole abrasion patch. The MCC image of NIR-G-B (**Figure 17b**) is analogous to WATSON visible images, and the G/NIR ratio image shows a clear distinction among the different mineral phases (**Figure 17c**). These relationships can be quantified in a graph of G vs NIR reflectances (**Figure 17d**).

Figure 17| PIXL MCC (Micro-context camera) data for the *Thornton Gap* abrasion, Sol 464. (a) MCC grayscale image, a portion of the *Thornton Gap* abrasion. (b) MCC false color of abrasion area; Red = MCC Near-IR; Green = MCC Green; Blue = MCC Blue. Location of PIXL XRF scans shown. (c) MCC ratio image Near-IR/Green reflectance. Location of PIXL XRF scan shown. (d) MCC reflectance ratios.

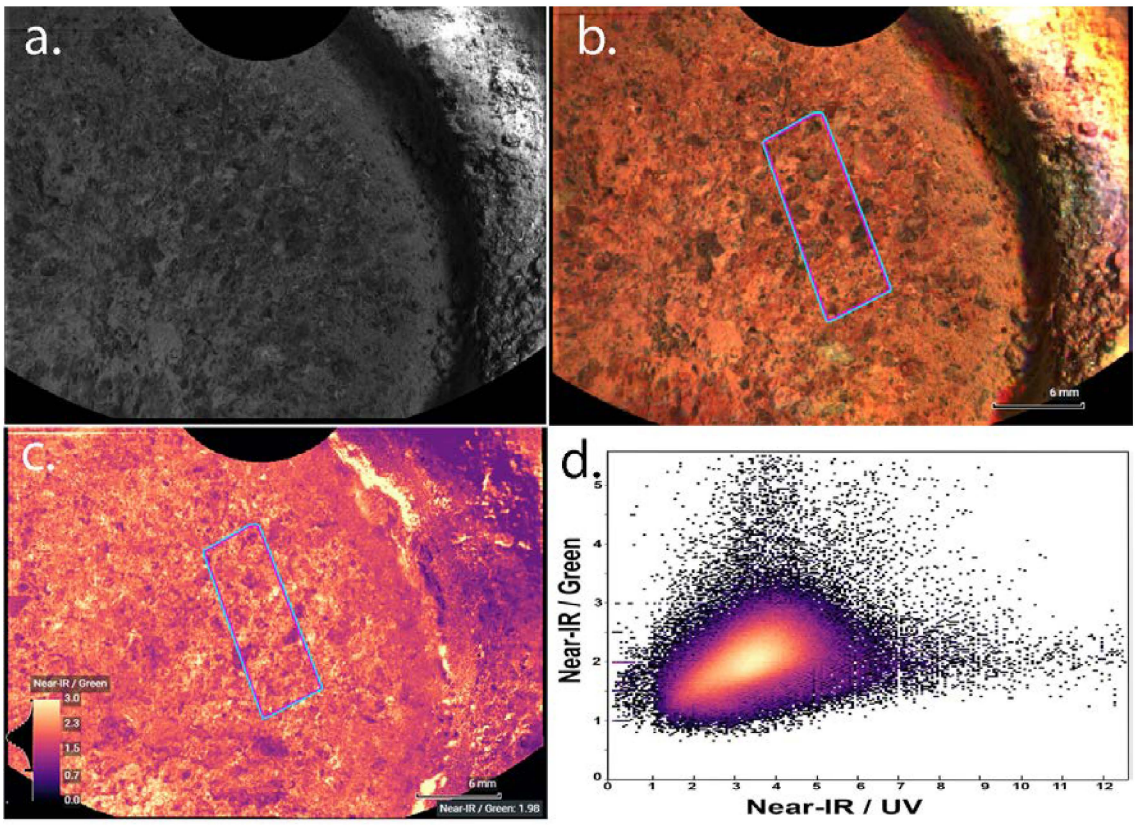

Mineralogy and Organics-SHERLOC

SHERLOC Raman and florescence spectra were obtained on two different areas of the *Thornton Gap* abrasion on Sol 489 by two HDR scans (7x7 mm, 100 points, 780 µm spacing, 500 pulses per point), two survey scans (5x5 mm, 1296 points, 144 µm spacing, 15 pulses per point) and two detail scans (1x1 mm, 100 points, 144 µm spacing, 500 pulses per point).

The Raman spectra contain peaks assigned to Fe/Mg carbonate (~1090 cm^{-1}), which map to both grains and cements in the rock (**Figures 18-19 and Table 2**). No other mineral peaks could be confidently identified. Fluorescence features at 285 nm and 330–340 nm, consistent with single and double ring aromatic organic molecules, were detected in two different areas where they are associated with lithic

grains (**Figures 18-19**). The relatively low intensity of fluorescence at all wavelengths and the absence of organic signals in Raman spectra suggest that any organics present are generally in low abundance except for some localized hot spots.

Preliminary mineral identifications are shown in **Table 2**.

Figure 18 | Sol 489 SHERLOC fluorescence and Raman spectral results for *Thornton Gap*. (a) Colorized ACI image of the *Thornton Gap* abrasion; blue rectangle indicates the detail scan area and white circles indicate regions of interest (ROIs) correlating to the fluorescence data presented in (b) and (c). (b) Detail scan maps showing the possible presence of organics. Upper panel shows an RGB map indicating the main regions of potential organic fluorescence (330–340 nm). The lower panel is blank for this abrasion patch because no Raman features have been identified that would indicate the presence of organic materials. (c) Fluorescence spectra. The upper panel shows the average fluorescence spectrum for the whole area of analysis and the lower panel includes spectra from selected fluorescence ROIs (see a and b). (d) Map showing the results of the Raman Detail 1 scan. The grid of red circles indicates the points analyzed (cf. panel a), and the other colored circles indicate mineral detections. The right panel includes selected Raman spectra from the detail 1 scan. The upper spectrum is an average of the detail 1 scan; given that the mineral detections were the same across a vast majority of the points, no specific point spectra are shown.

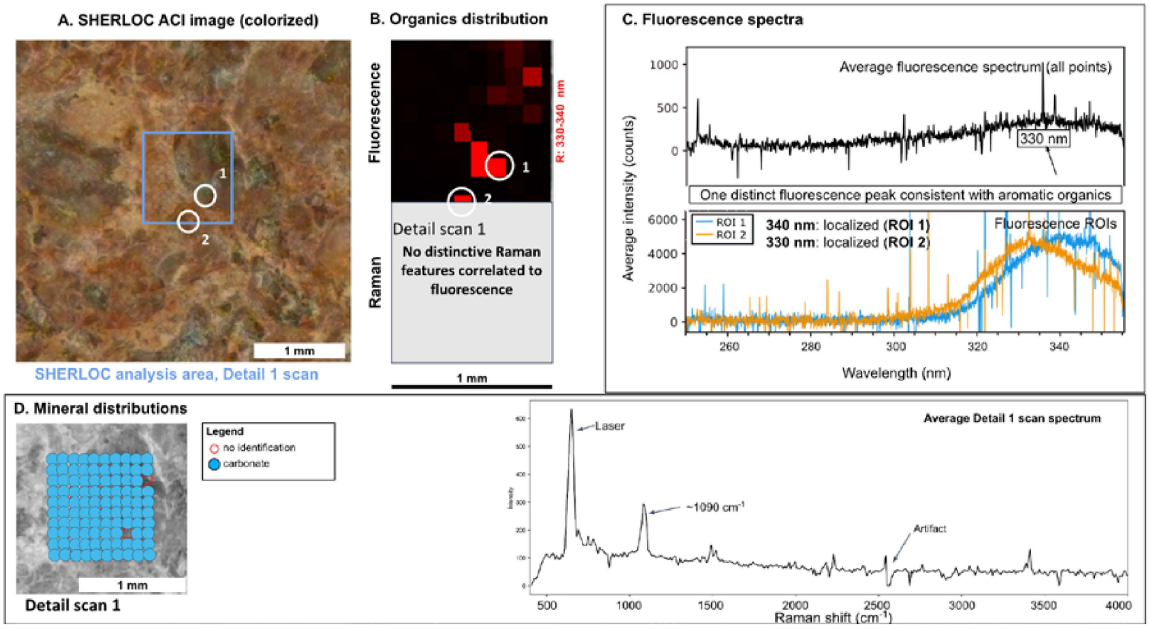

Figure 19 | Sol 489 SHERLOC fluorescence and Raman spectral results for *Thornton Gap*. (a) Colorized ACI image of the Thornton abraded patch; blue rectangle indicates the HDR scan area and white circles indicate regions of interest (ROIs) correlating to the fluorescence data presented in b and c. (b) HDR scan maps showing the possible presence of organics. Upper panel shows an RGB map indicating the main regions of potential organic fluorescence (285 nm). The lower panel is blank for this abrasion patch because no Raman features have been identified that would indicate the presence of organic materials. (c) Fluorescence spectra. The upper panel shows the average fluorescence spectrum for the whole area of analysis and the lower panel includes spectra from selected fluorescence ROIs (see a and b). (d) Map showing the results of the Raman HDR 2 scan. The grid of red points indicates the points analyzed (cf. panel a), and the other colored circles indicate mineral detections. The right panel includes selected Raman spectra from the HDR scan. The upper spectrum is the average spectrum of the HDR 2 scan; given that the mineral detections were the same across a vast majority of the points, no specific point spectra are shown.

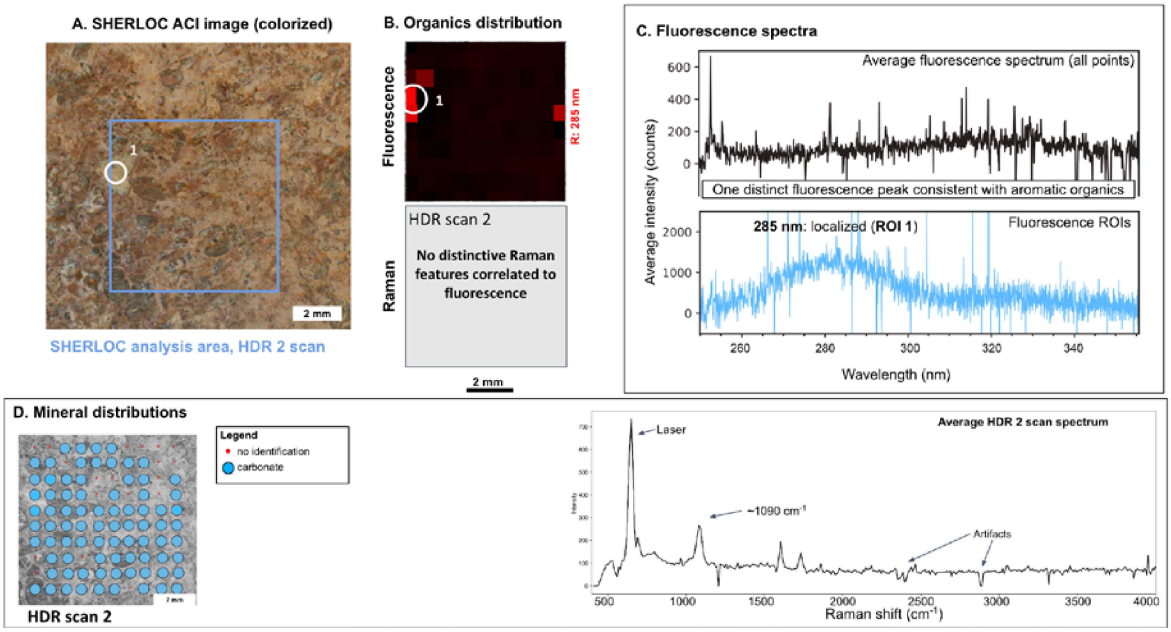

Table 2 | SHERLOC Raman spectra mineral ID.

Sample	Certain	Possible (not confirmed)	We looked for these, but cannot find them
Thornton Gap	Carbonate (most likely Fe/ Mg) *(associated with grains and cements across all scans)*	-	-

Elemental Geochemistry and Mineralogy - SuperCam

SuperCam RMIs of the *Thornton Gap* abrasion patch show dark and brown 0.5-2 mm wide, non-interlocking grains, many of which appear to be rounded (**Figure 20**). Some of the more angular grains are surrounded by light rims and separated by light areas, consistent with aqueous alteration of igneous grains, or cements.

Figure 20| **SuperCam RMI images of the *Thornton Gap* abrasion.** Imaged on Sol 493, mm-scale, dark angular grains surrounded by light rims, similarly-sized brownish red and light grains and areas are visible.

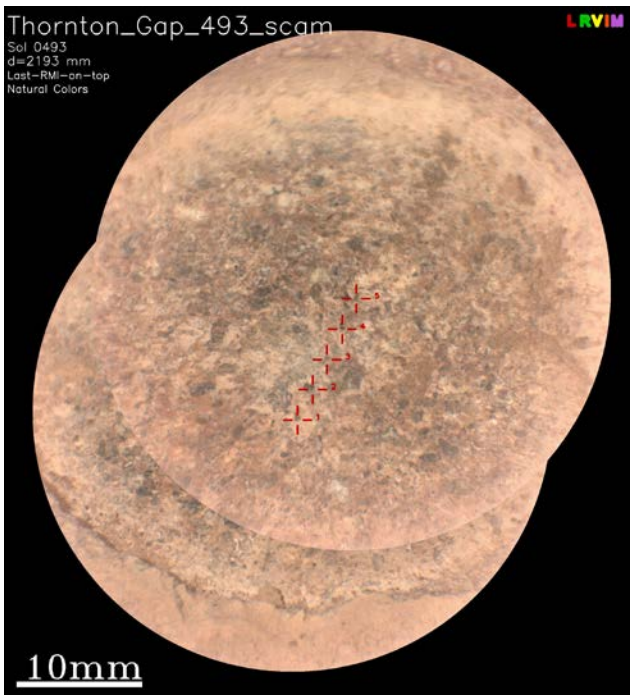

SuperCam LIBS observations of the *Skinner Ridge* outcrop and nearby targets (**Figure 21**) show that the rocks are compositionally heterogeneous, consistent with being coarse-grained on the scale of RMI images (**Figure 20**) and LIBS raster spacing (generally a few mm). The compositions of individual LIBS spots on the natural surfaces and on the abrasion are consistent with a possible mixture of pyroxene, olivine, and feldspar, with additional unrecognized phases. Between 20% and 40% of the points that were analyzed by LIBS on *Thornton Gap* abrasion patch had a total oxide content between 60 and 81 wt%, indicating the presence of elements that are not quantified by SuperCam such as H, C, S and Cl. These points sampled the lightest-toned areas of the abraded patch (e.g., points 1 and 5 in **Figure 20**). The enrichments in FeO_T and MgO_T and depletion in Al_2O_3 and SiO_2 (**Figure 22**) distinguishes these points from igneous minerals and suggests the presence of alteration phases such as Fe/Mg clays or carbonates. Point 2 in the LIBS analysis of *Thornton Gap* from Sol 486 has the lowest total oxide content (61 wt%), elevated sodium content and detectable chlorine, consistent with the presence of sodium chloride or a sodium oxychlorine salt. All points present evidence of hydration. The LIBS data indicate hydration, large compositional diversity between clasts, and the presence of phases that may have originated from aqueous alteration.

Figure 21|SuperCam LIBS major element oxide (MOC) analyses of *Skinner Ridge* rocks and natural surface analyses from Sols 420-512. Solid Solution fields for olivine, pyroxene, and feldspar compositions are included.

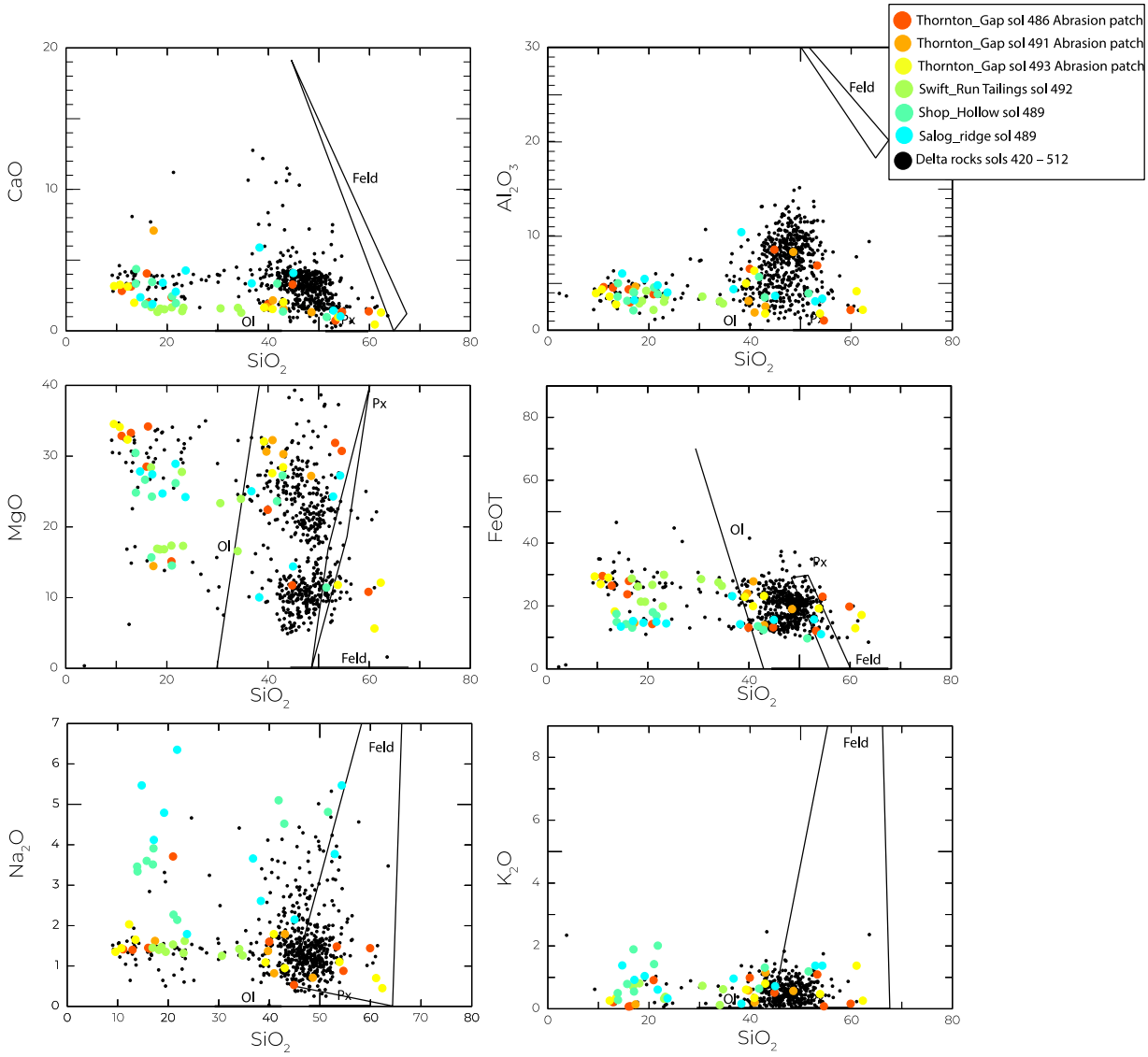

Figure 22| Molar compositions of the points in the LIBS raster of *Thornton Gap* from Sol 486 compared to various mineral standards. Analyzed points are shown by circles; yellow is *Thornton Gap* Sol 491, purple is *Thornton Gap* Sol 493 and orange is *Thornton Gap* Sol 498. The labelled points present a range of standards from igneous calibration targets (Ca-pyroxene, pyroxene, olivine, andesine, orthoclase) to other minerals (ankerite, siderite, calcite, serpentine). The green density cloud shows all data acquired during the mission up to Sol 523. The blue circle highlights four points that cluster toward the lower right vertex. These points were on the lighter toned areas of the abraded patch and had lower total major element oxide wt% values, a higher content of Fe+Mg and a lower content of Si+Al compared to the darker points and igneous calibration targets.

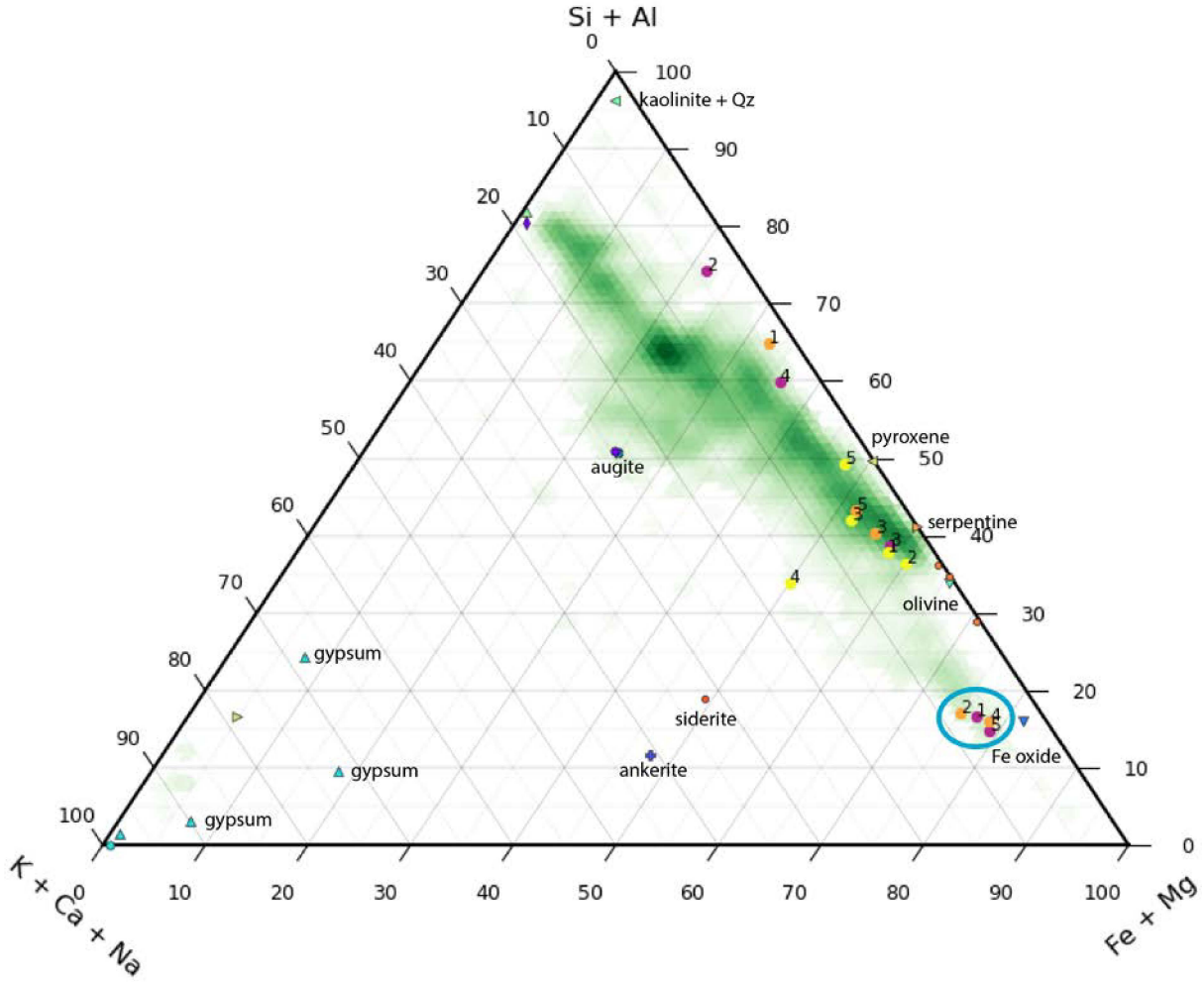

SuperCam VISIR rasters on the *Skinner Ridge* rocks (natural surface, abraded surface and tailings from coring activity; **Figure 23**) also reveal compositional heterogeneity, the presence of mafic minerals such as olivine and pyroxene and secondary phases produced during aqueous alteration. The SCAM VISIR technique is highly sensitive to hydrated minerals, so the signatures of hydration are present in the spectra even when these minerals are a minor proportion of the rock. **Figure 23** shows the absorption bands that indicate the presence of hydrated minerals. The main signals of hydration are present at 1.94 µm and 1.42 µm in abraded targets. The weak absorptions in the 2.1-2.5 µm range indicate some amount of Fe/Mg-clay minerals, possible carbonates (2.53 µm band), hydrated silica or Al-clay minerals (2.2 µm band) and sulfate (2.39 µm).

Figure 23| Mean reflectance spectra of the SuperCam VISIR rasters on the *Skinner Ridge* outcrop. Natural surface (orange and red), abraded surface (purple to red) and tailings from abrading activity (yellow). Lighter points near 2 µm indicate the spectral range possibly affected by the CO_2 absorption features after the atmospheric correction. Note that owing to temperature sensitivities in the IRS instrument, the calibration is still uncertain for wavelength longer than ~2.55 µm. Arrows indicate the absorption bands arising from the presence of hydrated minerals. Arrows in the 2.1-2.5 µm range point towards weak absorptions indicating small amounts of Fe/Mg-clay minerals, possible carbonates, and hydrated silica or Al-clay minerals.

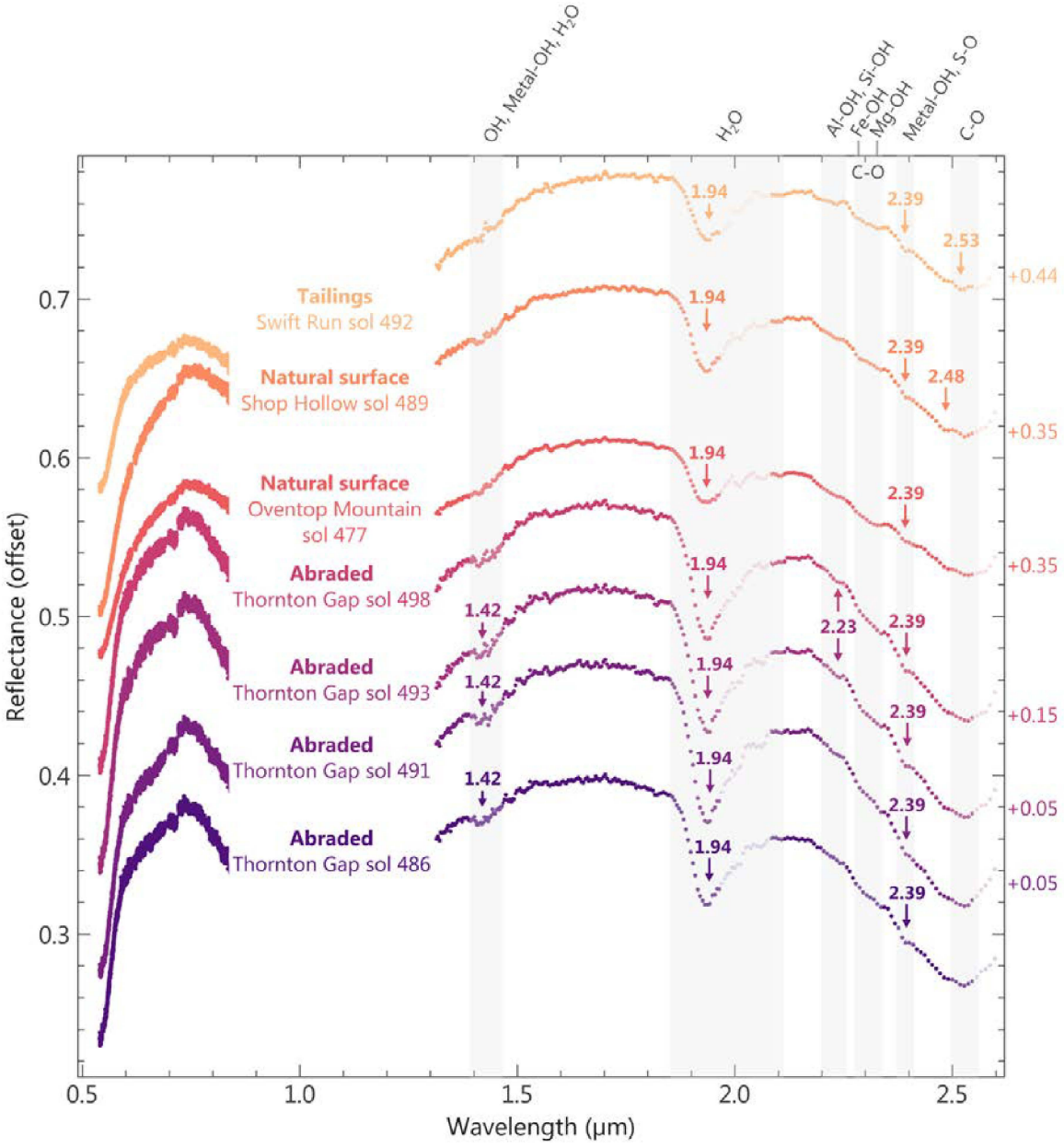

Subsurface Structure

The subsurface structure of the delta front from the *Skinner Ridge* outcrop southward is revealed by RIMFAX radargrams acquired between Sols 461 and 501 (**Figure 24a**). *Skinner Ridge* is a light-toned clastic sedimentary rock that outcrops as horizontal bedrock that is part of the lower *Rockytop* member of the Western Delta front. This unit sits above several other horizontally stratified units in the Delta front, all of which appear in both outcrop and in the subsurface as seen in RIMFAX radargrams (**Figure 24b**). The *Thornton Gap* samples were acquired near the base of the Lower *Rockytop* member, which, in the radargram, is represented by the uppermost ~1 m. *Hogwallow Flats*, *Boston Knob* (upper and lower), *Hughes River Gap*, and *Devils Tanyard* members have been extrapolated from surface outcrops (see Figure 1a). A base delta unconformity capping the underlying Séítah Formation strata may be apparent in RIMFAX data at depth -2542 to -2543 m. Burial depths have been calculated from two-way travel times using 0.15 m/ns.

Figure 24 | **Geological context and RIMFAX-derived subsurface stratigraphy of the delta front**. (**a**) Location of the *Thornton Gap* abrasion (made on the *Skinner Ridge* outcrop), within the delta front. Note the locations of the rover where RIMFAX data were collected. The blue circle indicates the Sol 502 end-of-day (EOD) position. The red line indicates the approximate transect of the radargram shown in panel b. (**b**) Radargram of the north to south section from *Thornton Gap* on Sol 477 (yellow star) southwards across the delta front. The section includes data collected on Sols 461 and 501; data were not collected along the transect between ~7 - 12 meters. The radargram shows strata with largely horizontal geometries above the Séítah Fm. (interpreted as the lowermost portion of the radargram).

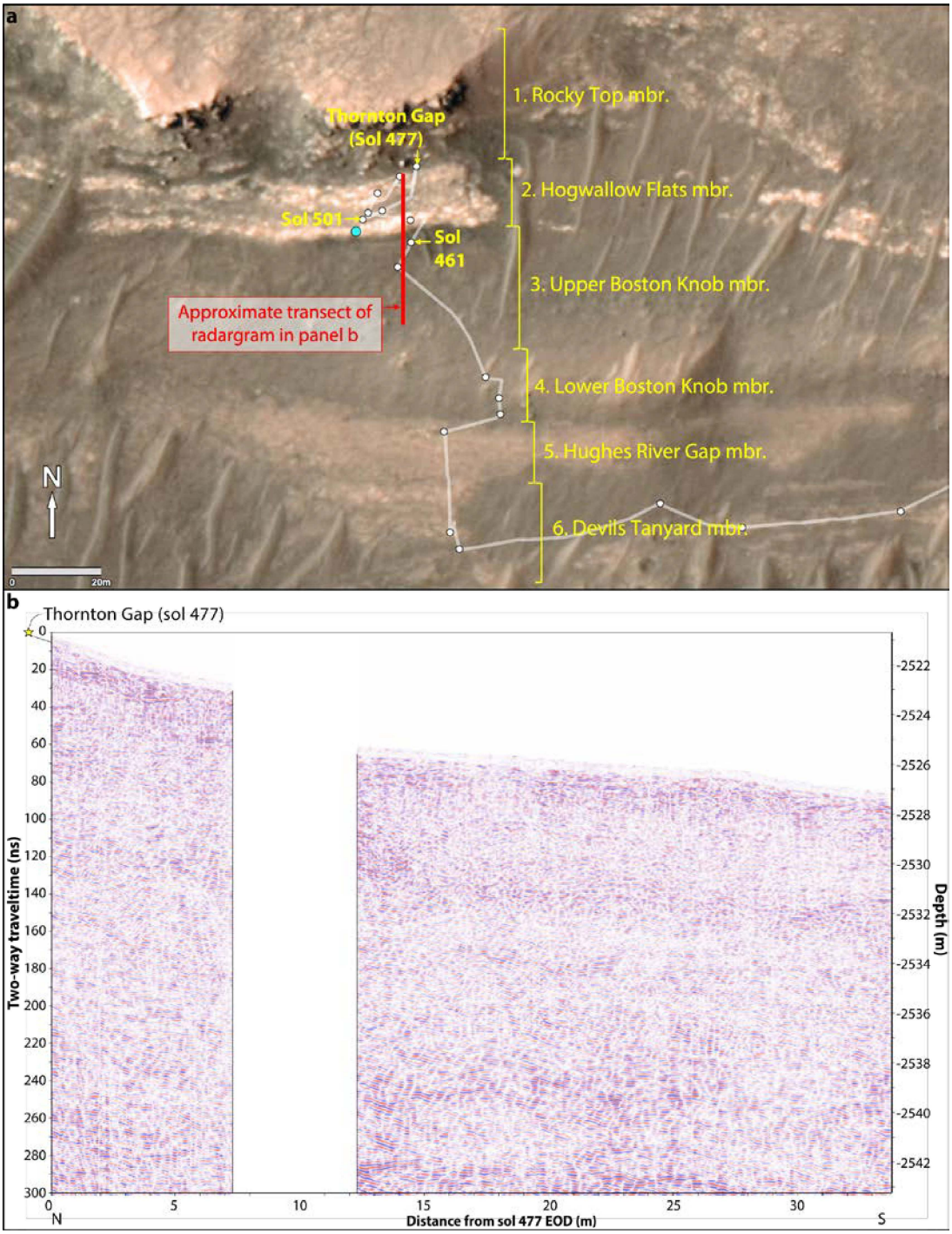

Core orientation

At the time of drilling and 6.4-cm pre-drilling WATSON imaging, the rover, coring drill, and WATSON had the following characteristics:

1. Rover orientation quaternion just after drilling but before unloading the stabilizers (transferring from RMECH to SITE frame): **bQll1** = (0.990075, 0.0411996, 0.11617, 0.0675102)
2. Coring Drill orientation quaternion just after drilling but before unloading the stabilizers (transferring from CORING DRILL to RMECH frame): **cdQb** = (0.69366, 0.217854, -0.646779, 0.230331)
3. Rover orientation quaternion at time of acquisition of WATSON image SIF_0485_0709994755_121FDR_N0261004SRLC00730_0000LMJ01: (transferring from RMECH to SITE frame): **bQll2** = (0.990376, 0.0408681, 0.113655, 0.067592)
4. WATSON orientation quaternion at time of acquisition of WATSON image SIF_0485_0709994755_121FDR_N0261004SRLC00730_0000LMJ01: (transferring from WATSON to RMECH frame): **wQb** = (0.695267, 0.221652, -0.645046, 0.226693)

Items 1 and 2 give a coring drill pointing vector estimate of

hade = 16.63°
azimuth = **355.94°**

Items 3 and 4 give an estimate of the angle between the WATSON y-axis and the Core y-axis projected into the WATSON image plane (**Figure 25**) of

core roll, α = **220.71°**

Figure 25 | Core orientation. 6.4-cm standoff WATSON image of *Swift Run* core target on Sol 485. Image scale is 30.2 µm pixel^{-1}. Orientation compass gives WATSON frame (**wx**, **wy**, **wz**). Core roll is **α = 220.71°**. Projection of Martian geographic north onto WATSON image plane is noted (clockwise angle of 225.07° from **wy**). WATSON image SIF_0485_0709994755_121FDR_N0261004SRLC00730_0000LMJ01.

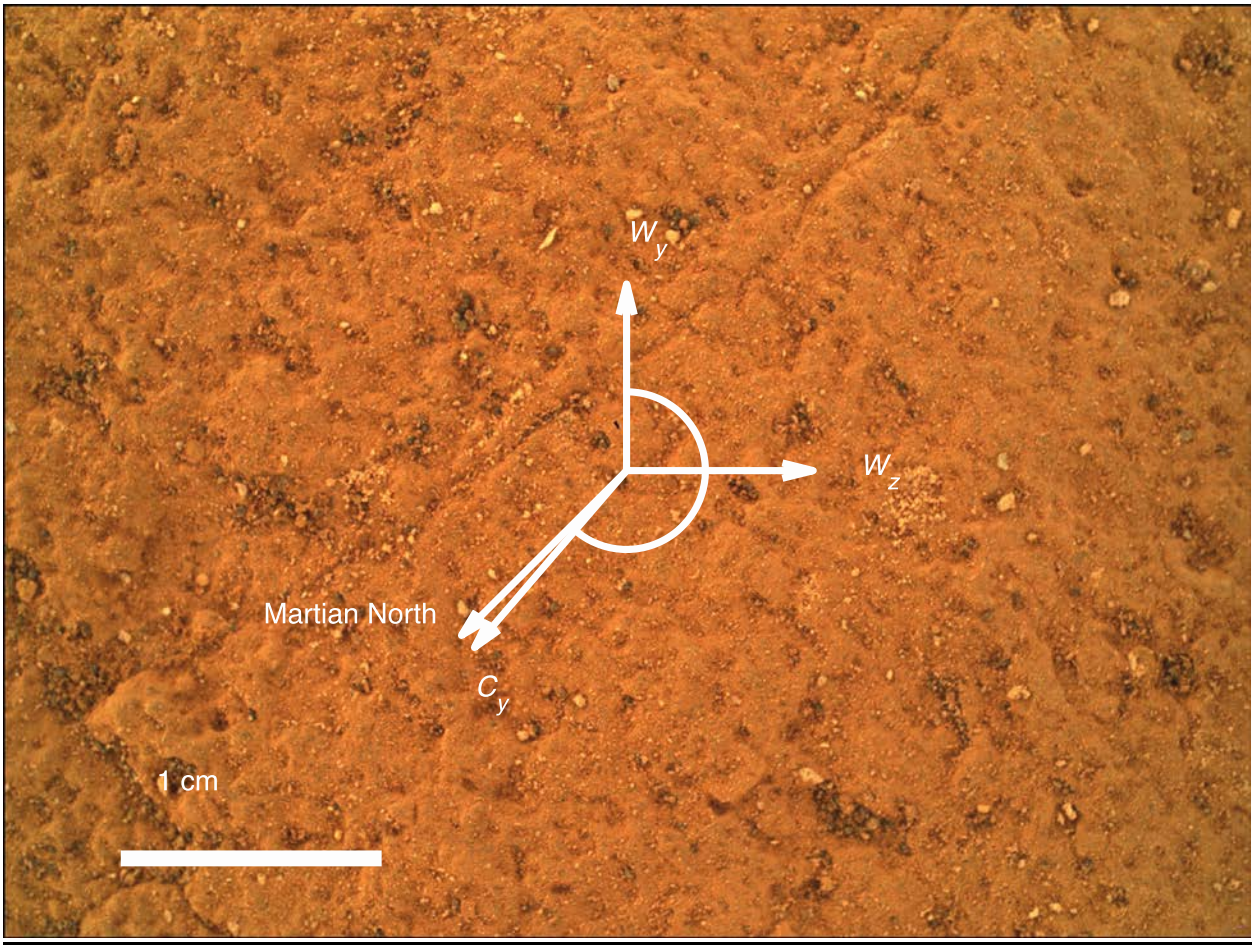

Preliminary Scientific Assessment

Synthetic sample description and preliminary interpretation

Sample type: **Clastic sedimentary rock: Sandstone**

1. **Relationship with surrounding rocks**
    a. *Swift Run* and *Skyland* were obtained from a position relatively low in the accessible stratigraphy of *Jezero Delta* near the base of the *Lower Rockytop* member, roughly 17 m vertically above the lowest exposed delta member *Devils Tanyard*, within the *Shenandoah* formation.
    b. Based on its appearance, concordance with surrounding outcrops, and apparent bedding and dip consistent with other nearby outcrops, the *Skinner Ridge* outcrop is interpreted to be an in-place portion of *Lower Rockytop*.
2. **Texture and fabric**
    a. Grain size: <0.03–2.0 mm
    b. Rock fabric (natural surface): the exposed planar surfaces are fairly smooth, with dust and/or regolith trapped along fractures and flakes. Individual grains are rarely visible in planar surfaces, but are observed in broken vertical faces.
    c. Rock fabric (abrasion patch): most grains are sand-sized and range from subangular to subrounded; the largest grains, up to 2 mm, are also subangular to subrounded. The grain size distribution is poorly sorted. Some areas show grains in contact with each other, while others have matrix support between grains.
    d. The rock appears to be an immature, fine/medium-grained sandstone.
3. **Mineralogy and chemistry**
    a. Minerals present: the rock has compositional heterogeneity among the clasts and the matrix. Igneous minerals were detected in the clasts, including olivine, pyroxene, and feldspar. A few clasts may be calcium sulfate. The matrix consists of at least two minerals: SiO_2 and MgO+FeO (with little SiO_2; likely Fe/Mg carbonate). Carbonates are associated with both clasts and with the matrix/cements. Minor minerals detected include Ca-phosphate, Ca-sulfate, Fe-Ti oxides, Fe-Cr oxides.
    b. The bulk composition is that of a mixed silicate-carbonate rock, a sediment with an average chemical composition classified as *Si-poor* and nearly *Fe-rich*.
    c. The rock appears to be an immature sandstone containing detrital minerals from diverse lithologies.
4. **Alteration/secondary characteristics**
    a. Evidence for alteration(s) exists both within some clasts and the matrix/cement.
    b. Secondary phases and/or cements indicative of aqueous alteration include hydrated minerals, hydrated silica, carbonates, Fe/Mg-clay minerals, and Al-clay minerals.

Returned Sample Science Considerations

Since before landing, the delta stratigraphy and the western Jezero delta front have been the primary astrobiologically-relevant mission sampling targets, i.e., sediments deposited into an ancient lake on Mars. Jezero Lake was likely present during the valley network-forming late Noachian to early Hesperian period of early Mars, and therefore delta sedimentary rock samples provide a potential record of the environmental conditions during that period. On Earth, early deltaic bottomset deposits often contain relatively fine-grained, organic-rich material, and can preserve ancient biosignatures. Coarser-grained (> mm) deltaic sedimentary units contain detritus that reveals the catchment source lithology and can be used to constrain delta deposition timing. Collectively, a set of coarse-grained *and* fine-grained sedimentary rock samples collected from the delta front in proximity provides a sample suite for addressing key goals of MSR.

The *Swift Run* and *Skyland* cores are samples of fine/medium-grained sandstones containing a diversity of detrital clast lithologies and late-stage cements and/or chemical weathering phases. Detrital clasts represent samples of crustal rocks sourced from outside, or the rim of, Jezero Crater. Laboratory-based investigations of these samples will enable the study of a sedimentary system on Mars and inform how surface environments and aqueous processes evolved through time, both within the catchment (i.e., before deposition), and within the delta sediments after deposition. Given the sediment clast size, these samples can enable multiple investigations to be conducted on the same detrital fragments, potentially including multi-phase geochronology, geochemistry, petrography, and paleomagnetism. Thus, the samples from *Skinner Ridge* can be used to address multiple science questions and objectives of the sampling campaign:

Geochronology: Crystallization ages of detrital igneous clasts within the *Skinner Ridge* samples will provide *upper* bounds on the timing of delta deposition and therefore the permissible timing of Lake Jezero. Geochronology of detrital grains can also provide information on igneous activity and planetary differentiation, and thermochronology can constrain subsequent crustal exhumation histories prior to their transport and deposition. The following minerals identified in *Skinner Ridge* are likely to enable different methods of isotopic geochronology (e.g., K-Ar, U-Th-Pb, Rb-Sr) and thermochronology (e.g., $^{40}Ar/^{39}Ar$, (U-Th)/He) upon sample return: feldspar, pyroxene, and possibly phosphates, carbonates, and Fe-oxides.

Geochronology of post-depositional phases within these samples, including cements and chemical weathering products, using a variety of geochronology methods (e.g., K-Ar, U-Th-Pb, Rb-Sr, U-Th/He) can quantify the timing of alteration, cementation and/or lithification of the delta sediments. In addition to quantifying the timing of late-stage aqueous activity, such information would place a *lower* bound on the timing of sediment/delta deposition. With the planned collection of another coarse-grained sample from higher in the delta stratigraphy, it may be possible to use a similar approach to then constrain the duration over which the exposed delta was deposited. Observations of stable cosmogenic nuclides (e.g., ^{3}He, ^{21}Ne, ^{36}Ar, ^{38}Ar) could quantify the material's integrated cosmic ray exposure duration, thereby helping to constrain the latest-stage erosional history of the delta and the most recent cosmic ray exposure of the rocks in this vicinity (including the *Hazeltop* and *Bearwallow* cores, collected from an underlying sedimentary unit; **Figure 4**).

Paleomagnetism: The sedimentary lithologies of the *Swift Run* and *Skyland* cores may enable relative measurements of the paleointensity of the martian dynamo. A conglomerate test on individual clastic grains could determine if the samples retained magnetization prior to, or after, deposition. In combination with geochronology, this could constrain the timing of the martian paleomagnetic field to test the hypothesis that martian atmospheric loss was driven by the cessation of an early dynamo. If the samples possess post-depositional magnetization, the orientations of the samples (**Figure 25**), combined with paleohorizontal indicators from the outcrop and sample, may enable measurements of the absolute paleodirection of the ancient field during or after deposition. This could constrain the dynamo's geometry and establish if the dynamo exhibited secular variation and polarity reversals. Because remanent magnetization can be overprinted by heating and recrystallization processes, paleomagnetic investigations would also constrain the aqueous and thermal alteration history of the samples and, by implication, the preservation state of any potential biosignatures.

Geochemistry: Elemental and mineralogical data from the *Thornton Gap* abrasion indicates a heterogeneous, coarse-grained sandstone that includes detrital grains that may have undergone aqueous alteration prior to deposition. Basic petrological and geochemical investigations of detrital grains/clasts in the *Swift Run* and *Skyland* cores will quantify variance in the sediment source region lithology, likely outside Jezero crater. High spatial resolution geochemical investigations of any detrital (i.e., transported) carbonate, calcium sulfate, and Al-phyllosilicate phases may also provide information on chemical weathering processes in the catchment prior to sediment transport and deposition. In addition, laboratory geochemical investigations of secondary phases present as matrix and cements (including Fe- and Mg-carbonates, Ca- and Mg-sulfates, K- and Na-bearing Cl salts likely to be perchlorates and/or chlorides, phosphates, and Al-bearing phyllosilicates) can inform models of post-deposition sediment diagenesis, including the cementation, dissolution, authigenesis, recrystallization, oxidation/reduction, and water/rock interactions. Investigating the fluid/mineral interactions will inform our understanding of the fluid chemistry (e.g., pH, Eh) and fluid sources the sediments may have experienced after deposition.

Habitability and Biosignature Preservation Potential: The *Swift Run* and *Skyland* cores originate from a paleoenvironment (i.e., a pro-delta, to offshore, lacustrine depositional environment) that was likely habitable, owing to a record of sediment-water interactions during the aqueous deposition of the sandstone. On Earth, the surfaces of sand grains and pore spaces in sandstones in lacustrine environments provide habitats for microorganisms. Solid phases that bind grains into sandstones can also preserve signals of microbial life, contributing to a documented (e.g., Vidal, 1974), albeit not exceptionally high or uncontroversial (e.g., Wacey et al., 2011), potential for biosignature preservation in aqueously deposited sandstones on Earth. The cements and aqueously formed phases in the sandstones of *Thornton Gap* have the potential to preserve organics and signals of any microbial life that may have colonized the sediments or lived in the water column.

Rover observations of the *Thornton Gap* abrasion detect Fe/Mg carbonate minerals around grains and in some composite clasts, indicating post-depositional aqueous alteration of primary igneous minerals and the cementation of some clastic grains before deposition into the sandstone at *Skinner Ridge*. Because SHERLOC fluorescence signals from the *Thornton Gap* abrasion are generally low, but indicate the presence of single and double ring aromatic organic molecules (in low abundance) associated with some clasts that contain carbonate, high-resolution laboratory chemical investigation of the alteration phases in and around composite clasts can help determine whether these organic signals

(along with any potential biosignatures) may have been incorporated into clasts before they were transported and then cemented into sandstone. If so, these samples would inform our understanding of the habitability and biosignature preservation potential during the formation of clasts, but before the cementation of the sandstone at *Thornton Gap*. Due to the relatively high detection limits of the rover payload and potential for Fe attenuation of signals, the absence of strong fluorescence or Raman organic signals originating from cement phases should not be interpreted as an absence of organic material. Likewise, the micrometer scale of many known microbial biosignatures (microbial cells) and organic inclusions preserved in rocks precludes detection on the scale of the SHERLOC instrument. Thus, sample return and microscopic analyses are required to definitively map the distributions of organic compounds in different cements, look for the presence of putative biosignatures and to understand the potential habitability of the *Lower Rockytop* member of the Delta front.

Sediment transport: Images of the *Thornton Gap* abrasion reveal both rounded and less rounded grains. Higher resolution laboratory studies of detrital grain morphology can inform our understanding of the transport processes they experienced, including aqueous flow conditions, discharges, and sediment fluxes.

References

Mangold, N., Schmidt, M. E., Fisk, M. R., Forni, O., McLennan, S. M., Ming, D. W., ... & Wiens, R. C. (2017). Classification scheme for sedimentary and igneous rocks in Gale crater, Mars. *Icarus*, *284*, 1-17.

Stack, K.M. et al. (2020). Photogeologic Map of the Perseverance Rover Field Site in Jezero Crater Constructed by the Mars 2020 Science Team. *Space Science Reviews*, 216, 127, doi:10.1007/s11214-020-00739-x.

Vidal, G. (1974). Late Precambrian microfossils from the basal sandstone unit of the Visingsö beds, South Sweden. *Geologica et Palaeontologica*, *8*, 1-14.

Wacey, D., Kilburn, M. R., Saunders, M., Cliff, J., & Brasier, M. D. (2011). Microfossils of sulphur-metabolizing cells in 3.4-billion-year-old rocks of Western Australia. *Nature Geoscience*, *4*(10), 698-702.

INITIAL REPORT

M2020-495-12 *Skyland*

Sample Designation: M2020-495-12 *Skyland*

Date of Coring: 11-July-2022

Mars Time of Sample Core Sealing: 21:22 LMST, Sol 495, Ls 264.6

Latitude (N), Longitude (E), Elevation: 18.458931˚, 77.40617078˚, –2520.185m

Campaign: Delta Front

Region of Interest: *Hawksbill Gap*

Lithology: Fine to medium-grained sandstone deposited in a prodelta setting. Poorly-sorted subrounded to subangular grains range from <0.03 to 2 mm in diameter. Detrital fragments have diverse compositions, including olivine and pyroxene grains, possible alteration minerals rich in Si and Al (phyllosilicates), and lithic fragments. A fine-grained matrix or cement appears depleted in Si and Al and enriched in Fe and Mg, much of which is interpreted to be Fe-Mg carbonate. Evidence of hydration, Na and Cl salts, and oxidation (ferric Fe) were also detected.

Estimated Volume Recovered: 8.3 cm^3

Coring Bit Number: 1

Core Orientation: 17.18°; azimuth = 4.68°; core roll = 240.38°

Sample Serial Numbers: Tube SN272; Seal SN192; Ferrule SN068

ACA Temperature at Time of Sealing: 40^{o}C

Estimated Rover-Ambient Pressure and Temperature at Time of Sealing: 808 Pa, 210 K

Estimated Amount of Martian Atmosphere Headspace Gas: 1.71×10^{-6} mol

Anomalous Sample Behavior (if applicable): None

Abrasion Patch Name and Depth: *Thornton Gap*, 7 mm

August 29, 2022

D. L. Shuster, K. A. Farley, T. Bosak, B. A. Cohen, A. D. Czaja, E. M. Hausrath, L. E. Mayhew, S. Siljeström, J. I. Simon, K. M. Stack, A. Treiman, B. P. Weiss, B. V. Wogsland, M.-P. Zorzano, H.E.F. Amundsen, F. J. Calef III, D. Flannery, J. Hurowitz, T. Kizovski, L. Mandon, E. N. Mansbach, D.A.K. Pedersen, M.M. Tice, A. Udry, S. Van Bommel, K. Williford, and the Mars 2020 Team

Summary Description

This sample is paired with M2020-490-11 *Swift Run*. Only the core orientation for *Skyland* is described below. See the Initial Report for M2020-490-11 *Swift Run* for sample details.

Core orientation

At the time of drilling and 6.2-cm pre-drilling WATSON imaging, the rover, coring drill, and WATSON had the following characteristics:

1. Rover orientation quaternion just after drilling but before unloading the stabilizers (transferring from RMECH to SITE frame): **bQll1** = (0.990082, 0.041088, 0.116157, 0.0675021)
2. Coring Drill orientation quaternion just after drilling but before unloading the stabilizers (transferring from CORING DRILL to RMECH frame): **cdQb** = (0.719608, 0.136234, -0.656689, 0.1799)
3. Rover orientation quaternion at time of acquisition of WATSON image SIF_0485_0709996024_867FDR_N0261004SRLC00730_0000LMJ01: (transferring from RMECH to SITE frame): **bQll2** = (0.990385, 0.0409456, 0.113539, 0.0676066)
4. WATSON orientation quaternion at time of acquisition of WATSON image SIF_0485_0709996024_867FDR_N0261004SRLC00730_0000LMJ01: (transferring from WATSON to RMECH frame): **wQb** = (0.721544, 0.138711, -0.655143, 0.175847)

Items 1 and 2 give a coring drill pointing vector estimate of

hade = 17.18°
azimuth = **4.68°**

Items 3 and 4 give an estimate of the angle between the WATSON y-axis and the up-dip direction in SITE coordinates projected into the WATSON image plane (**Figure 25**) of

core roll, α = **240.38°**

Figure 25 | Core orientation. 6.2-cm standoff WATSON image of *Skyland* core target on sol 485. Image scale is 29.4 µm pixel^{-1}. Orientation compass gives WATSON frame (**wx, wy, wz**). Core roll is **α = 240.38°**. Projection of Martian geographic north onto WATSON image plane is noted. Projection of Martian geographic north onto WATSON image plane is noted (clockwise angle of 235.61° from **wy**). WATSON image SIF_0485_0709996024_867FDR_N0261004SRLC00730_0000LMJ01.

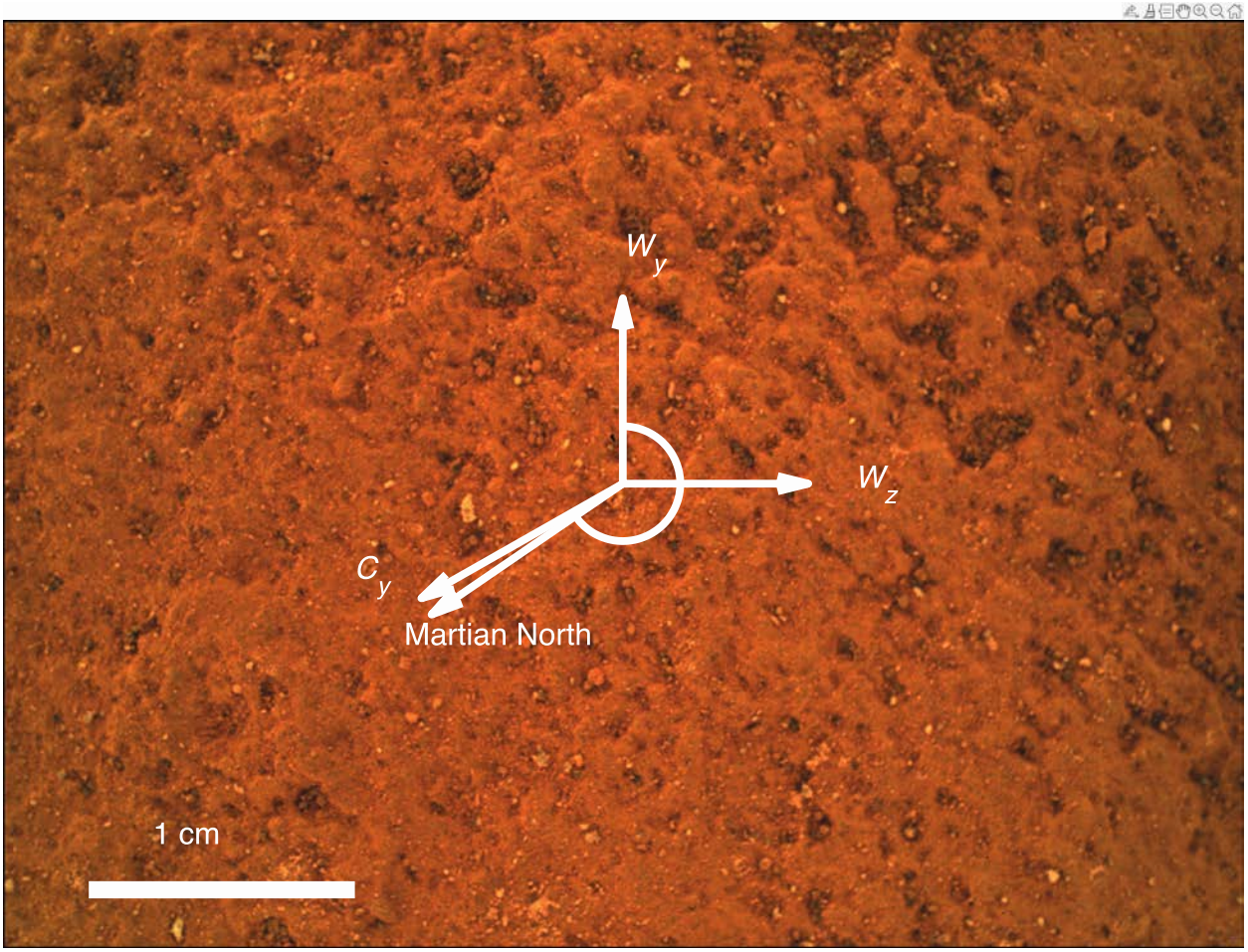

INITIAL REPORT

M2020-499-13 WB2

Witness Tube Designation: M2020-499-13 WB2

Date of Initial Witness Exposure: 16-July-2022

Date of Activation: 16-July-2022

Date of Sealing: 16-July-2022

Mars Time of Witness Tube Sealing: 20:14:37 LMST, Sol 499, Ls 267.1

Latitude (N), Longitude (E), Elevation: 18.45892814, 77.40617557, -2521.454 m

Sample Serial Numbers: Tube SN205; Seal SN119; Ferrule SN070

ACA Temperature at Time of Sealing: 40° C

Estimated Rover-Ambient Pressure and Temperature at Time of Sealing: 798 Pa, 213 K

Estimated Amount of Martian Atmosphere Headspace Gas: 2.7×10^{-6} mol

Anomalous Behavior: None

August 15, 2022

S. Siljeström, M.-P. Zorzano, K. A. Farley, K. Benison, T. Bosak, Y. Goreva, C. Herd, L. Mayhew, R. Moeller and the Mars 2020 Team

Summary Description

Perseverance carries 5 Witness Tube Assemblies (WTA's) which will be used to document the evolving rover contamination environment (organic, inorganic and particulates) over the course of the mission (Moeller et al., 2020). Four of these "witness tubes" are identical and located in sheaths just like sample tubes within the ACA (ACA WTA). The main purpose of the ACA WTAs is to record potential contaminants from the rover to which the rock cores might have been exposed during the several hours of handling needed to acquire and process a sample. The four witness tubes are protected from particle accumulation by fluid mechanical particle barriers and are isolated from volatile organic molecules by a tortuous path of gettering surfaces (Moeller et al., 2020) until activation. To activate the WTA the seal is punctured using the volume probe inside the ACA. Thereafter, they are processed in the same way as the rock cores except there is no contact between drill bit and rock.

To capture the evolving contamination throughout the whole mission, it was decided to process two ACA WTAs early in the mission when the largest outgassing from the rover is expected. The earliest opportunity, considering engineering constraints, came during the Delta Campaign.

The M2020-499-13 WB2, the first of the ACA WTA tubes, was processed at *Skinner Ridg*e at *Lower Rocky Top* after the sampling sol path of samples *Swift Run* and *Skyland* (Figure 1). It was processed on sol 499 after the cleaning of the chuck on sol 498. The stabilizers were placed on the outcrop, where the chuck had been cleaned, next to the abrasion patch and the drill holes (Figure 1). After activation, the WTA was exposed to simulated sampling, i.e., it was placed in the corer and moved in a fashion similar to rock core acquisition.

It should be noted that on sol 495 a string-like piece of foreign object debris (FOD) similar to materials released during EDL was observed in the workspace images. On sol 499 this object was no longer observed, presumably because it blew out of the scene. This observation suggests the possibility of FOD in tubes sealed in this general area.

Operations

1. This witness tube was activated by the volume probe inside ACA on 14:46:36 LMST, sol 499.

2. It was then moved through a simulated sampling path on sol 499.

3. It was finally sealed on 20:14:37 LMST, sol 499.

Figure 1 | NavCam left Sol 499 mosaic showing *Skinner Ridge* with abrasion patch *Thornton Gap* and drill holes of the samples *Swift Run* and *Skyland*. The placement of the corer where the WTA was processed is indicated by white circle.

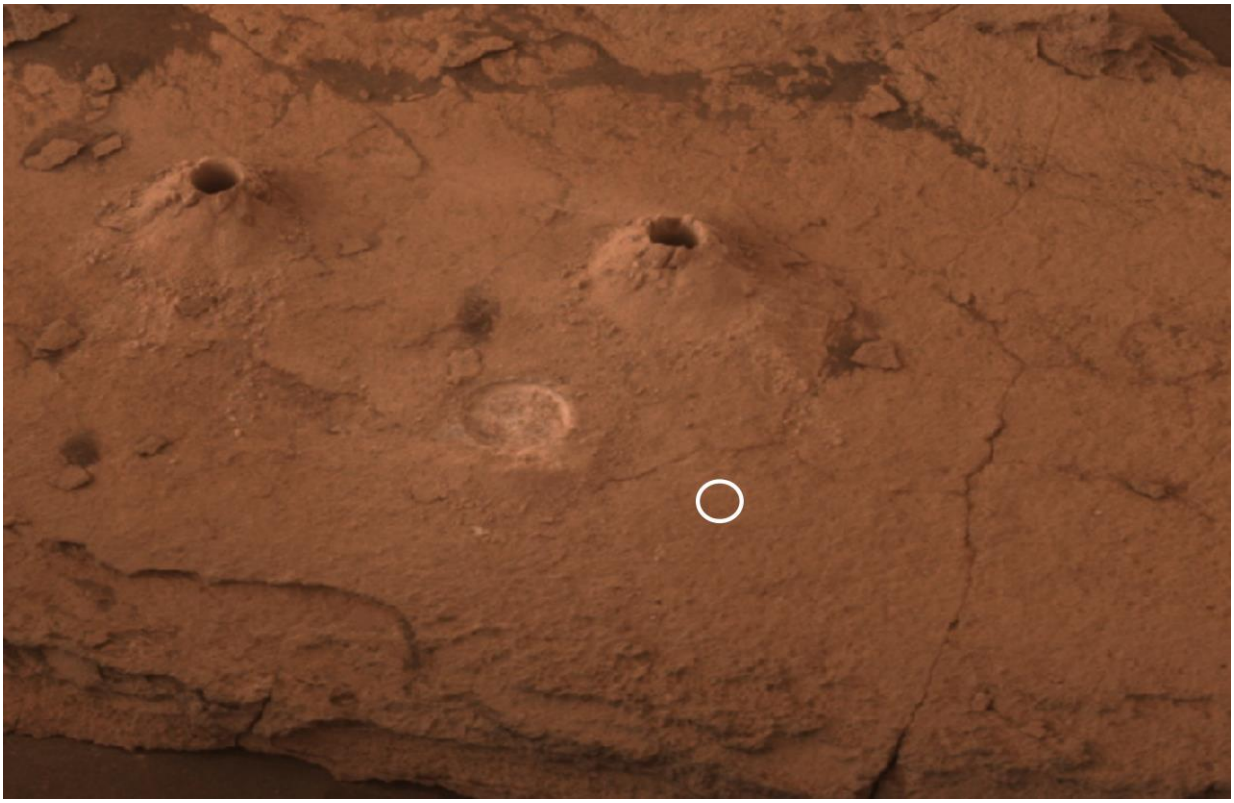

INITIAL REPORT

M2020-509-14 *Hazeltop*

Sample Designation: M2020-509-14 *Hazeltop*

Date of Coring: 25-July-2022

Mars Time of Sample Core Sealing: 20:57 LMST, Sol 509, Ls 273.7

Latitude (N), Longitude (E), Elevation: 18.45863707˚, 77.40588851˚, -2523.0974 m

Campaign: Delta Front

Region of Interest: *Hawksbill Gap*

Lithology: Fine-grained, well-sorted sedimentary rock likely deposited in a lacustrine setting; a sulfate-bearing coarse mudstone. The rock is rich in weakly-hydrated Mg-Fe sulfate. Also detected were small amounts of Fe-Mg-clay minerals, hydrated silica or Al-clay minerals, and possibly carbonates. Numerous fluorescence detections may arise from aromatic organic compounds. The rock is cut by scattered veins and patches enriched in Ca sulfate, likely anhydrite, whereas the sulfate in the rock matrix is more magnesian.

Estimated Volume Recovered: 8.4 cm^3

Coring Bit Number: 2

Core Orientation: hade = 13.78°; azimuth = 3.53°; core roll = 341.30°

Sample Serial Numbers: Tube SN172; Seal SN157; Ferrule SN099

ACA Temperature at Time of Sealing: 40°C

Estimated Rover-Ambient Pressure and Temperature at Time of Sealing: 800 Pa, 212 K

Estimated Amount of Martian Atmosphere Headspace Gas: 1.63×10^{-6} mol

Anomalous Behavior: None

Abrasion Patch Name and Depth: *Berry Hollow*, 8 mm

September 21, 2022

D. L. Shuster, K. A. Farley, T. Bosak, B. A. Cohen, A. D. Czaja, E. M. Hausrath, L. E. Mayhew, S. Siljeström, J. I. Simon, K. M. Stack, A. Treiman, B. P. Weiss, B. V. Wogsland, M.-P. Zorzano, H.E.F. Amundsen, F. J. Calef III, D. Flannery, J. Hurowitz, T. Kizovski, A. Knight, L. Mandon, E. N. Mansbach, D.A.K. Pedersen, M.M. Tice, A. Udry, S. Van Bommel, K. Williford, and the Mars 2020 Team

Summary Description

Hazeltop and Bearwallow, the pair of cores representing the sixth sample target of the Mars 2020 mission, were collected from *Wildcat Ridge*, an outcrop of the *Hogwallow Flats* member of the *Hawksbill Gap* region of the western Jezero delta front. *Wildcat Ridge* lies near the base of ~3 vertical meters of exposed sedimentary rock layers of *Hogwallow Flats* (**Figures 1 - 5**) and is likely to be in place. The outcrop is a horizontally layered, fine-grained, and well-sorted sedimentary rock; it is a sulfate-bearing coarse mudstone (**Figures 3, 5**). We sampled this sedimentary rock because it is from a low stratigraphic position within the exposed delta and contains a fine-grained texture, likely deposited on the floor of a lake. The rock is rich in weakly-hydrated Mg-Fe sulfate with evidence of small amounts of Fe-Mg clay minerals, hydrated silica or Al-clay minerals, and possibly carbonates. Thus, this rock has high potential for biosignature preservation.

The *Berry Hollow* abrasion patch, acquired on *Wildcat Ridge*, is homogeneous in its color, composition, and grain size, with observable grains ranging from <0.03 to ~2 mm, and a fine-grained cement and/or secondary chemical weathering phases. *Berry Hollow* is Fe- and Mg-rich and chemically homogeneous. Sulfates and phyllosilicates are present, as possibly are carbonates. Phyllosilicates potentially include nontronite and saponite. Strong and abundant fluorescence signals are associated with sulfate, suggesting the possible presence of organic matter in sulfate minerals. Ca-sulfate is present in a fracture or vein, and increased fluorescence in this vein (and elsewhere) is consistent with single- and double-ring aromatic compounds. Possible veins were also observed in the collected cores.

Wildcat Ridge was deposited in a subaqueous paleoenvironment that, due to the presence of liquid water, is interpreted as formerly habitable. The potential organic detections are strongly correlated with sulfate minerals, suggesting that both sulfates and organics were deposited and concentrated in this area when a lake was evaporating. Sulfate minerals precipitate in modern hypersaline, and sometimes acidic, lacustrine environments and have recognized biosignature preservation potential. Thus, the returned sample science objectives of the *Hazeltop and Bearwallow* cores include combined microscopic textural, geochemical, and isotopic analyses of samples with high potential for biosignature preservation, paleomagnetism, the history of climate and water on Mars, and water–rock interactions during sedimentary deposition and in the delta sediments after deposition, and possibly geochronology. High spatial resolution elemental and mineralogical analyses could be used to link the component materials to either (1) geochemical conditions in the environment where *Wildcat Ridge* was deposited or (2) the post-depositional diagenetic processes that acted upon the sediments.

The *Hazeltop* core was collected on Sol 509, has a core length of 59.7 mm, and based on Cachecam and ZCAM images, appears to be a coherent piece of rock. The *Bearwallow* core was collected on Sol 516, has a core length of 62.4 mm, and based on Cachecam and ZCAM images also appears to be a coherent piece of rock. These cores were collected from a stratigraphic position ~3 vertical meters below the *Swift Run* and *Skyland* sandstone cores collected from the *Lower Rockytop* member, ~20 m to the northeast (**Figures 2, 4**).

Stratigraphic and Geologic Context

The *Hogwallow Flats* member of the *Shenandoah* formation, which contains *Wildcat Ridge*, is stratigraphically above the *Knob Mountain* member and below the cliff-forming *Upper Rockytop* and *Lower Rockytop* members in the *Hawksbill Gap* region of the western Jezero delta front (**Figures 1 - 4**). *Wildcat Ridge* is stratigraphically ~14 meters above the lowest exposed delta member, *Devils Tanyard*, which defines the base of the *Shenandoah* formation (**Figure 4**). Based on orbital mapping, *Devils Tanyard* lies at the contact between the Crater floor fractured rough (*Cf-fr*) and the Delta thinly layered (*D-tnl*) photogeologic units mapped in orbiter images (Stack et al., 2020). *Wildcat Ridge* is ~47 vertical meters below the nearby *Franklin Cliffs* ~0.18 km to the northeast, and ~129 vertical meters below the highest exposed delta surfaces ~3.2 km to the northwest. Thus, *Wildcat Ridge* is from a relatively low stratigraphic position within the exposed delta.

The *Hogwallow Flats* member is a low relief slope-forming unit consisting of light-toned strata cropping out above and below thin, platy bedrock that appears darker-toned in orbiter images. The *Hogwallow Flats* interval can be traced laterally in orbiter images at least ~1.5 km along the delta front. Some of the units lower than *Hogwallow Flats* form subtle benches, e.g., the *Boston Knob* member (**Figure 2**), while others weather recessively (e.g., *Hughes River Gap* and *Devils Tanyard* members). Overall, these different horizontal layers indicate that the explored stratigraphy of the delta front is comprised of several distinct units and facies, that are largely, if not entirely, sedimentary in origin. This stratigraphy appears to be representative of the base of the exposed delta. However, because the contact between this stratigraphy and the crater floor basement rocks is covered by regolith, the oldest units deposited on the crater floor basement rocks may not be evident.

Operations

Sampling objectives of the *Delta Front Campaign* included the collection of both fine-grained (<0.06 mm) sedimentary rocks, ideally rich in clay minerals, and coarse-grained sedimentary rocks containing lithologically diverse clasts. The *Hazeltop and Bearwallow* cores were collected to fulfill the fine-grained sedimentary rock sampling objective of the campaign.

The Delta Front Campaign planning process occurred during February and March of 2022 and identified four paired samples to be collected from relatively low stratigraphic positions within the western Jezero delta, and prior to depositing the initial cache: (1 & 2) two different samples of lacustrine sediments with potential for biosignature preservation (ideally fine-grained mudstone and/or fine sandstone containing clay minerals and reduced phases indicative of anoxic preservation conditions), (3) one relatively coarse-grained sediment sample (ideally containing medium sand size particles, >250 μm, with a lithologic diversity of detrital material) for delta deposition geochronology and Jezero catchment provenance studies, and (4) one regolith sample.

On Sol 424, Perseverance encountered the first delta rock outcrops of the mission at a site called *Enchanted Lake* at the base of *Cape Nukshak* (**Figure 1**). *Enchanted Lake* contained the *Kaguyak* sandstone and overlying *Amalik* fine-grained, gray rocks. SCAM RMI observations at *Cape Gull* (on *Kaguyak*) and *Hook Glacier* (on *Amalik*) revealed sedimentary facies consistent with distal subaqueous deposition. The team then decided to explore a laterally equivalent section of the lower delta exposure in the *Hawksbill Gap* region with the intention to execute proximity science and sampling activities

(**Figure 1**). From Sols 426-441, Perseverance drove over 700 m from *Cape Nukshak* to *Hawksbill Gap*, arriving at the lowest exposed delta deposits of *Devils Tanyard* on Sol 441. Between Sols 441 and 474, Perseverance drove up-section through the following delta members while collecting remote sensing data and seeking outcrops suitable for potential proximity science and sampling: *Devils Tanyard*, *Hughes River Gap, Boston Knob*, *Hogwallow Flats*, and *Rockytop* (**Figure 2, 4**).

Although remote sensing observations of *Devils Tanyard* and *Sunset Hill* (*Hughes River Gap member)* outcrops were consistent with fine- to medium-grained sandstones, throughout this interval the science and engineering teams struggled to locate outcrops suitable for proximity science. An abrasion of *Rose River Falls* within the *Hughes River Gap* member at *Sunset Hill* was conducted on Sol 452 but resulted in depression of the rock into unconsolidated, fine-grained regolith, precluding PIXL placement and other proximity science activities. On Sol 463, Perseverance arrived at *Hogwallow Flats*. Natural surface SCAM observations of *Smith Mountain* revealed a fine-grained sedimentary rock with indications of sulfate, phyllosilicates, and hydration. SHERLOC fluorescence signals (probable organics) were observed at natural surface target *Pignut Mountain.* An abrasion of *Elkwallow Flats* within *Hogwallow Flats* was conducted on Sol 471. However, due to the rock breaking during abrasion, neither PIXL nor SHERLOC could be placed for proximity science observations. Thus, the science team decided to move Perseverance to *Betty's Rock* on Sol 474, while the science and engineering teams studied existing images to identify other *Hogwallow Flats* outcrops likely to be suitable for proximity science and sampling. On Sol 477, Perseverance arrived at *Skinner Ridge* and conducted proximity science observations of the *Thornton Gap* abrasion and sampled the *Swift Run* and *Skyland* cores. Perseverance then processed a Witness Tube (M2020-499-13 WB2) on Sols 499-500 and drove away from the *Skinner Ridge* workspace towards *Wildcat Ridge* on Sol 501.

On Sol 502, Perseverance arrived at the *Wildcat Ridge* outcrop. On Sol 503, we selected three potential targets for abrasion and sampling (*Hazeltop, Bearwallow, and Berry Hollow*) and acquired WATSON images of each. *Berry Hollow* was selected as the abrasion target; the abrasion was successfully conducted on Sol 504. Initial images of the abrasion patch revealed fine particle sizes (<100 μm) displaying a narrow range of both size and color. PIXL and SHERLOC data were acquired on *Berry Hollow* on Sol 505. Remote-sensing and abrasion patch proximity science observations revealed that *Wildcat Ridge* possessed multiple desired characteristics for a fine-grained sedimentary rock sample with high potential for biosignature preservation, including: (1) clay- or silt-sized particles, <63 μm (2) the presence of cements or authigenic minerals, including sulfate; (3) the presence of clay minerals; (4) the presence of organic compounds; (5) sediment associated with delta deposition; and (6) a relatively low stratigraphic position in the delta (see above). Thus, the team decided to move forward with sampling and completing the STOP list activities. We acquired the *Hazeltop* core on Sol 509 and the *Bearwallow* core on Sol 516. The *Hazeltop* and *Bearwallow* cores are the second sedimentary rock samples collected by the Perseverance Rover. Interpreted to be a sulfate-bearing, coarse mudstone, these samples satisfy the desires for the delta front fine-grained sedimentary rock sample with biosignature preservation potential and meet the campaign objective of collecting one of two pairs of such cores prior to the initial cache placement.

Figure 1 | Regional context of Perseverance rover operations. (a) Geologic map with topography showing Jezero crater floor and western delta units, as defined by Stack et al. 2020. (b) Inset map showing the Delta Front Campaign regions of interest, *Cape Nukshak* and *Hawksbill Gap*, the *Hazeltop* and paired core *Bearwallow* location (red point), and rover drive route (white lines). Elevation contours are meters relative to the Mars aeroid.

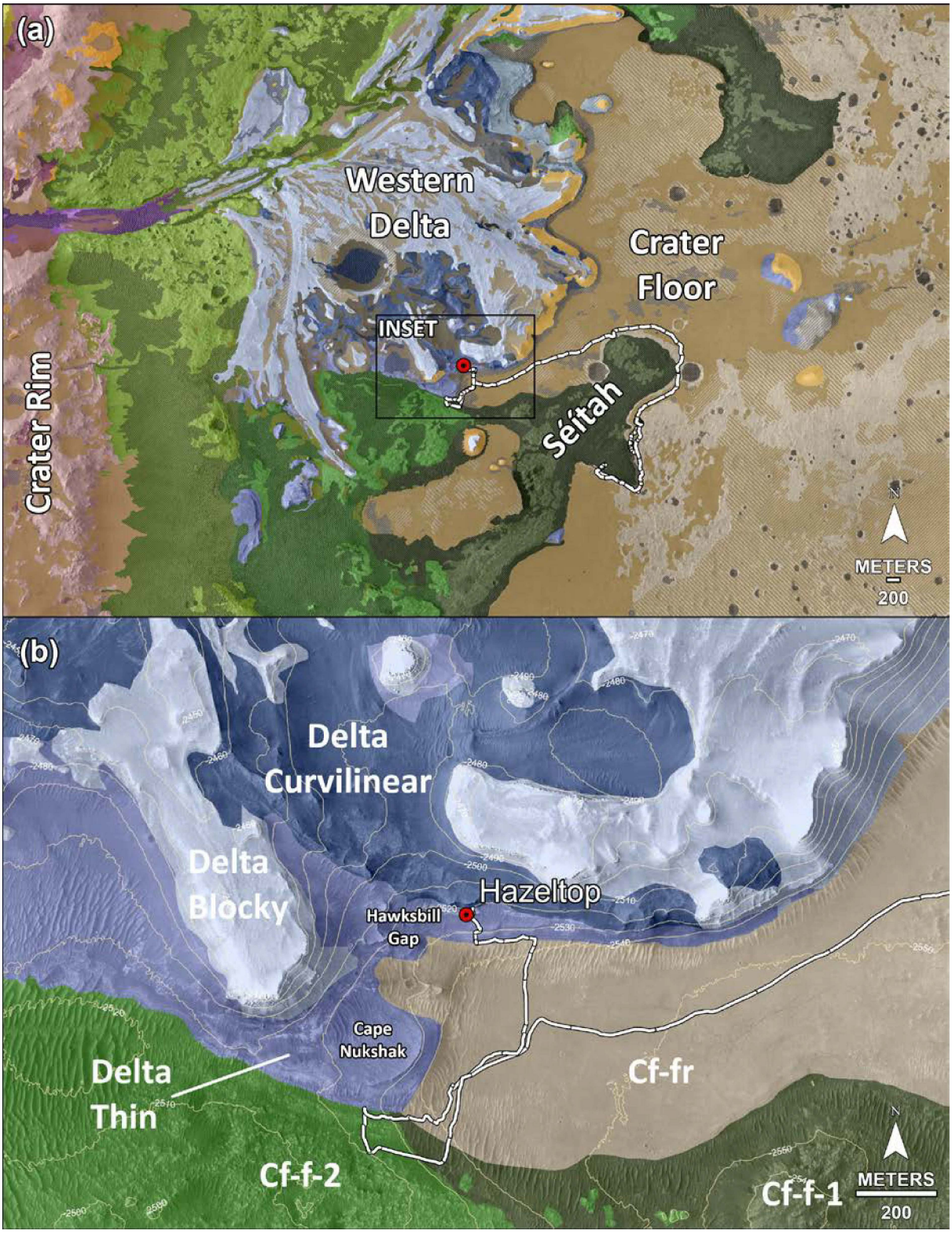

Figure 2 | Local context of Perseverance rover operations during *Hazeltop* and *Bearwallow* sampling. HIRISE map showing the locations of sample collection together with other notable outcrops investigated during the sol path leading to *Wildcat Ridge*. Location of *the Hazeltop and Bearwallow* cores is indicated with a red circle.

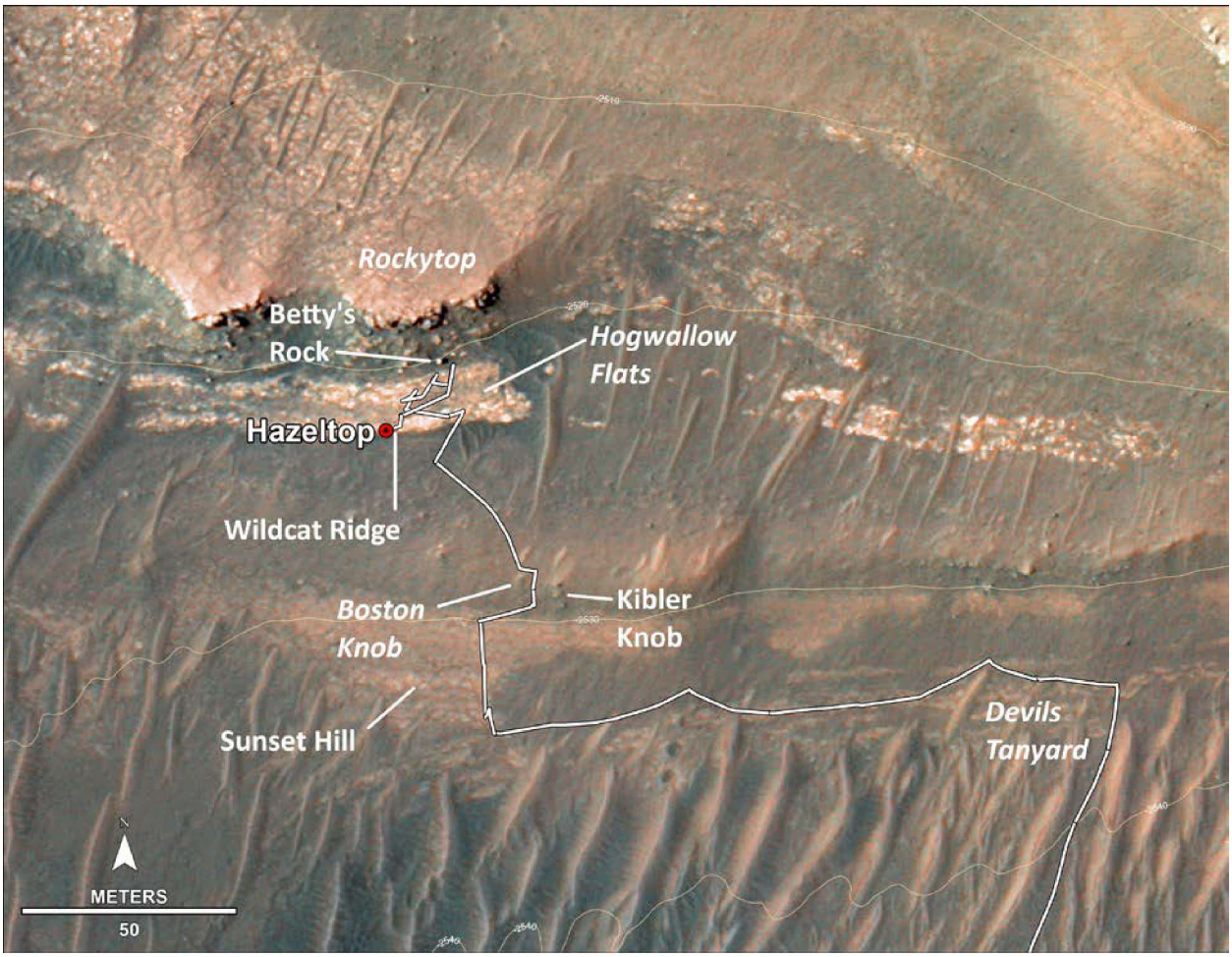

Figure 3 | View of *Hogwallow Flats* at the base of the *Rockytop* ridge within the *Hawksbill Gap* delta front stratigraphy. (a) The *Wildcat Ridge* outcrop is located at the base of the exposed *Hogwallow Flats* member, which underlies *Lower Rockytop*. The *Franklin Cliffs* in the distance (upper right) are comprised of stratigraphically higher delta units. Lower stratigraphic units and crater floor lie below the bottom of the image. The *Wildcat Ridge* block is ~0.4 m across. The *Skinner Ridge* block is ~1 m across; the vertical distance from *Skinner Ridge* to the highest point of *Upper Rockytop* seen in this image is ~6.5 m. View is to the NW; Sol 459, zcam08479, Z110 enhanced color. **(b)** The *Wildcat Ridge* outcrop viewed from the sampling workspace; View is to the NW; Sol 518, zcam05842, Z034 enhanced color.

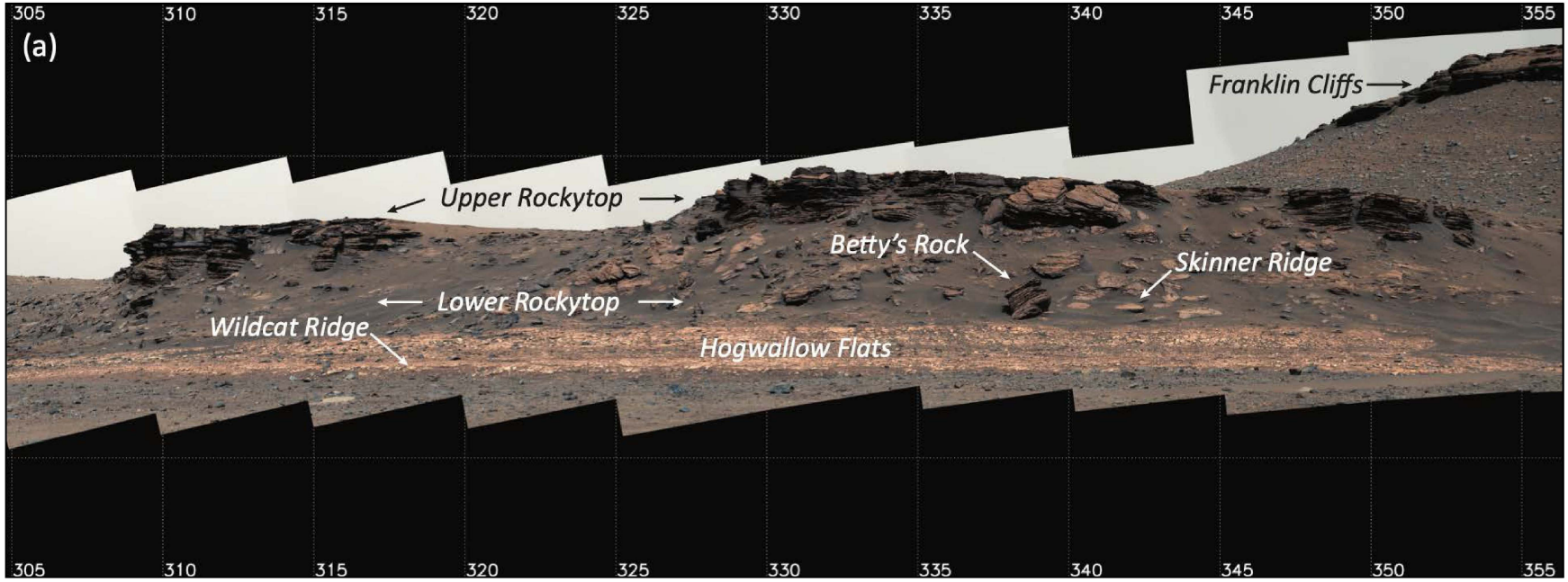

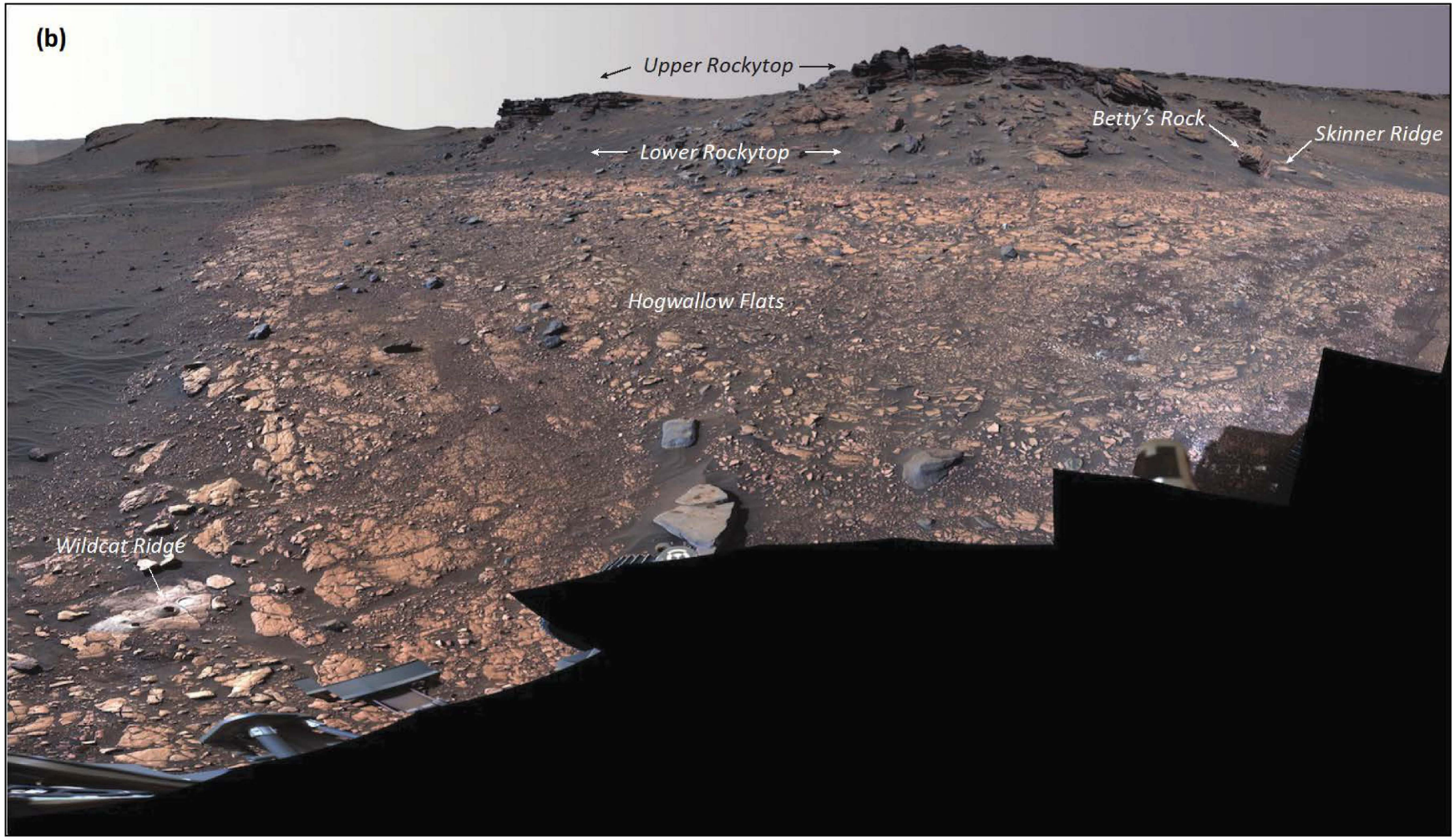
(b)
Upper Rockytop
Lower Rockytop
Betty's Rock
Skinner Ridge
Hogwallow Flats
Wildcat Ridge

Figure 4 | Stratigraphic column of the *Shenandoah* formation explored at *Hawksbill Gap* between Sols 439-538. c/si/vf = clay/siltstone/very fine sandstone; f = fine sandstone; m = medium sandstone; C = coarse sandstone; vC = very coarse sandstone.

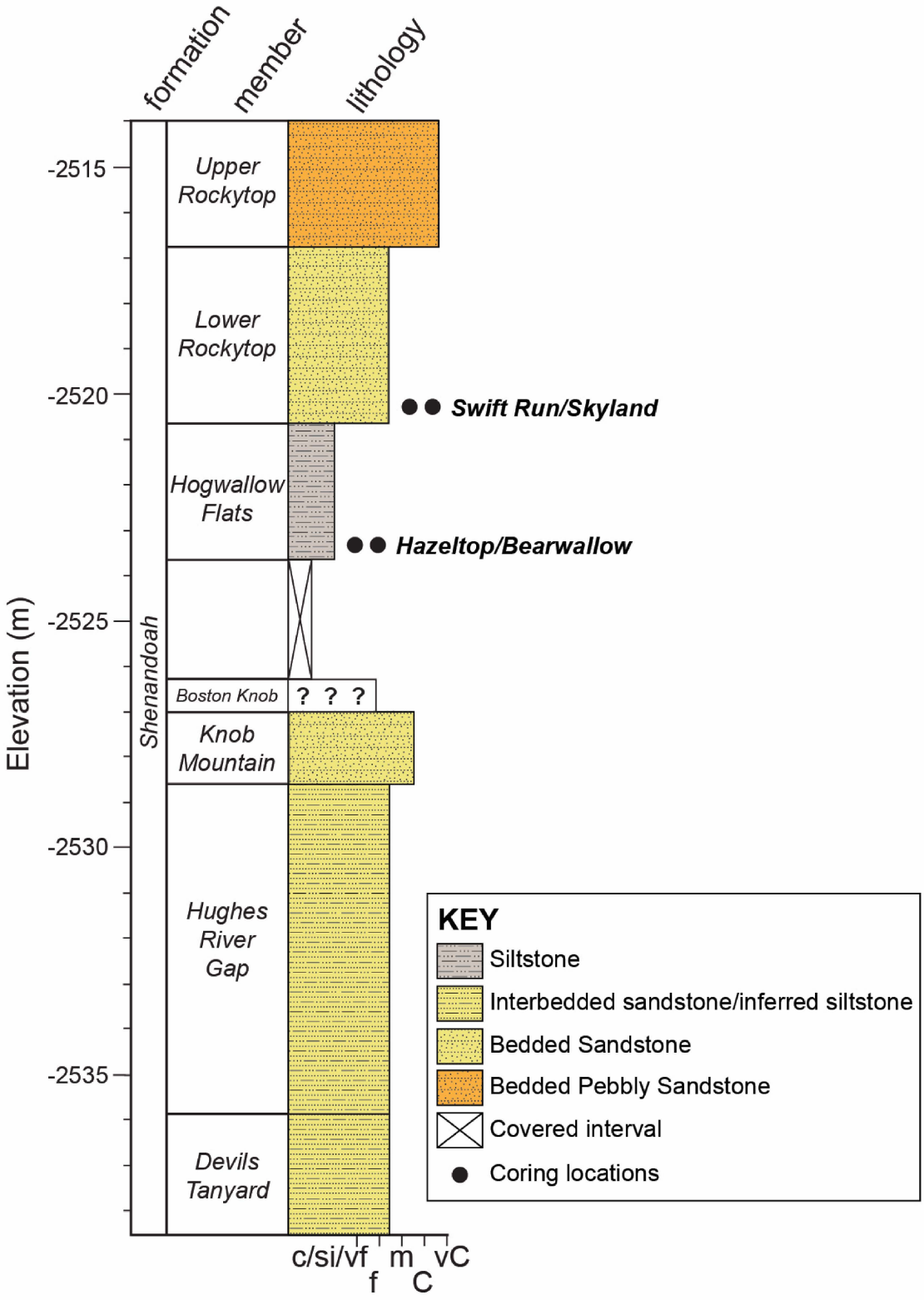

Sample-Related Observations

Workspace Images

Figure 3 shows a Mastcam-Z panorama of the *Wildcat Ridge* outcrop within its local context of lower *Hogwallow Flats*. **Figure 5** shows a Mastcam-Z workspace mosaic with the *Berry Hollow* abrasion patch and *Hazeltop*. The *Bearwallow* sample was collected after this image was taken. The surface of *Wildcat Ridge* is fractured, dusty, and light-toned. The large fractures are filled with a dark sand whereas the small fractures are visible as linear depressions surrounding raised polygons. No grains are visible in the surface of the rock. *Wildcat Ridge* has many diagenetic features including multiple linear sets of raised nodules visible to the left of the *Hazeltop* tailings pile. Additional larger nodules between *Hazeltop* and *Berry Hollow* appear to have a random spatial distribution.

Wildcat Ridge is surrounded by regolith, precluding observation of faces that might reveal bedding planes. However, outcrops to either side of and below the workspace show horizontal parallel bedding. The *Wildcat Ridge* block appears to be in-place. The only changes to the workspace that occurred during abrasion and sampling were the settling of sand within large fractures.

SCAM RMI images of *Wildcat Ridge* (**Figure 6**) show an uneven, undulatory, fractured, and dusty surface. The rock contains surface mounds that are 1-10 millimeter in height, as well as ridges and layers with millimeter-scale surface topography, but does not exhibit distinctly recessive layers nor visible grains at the surface. **Figure 6a** shows a pair of nodules, 5 mm and 8 mm in diameter, that we interpret as diagenetic features. A few cm away are multiple concentric raised features around 300 µm thick. Fractures in the bedrock visible in the ZCAM images are also visible in the RMIs and crosscut these diagenetic features, indicating the diagenetic features predate fracturing. **Figure 6b** shows an RMI of the LIBS-marked core top of the *Bearwallow* sample. The image is centered on a set of small fractures that are visible as linear surface depressions. Dust and sand-sized grains are present as surface debris in both RMIs.

Figure 5 | **Mastcam-Z workspace image of *Wildcat Ridge*.** *Wildcat Ridge* after sampling *Hazeltop* and abrasion of *Berry Hollow*. The abrasion patch diameter is 5 cm. Sol 513, zcam08537, Z110 enhanced color.

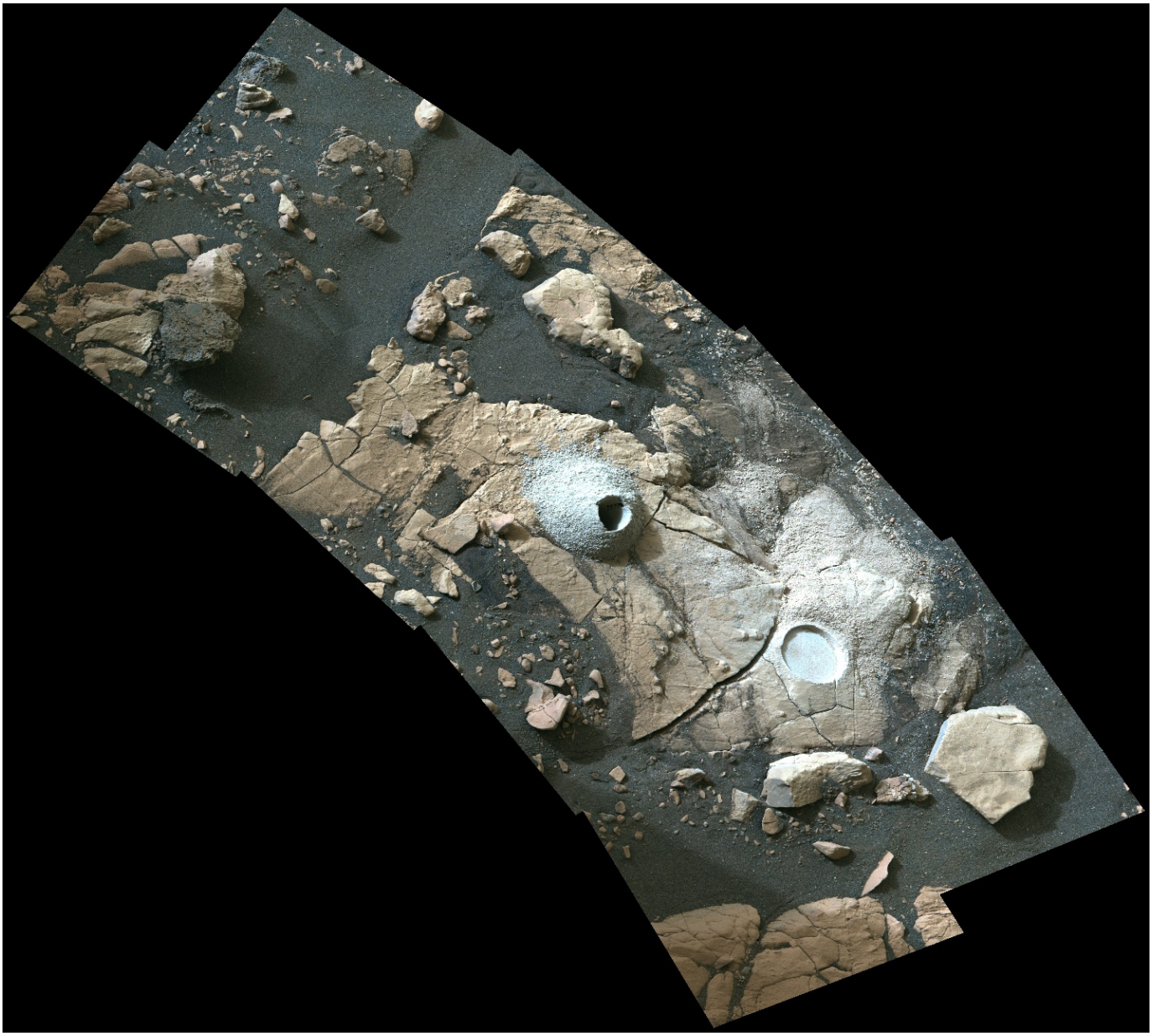

Figure 6 | **SCAM RMIs of Wildcat Ridge.** Gaussian stretch RMIs of two different natural surface targets on the *Wildcat Ridge* outcrop. **Left:** *Hightop* showing multiple diagenetic features; smooth protrusions are potential concretions and are surrounded by mm-scale concentric layers with curved edges. **Right:** *Bearwallow* showing the undulatory surface texture and small fractures.

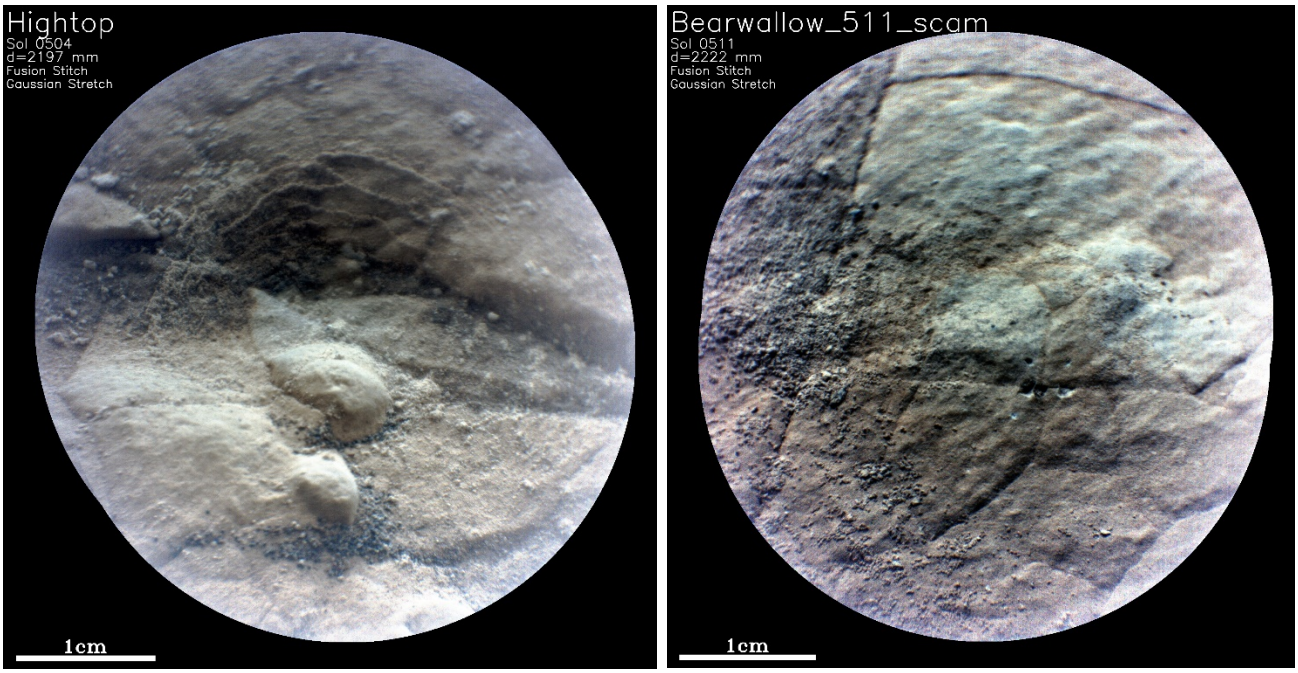

Pre and Post Coring/Abrasion Images

The *Wildcat Ridge* outcrop is one of numerous low-relief, extensively fractured rocks exposed within *Hogwallow Flats* that presented challenges to placing abrasion and coring hardware. *Wildcat Ridge* was selected for abrasion and sampling after assessing multiple outcropping rocks in *Hogwallow Flats*; it was found to be sufficiently large and flat for abrasion and coring, and was free of through-going cracks.

The natural surface of *Wildcat Ridge* (**Figure 7**) is light-toned and fine-grained; few grains are visible. There is minimal relief on the surface, and visible ventifacts and coatings are absent. Prior to rover activities, dust and sand had accumulated in the low-lying outcrop margins and along fractures. Diagenetic features, such as concretions and veins, are common throughout *Hogwallow Flats* and expressed in *Wildcat Ridge* as cm-sized protrusions (e.g., **Figure 7**). The Bearwallow core was acquired within a few cm of surface lumps interpreted to be concretions (Figure 7). The Hazeltop core was acquired in a surface with multiple lumpy surface features, including a large prominent possible

Figure 7 | Sol 511 WATSON 40 cm standoff image of *Wildcat Ridge*, showing the Berry Hollow abrasion patch (right) and the *Hazeltop* core tailings (left). The center inset is a WATSON 7 cm image inset of the *Bearwallow* target (pre-core).

The *Berry Hollow* abrasion (**Figure 8**) revealed that the underlying rock is composed largely of silt-sized to very fine sand-sized material. Most of the grains are a tan color and are subrounded and have similar size indicating extensive sorting. The grains are surrounded by a reddish-brown matrix that fills nearly all intergranular spaces, creating a nonporous appearance. A few small cavities or vugs are present. Several bright white curvilinear veins a few mm wide and up to a cm long are visible. The rock appears to be a mudstone that has experienced diagenesis.

Figure 8 | WATSON 7-cm standoff daytime image of *Berry Hollow* abrasion patch. This image nicely shows the bright white veins.

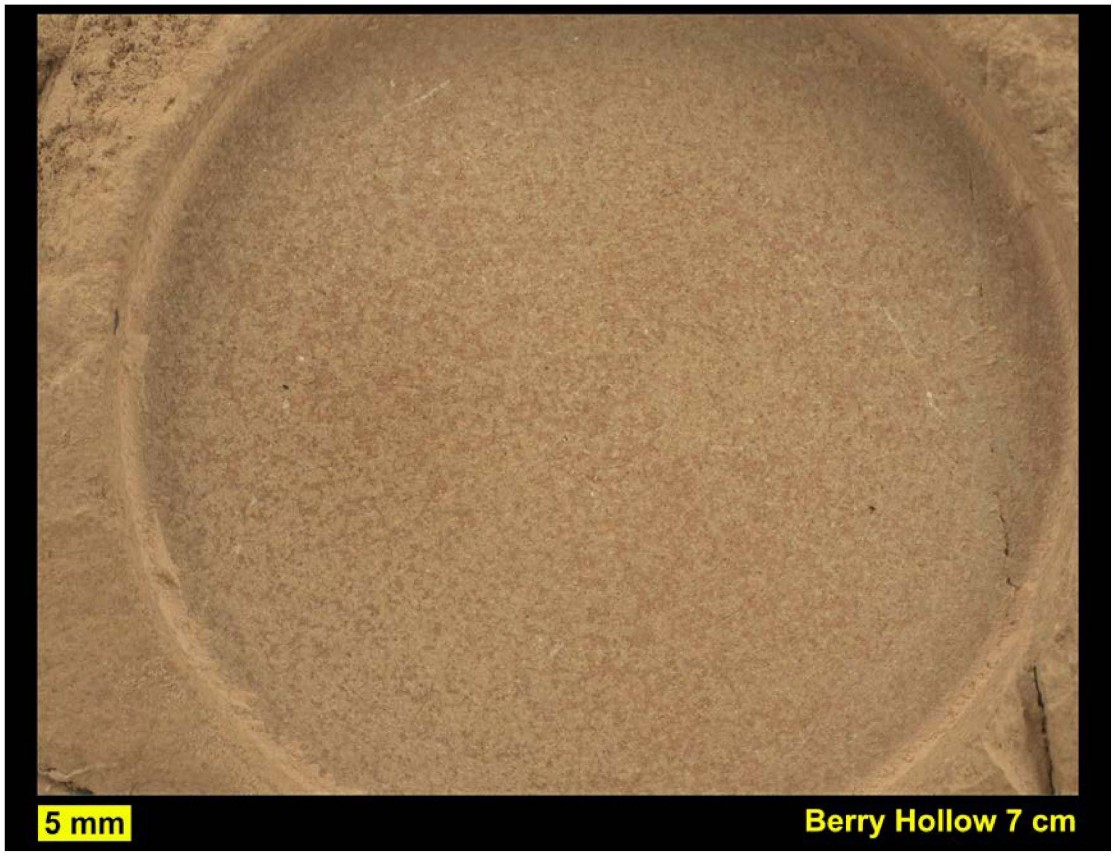

Figure 9 | Grain size distribution of *Berry Hollow*.

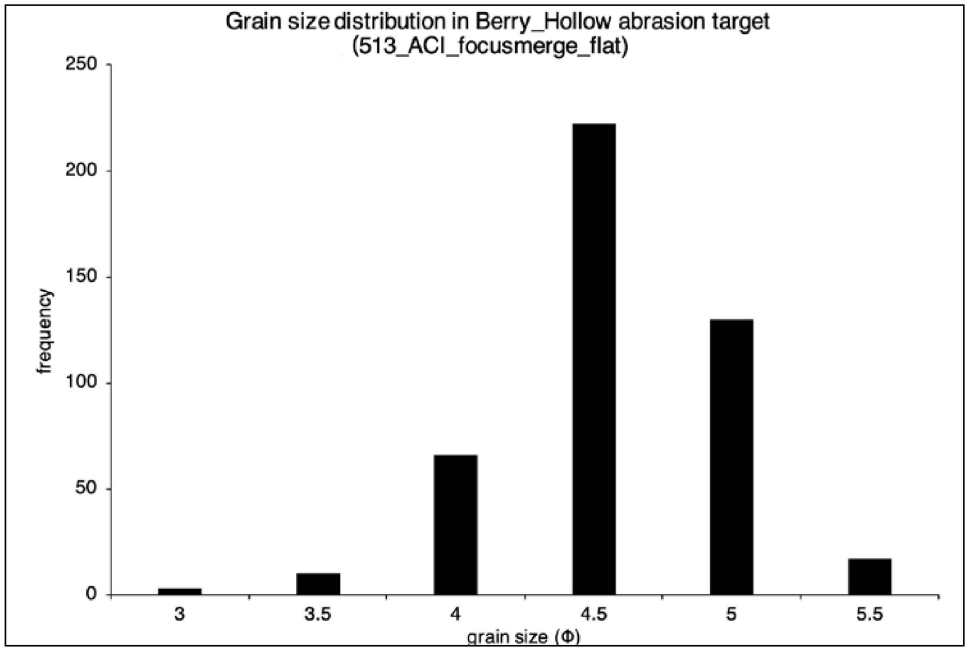

Figure 9 shows the distribution of grain sizes in *Berry Hollow*. Equivalent diameters of 448 grains were measured at intersection points of a grid with 0.5 mm spacing, projected on a mosaic of SHERLOC ACI images of the abrasion patch. Grains in *Berry Hollow* show a unimodal distribution, with the mode at φ=4.5 (silt, 44 μm), mean grain size of φ =4.3 (silt, 50 μm), and standard deviation of φ=0.4 (well-sorted). [$\varphi = -\log_2(D)$, where D is the diameter of a grain in millimeters.] Measured grains range in size from 0.18 mm down to the limit of ACI resolution (10.1 μm/pixel, enabling objects of >30 μm to be resolved). Grains are typically subrounded (**Figure 8**). Using the textural classifications defined by Lazar et al. (2015), this rock is a coarse mudstone.

The *Hazeltop* and *Bearwallow* core-end images (**Figure 10**) show a smooth and flat core termination that exposes the fine-grained nature of the rock as well as a few white veins and spots. The hole created by *Hazeltop* coring is coated with tailings that completely obscure any wall features (**Figure 11**).

Figure 10 | (**a-b**) Cachecam images (stretched) and (**c-d**) ZCAM images of the *Hazeltop* (left) and *Bearwallow* (right) core samples The volume probe measured sample lengths were 59.7 mm (*Hazeltop*) and 62.4 mm (*Bearwallow*). The core diameters are 13 mm, for scale.

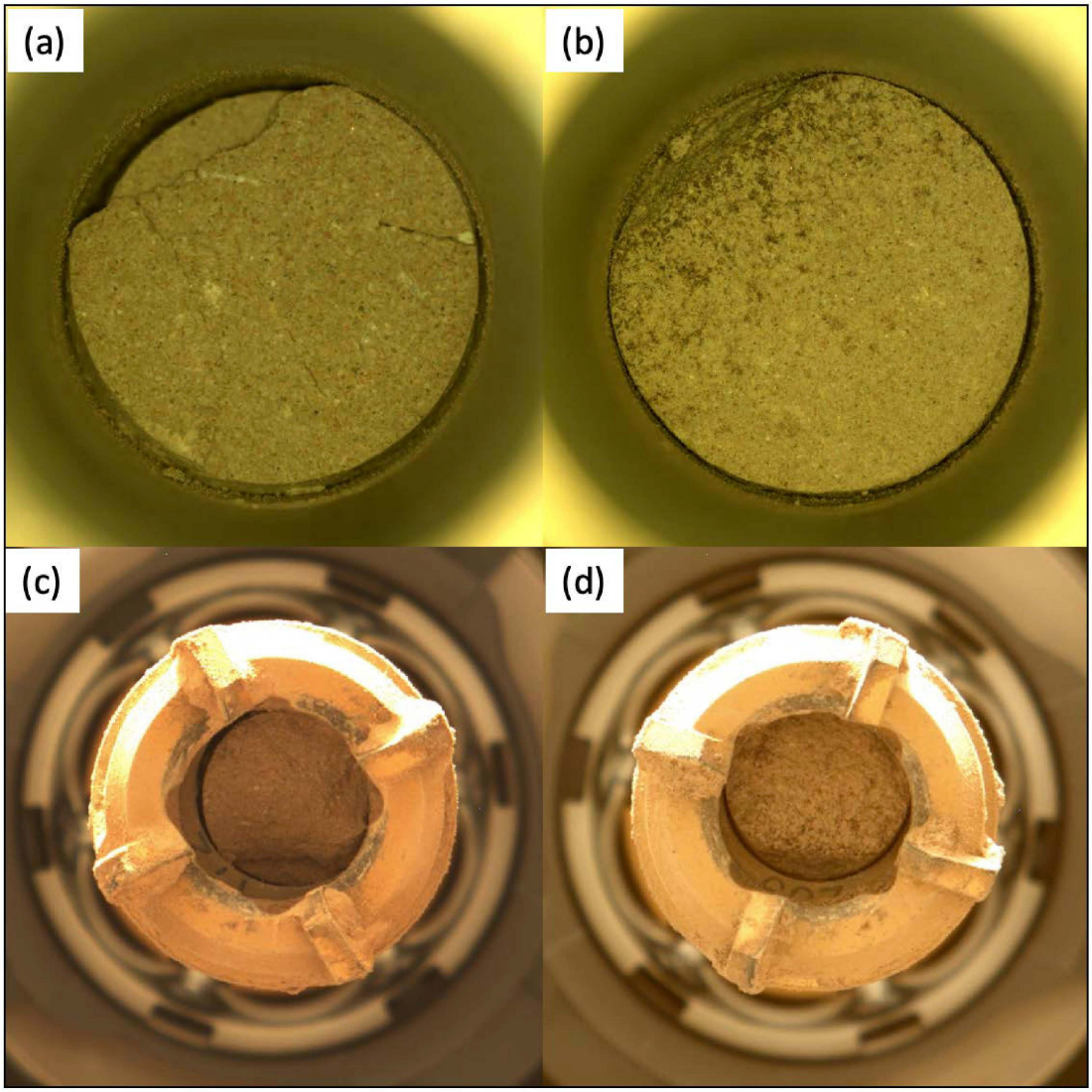

Figure 11 | WATSON down-borehole image after *Hazeltop* core extraction.

Elemental Geochemistry - PIXL

Elemental geochemistry for the *Wildcat Ridge* rock is from PIXL X-ray fluorescence (XRF) mapping of the *Berry Hollow* abrasion patch on Sols 505, 507, and a partial scan on 513 (**Figure 12**). The Sol 505 scan was 12.5 x 4 mm in extent, with points spaced 0.125 mm apart: it targeted visually representative material in the abrasion patch. The Sol 507 scan was 7 x 4 mm, with points spaced 0.125 mm apart; it targeted a white vein. The Sol 513 scan was intended as a 7 x 7 mm grid with points spaced 0.5 mm apart, in support of a SHERLOC observation across a white vein. The Sol 513 scan faulted and at this time the associated data is still being recovered. Unless noted, data here are from the Sol 505 scan.

Figure 12 | **PIXL raster scans on the *Berry Hollow* abrasion patch, Sols 505, 507, and 513.** Opaque green patches are the analysis areas, semi-transparent green are footprints of MCC images (**Figure 16**). Locations overlain on ZCAM images ZRF_0505_0711770186_519FDR_N02621222ZCAM03405_1100LMJ01 and SHERLOC / WATSON image SIF_0504_0711696567_636FDR_N02621222SRLC01034_0000LMJ01. Abrasion patch is ~5 cm diameter.

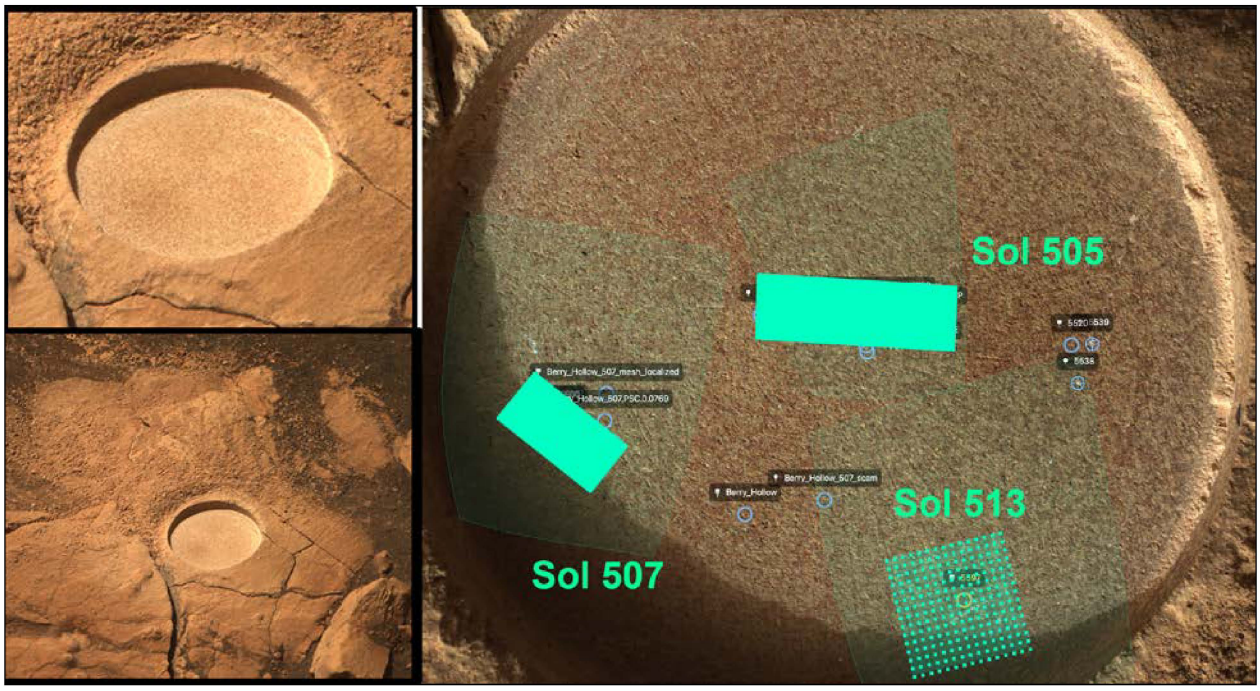

The bulk sum analysis, i.e., the average chemical composition, for the Sol 505 raster is given in **Table 1.** Beyond what is in the table, the *Berry Hollow* bulk composition contains no potentially detectable elements (e.g., Ni, Sr) at levels above their detection limits. Chemically, *Berry Hollow* is mixed silicate-sulfate rock, as shown by the moderate silica content and high abundances of FeO, MgO, and, most notably, ~20% SO_3. Also shown in the table is a selected average analysis for the white vein observed on Sol 507. The vein is dominated by $CaSO_4$, and the individual points are consistent with mixtures of pure $CaSO_4$ with the dominant silicate and sulfate components of the rock.

Table 1 | **Chemical Compositions by PIXL XRF.**

	Bulk Raster 0505		Ca-sulfate rich region (Sol 507)*	
Wt %	N=3342	Err 1σ	N=10	Err 1σ
Na_2O	1.9	1.0	3.5	1.3
MgO	13.1	1.3	7.3	0.8
Al_2O_3	5.0	0.8	2.5	0.6
SiO_2	32.5	4.5	14.7	3.1
P_2O_5	0.6	0.5	0.1	0.1
SO_3	20.0	4.4	45.4	3.1
Cl	0.4	0.1	0.5	0.1
K_2O	0.1	0.05	0.0	0.0
CaO	1.5	0.6	22.7	2.9
TiO_2	0.8	0.4	0.4	0.2
Cr_2O_3	0.1	0.3	0.0	0.04
MnO	0.1	0.1	0.0	0.02
FeO-T	17.5	1.8	8.5	2.2
Sum %	94.5		105.4	3.6
Mg#	57			

N is number of analyses averaged. Err is uncertainty (1σ) from calibration and counting statistics**.**
Mg# is molar Mg/(Mg+Fe), in percent.
*Corrected for roughness and diffractions.

The strong inverse correlation between SO_3 and SiO_2 (**Figure 13a**) shows that *Berry Hollow* is dominated by two phases, a sulfate and a silicate. For almost all points, and independent of sulfate content, analytical totals are significantly low, averaging 94% (**Figure 13b**). This indicates the presence of low-Z elements that PIXL does not detect directly (e.g., carbon, hydrogen). **Figure 13c** shows that the sulfate phase has molar (Fe+Mg+Mn)/S = 1 and that the silicate phase has (Fe+Mg+Mn)/Si = ~3/5. Both the sulfate phase (at Si=0) and the silicate phase (at high Si) have (nearly) identical molar Mg numbers of ~56%; see **Table 1** and **Figure 13d**. **Figure 13e** shows that Al is all in the silicate phase, that the sulfate phase is richer in Mg than the silicate, and that iron is about equally distributed between the two phases. In a ternary diagram of molar Al_2O_3-(CaO+Na_2O+K_2O)-(FeO_T+MgO) (**Figure 13f**) the Fe-Mg sulfate plots near the FeO+MgO apex. Much of the silicate phase plots in the region typical for Fe-Mg-bearing phyllosilicate minerals.

Figures 14 and **15** show multi-element color maps of the PIXL scans. **Figure 14** shows maps of the Sol 505 scan area. **Figure 14a** is primarily for comparison with element maps in other Initial Reports, because this presentation is more useful for igneous rocks and coarse clastic sediments than for the *Wildcat Ridge* mudstone. **Figure 14b** is more informative, as the silicate material (blue-green) and the sulfate rich (red) contrast strongly with each other. The rarity of yellow spots implies that alunite-group minerals (i.e, iron sulfates that require acidic conditions to form) are very uncommon. **Figures 14c** and **14d** address the distribution of minor phases (Ca-bearing & iron oxides) in the scan. **Figure 15** focuses on the white vein in the Sol 507 scan. **Figure 15a** is a multi-element map of the scan showing the extent of Ca sulfate in the vein, and its absence outside the vein. **Figure 15b** is exactly comparable to **Figure 13f**.

PIXL Micro-Context Camera images of the *Berry Hollow* abrasion patch (**Figure 16**) show more of the abrasion area than the XRF scans (**Figure 12**) and are used to extrapolate phase proportions from those of the XRF scan areas to nearly the whole abrasion patch. The MCC image of NIR-G-B (**Figure 16b**) is analogous to WATSON visible images. **Figure 16c,** the G/NIR ratio image, emphasizes iron mineralogy. Fe^{3+}-bearing minerals tending to have low values, and Fe^{2+}-bearing phases tending to have high values. These relationships can be quantified in a graph of UV, G, & NIR reflectance (**Figure 16d**).

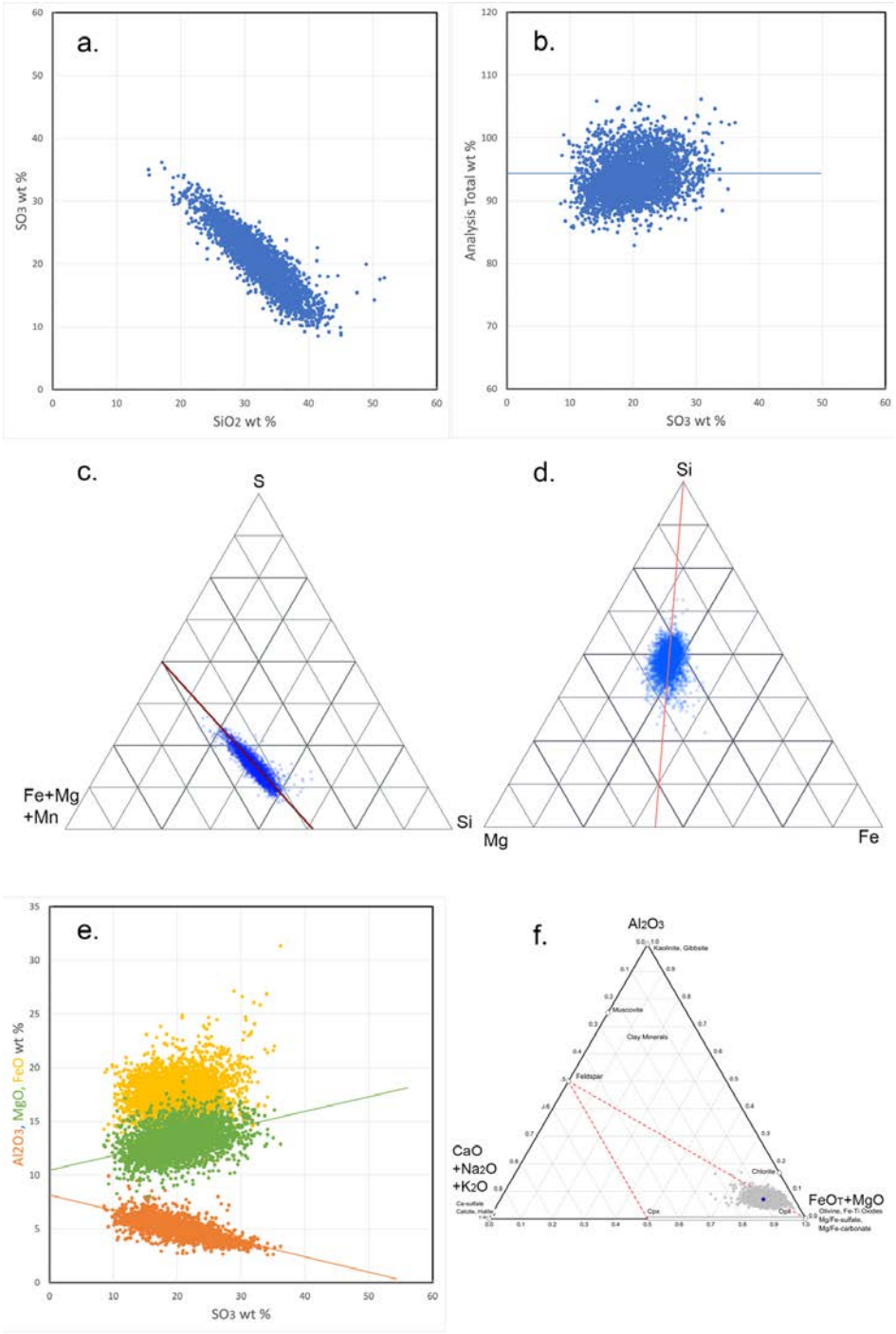

Figure 13 | **Element abundance relations, PIXL scan Sol 505.** (a) SO_3 vs SiO_2. (b) Analytical sum vs SO_3. (c) Ternary of molar S, Si, and Fe+Mg+Mn. (d) Ternary of molar Si, Mg, and Fe. (e) Multi-element correlations with SO_3 (f) Ternary of molar Al_2O_3-(CaO+Na_2O+K_2O)-(FeO_T+MgO), with common primary igneous and secondary minerals plotted for reference. The red dashed triangular envelope denotes a field in which mixtures of the primary igneous minerals olivine, pyroxene, and feldspar would plot.

Figure 14 | **PIXL multi-element maps for the *Berry Hollow* scan on Sol 505**. (a) Red=FeO_T (10.8 to 30.4%), Green=Al_2O_3 (2.6 to 9.6%), Blue=CaO (0.4 to 7.5%). The few green spots represent an Al-rich phase, likely the purest areas of the silicate mineral (Figure 13e). (b) Red=SO_3 (8.5 to 34.9%), Green= Al_2O_3 (2.6 to 9.6%), Blue= SiO_2 (15.0 to 51.0%). The analysis spots in red-purple-blue represent mixtures of the sulfate and silicate phases (Figure 13c). (c) Red=CaO (0.4 to 7.5%), green=P_2O_5 (0.0 to 8.0%), blue=SO_3 (8.5 to 34.9%). Yellow and green analysis spots are rich in Ca & P and are inferred to be calcium phosphates. The purple spots are rich in Ca sulfate. (d) Red=FeO_T (10.8 to 30.4%), green=TiO_2 (0.2 to 7.6%), blue=Cr_2O_3 (0.0 to 5.1%). Purple and green spots might represent chromium- and titanium-rich Fe oxides.

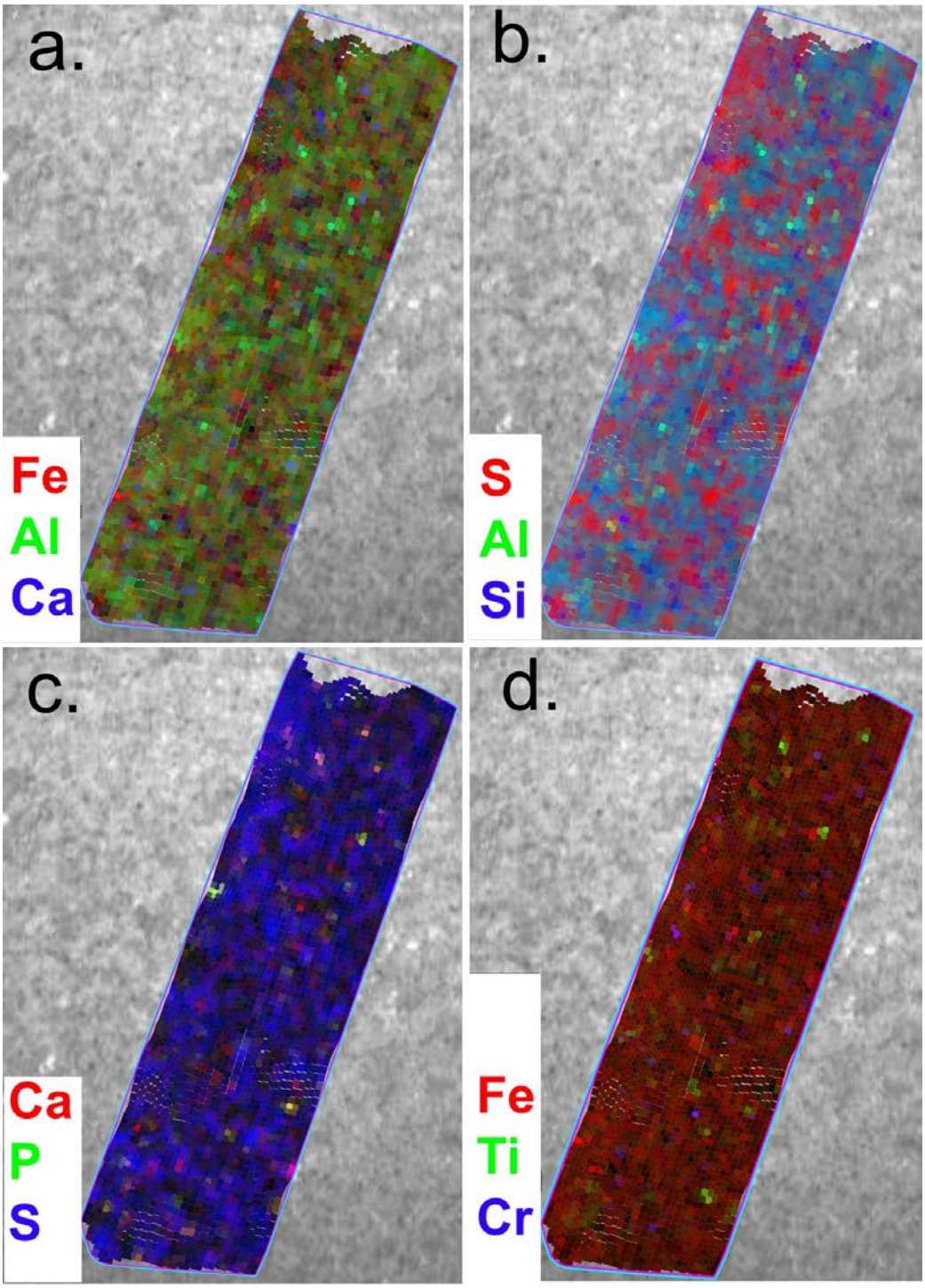

Figure 15 | **PIXL *Berry Hollow* scan on Sol 507**. **(a)** Red=CaO (0.4-25.8%), Green=SO_3 (8.1-46.6%), Blue=MgO (6.4 to 18.1%). The white vein visible in optical images (**Figure 12**) is composed of calcium sulfate (yellow pixels). There is little Ca elsewhere in the scan; the blue spots are the silicate component, the blue-green are the sulfate. **(b)** Ternary diagram (axes same as **Figure 13f**) for the Sol 507 scan of *Berry Hollow*. Data exhibits the same distribution as for the 505 scan (**Figure 13f**) except for the string of points heading to the Ca+Na+K apex; those are interpreted as containing a calcium sulfate, probably anhydrite.

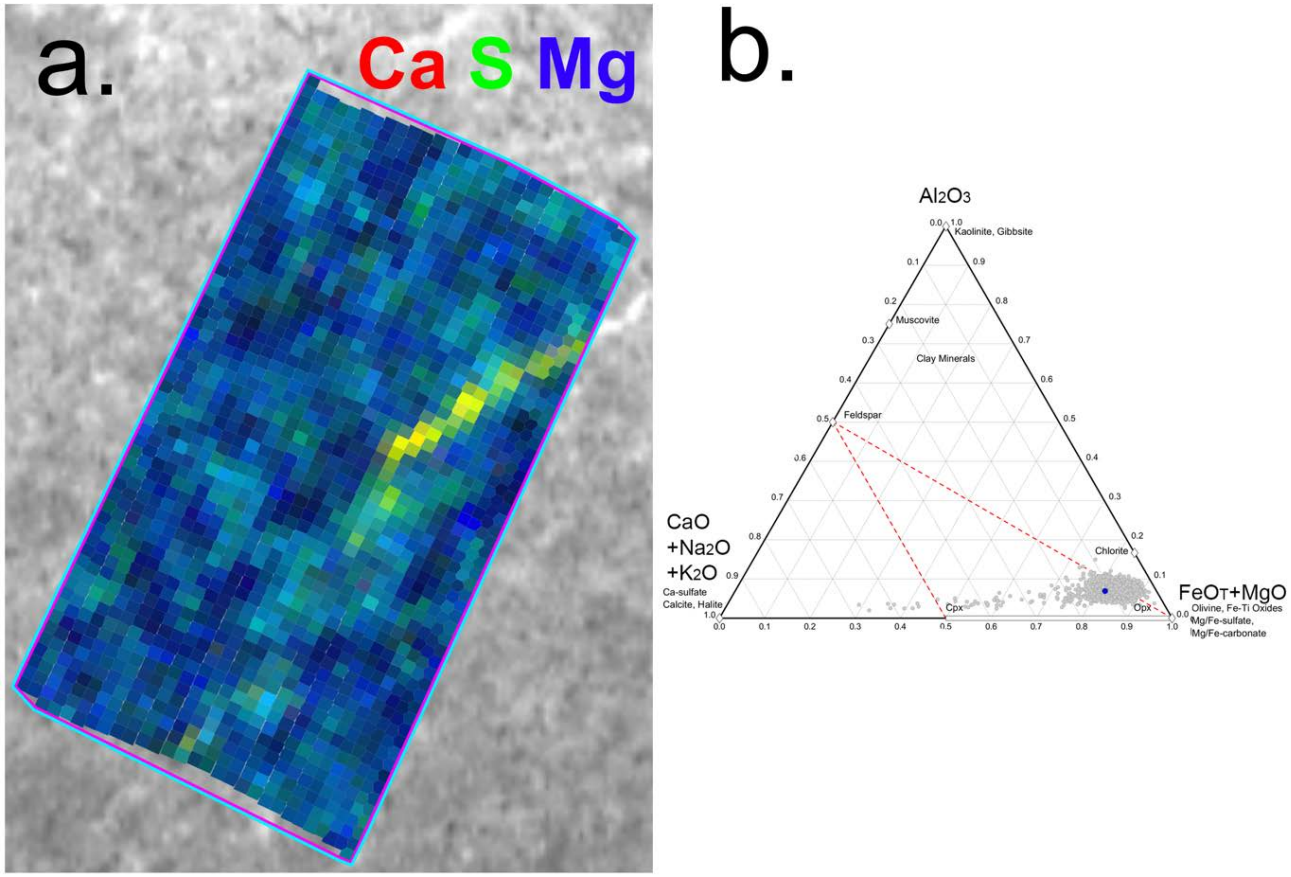

Figure 16| PIXL MCC (Micro-context camera) data for the *Berry Hollow* abrasion of Sol 505 (scan area outlined). **(a)** MCC Green grayscale image, a portion of the *Berry Hollow* abrasion. **(b)** MCC false color of abrasion area; Red = MCC Near-IR; Green = MCC Green; Blue = MCC Blue. **(c)** MCC ratio image of Green/Near-IR reflectance. **(d)** MCC reflectance ratios.

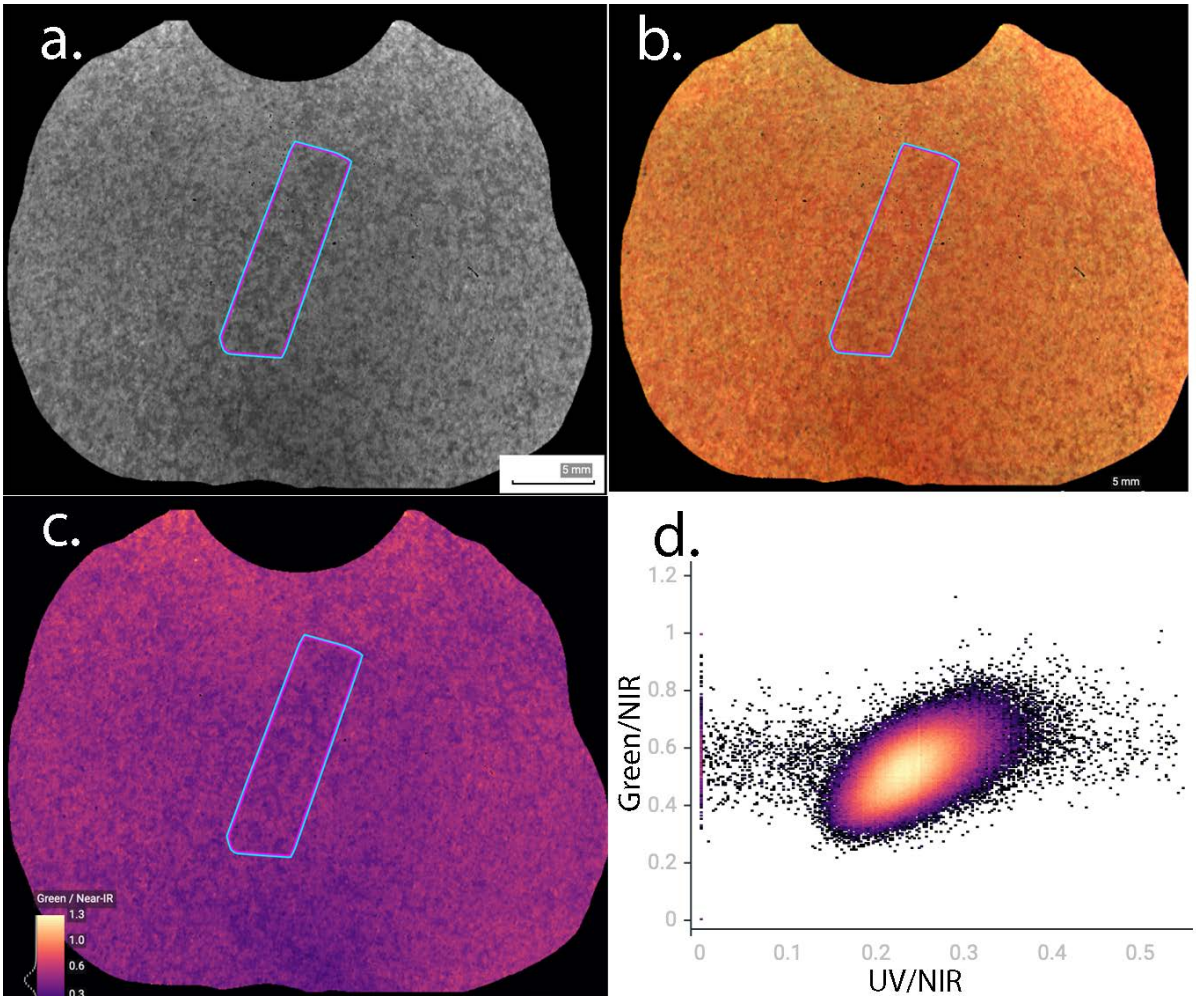

Mineralogy and Organics-SHERLOC

SHERLOC Raman and florescence spectra were obtained from two different areas of the *Berry Hollow* abraded patch, on Sols 505 and 513. The targeted area on Sol 505 contained no veins, while the area on Sol 513 contained a white vein crosscutting the matrix. The scans included one HDR scan (7x7 mm, 100 points, 780 µm spacing, 500 pulses per point), two survey scans (one 5x 5 mm and one 3.5x 3.5 mm, 1296 points, 144 µm spacing, 15 pulses per point) and five detailed scans (1x1 mm, 100 points, 144 µm spacing, 500 pulses per point).

The Raman spectra from scans on Sol 505 and 513 contain peaks (~1010 cm^{-1}, ~1125 cm^{-1} and a possible ~500 cm^{-1}) assigned to Mg/Ca sulfates (some weakly hydrated). These sulfates were found in many pixels of the scans, with more intense sulfate peaks in the bright white vein than the matrix outside the vein (**Figures 17 & 18** and **Table 2**). In the Raman spectra from Sol 505 scans (not shown)

there also peaks that can be assigned to carbonates (**Table 2**). The fluorescence signals are dominated by a double fluorescence feature at 303 and 325 nm, which is consistent with a mix of aromatic compounds or a single compound (possibly a heterocycle) and is found in varying intensity in almost every pixel in all the scans from both Sols 505 and 513. In the pixels with the most intense signal, the fluorescence signal saturated the detector. The survey scan on Sol 513 shows that the signal of the doublet fluorescence feature (303 and 325 nm) is most intense in the sulfate vein (**Figure 17**). PIXL data shows the vein is enriched in Ca sulfate compared with the matrix, which is more Mg-rich. In addition to the fluorescence doublet, there are also fluorescence features at 280 nm and 340 nm, consistent with single and double ring aromatic organic molecules, detected in a few pixels (**Figure 18**). Despite the high intensity fluorescence signal, the absence of organic signals in the Raman spectra suggests that organic compound concentrations are below the relatively high Raman detection limit.

The fluorescence and Raman signals observed in *Berry Hollow* are similar to those observed in scans collected on the natural surface target *Pignut Mountain*, also located in *Hogwallow Flats* and analyzed on Sol 463. The spectra of this target also contained a double fluorescence feature (303 and 325 nm) associated with sulfates (minimally hydrated) and a 330-340 nm fluorescence feature. The fluorescence signals observed at *Pignut Mountain* are the strongest ones observed so far on natural surfaces (the other analyzed natural surface targets being *Foux* and *Nataani* on the crater floor).

SHERLOC mineral identifications are shown in **Table 2**.

Figure 17 | **Sol 513 SHERLOC fluorescence and Raman spectral results for *Berry Hollow*. (a)** Colorized ACI image of the *Berry Hollow* abraded patch; blue rectangle indicates the survey scan area and white circles indicate regions of interest (ROIs) correlating to the fluorescence data presented in panels b and c. **(b)** Survey scan maps suggesting the presence of organics. Upper panel shows an RGB map indicating the main regions of organic fluorescence (303 and 325 nm). The lower panel is blank for this abrasion patch because no Raman features have been identified that would indicate the presence of organic materials**. (c)** Fluorescence spectra. The upper panel shows the average fluorescence spectrum for the whole area of analysis and the lower panel includes spectra from selected fluorescence ROI (see a and b). **(d)** Map showing the results of the Raman Survey scan. The grid of points indicates the points analyzed (cf. panel a). The blue circles indicate the points associated with the bright vein, whereas the red circles are the bulk of the analyzed area (matrix). The right panel includes average Raman spectra from the Survey scan. The upper spectrum is the average spectrum of the vein (blue circles in left panel), and the lower spectrum is the average spectrum of the matrix (red circles in left panel).

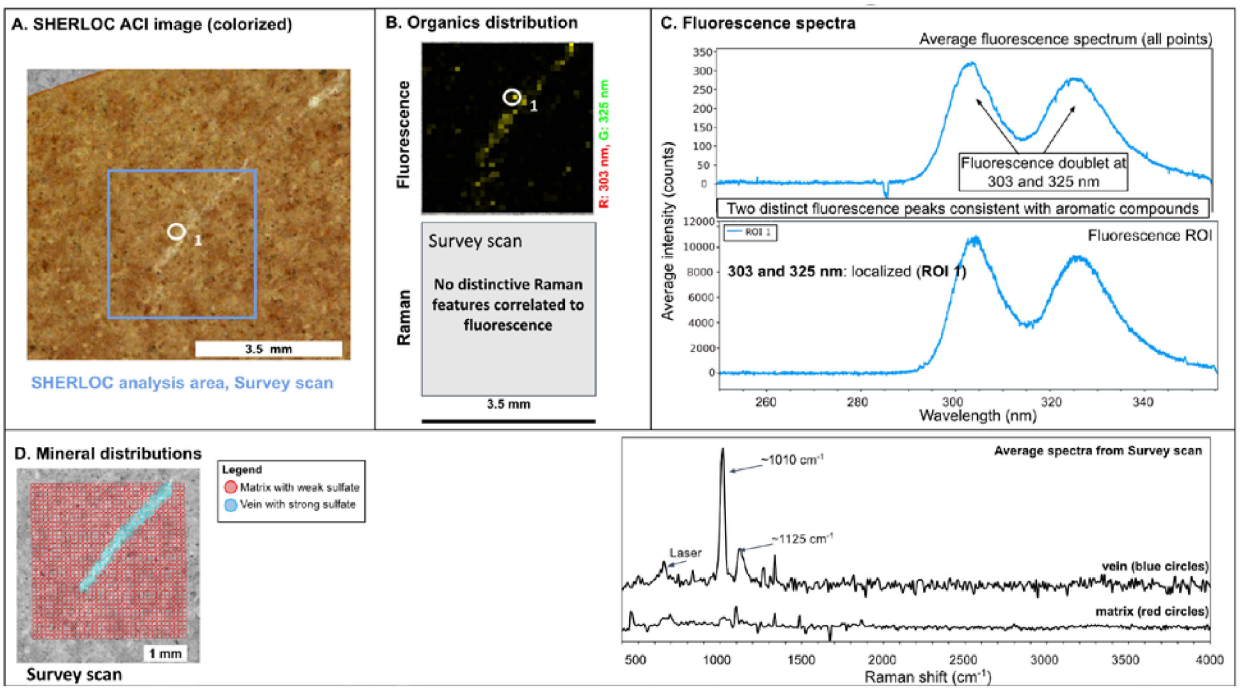

Figure 18 | Sol 513 SHERLOC fluorescence and Raman spectral results for *Berry Hollow*. (a) Colorized ACI image of the *Berry Hollow* abraded patch; blue rectangle indicates the detail 1 scan area and white circles indicate regions of interest (ROIs) correlating to the fluorescence data presented in panels b and c. **(b)** Detail 1 scan maps suggesting the presence of organics. Upper panel shows an RGB map indicating the main regions of potential organic fluorescence (280, 303, 325 and 340 nm). The lower panel is blank for this abrasion patch because no Raman features have been identified that would indicate the presence of organic materials. **(c)** Fluorescence spectra. The upper panel shows the average fluorescence spectrum for the whole area of analysis and the lower panel includes spectra from selected fluorescence ROIs (see a and b). **(d)** Map showing the results of the Raman detail 1 scan. The grid of points indicates the points analyzed (cf. panel a). The blue circles indicate the points associated with the bright vein, whereas the red circles are the bulk of the analyzed area (matrix). The right panel includes average Raman spectra from the detail 1 scan. The upper spectrum is the average spectrum of the vein points (blue circles in left panel), and the lower spectrum is the average spectrum of the matrix (red circles in left panel).

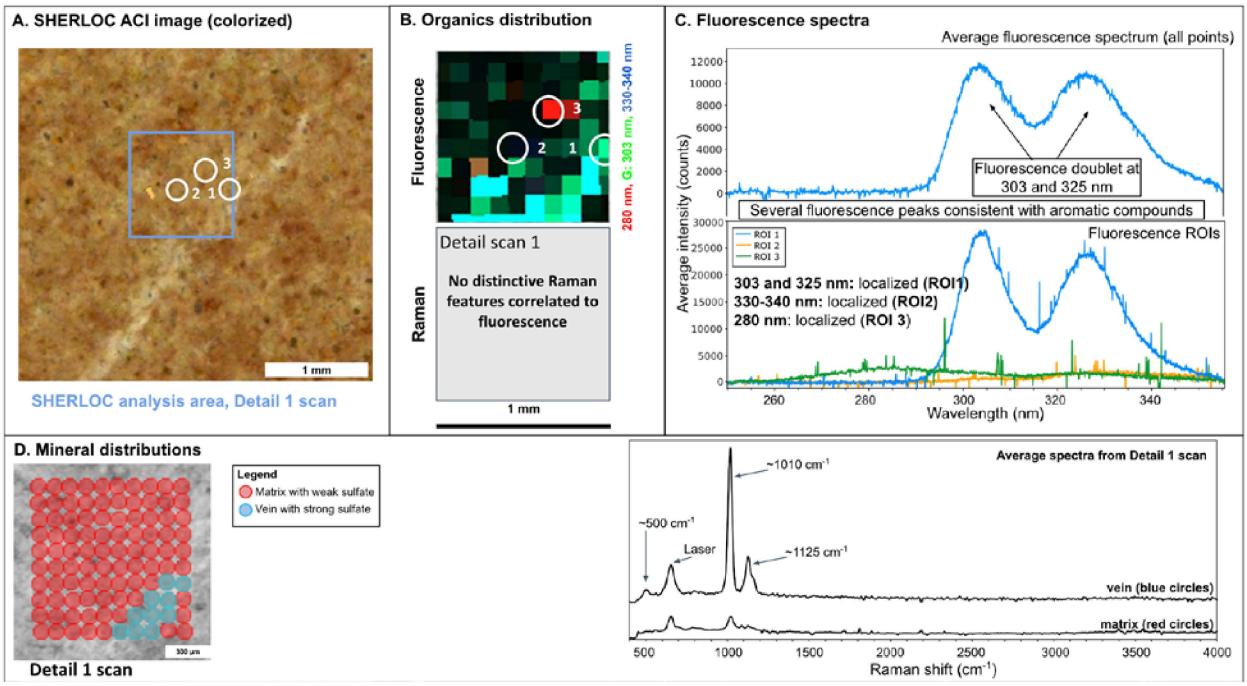

Table 2 | SHERLOC Raman spectra mineral ID.

Sample	Certain	Possible (not confirmed)	We looked for these, but cannot find them
Berry Hollow	Sulfates (weakly hydrated, most likely Mg/Ca) *(associated with both with white vein and matrix of the rock)* Carbonates (Fe/Mg)	-	-

Elemental Geochemistry and Mineralogy – SuperCam.

SuperCam remote micro-imaging (RMI) of *Berry Hollow* shows finely interspersed brown and grey areas with difficult-to-discern individual grains (**Figure 19**). The abraded patch exhibits some white veins less than one millimeter wide (**Figure 19**). Larger, centimeter-scale knobby veins can be seen extending above the surface of a rock adjacent to *Wildcat Ridge* (target *Mill Prong*). The presence of surface knobs, thin surface layers, ridges and veins and the absence of interlocking igneous grains support the interpretation of the *Hazeltop* and *Bearwallow* cores as samples of sedimentary rocks that have grains smaller than the scale resolvable by the RMI images (~200 μm) and that experienced post-depositional fracturing and fluid flow that created veins.

Figure 19| **SuperCam RMI images of the *Berry Hollow* abrasion, Sol 507**. Interspersed irregularly shaped brown and grey areas are visible, but individual grains are not. Red crosses show spots analyzed by LIBS that sample both brown and grey areas of the rock. Two white veins thinner than 1 millimeter are also present in the left and the top right part of the abraded area.

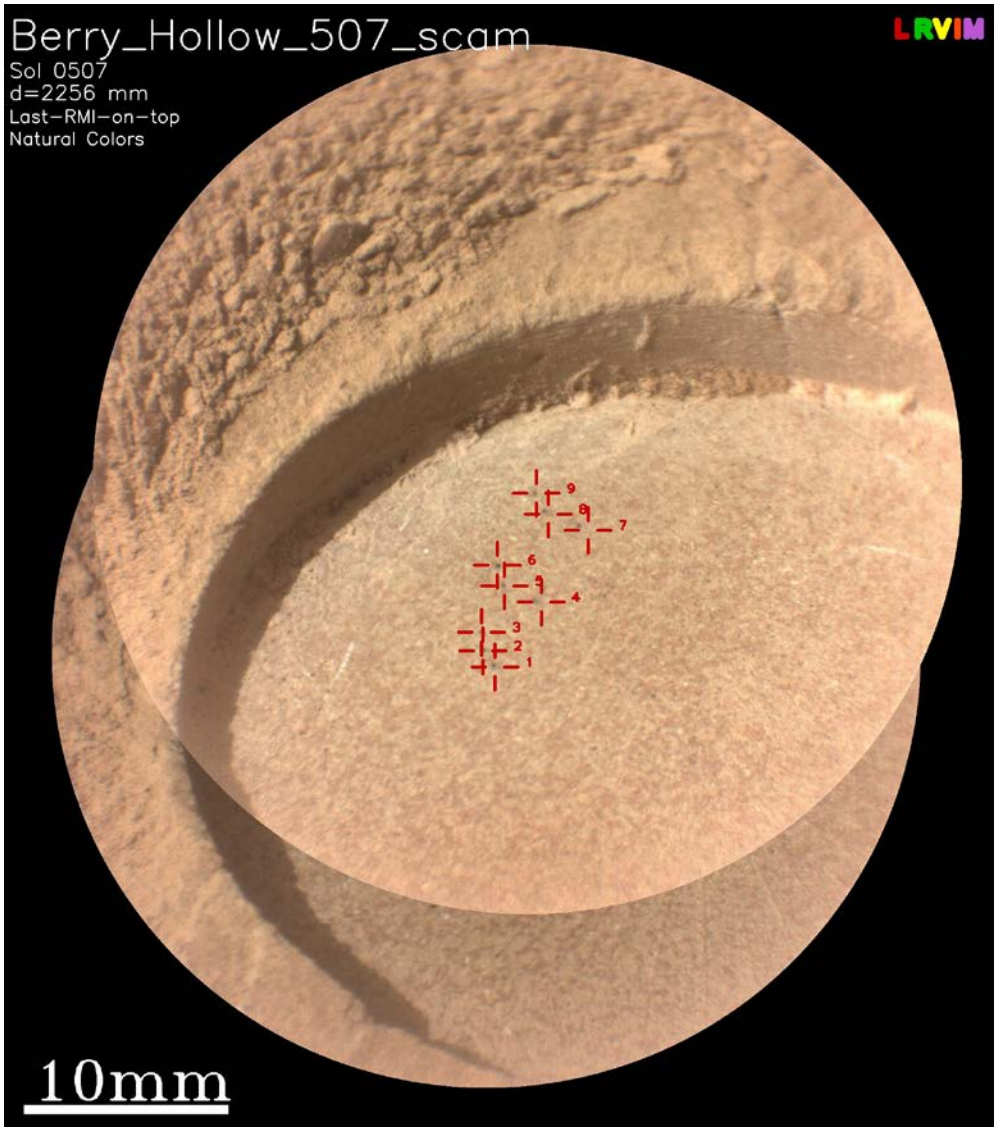

SuperCam LIBS observations of *Wildcat Ridge* and nearby targets (**Figure 20**) show that the rocks are compositionally heterogeneous on the scale of RMI images (**Figure 19**) and LIBS raster spacing (generally a few mm), but with a smaller compositional spread relative to the coarse-grained rocks at *Skinner Ridge*, where the previous two cores of aqueously deposited sandstone were acquired. The LIBS data on the natural and abraded surfaces of *Wildcat Ridge* and on the tailings after the core collection show that the analyzed points are enriched in SiO_2 and Al_2O_3 (**Figure 20**). The points analyzed by LIBS compositionally group with pyroxene minerals (**Figures 20, 21**), although none seem to match pyroxene calibration standards and on-board calibration targets (**Figure 21**). None of the points from *Wildcat Ridge* group with olivine or serpentine (**Figure 20**). The compositions of individual LIBS spots on the natural surfaces and on the abrasion patch *Berry Hollow* are consistent with a possible mixture of low-Ca pyroxene and additional unrecognized phases, all with grain sizes smaller than the LIBS spots. About 25% of the points that were analyzed by LIBS on *Berry Hollow* abrasion patch had a total oxide content lower than 85 wt%, indicating the presence of elements that are not quantified by SuperCam such as H, C, S and Cl. All points presented evidence of hydration. The white vein on the target *Mill Prong* analyzed on Sols 517 and 521 contains spots that group with gypsum (**Figure 21**), consistent with the post-depositional formation of gypsum within *Wildcat Ridge.* In combination, these observations support the interpretation of *Hazeltop* and *Bearwallow* cores as samples of a sub-aqueously deposited and altered sedimentary rock with grains finer than the resolution of the RMI images and LIBS spots (~200-250 μm).

Figure 20| SuperCam LIBS major element oxide (MOC) analyses of *Wildcat Ridge rocks*. Solid solution fields for olivine, pyroxene, and feldspar compositions are included. Black points show the delta rocks analyzed from Sols 420-540.

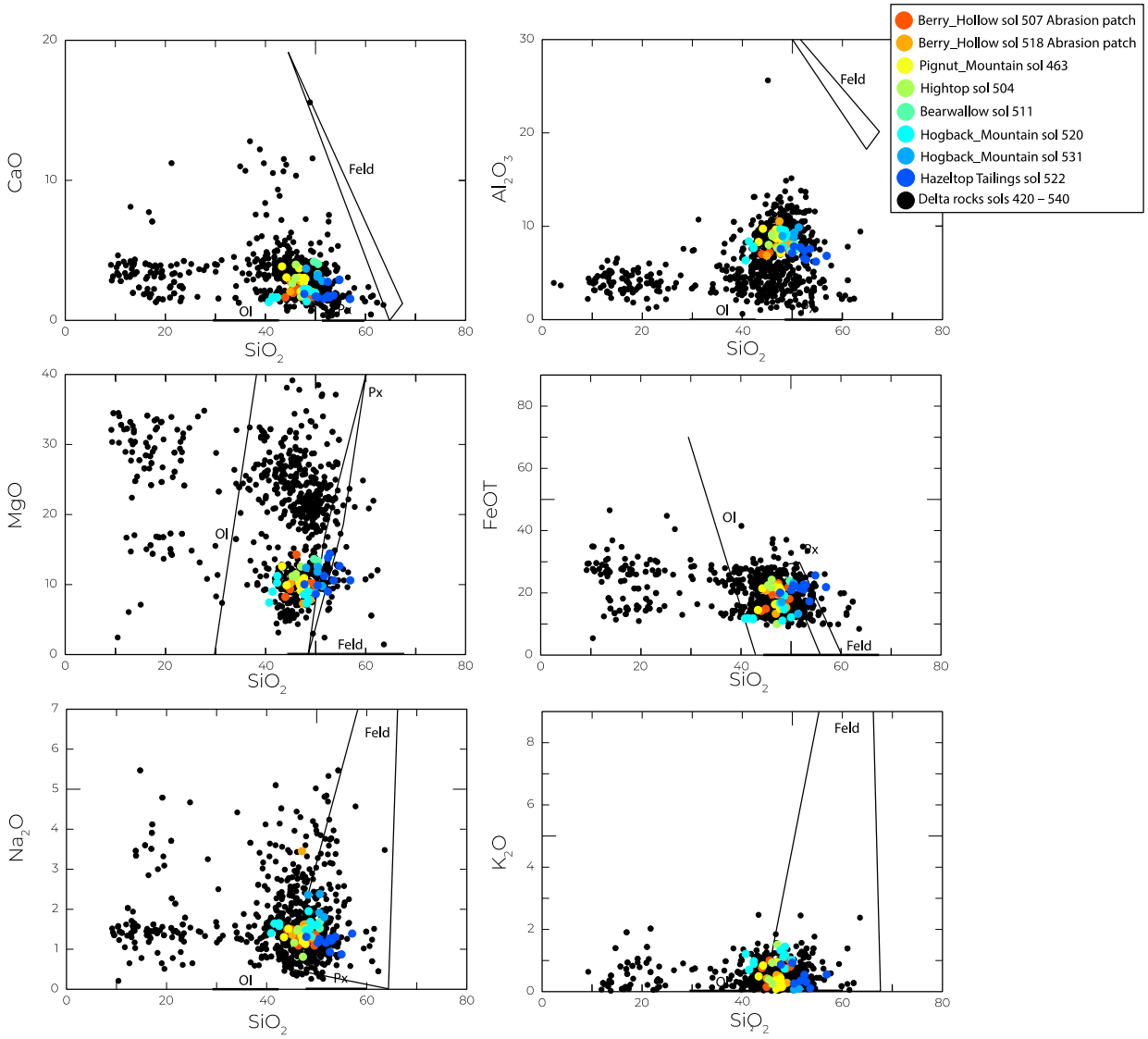

Figure 21| Molar compositions of the points in the SCAM LIBS raster of *Wildcat Ridge.* Data are from Sols 507, 511, 515, 517, 520, 521, 522 and 531 compared to various minerals and on-board calibration standards. Blue and purple circles show points analyzed on the natural surface targets *Bearwallow* on Sol 511 and *Hogback Mountain* on Sols 520 and 531. Fuchsia and red circles show the composition of the points analyzed on target *Mill Prong* from Sols 517 and 521. This target contained a vein enriched in calcium; points analyzed in this vein cluster with gypsum in the left lower corner of the ternary diagram. Orange circles show points on the abraded patch *Berry Hollow* analyzed on Sols 507 and 515. Darker and lighter yellow circles show the composition of the tailings on the target *Hazeltop* on Sols 511 and 522. The legend presents a range of standards from igneous calibration targets (Ca-pyroxene, pyroxene, olivine) to other minerals (calcite, ankerite, siderite, serpentine, gypsum). The green cloud shows all data points acquired up to Sol 540.

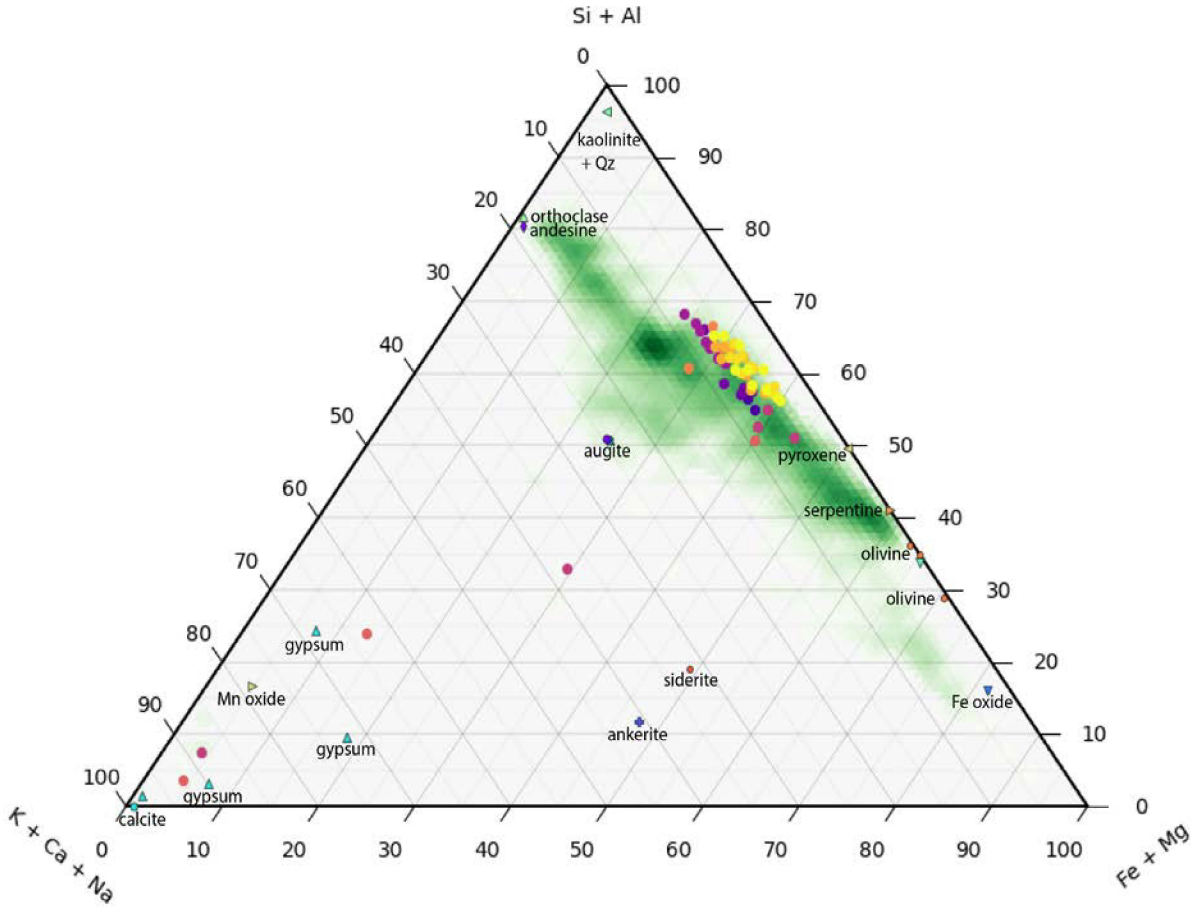

SuperCam VISIR rasters on the *Wildcat Ridge* natural and abraded surface targets and tailings from the coring activity (**Figure 22**) reveal the presence of hydration and phases produced during aqueous alteration. The SCAM VISIR technique is highly sensitive to hydrated minerals, so the signatures of hydration are present in the spectra even when hydrated minerals are a minor proportion of the rock. **Figure 22** shows the absorption bands that indicate the presence of hydrated minerals. The main signals of hydration are present at 1.94 µm and 1.42 µm in abraded targets. The weak absorptions in the 2.1-2.5 µm range indicate small amounts of Fe/Mg-clay minerals, possible carbonates (2.53 µm band), hydrated silica or Al-clay minerals (2.2 µm band) and sulfate at 2.39 µm that is stronger compared to previous outcrops. The absorption at 0.43 µm, possibly attributed to ferric sulfate minerals, is observed for the first time here at *Wildcat Ridge*. The VISIR spectra are greatly affected by the grain size, contributing to

the differences in the tailings and rock spectra, but all support the presence of hydrated, sulfate-rich, sub-aqueously deposited and aqueously altered rocks in *Wildcat Ridge*.

Figure 22| Mean reflectance spectra of the SuperCam VISIR rasters on the *Wildcat Ridge* outcrop. Mean reflectance spectra of the SuperCam VISIR rasters on the *Wildcat Ridge* outcrop (abraded surface and tailings from coring activity). Lighter lines near 2 µm indicate the spectral range possibly affected by the CO_2 absorption features that could remain after the atmospheric correction. The UV region was smoothed using a *Savitzky-Golay* filter. Note that owing to temperature sensitivities in the IRS instrument, the calibration is still uncertain for wavelength longer than ~2.55 µm. The absorption centers are indicated with arrows and their positions point towards the presence of hydrated minerals: sulfates with the absorption around 2.39 µm, Fe/Mg-phyllosilicates with the absorption at 2.23 and around 2.3 µm and/or carbonates.

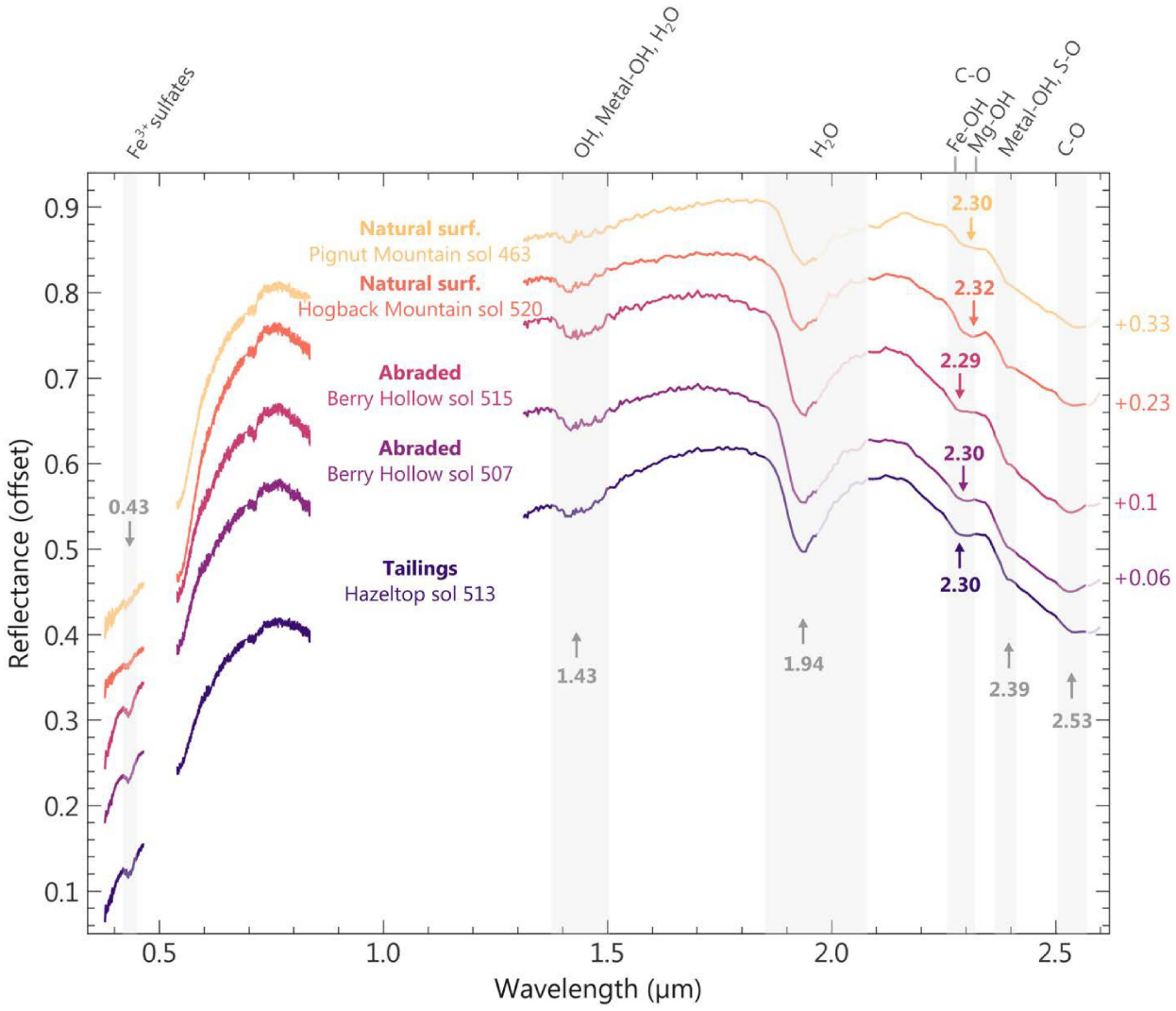

Subsurface Structure

The subsurface structure of the delta front from the *Wildcat Ridge* outcrop southward is revealed by RIMFAX radargrams acquired between Sols 461 and 501 (**Figure 23a**). *Wildcat Ridge* is a light-toned sedimentary rock that outcrops as horizontal bedrock that is part of the lower *Hogwallow Flats* member of the Western Delta front. This unit is above several horizontally stratified units in the Delta front, all of which appear in both outcrop and in the subsurface as seen in RIMFAX radargrams (**Figure 23b**). The *Wildcat Ridge* samples were acquired near the base of the *Hogwallow Flats* member, which, in the radargram, is represented by the uppermost ~3 m. *Hogwallow Flats*, *Boston Knob* (upper and lower), *Hughes River Gap*, and *Devils Tanyard* members have been extrapolated from surface outcrops (see **Figure 1a**). A base delta unconformity capping the underlying Séítah Formation strata may be presesnt in RIMFAX data at depth -2542 to -2543 m. Subsurface depths have been calculated from two-way travel times using a velocity of 0.15 m/ns.

Figure 23 | **Geological context and RIXFAX-derived subsurface stratigraphy of the delta front**. (**a**) Location of the *Berry Hollow* abrasion (made on the *Skinner Ridge* outcrop), within the delta front. Note the rover routes (in white) where RIMFAX data were collected. The blue circle indicates the Sol 502 EOD position. The red line indicates the approximate transect of the radargram shown in panel **b**. (**b**) Radargram of the N-S section from *Skinner Ridge* to *Wildcat Ridge* (and *Berry Hollow*) on Sol 502 (yellow star) and southward long the delta front. The section includes data collected on Sols 461 and 501; data were not collected along the transect between ~7-12 meters. The radargram shows strata with largely horizontal geometries above the Séítah Fm. (interpreted as the lowermost portion of the radargram).

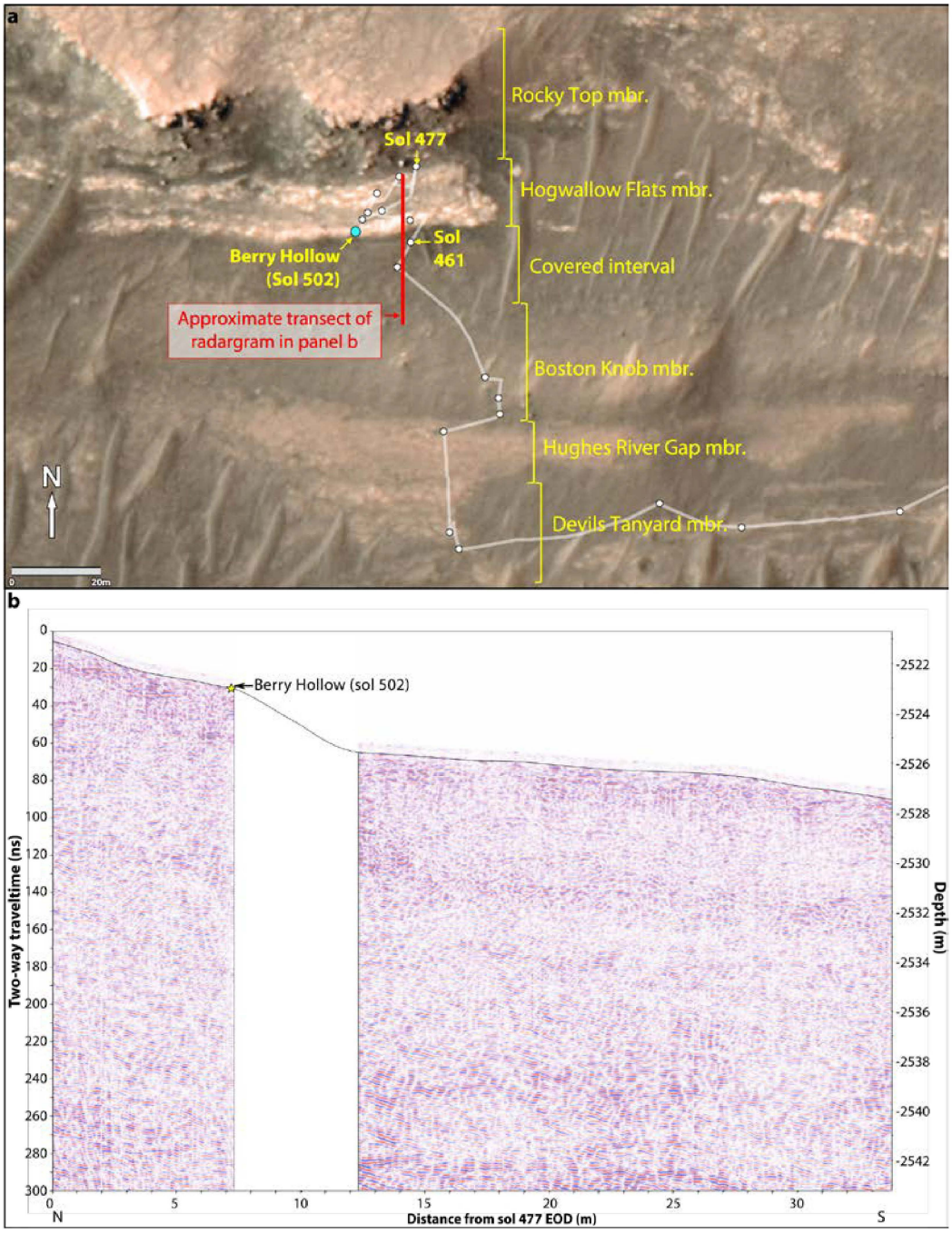

Core orientation

At the time of drilling and 6.6-cm pre-drilling WATSON imaging, the rover, coring drill, and WATSON had the following characteristics:

1. Rover orientation quaternion just after drilling but before unloading the stabilizers (transferring from RMECH to SITE frame): **bQll1** = (0.583193, -0.0843587, 0.0916021, -0.802732)
2. Coring Drill orientation quaternion just after drilling but before unloading the stabilizers (transferring from CORING DRILL to RMECH frame): **cdQb** = (0.63817, 0.251639, -0.683091, 0.250607)
3. Rover orientation quaternion at time of acquisition of WATSON image SIF_0505_0711773216_015RAS_N0261222SRLC00730_0000LMJ01: (transferring from RMECH to SITE frame): **bQll2** = (0.582866, -0.0866888, 0.0898041, -0.802924)
4. WATSON orientation quaternion at time of acquisition of WATSON image SIF_0505_0711773216_015RAS_N0261222SRLC00730_0000LMJ01: (transferring from WATSON to RMECH frame): **wQb** = (0.631282, 0.225406, -0.69697, 0.254771)

Items 1 and 2 give a coring drill pointing vector estimate of

hade = 13.78°
azimuth = **3.53°**

Items 3 and 4 give an estimate of the angle between the WATSON y-axis and the Core y-axis projected into the WATSON image plane (**Figure 24**) of

core roll, α = **341.30°**

Figure 24 | Core orientation. 6.6-cm standoff WATSON image of *Hazeltop* core target on Sol 505**.** WATSON image SIF_0505_0711773216_015RAS_N0261222SRLC00730_0000LMJ01. Image scale is 31.0 µm pixel^{-1}. Orientation compass gives WATSON frame (wx, wy, wz). Core roll is $\boldsymbol{\alpha}$ = 341.30°. Projection of Martian geographic north onto WATSON image plane is noted. Projection of Martian geographic north onto WATSON image plane is noted (clockwise angle of 337.14° from **wy**).

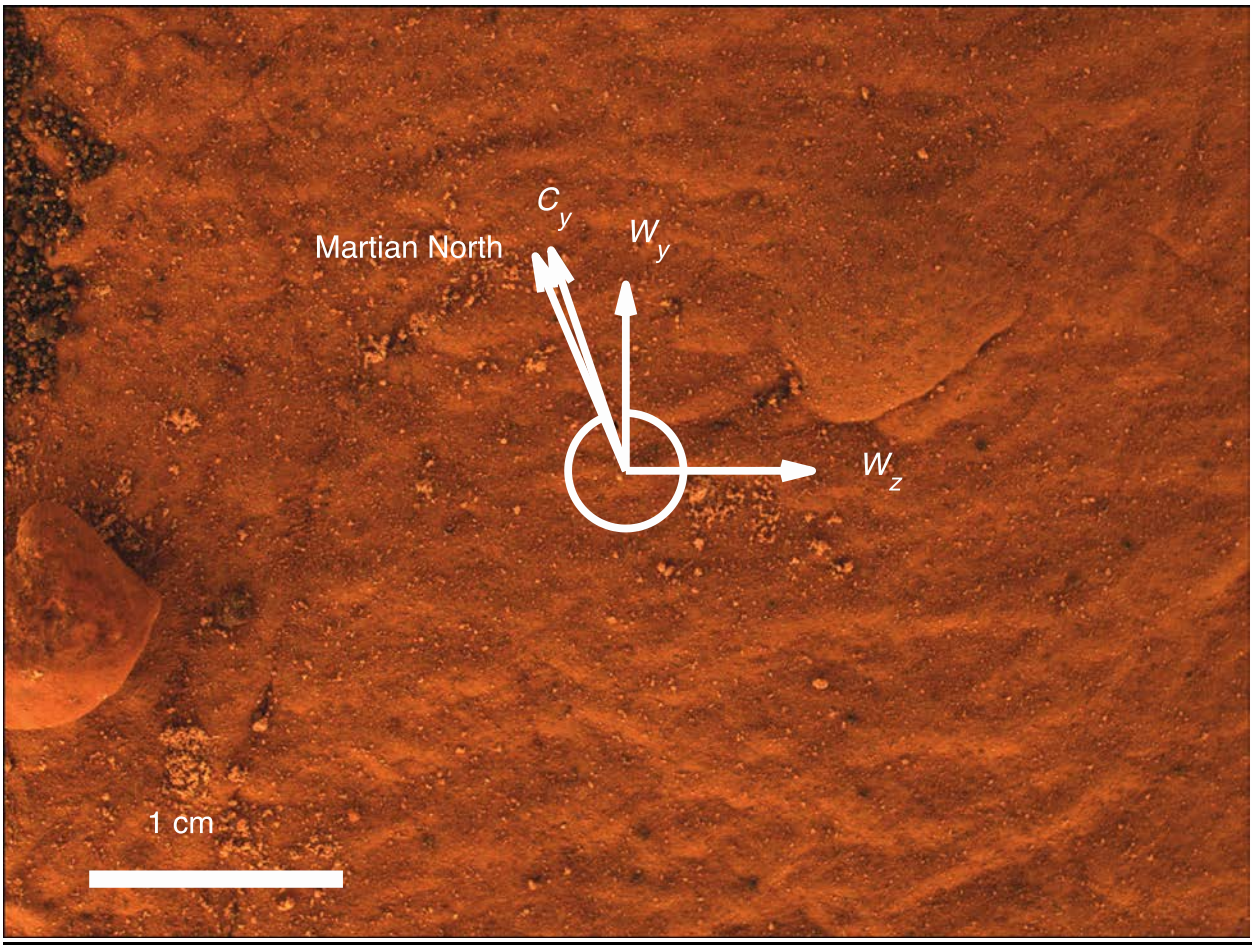

Preliminary Scientific Assessment

Synthetic sample description and preliminary interpretation

Sample type: **Fine-grained, well-sorted sedimentary rock; a sulfate-bearing coarse mudstone.**

1. **Relationship with surrounding rocks**
    a. *Hazeltop* and *Bearwallow* were obtained from a position relatively low in the accessible stratigraphy of Jezero Delta near the base of the *Hogwallow Flats* member, roughly 14 m vertically above the lowest exposed delta member *Devils Tanyard*, within the *Shenandoah* formation.
    b. Based on its appearance and concordance with surrounding outcrops in overall color and composition, the *Wildcat Ridge* outcrop is interpreted to be an in-place portion of *Hogwallow Flats*.
2. **Texture and fabric**
    a. Grain size: <0.03–0.18 mm
    b. Rock fabric (natural surface): the exposed surface is fractured, dusty, and light toned. Individual grains are not visible on the surfaces. The surface has diagenetic features including linear sets of raised nodules.
    c. Rock fabric (abrasion patch): grains are silt sized (50 μm), with a unimodal size distribution and are typically subrounded; the largest observed grains do not exceed 180 μm. The grain size distribution is well sorted.
    d. The rock appears to be a well sorted, coarse mudstone.
3. **Mineralogy and chemistry**
    a. Minerals present: the rock matrix is compositionally homogeneous and is cut by small veins. Minerals detected in the matrix include weakly hydrated Mg-Fe sulfates and Mg-Fe silicates (possibly smectite). The small veins are enriched in Ca sulfate (likely anhydrite). Minor minerals detected include possible carbonates, hydrated silica or Al-clay minerals.
    b. The rock appears to be minimally hydrated sulfate-bearing mudstone.
4. **Alteration/secondary characteristics**
    a. The presence of hydrated phases and the Ca-sulfate veins may indicate late-stage aqueous alteration after deposition.
    b. Secondary phases and/or cements indicative of aqueous alteration include small amounts of Fe-Mg-clay minerals, possible carbonates, hydrated silica or Al-clay minerals.

Returned Sample Science Considerations

Since before landing, the delta stratigraphy and the western Jezero delta front have been the primary astrobiologically relevant mission sampling targets, i.e., sediments deposited into an ancient lake on Mars. Jezero Lake was likely present during the valley network-forming late Noachian to early Hesperian period of early Mars, and therefore delta sedimentary rock samples provide a potential record of the environmental conditions during that period. On Earth, early deltaic bottomset deposits often contain relatively fine-grained, organic-rich material, and can preserve ancient biosignatures. Coarser-grained (> mm) deltaic sedimentary units contain detritus that reveal the catchment source lithology and can be used to constrain delta deposition timing. Collectively, a set of coarse-grained *and* fine-grained sedimentary rock samples collected from the delta front in proximity provides a sample suite for addressing key goals of MSR.

The *Hazeltop* and *Bearwallow* cores are samples of fine-grained (<100 μm) sedimentary rocks collected by the Perseverance Rover. These samples partially fulfill the objective of collecting 2 paired samples of fine-grained material with biosignature preservation potential prior to placement of the contingency cache. *Hogwallow Flats*/*Wildcat Ridge* was chosen for sampling because it possessed several desired sample characteristics for a fine-grained sedimentary rock sample including: (1) grains <100 μm; (2) both siliciclastic and salt-rich components; (3) cements (sulfate); (4) a low delta/stratigraphic position; (5) deposition associated with the delta; and (6) detrital grains appear minimally aqueously altered.

Wildcat Ridge is a fine-grained sedimentary rock that was deposited in a sub-aqueous environment within a lacustrine basin. Thus, the *Hazeltop* and *Bearwallow* cores record paleoenvironmental and paleoclimatic conditions of a formerly habitable environment. Laboratory-based investigations of these samples will enable characterization of the distribution and chemical diversity of organic molecules and the search for morphological and chemical biosignatures. These analyses will also enable reconstruction of chemical conditions in a subaqueous paleoenvironment, and interpretation of a sedimentary system in which aqueous processes occurred in Mars's past. The samples from *Wildcat Ridge* can be used to address multiple science questions and objectives of the mission sampling campaign:

Geochronology: The observed mineralogy and fine grain scales observed in *Wildcat Ridge* are not well-suited for existing methods of isotopic geochronology. This is one of the reasons it was important to collect such a fine-grained sedimentary rock in close association with a coarser sedimentary rock (e.g., *Skinner Ridge*), which can be used to constrain the deposition timing of *Wildcat Ridge*. However, it may be possible for existing methods of isotopic geochronology to be applied (or developed and/or refined) to constrain the timing of sulfate precipitation (either primary or diagenetic). In addition to quantifying the timing of late-stage aqueous activity, such information would place a *lower* bound on the timing of sediment/delta deposition. Observations of stable cosmogenic nuclides (e.g., ^{3}He, ^{21}Ne, ^{36}Ar, ^{38}Ar) in bulk *Hazeltop* and *Bearwallow* samples could quantify the material's integrated cosmic ray exposure duration, thereby helping to constrain the latest-stage erosional history of the delta and the most recent cosmic ray exposure of the rocks in this vicinity (including the *Swift Run* and *Skyland* cores, collected from an overlying sandstone unit; **Figure 4**).

Paleomagnetism: The sedimentary lithologies of the *Hazeltop*/*Bearwallow* cores may enable relative measurements of the paleointensity of the Martian dynamo. In combination with geochronology, this

could constrain the timing of the martian paleomagnetic field to test the hypothesis that martian atmospheric loss was driven by the cessation of an early dynamo. The orientations of the samples (**Figure 24)**, combined with paleohorizontal indicators from the outcrop and sample, may enable measurements of the absolute paleodirection of the ancient field during or after deposition. This could constrain the dynamo's geometry, determine if the dynamo exhibited secular variation and polarity reversals, and constrain tectonic processes. Paleomagnetic investigations would also constrain the aqueous and thermal alteration history of the samples and, by implication, the preservation state of any potential biosignatures. The small size of the grains may preclude the ability to conduct a conglomerate test to determine if the sample magnetization was acquired prior to or after deposition.

Texture: A key component of understanding fine-grained sedimentary rocks and the diagenetic processes that acted upon them, is the ability to distinguish between authigenic and allogenic minerals. The fine grain size of the *Hazeltop* and *Bearwallow* cores (**Figure 8, 9**) precludes making this distinction using Perseverance's in-situ instrumentation. Only returning samples for microscopic investigations would enable this level of understanding. This distinction is key to the search for potential biosignatures and distinction of primary/catchment processes from post-depositional processes experienced by these rocks.

Geochemistry: Elemental and mineralogical data from the *Berry Hollow* abrasion and the *Hazeltop* borehole indicate that the *Wildcat Ridge* outcrop is rich in Fe- and Mg-sulfate. LIBS analyses plot between pyroxene and feldspar compositions. VISIR data show a strong sulfate signal, consistent with sulfur detections by PIXL and the detections of sulfate by SHERLOC. Salt-subtracted elemental compositions and low element totals from PIXL are consistent with hydrated (phyllo)silicate mineral phases such as nontronites and saponites. VISIR data also suggest the presence of some phyllosilicates and/or carbonates.

Laboratory-based microscopic imaging and chemical mapping of the grains and grain boundaries at resolutions higher than Perseverance's in-situ instrumentation would enable distinction between authigenic, allogenic, and diagenetic solid phases. Chemical mapping at similarly high resolution can also determine whether organic compounds are preferentially distributed in and around particular solid phases (i.e., sulfate minerals or phyllosilicate grains). Subsequent high-resolution elemental and mineralogical analyses can also be used to link the component materials to either (1) geochemical conditions in the environment where *Wildcat Ridge* was deposited or (2) the post-depositional diagenetic processes that acted upon the sediments. Sulfur isotope variability between Ca-sulfate veins and the surrounding Mg and Fe sulfate can test for the presence of different generations of sulfate-bearing fluids. Sulfur isotope composition in precipitated sulfate minerals, particularly compared to those of any coexisting sulfide-bearing minerals may document global abiotic redox processes such as atmospheric mass independent sulfur isotope fractionation and local biological processes such as microbial sulfate reduction. The presence of sulfide-bearing minerals and other minerals indicating reducing conditions in *Wildcat Ridge* is yet to be established.

Habitability and Biosignature Preservation Potential: The *Hazeltop* and *Bearwallow* cores were deposited in a subaqueous paleoenvironment that, due to the presence of liquid water, is interpreted as formerly habitable. Sulfate minerals precipitate in modern hypersaline, and sometimes acidic, lacustrine environments and have a recognized biosignature preservation potential. SHERLOC fluorescence data from the *Berry Hollow* abrasion patch indicate a strong signal likely attributable to single and double ring

aromatic organic molecules. The most intense fluorescence signal is associated with a Ca-sulfate vein identified within the abrasion patch. Other potential organic detections may be associated with Mg-sulfates that are not located within apparent veins. Laboratory based, high resolution microscopic mapping of the mineral and organic distribution in the cores, along with analyses of organics extracted from these cores, will provide more detailed information on the organic signals and any associations with solid phases that precipitated from solution and/or pore waters or formed during early or late diagenesis. These phases include Mg and Fe sulfates, phyllosilicates, Ca sulfate and possibly others not yet identified. Analyses that characterize the compositional, structural, and isotopic diversity of organic compounds present in *Wildcat Ridge* can also help distinguish any organics produced by prebiotic or abiotic processes from organics delivered from space.

Due to the small mineral grain sizes, constraints on the environmental conditions during the deposition of *Wildcat Ridge* require textural analyses, identification of the coexisting primary mineral phases, and chemical modeling. These analyses will test whether the fluids were acidic or circum-neutral, oxidizing or reducing, and whether and how the original minerals were altered during diagenesis. These constraints will help establish whether this formerly habitable environment was extreme (e.g., acidic and hypersaline) or more amenable to microbial life. In either case, sediments deposited in the delta may have provided a habitat for active microorganisms and may have preserved microbial life that was present in the water column of Lake Jezero. Cells and/or other organic materials could have been trapped in precipitated cement phases during lithification and diagenesis. Microscopic analyses of thin sections of the cores from *Wildcat Ridge* could contain organic inclusions or even body fossils encapsulated within or preserved by mineral phases detected in the *Berry Hollow* abrasion patch (e.g., sulfate crystals or phyllosilicates). Sample return and detailed analyses are required to search for these types of biosignatures.

References

Lazar, O. R., Bohacs, K. M., Macquaker, J. H., Schieber, J., & Demko, T. M. (2015). Capturing Key Attributes of Fine-Grained Sedimentary Rocks In Outcrops, Cores, and Thin Sections: Nomenclature and Description Guidelines MUDSTONES: NOMENCLATURE AND DESCRIPTION GUIDELINES. *Journal of Sedimentary Research*, *85*(3), 230-246.

Stack, K.M. et al. (2020). Photogeologic Map of the Perseverance Rover Field Site in Jezero Crater Constructed by the Mars 2020 Science Team. *Space Science Reviews*, 216, 127, doi:10.1007/s11214-020-00739-x.

INITIAL REPORT

M2020-516-15 *Bearwallow*

Sample Designation: M2020-516-15 *Bearwallow*

Date of Coring: 2-August-2022

Mars Time of Sample Core Sealing: 20:27 LMST, Sol 516, Ls 278.13

Latitude (N), Longitude (E), Elevation: 18.45863832˚, 77.40588685˚, -2523.077677 m

Campaign: Delta Front

Region of Interest: *Hawksbill Gap*

Lithology: Fine-grained, well-sorted sedimentary rock likely deposited in a lacustrine setting; a sulfate-bearing coarse mudstone. The rock is rich in weakly-hydrated Mg-Fe sulfate. Also detected were small amounts of Fe-Mg-clay minerals, hydrated silica or Al-clay minerals, and possibly carbonates. Numerous fluorescence detections may arise from aromatic organic compounds. The rock is cut by scattered veins and patches enriched in Ca sulfate, likely anhydrite, whereas the sulfate in the rock matrix is more magnesian.

Estimated Volume Recovered: 8.8 cm^3

Coring Bit Number: 2

Core Orientation: hade = 15.28°; azimuth = 358.37°; core roll = 333.17°

Sample Serial Numbers: Tube SN259; Seal SN177; Ferrule SN110

ACA Temperature at Time of Sealing: 40°C

Estimated Rover-Ambient Pressure and Temperature at Time of Sealing: 797 Pa, 214 K

Estimated Amount of Martian Atmosphere Headspace Gas: 1.43×10^{-6} mol

Anomalous Behavior: None

Abrasion Patch Name and Depth: *Berry Hollow*, 8 mm

September 21, 2022

D. L. Shuster, K. A. Farley, T. Bosak, B. A. Cohen, A. D. Czaja, E. M. Hausrath, L. E. Mayhew, S. Siljeström, J. I. Simon, K. M. Stack, A. Treiman, B. P. Weiss, B. V. Wogsland, M.-P. Zorzano, H.E.F. Amundsen, F. J. Calef III, D. Flannery, J. Hurowitz, T. Kizovski, A. Knight, L. Mandon, E. N. Mansbach, D.A.K. Pedersen, M.M. Tice, A. Udry, S. Van Bommel, K. Williford, and the Mars 2020 Team

Summary Description

This sample is paired with M2020-509-14 *Hazeltop*. Only the core orientation for *Bearwallow* is described below. See the Initial Report for M2020-509-14 *Hazeltop* for sample details.

Core orientation

At the time of drilling and 7.2-cm pre-drilling WATSON imaging, the rover, coring drill, and WATSON had the following characteristics:

1. Rover orientation quaternion just after drilling but before unloading the stabilizers (transferring from RMECH to SITE frame): **bQll1** = (0.583193, -0.0844151, 0.0915364, -0.802733)
2. Coring Drill orientation quaternion just after drilling but before unloading the stabilizers (transferring from CORING DRILL to RMECH frame): **cdQb** = (0.643634, 0.250863, -0.671522, 0.26807)
3. Rover orientation quaternion at time of acquisition of WATSON image SIF_0511_0712314955_726FDR_N0261222SRLC00773_0000LMJ01: (transferring from RMECH to SITE frame): **bQll2** = (0.582882, -0.0866339, 0.0897449, -0.802925)
4. WATSON orientation quaternion at time of acquisition of WATSON image SIF_0511_0712314955_726FDR_N0261222SRLC00773_0000LMJ01/: (transferring from WATSON to RMECH frame): **wQb** = (0.647031, 0.254311, -0.668715, 0.263623)

Items 1 and 2 give a coring drill pointing vector estimate of

hade = 15.29°
azimuth = **358.37°**

Items 3 and 4 give an estimate of the angle between the WATSON y-axis and the Core y-axis projected into the WATSON image plane (**Figure 1**) of

core roll, α = **333.17°**

Note that the rock surface was marked using SuperCam prior to drilling (inset to **Figure 1**).

Figure 1 | Core orientation. 7.2-cm standoff WATSON image of *Bearwallow* core target on sol 511. WATSON image SIF_0511_0712314955_726FDR_N0261222SRLC00773_0000LMJ01. Image scale is 33.1 µm pixel^{-1}. Orientation compass gives WATSON frame (**wx**, **wy**, **wz**). Core roll is **α** = **333.17°**. Projection of Martian geographic north onto WATSON image plane is noted. Projection of Martian geographic north onto WATSON image plane is noted (clockwise angle of 334.92° from **wy**). Inset shows three pits created by SCAM laser marking in the white circles. The three pits make an "L" shape with the long side spanning ~2.5 mm and the short side ~1 mm.

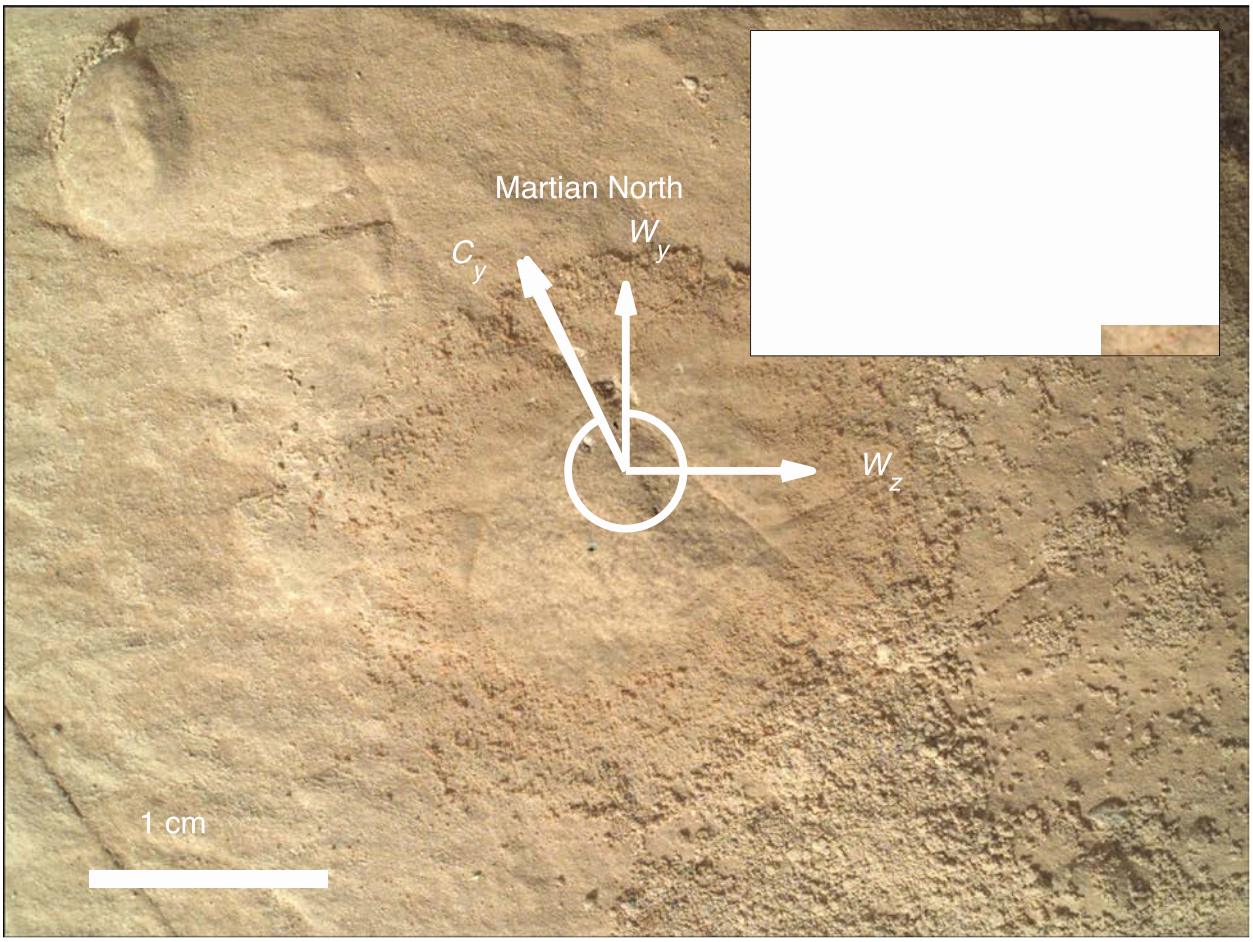

INITIAL REPORT

M2020-575-16 *Shuyak*

Sample Designation: M2020-575-16 *Shuyak*

Date of Coring: 2-Oct-2022

Mars Time of Sample Core Sealing: 19:40 LMST, Sol 575, Ls 314.59

Latitude (N), Longitude (E), Elevation: 18.45068954˚, 77.40143171˚, -2526.322706 m

Campaign: Delta Front

Region of Interest: *Cape Nukshak*

Lithology: Fine-grained, well-sorted sedimentary rock likely deposited in a lacustrine setting; an olivine-bearing coarse mudstone. The rock primarily contains detrital olivine and aqueous alteration products of olivine (e.g., serpentine) plus minor salts. Minor phases detected may include chromite, ilmenite, apatite, and zircon/baddeleyite. No clear evidence of sand-sized pyroxene or feldspar was observed. The rock contains little, if any, evidence of sulfate minerals and a possible/weak fluorescence signal potentially related to organics.

Estimated Volume Recovered: 7.8 cm^3

Coring Bit Number: 4

Core Orientation: hade = 16.72°; azimuth = 219.48°; core roll = 259.41°

Sample Serial Numbers: Tube SN264; Seal SN068; Ferrule SN085

ACA Temperature at Time of Sealing: 40^{o}C

Estimated Rover-Ambient Pressure and Temperature at Time of Sealing: 750 Pa, 218 K

Estimated Amount of Martian Atmosphere Headspace Gas: $1.73x10^{-6}$ mol

Anomalous Behavior: None

Abrasion Patch Name and Depth: *Novarupta*, 8 mm

January 15, 2023

D. L. Shuster, K. A. Farley, T. Bosak, A. D. Czaja, E. M. Hausrath, L. E. Mayhew, M. E. Minitti, S. Siljeström, J. I. Simon, K. M. Stack, A. Treiman, B. P. Weiss, B. V. Wogsland, M.-P. Zorzano, A.C. Allwood, H.E.F. Amundsen, F. J. Calef III, B.C. Clark III, D. Flannery, J.A. Hurowitz, T. Kizovski, A. Knight, L. Mandon, E. N. Mansbach, D.A.K. Pedersen, M.E. Schmidt, M.M. Tice, A. Udry, S. Van Bommel, K. Williford, and the Mars 2020 Team

Summary Description

Shuyak and Mageik, the pair of cores representing the seventh sample target of the Mars 2020 mission, were collected from *Amalik*, an outcrop of the *Enchanted Lake* member of the *Cape Nukshak* region of the western Jezero delta front. *Amalik* lies near the base of the exposed delta sedimentary rocks in the *Cape Nukshak* region, ~4 vertical meters below the rim of *Cape Nukshak* (i.e., the *Alagnak* outcrop) (**Figures 1 - 5**) and is likely to be in place. The outcrop is a horizontally layered, fine-grained, and well-sorted sedimentary rock; it is an olivine-bearing coarse mudstone (**Figures 3, 5**). We sampled this sedimentary rock because it is from a low stratigraphic position within the western Jezero delta and contains a fine-grained texture, likely deposited on to the floor of a lake. The rock primarily contains detrital olivine with evidence for hydration and aqueous alteration products (e.g., serpentine), phyllosilicates, dolomite and some silica. Thus, this rock has potential for biosignature preservation.

The *Novarupta* abrasion patch, acquired at *Amalik*, is homogeneous in its color, composition, and grain size, with observable grains ranging from <0.03 to ~1 mm, and a fine-grained cement and/or secondary chemical weathering phases. Chemical compositions are spatially uniform and consistent with olivine and aqueous alteration products of olivine plus minor salts. *Novarupta* consists of fine-grained olivine with additional signals consistent with pyroxene, feldspar, clay minerals, sulfate, carbonates, and heavy minerals. Weak fluorescence is observed, but not clearly associated with specific minerals; it may originate from organic compounds, likely in low abundance. Both the natural surface and abraded surface contain dispersed fluorescence, and the abraded surface also contains localized more intense fluorescence. The natural surface of *Novarupta* appears to have a shiny, purplish coating or dust crust.

The *Shuyak* core was collected on Sol 575, has a core length of 55.5 mm, and based on Cachecam and ZCAM images, appears to be a coherent piece of rock with one small associated fragment. The *Mageik* core was collected on Sol 579, has a core length of 73.6 mm, and based on Cachecam and ZCAM images, also appears to be a coherent piece of rock. Due to faults during tube sealing, the *Mageik* core was not sealed until Sol 619 (40 sols after coring). Between coring and sealing *Mageik* was stored within the adaptive caching assembly, behind a fluid mechanical particle barrier, except during multiple failed attempts at sealing.

The *Shuyak* and *Mageik* cores originate from a subaqueous paleoenvironment that, due to the presence of liquid water, is interpreted as formerly habitable. The returned sample science objectives of the *Shuyak* and *Mageik* cores include combined microscopic textural, geochemical, and isotopic analyses of samples with high potential for biosignature preservation, paleomagnetism, the history of water and water–rock interactions during sedimentary deposition and in the delta sediments after deposition, and possibly geochronology. High spatial resolution elemental and mineralogical analyses can be used to link the component materials to (1) geochemical conditions of the sediment source/catchment lithology, (2) geochemical conditions in the environment when *Amalik/Enchanted Lake* was deposited and/or (3) the post-depositional diagenetic processes that acted upon the sediments.

Stratigraphic and Geologic Context

The *Amalik* member of the *Shenandoah* formation, which contains the *Amalik* outcrop, is stratigraphically above the contact with *Séítah* and below the low relief, slope-forming *Knife Creek* member and the cliff-forming *Alagnak* member in the *Cape Nukshak* region of the western Jezero delta front (**Figures 1 - 4**). *Amalik* is stratigraphically ~1 meter above the light-toned, laminated *Kaguyak* sandstone (**Figure 3**), which defines the base of the *Shenandoah* formation in the *Cape Nukshak* region (**Figure 4**). Based on orbital mapping, *Kaguyak* lies at the contact between the Crater floor fractured rough (*Cf-f-2*) and the Delta thinly layered (*D-tnl*) photogeologic units mapped in orbiter images (Stack et al., 2020). *Amalik* is ~63 vertical meters below the top of nearby *Whale Mountain,* ~0.37 km to the northwest, and ~133 vertical meters below the highest exposed delta surfaces ~3.2 km to the northwest.

Knife Creek and underlying *Amalik* and *Kaguyak* members may be restricted to the *Cape Nukshak* section. The cliff-forming *Alagnak* member and light and dark layered units seen at *Yori Pass* are similar and may correlate to the *Rockytop* and *Hogwallow Flats* units, respectively, found at *Hawksbill Gap*. Below *Amalik* and *Kaguyak* is a broadly recessive zone that likely includes the contact between the delta and crater floor (**Figure 4**). This stratigraphy appears to be representative of the base of the delta but could include some pre-delta units. Unlike the stratigraphy at *Hawksbill Gap,* the lower delta front at *Cape Nukshak* is not significantly covered by regolith, and therefore likely includes the earliest units deposited on the crater floor basement rocks. Thus, *Amalik* is from a relatively low stratigraphic position within the exposed delta.

The *Enchanted Lake* member is a low relief slope-forming unit consisting of relatively light-toned strata cropping out above and below thin, platy bedrock that appears darker-toned in orbiter images. Within the member, the *Amalik* outcrop appears grey on its natural surfaces, and the *Kaguyak* outcrop just beneath it appears more tannish in color. The *Enchanted Lake* interval can be traced laterally in orbiter images at least ~0.5 km along the delta front to the northwest. The units above *Enchanted Lake* form subtle benches, e.g., the *Alagnak* member (**Figure 2**), while others weather recessively (e.g., *Knife Creek* and *Yori Pass* members). Overall, these different horizontal layers indicate that the explored stratigraphy of the delta front is comprised of several distinct units and facies, that are largely, if not entirely, sedimentary in origin. This stratigraphy appears to be representative of the base of the exposed delta.

Operations

Sampling objectives of the *Delta Front Campaign* included the collection of both fine-grained (<0.06 mm) sedimentary rocks, ideally rich in clay minerals, and coarse-grained sedimentary rocks containing lithologically diverse clasts. The *Shuyak and Mageik* cores were collected to fulfill the fine-grained sedimentary rock sampling objectives of the campaign.

The Delta Front Campaign planning process occurred during February and March of 2022 and identified four paired samples to be collected from relatively low stratigraphic positions within the western Jezero delta, and prior to depositing the initial cache: (1 & 2) two different samples of lacustrine sediments with potential for biosignature preservation (ideally fine-grained mudstone and/or fine

sandstone containing clay minerals and reduced phases indicative of anoxic preservation conditions), (3) one relatively coarse-grained sediment sample (ideally containing medium sand size particles, >250 μm, with a lithologic diversity of detrital material) for delta deposition geochronology and Jezero catchment provenance studies, and (4) one regolith sample.

On Sol 424, Perseverance encountered the first delta rock outcrops of the mission at a site called *Enchanted Lake* at the base of *Cape Nukshak* (**Figure 1**). *Enchanted Lake* contained the *Kaguyak* sandstone and overlying *Amalik* fine-grained, gray rocks. SCAM RMI observations at *Cape Gull* (on *Kaguyak*) and *Hook Glacier* (on *Amalik*) revealed sedimentary facies consistent with distal subaqueous deposition. The team then decided to explore a laterally equivalent section of the lower delta exposure in the *Hawksbill Gap* region with the intention to execute proximity science and sampling activities (**Figure 1**). From Sols 426-441, Perseverance drove ~700 m from *Cape Nukshak* to *Hawksbill Gap*, arriving at the lowest exposed delta deposits of *Devils Tanyard* on Sol 441. Between Sols 441 and 474, Perseverance drove up-section through the following delta members while collecting remote sensing data and seeking outcrops suitable for potential proximity science and sampling: *Devils Tanyard*, *Hughes River Gap, Boston Knob*, *Hogwallow Flats*, and *Rockytop* (**Figure 1**).

From Sols 463 to 516, Perseverance collected sedimentary rock cores from *Skinner Ridge* (the relatively coarse-grained *Swift Run* and *Skyland* cores), processed a Witness Tube (M2020-499-13 WB2), and collected sedimentary rock cores from *Wildcat Ridge* (the relatively fine-grained and sulfate-rich *Hazeltop* and *Bearwallow* cores). On Sol 535, Perseverance began a multi-sol drive back to the *Amalik* outcrop (**Figure 1**) with the specific objective of sampling this stratigraphically lower and more grey fine-grained sedimentary rock.

On Sol 557, Perseverance arrived at the *Amalik* outcrop. After target assessment, an abrasion was attempted on Sol 562, but faulted. Thus, we repositioned Perseverance to a new workspace on the *Amalik* outcrop. On Sol 566, we selected three potential targets for abrasion and sampling (*Novarupta, Shuyak, and Mageik*) and acquired WATSON images of each. *Novarupta* was selected as the abrasion target; natural surface proximity science was conducted on Sol 567, and the abrasion was successfully conducted on Sol 568. Initial images of the abrasion patch revealed fine particle sizes (<100 μm) displaying a narrow range of both size and color. PIXL and SHERLOC data were acquired on *Novarupta* between Sols 570-578. Remote-sensing and abraded proximity science observations revealed that *Amalik* possessed multiple desired characteristics for a fine-grained sedimentary rock sample with potential for biosignature preservation, including: (1) clay- or silt-sized particles, <63 μm (2) the presence of cements or authigenic minerals; (3) the presence of clay minerals; (4) sediment associated with delta deposition; and (5) a relatively low stratigraphic position in the delta (see above). Thus, the team decided to move forward with sampling and completing the STOP list activities. We acquired and sealed the *Shuyak* core on Sol 575 and acquired the *Mageik* core on Sol 579. Due to a series of failed attempts to dispense the paired seal for the *Mageik* tube, this core was not sealed until Sol 619 using a different seal. The *Shuyak* and *Mageik* cores are the third sedimentary rock samples collected by the Perseverance Rover. Interpreted to be an olivine-rich, coarse mudstone that has experienced aqueous alteration(s), these samples fulfill the desired characteristics for a delta front fine-grained sedimentary rock sample with biosignature preservation potential.

Figure 1 | Regional context of Perseverance rover operations. (a) Geologic map with topography showing Jezero crater floor and western delta units, as defined by Stack et al. 2020. (b) Inset map showing the Delta Front Campaign regions of interest, *Cape Nukshak* and *Hawksbill Gap*, the *Shuyak* and paired core *Mageik* location (red point), and rover drive route (white lines). Elevation contours are meters relative to the Mars aeroid.

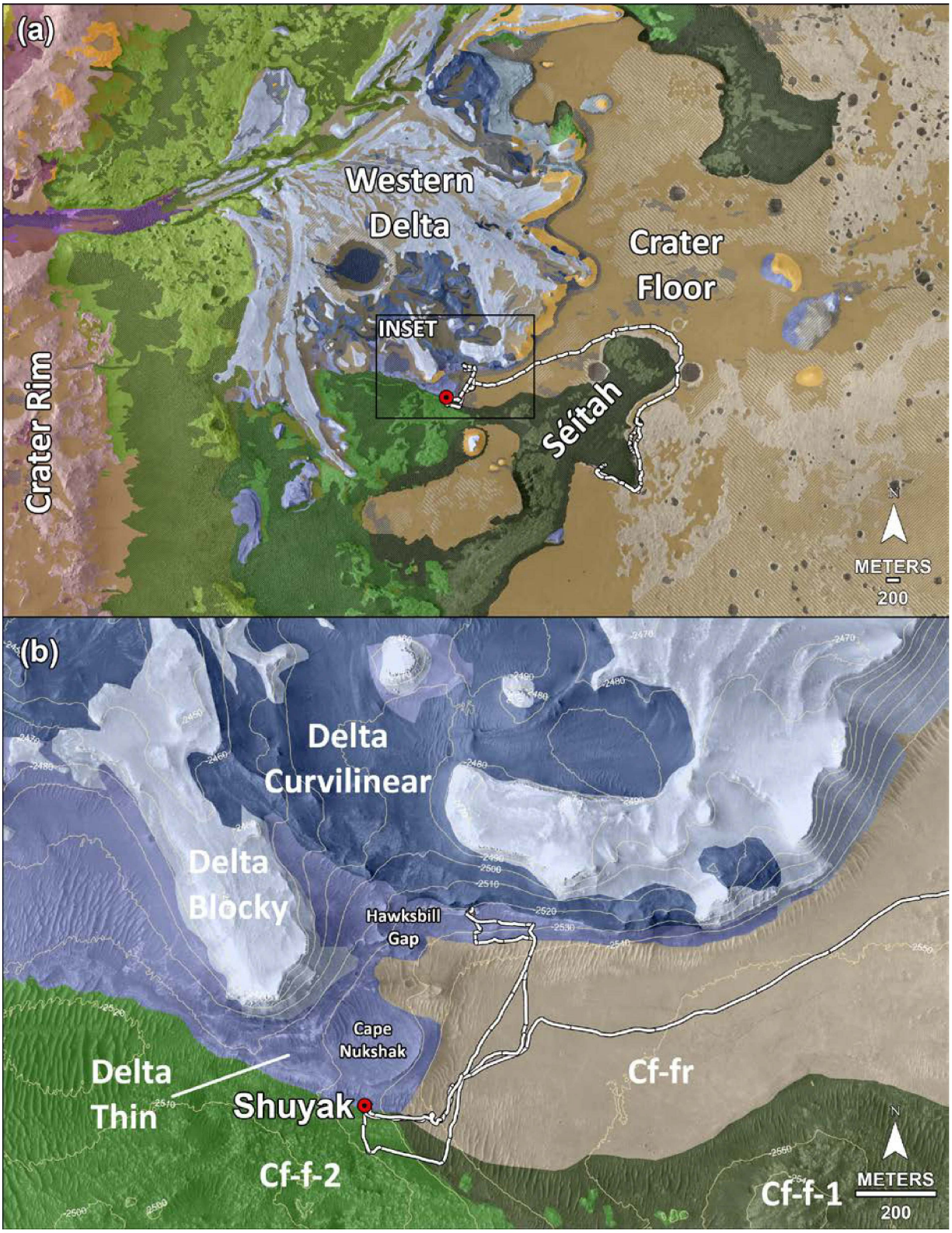

Figure 2 | Local context of Perseverance rover operations during *Shuyak* and *Mageik* sampling. HIRISE map showing the locations of sample collection together with other notable outcrops investigated during the sol path leading to *Amalik*, a rock outcrop of the *Enchanted Lake* member. Location of *the Shuyak and Mageik* cores is indicated with a red circle.

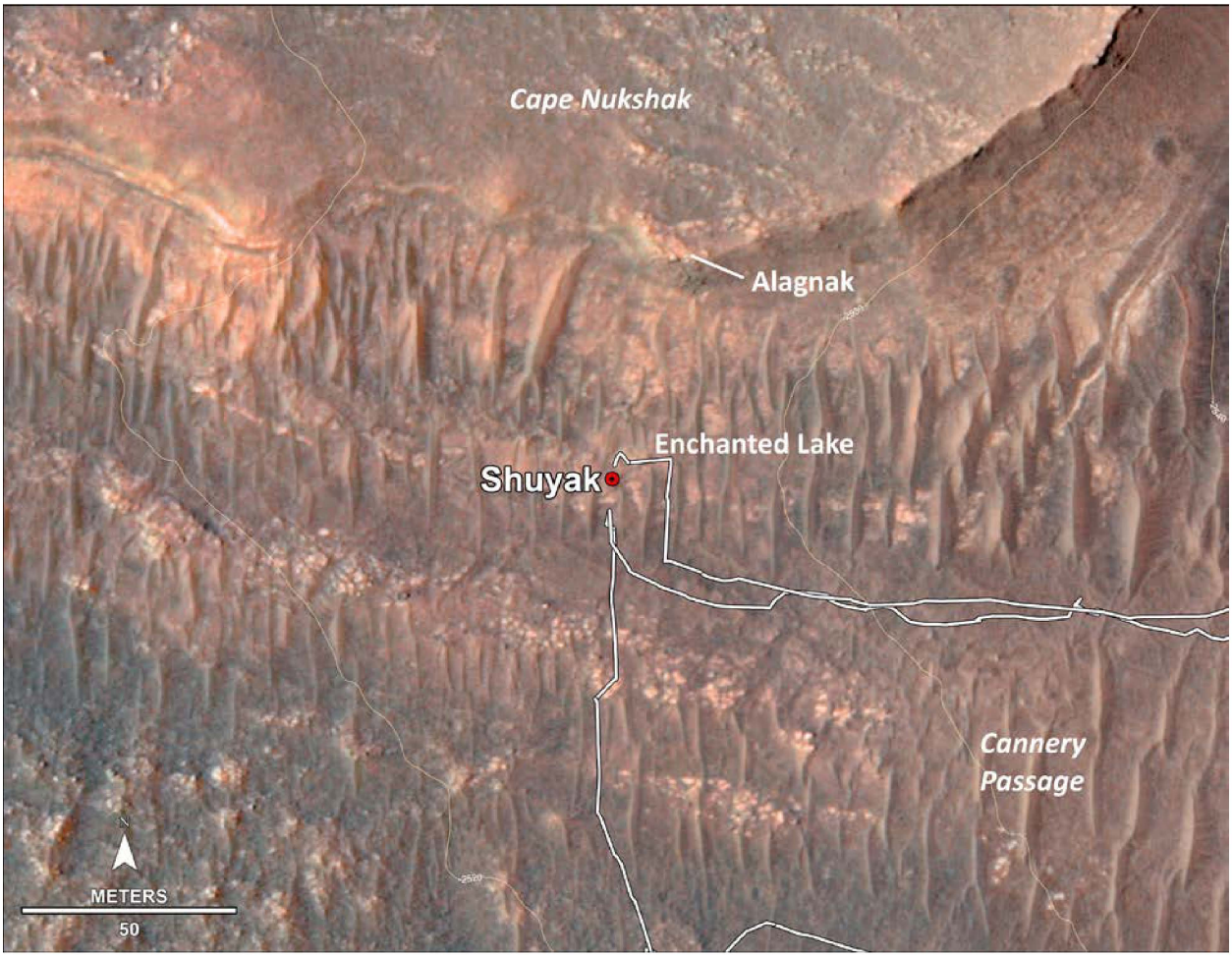

Figure 3 | View of *Enchanted Lake* at the base of the *Alagnak* ridge within the lower *Cape Nukshak* delta front stratigraphy. (a) The *Amalik* outcrop is located near the top of the *Amalik* member, which underlies *Knife Creek and Alagnak,* and overlies the *Kaguyak* member. The *Franklin Cliffs* in the distance (upper right) are comprised of stratigraphically higher delta units. Lower stratigraphic units and crater floor lie below the bottom of the image. The *Amalik* outcrop is ~5 m across; the vertical distance from *Amalik* to the upper surface of *Cape Nukshak* (the top of the *Alagnak* cliff) seen in this image is ~4 m. View is to the N; Sol 425, zcam08450, Z110 enhanced color. *Observation Mountain* is the location of the regolith samples (*Atmo Mountain* and *Crosswind Lake*). A zone of poorly outcropping recessive material at the base of this stratigraphy likely includes the contact with the crater floor that lies outside of view.

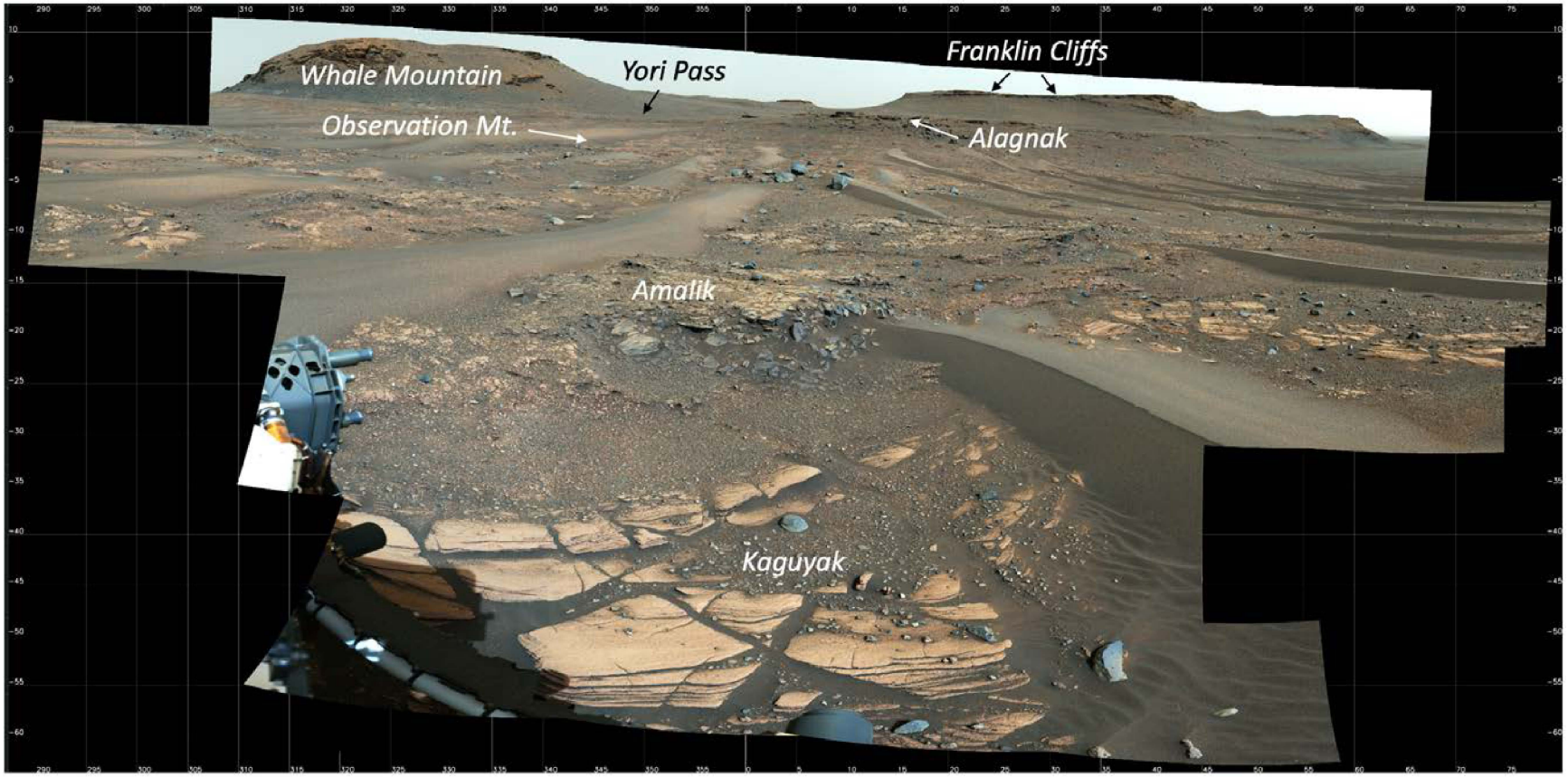

Figure 4 | Stratigraphic column of the *Shenandoah* formation explored at *Hawksbill Gap* between Sols 439-538 and *Cape Nukshak* primarily between Sols 556-643. c/si/vf = clay/siltstone/very fine sandstone; f = fine sandstone; m = medium sandstone; C = coarse sandstone; vC = very coarse sandstone; gr = granule; pb = pebble.

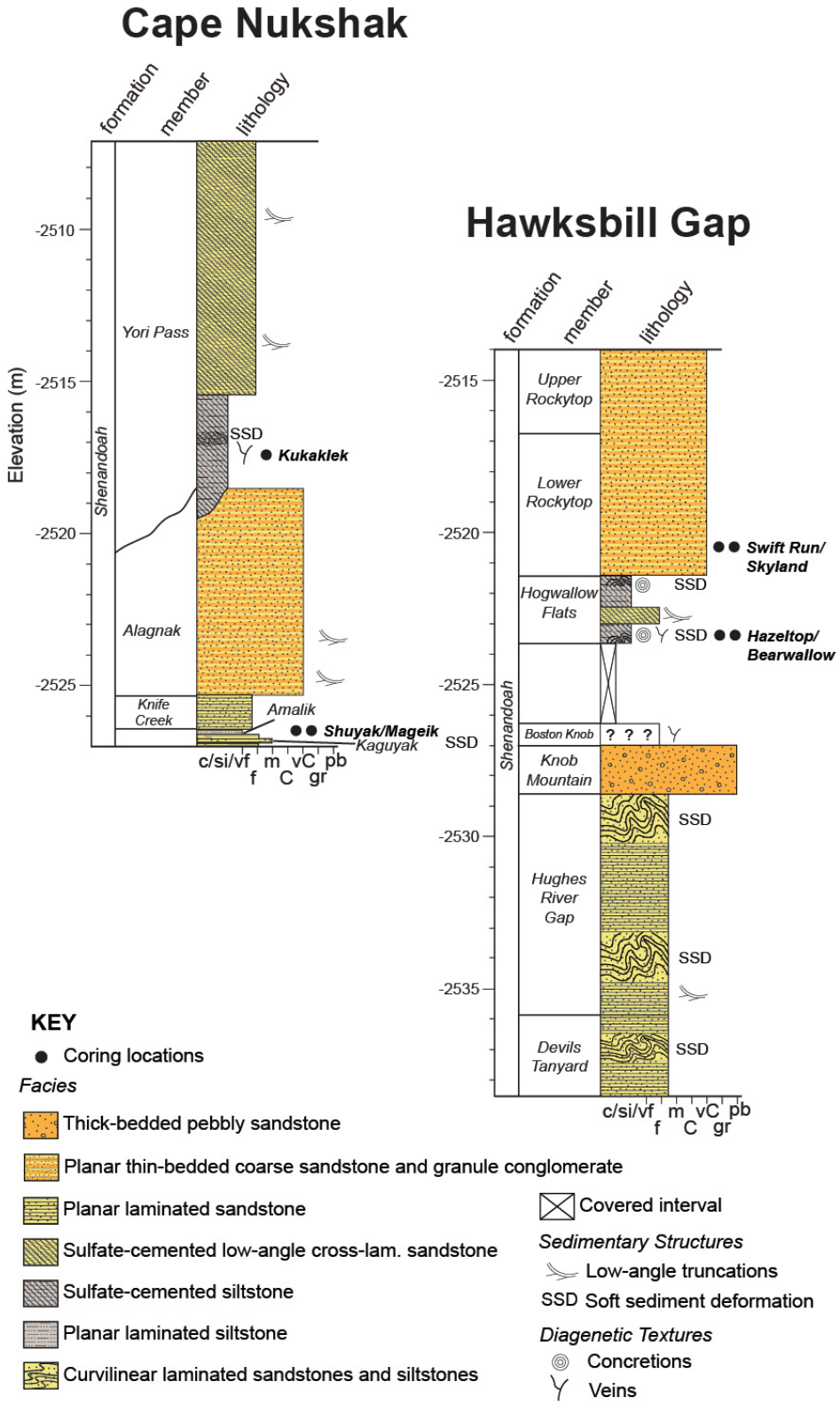

Sample-Related Observations

Workspace Images

Figure 5a shows a Mastcam-Z panorama of the *Amalik* workspace before precision approach. View is downslope, down-section, and to the south. Abrasion targets *Chiniak* and *Novarupta* are pointed out with red arrows; abrasion activities occurred after this image was taken. The *Chiniak* target was severely fractured during abrasion, so a precision approach was made to the *Raspberry Island* workspace (**Figure 5b**). The *Novarupta* abrasion patch and the sample boreholes *Shuyak* and *Mageik* are visible in **Figure 5c**. The surfaces of *Amalik* are sub-parallel with bedding and have a flagstone-like fracture pattern. Large fractures are filled with regolith and the bedrock surfaces are variably dust covered. The outcrop appears to be an interbedding of thinly bedded conglomerates (e.g., *Kelez*) and fine sandstones/siltstones (*Chiniak* and *Novarupta*).

Amalik shows evidence for bedding planes on the exposed downslope section of the flagstonesThe generally coherent structure of this outcrop provides confidence that the rocks in the workspace are in place. This is further supported by the fact that there were only small changes to the workspace after abrading (*Novarupta*) and coring (*Mageik*). However, *Shuyak* sampling broke apart the target block, fracturing it along previously identified and new fractures, center of **Figure 5c**.

SuperCam remote micro-imaging (RMI) of rocks at *Amalik* shows an outcrop consisting of dusty plates that are flat at scales larger than ~5 mm. The surfaces of plates exhibit millimeter-thick layers and millimeter-scale irregularities that indicate the presence of grains (**Figure 6**). In areas where surface dust is absent, the surfaces have a glossy, dark brown or purplish appearance likely due to a surface coating. RMI images of natural surface *Raspberry Island* (**Figure 6**) show wind-polished undulatory surfaces. Shiny coatings are visible on the surfaces of natural targets *Hook Island* (Sol 472), *Chiniak* (Sol 558), *Walatka* and *Becharof* (Sol 561), *Swikshak* (Sol 563) and *Novarupta* before abrasion (Sol 567). The RMI of the abraded patch *Novarupta* from Sol 572 shows darker and lighter brown grains, indicating that some grains are larger than ~0.2 mm (**Figure 6**). The same RMI image (**Figure 6**) shows the ~ 1 mm thick shiny surface coating surrounding the abraded patch.

Fractures are apparent on the surface as sublinear depressions; these fractures were activated during coring. The *Raspberry Island* RMI textures are consistent with the pre-abrasion RMI on *Novarupta,* not shown. *Kelez*, **Figure 6b**, is stratigraphically above *Novarupta* and the core samples, but below *Chiniak*. The surface of *Kelez* is less wind-polished and dustier than *Raspberry Island* and *Novarupta.* Potential grains are visible in the RMI ranging from coarse sand to fine sand (0.75-0.18 mm). Therefore, *Kelez* is coarser than *Novarupta*, which is interpreted as a very fine sand to siltstone. Dust and sand-sized grains are visible as surface debris in both RMIs.

Figure 5 | Mastcam-Z context images for the *Amalik outcrop*. **(a)** The *Amalik* workspace; *Novarupta* and *Chiniak* targets are indicated. Sol 557, zcam08578, Z110 enhanced color. **(b)** The unmodified workspace ZCAM mosaic. Sol 565, zcam07101, Z110 enhanced color. **(c)** The workspace after abrasion and sampling activities, showing the fracturing that occurred after *Shuyak* was cored (center) and the regolith that settled during abrasion of the *Novarupta* abrasion (right) and sampling of *Mageik* (left). Sol 582, zcam08595, Z63 enhanced color.

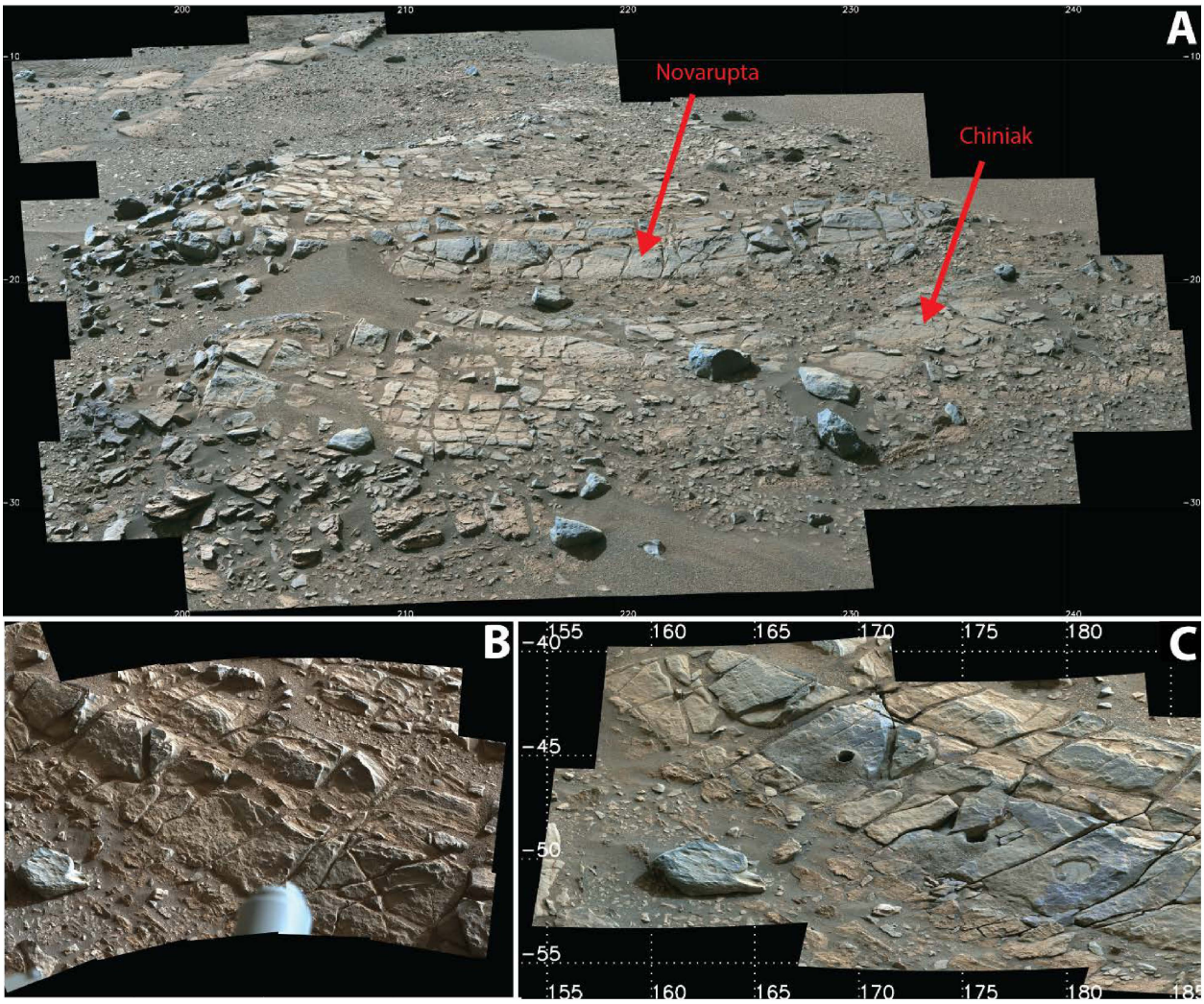

Figure 6 | SuperCam RMI images of rocks in the *Amalik* workspace. Gaussian stretch RMIs of natural surface targets within the *Amalik* workspace. **(a)** *Raspberry Island* showing a polished undulatory surface and fractures. **(b)** *Kelez* showing coarser grains and thin bedding planes; *Kelez* is above *Raspberry Island*. **(c)** *Chiniak* showing a thin overhang above the surface depression in the right part of the image and linear features that meet at 90-120 degree angles in the lower part of the image indicate the presence of cemented layers. Two shiny dark centimeter-wide spots in the center reveal a surface coating in the areas from which dust is absent. **(d)** Abraded patch *Novarupta* imaged on Sol 572. The reddish and grey-brown areas indicate the presence of compositionally different grains, although tool marks obscure individual grains in the patch. Red circles show spots analyzed by infrared spectroscopy. A shiny reddish-brown coating is visible around the abraded patch. A grainy unabraded area with the coloration like that of the abraded patch underlies the coating and overlies the abraded patch.

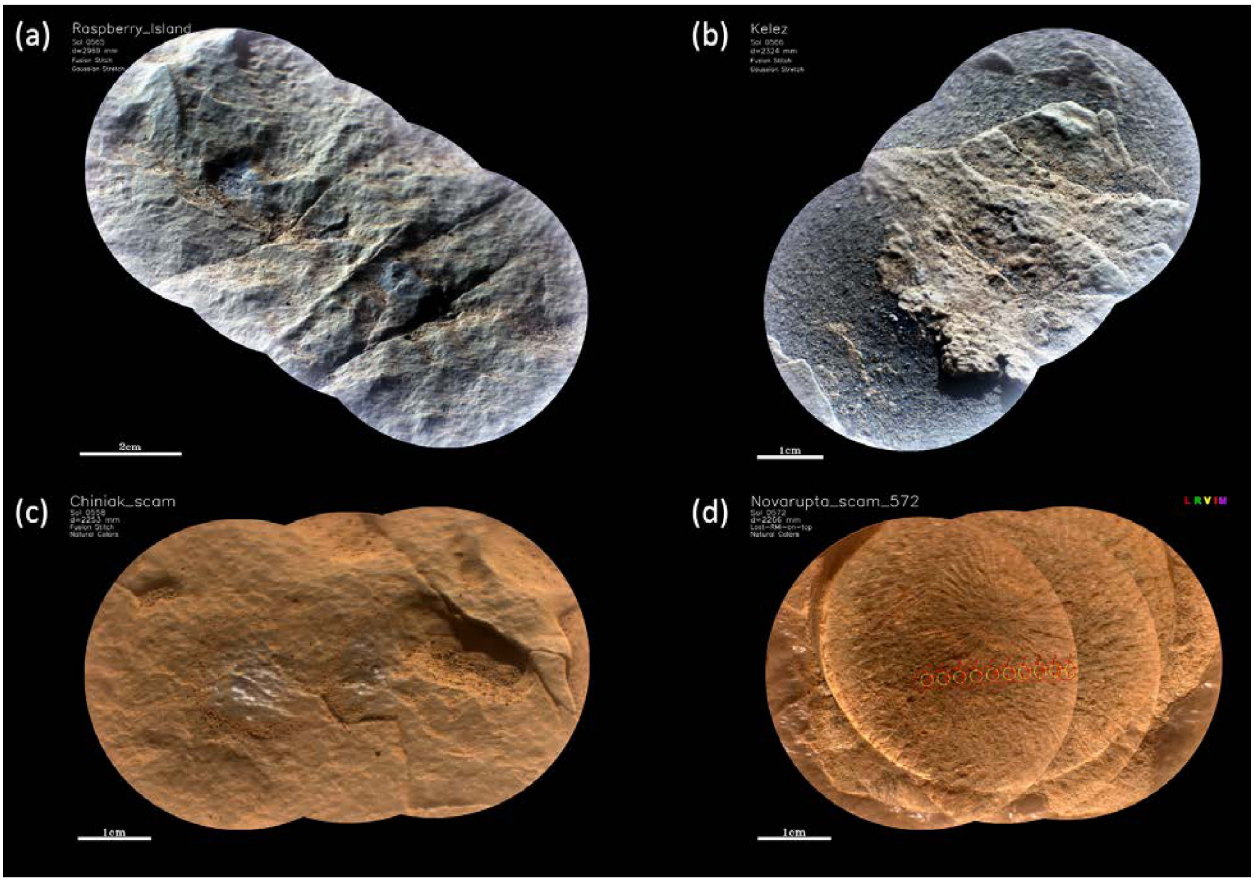

Pre and Post Coring/Abrasion Images

The target selected for abrasion within the *Amalik* workspace, *Novarupta*, is a gray, layered bedrock slab (**Figure 7**). Aeolian abrasion has exposed layers along the vertical edge of the bedrock slab and has stripped back layers across the top surface creating broad shelves each multiple millimeters thick. In some areas, the top surface exhibits shallow, irregularly shaped pits, many of which have collected sand and dust. The bedrock slab is cut by fractures that are at a high angle to layering, some of which are significant enough to break the larger workspace into discreet blocks or plates.

The pre-abrasion surface is texturally homogeneous with gray and red mottling visible through less-dusty patches. Black to darker gray, high-contrast features are occasionally visible, with long axes

ranging between 100-200 μm; these are interpreted as grains. On some pre-abrasion surfaces cleared of surface dust by the LIBS laser, the gray and red mottling persists and correlates with smooth shiny surfaces.

The *Novarupta* abrasion patch, which is 8 mm deep, exhibits prominent radial tool marks from the rotating and percussing action of the abrasion bit (**Figures 7b, c**). The tool marks form ridges and mesas with smooth surfaces in which the texture of the underlying rock is obscured. Outside the abrasion patch, the gray and red mottling of the natural surface is revealed to be related to a coating, clearly spalled off in several areas surrounding the abrasion patch. Where sufficient vertical section exists to measure the coating thickness, it ranges between ~90 and650 μm (**Figure 7c**).

Figure 7 | Sol-511 WATSON images of *Novarupta*, pre- and post-abrasion. In all panels, sunlight illumination is from the upper left. Yellow boxes delineate the field of view of the adjacent panel. **(a)** Pre-abrasion image, 40 cm standoff. Image provides a plan view perspective of layers within the target. **(b)** Post-abrasion image, 25 cm standoff. **(c)** Post-abrasion focus merge, 10 cm standoff.

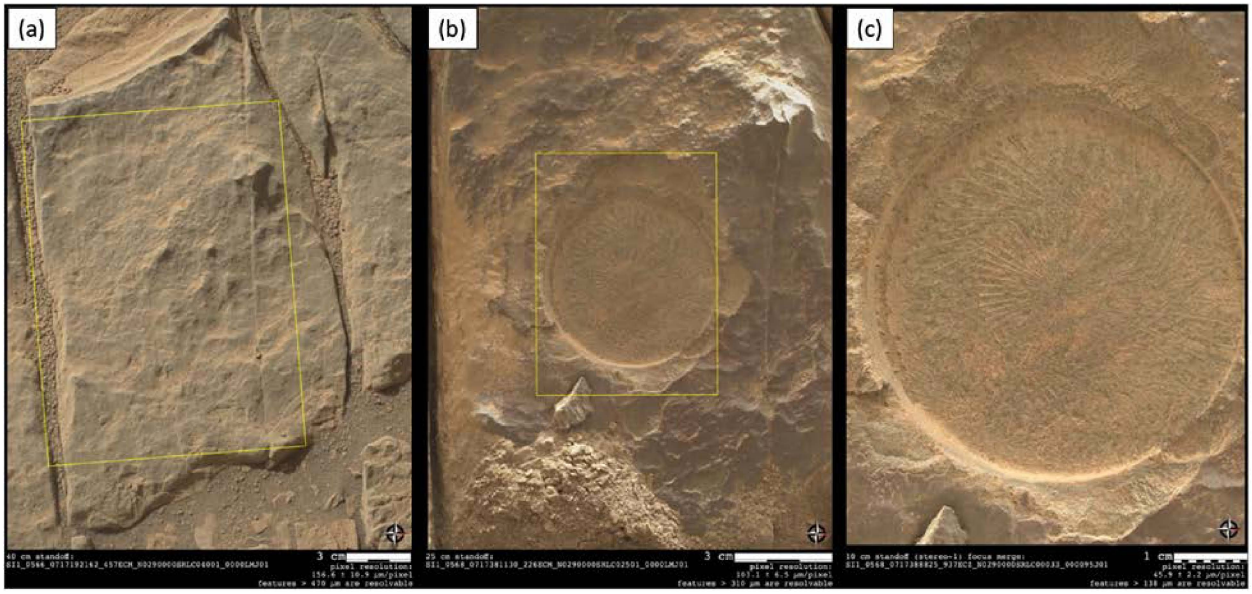

Under sunlight illumination, the overall color of the abraded patch is gray, with patchy zones of orange (**Figure 8**). Away from the tool marks, the rock has a uniform, granular texture with resolvable silt to very fine sand grains that are black, gray, white, or red. The grains are too small to evaluate shape or rounding in detail, but are generally equant. The grain size of the target is similar to the *Berry Hollow* abrasion at the *Wildcat Ridge* workspace, although the chemistry and mineralogy of the two targets differ. The matrix of the rock is lighter gray than the grains within it, with two exceptions. In some patches the rock matrix is orange; also, heterogeneously distributed, small, irregularly-shaped white patches appear to occur where either the rock matrix is white or has been replaced by a white material. The distribution of grains and matrix, and the overall grain size support identification of the target as a coarse mudstone.

Figure 8 | WATSON post-abrasion focus merge from 4.1 cm standoff of the interior of the *Novarupta* abrasion with the footprints of the Sol 570 SHERLOC spectroscopy (pink, white) and PIXL map (cyan) analyses overlain. Sunlight illumination is from the upper left.

Figure 9 | Grain size distribution of *Novarupta*.

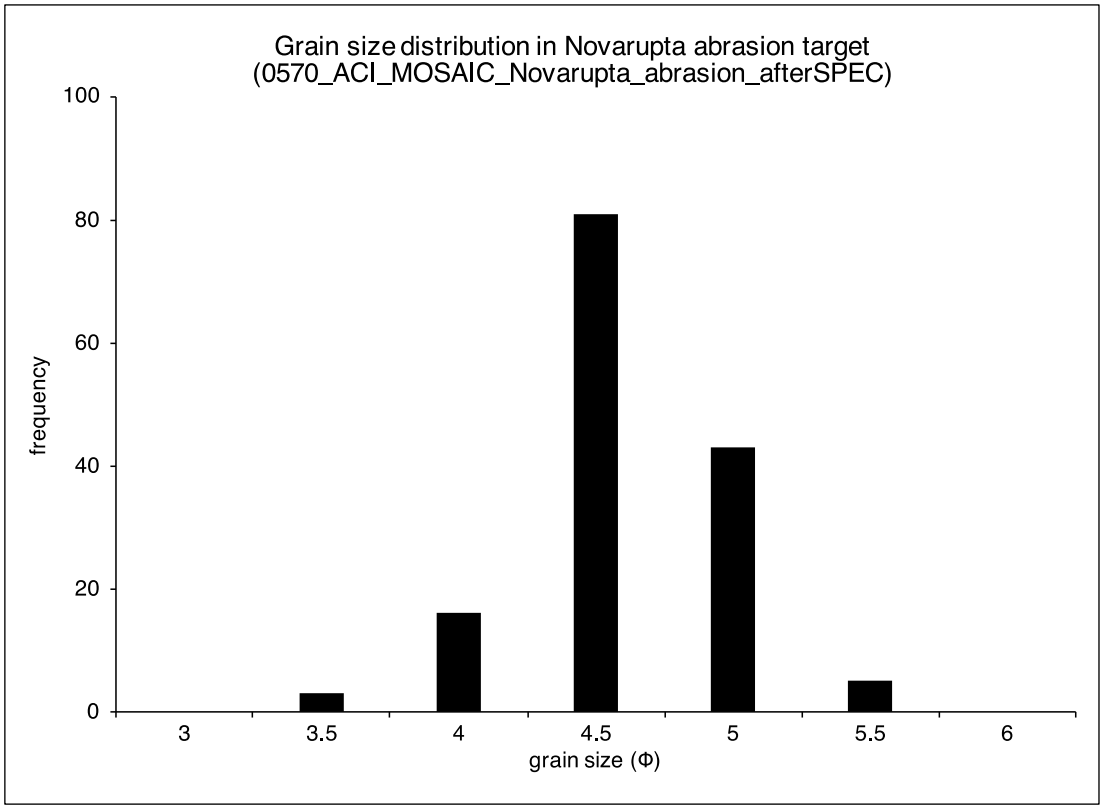

Figure 9 shows the distribution of grain sizes in *Novarupta*. Equivalent diameters of 148 grains were measured at intersection points of a grid with 0.5 mm spacing, projected on a mosaic of SHERLOC ACI images of the abrasion patch. Grains in *Novarupta* show a unimodal distribution, with the mode at φ=4.4 (silt, 47 μm), mean grain size of φ =4.3 (silt, 51 μm), and standard deviation of φ=0.35 (well-sorted). [$\varphi = -\log_2(D)$, where D is the diameter of a grain in millimeters.] Measured grains range in size from 94 μm down to the limit of ACI resolution (10.1 μm/pixel, enabling objects of >30 μm to be resolved). Grains are generally equant (**Figure 8**). Using the textural classifications defined by Lazar et al. (2015), this rock is a coarse mudstone.

The textures observed in the abrasion patch are consistent with those on the fresh, broken surfaces of the ends of both cores (**Figure 10**). The coarsest grains are fine sand, but they are rare relative to the resolvable silt to very fine sand grains comprising the clastic texture of the rock. The color stretch applied to the images challenges assessment of absolute color, but the relative patterns from the abrasion patch are present in the core ends with some notable deviations. Within the *Shuyak* core (**Figure 10a**), the matrix of the rock largely resembles that of the abrasion patch (variations from gray to orange to white), but there is an ~2 mm patch of matrix material that is darker and more resistant (higher standing) than the rest of the matrix materials within the core surface (**Figure 10a**, top center). This darker material envelops matrix and grains that otherwise resemble the texture in the rest of the core. The darker patch could be evidence for differential cementation or secondary alteration. The color stretch highlights redder (relative to the rest of the abrasion), small, irregular patches that might

represent another matrix material or alteration product. On the *Mageik* core face, relatively redder patches are also present, and in some instances appear to envelop individual, smaller grains (**Figure 10b**). The bright, arcuate swath on the core face where the granular texture of the core is muted (**Figure 10b**, left center) is likely a scrape mark from the tool used to break the core at the bottom of the borehole. For both cores, if the orange, white and/or red matrices are related to alteration, it suggests such alteration extends to a depth of at least 6 cm in the rock.

As we have noted with previous samples, the borehole is heavily coated by tailings, obscuring any structures possibly present in the borehole walls or floor (**Figure 11**).

Figure 10 | (**a-b**) Cachecam images (color stretched) and (**c-d**) ZCAM images of the *Shuyak* (left) and *Mageik* (right) core samples. Core lengths are 55.5 mm (*Shuyak*) and 73.6 mm (*Mageik*). Core diameter is 13 mm, for scale.

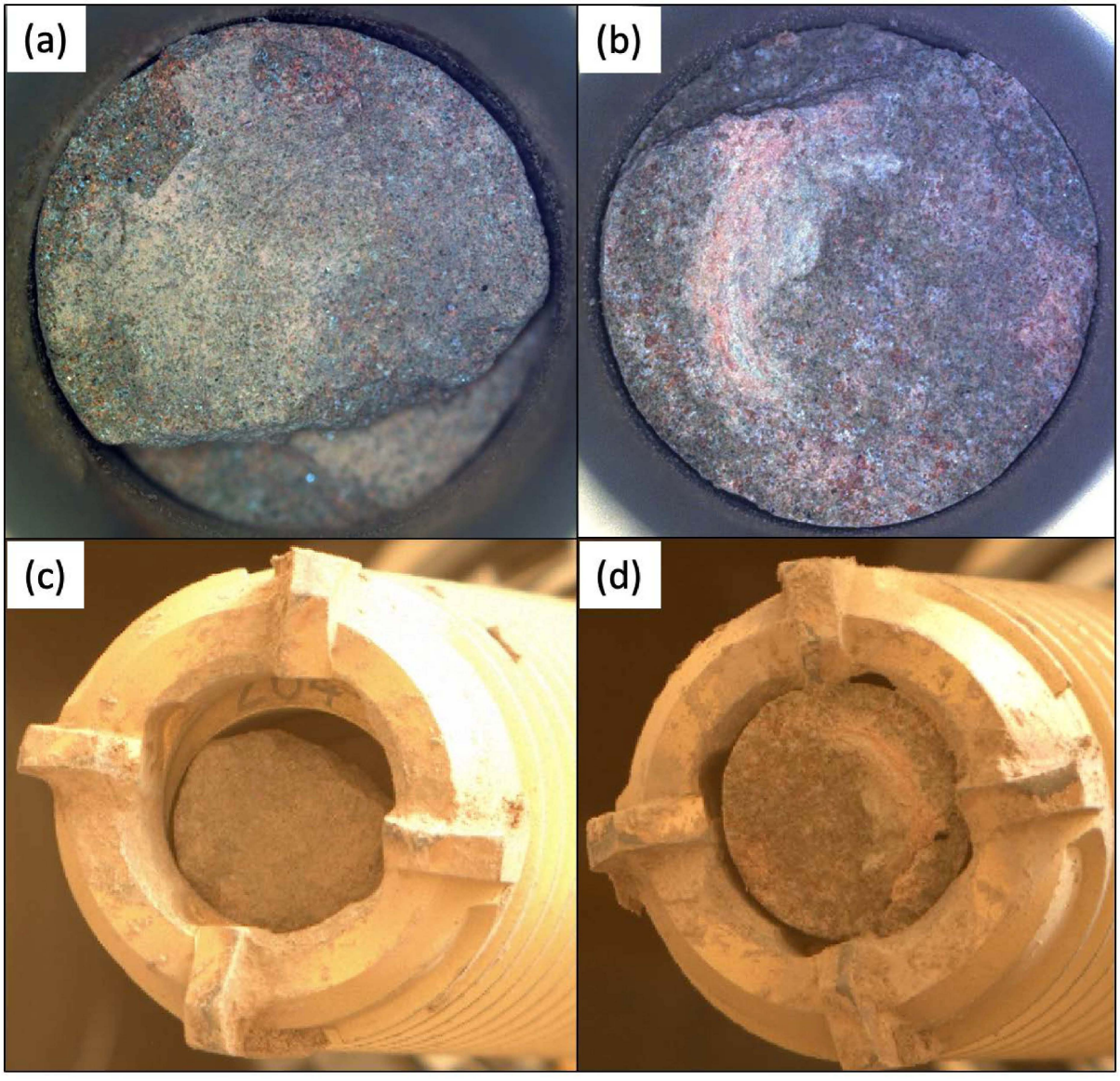

Figure 11 | WATSON borehole image after *Mageik* core extraction (Sol 582).

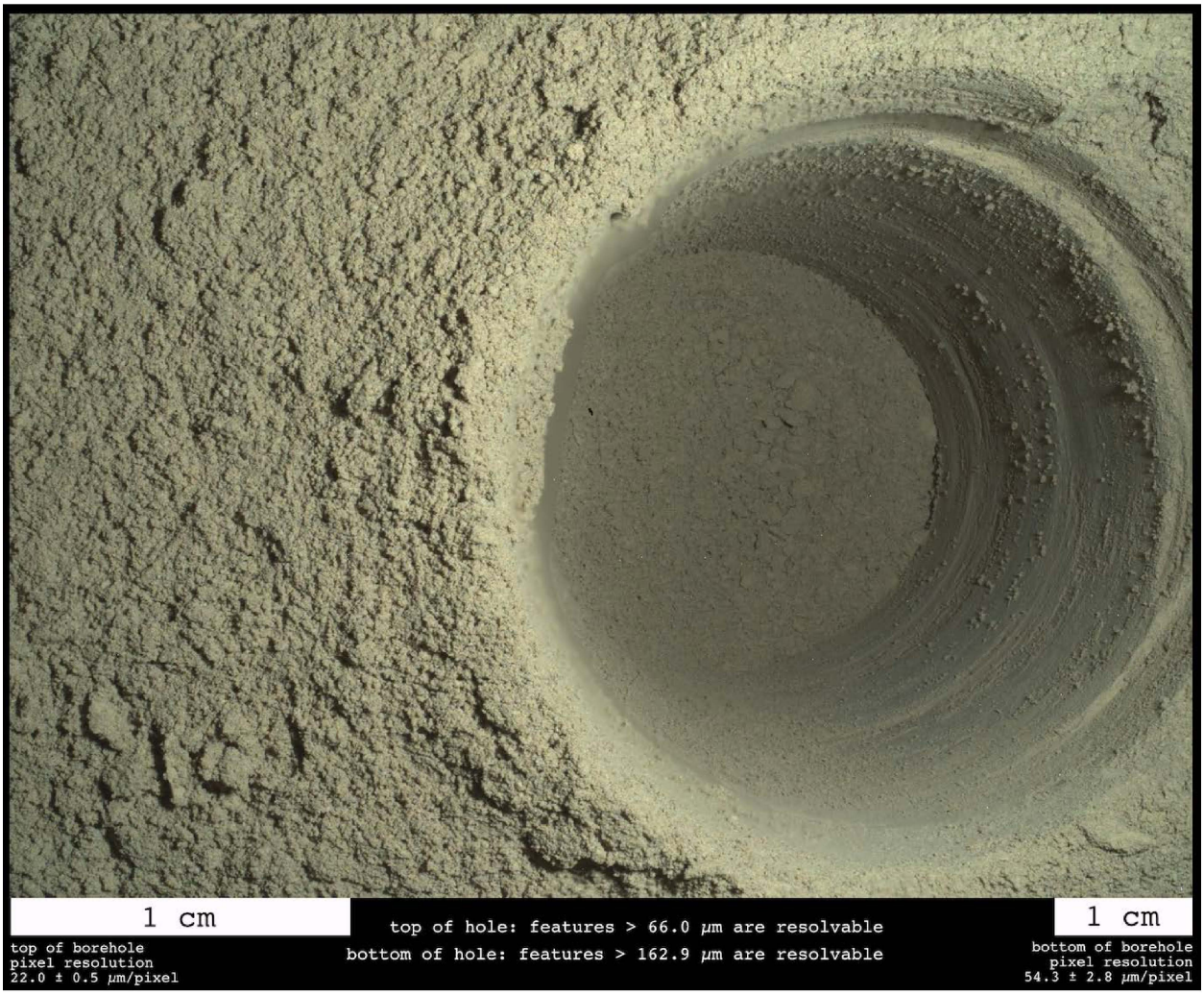

Elemental Geochemistry - PIXL

Amalik is a coarse mudstone consisting primarily of small grains (<120 µm) of Mg-Fe silicates. The major element composition of the abrasion surface *Novarupta2* is like that of *Dourbes* in the *Séítah* formation, but with lower silica and more Ti and Cr. The compositions of most analysis spots are consistent with olivine and aqueous alteration products of olivine, plus minor salts. The distribution of diffracting and non-diffracting spots implies that crystalline domains are generally <60 µm in diameter, and most of the grains comprise small domains of minimally altered olivine with intergrown alteration products. Pyroxene and feldspar, which are abundant in the crater floor rocks (*Séítah* and *Máaz* formations), are notably absent as sand-size grains. The rock is chemically and mineralogically layered, with distinct planar concentrations of heavy minerals such as chromite, ilmenite, and apatite. The natural surface of the rock is chemically and texturally distinct from the interior – it appears to be a crust with similar properties and composition as observed elsewhere in Jezero crater. Chemically, the crust is consistent with airfall dust plus sulfate and chlorine-bearing salts.

Figure 12 | **PIXL raster scans on the *Novarupta* abrasion patch, sols 567, 570, and 0573.** Green areas and outlines are the analysis footprints; white outlines are SHERLOC scans. **(a)** *Novarupta* area before abrasion (SI1-0566_0717192162_457ECM_N0290000SRLC04001_0000OMJ01). **(b)** *Novarupta* area after abrasion (SI1-0566 07171381130_226ECM_N0290000SRLC02501_0000OMJ01). **(c)** Location of the PIXL natural surface scan. *Novarupta1* was a 5x7 mm map. **(d)** Locations of PIXL scans on abrasion patch, which is ~5 cm diameter. The 570 area was a 12.5x4 mm map; the 573 scan was an incomplete 7x7 mm grid.

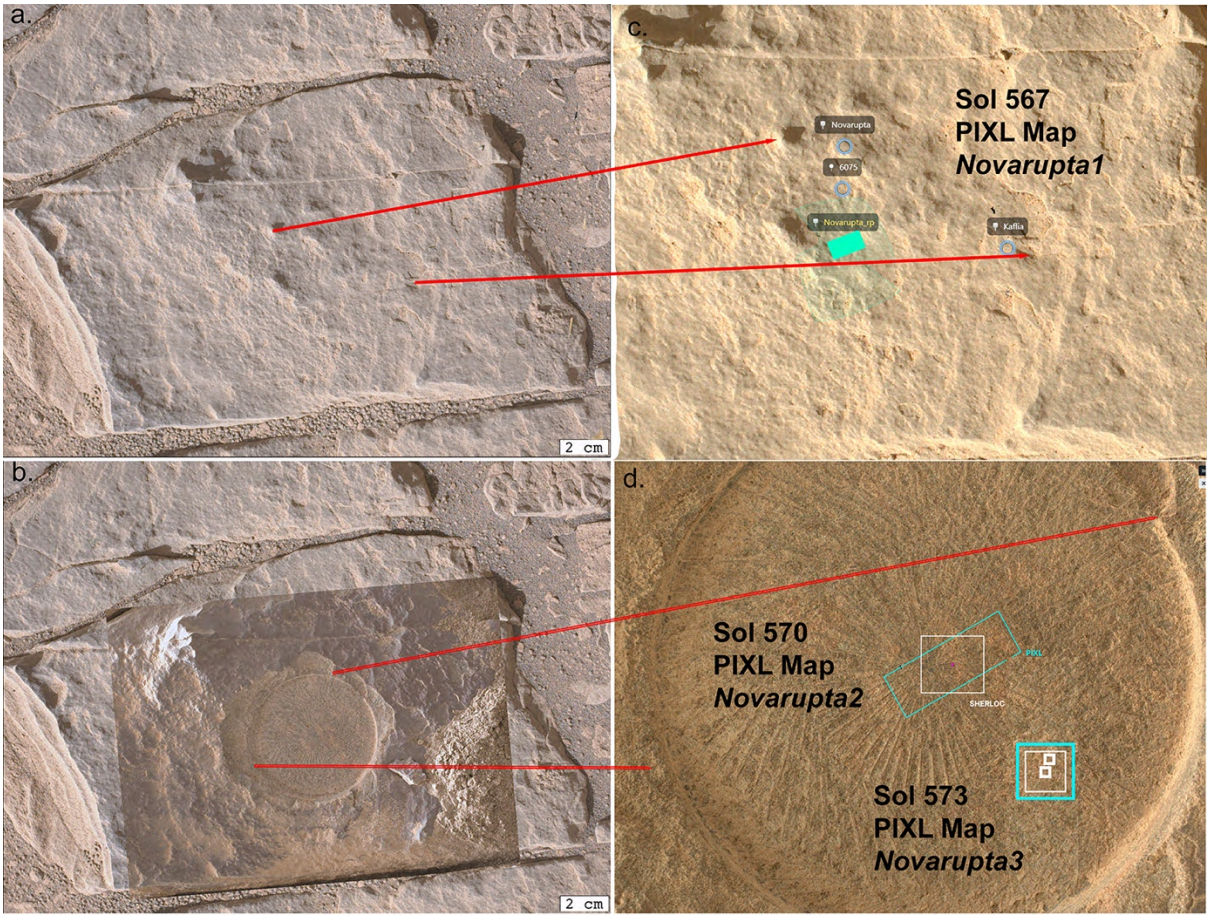

Elemental geochemistry of *Amalik* is from X-ray fluorescence (XRF) mapping by the PIXL instrument of the *Novarupta* area, pre- and post-abrasion. The *Novarupta* abrasion was mapped by PIXL on sol 570 (12.5x4 mm, 0.125 mm point spacing) and again on sol 573, **Figure 12**. The former is map *Novarupta2*; the latter is *Novarupta3*, data from which is not reported here. The natural, unabraded surface was mapped on sol 567, reported here as *Novarupta1*. The analyzed surface had been cleared of dust by a line of SuperCAM-LIBS laser shots. *Novarupta1* was a 5x7 mm map scan (0.125 mm point spacing), **Figure 12**. We discuss the abraded rock and the natural surface separately.

PIXL scans on the *Chiniak* area (sols 558 & 560) are likely of the same material as *Novarupta*, but are not discussed here, except for the average composition of its natural surface.

Table 1 gives the bulk chemical composition of the *Novarupta2* map scan, its least altered olivine composition, and for comparison the bulk composition of *Dourbes* (a *Séítah* formation abrasion patch). Many spots in the scan have chemistry consistent with unaltered olivine, such as was analyzed in *Dourbes*.

Also, the *Novarupta2* abrasion bulk composition is very similar to *Dourbes* (**Table 1**). This similarity supports the hypothesis that the *Shuyak/Mageik* cores represent a sediment derived from rocks with *Séítah*-like composition. Compared to *Dourbes*, *Novarupta2* has: ~3/4 of the SiO_2, much more Cr_2O_3, TiO_2, and SO_3; less P_2O_5; and significantly more unanalyzed components (i.e., from the low analytical sum). These differences could be explained by mechanical weathering and disaggregation, hydraulic sorting, and alteration that removed silica and added sulfate and LZE (low-Z-elements, undetected by PIXL) volatiles. There is little evidence for a contribution from the *Máaz* basaltic rocks, which are Fe-rich and Cr-poor.

The *Amalik* rock is composed of sand-sized grains, ~50 μm in diameter. In such a fine-grained rock, the observed limited distribution of spot compositions (**Figures 13, 15**) could represent either a mixture of olivine grains and completely altered olivine grains, or grains composed of finely disseminated olivine and alteration products. The distribution of diffraction peaks in the abrasion patch can be used to differentiate between these endmember cases. Diffraction peaks are present in spectra from ~13-20% of analysis spots, but the same peaks are rarely, if ever, present within two or more neighboring points. This indicates that the mineral crystalline domains in this sample are generally <60 μm in diameter. The distribution of diffraction peaks and the typical olivine/altered olivine composition of analysis spots implies that most sand-size grains comprise small domains of minimally-altered olivine intergrown with its alteration products. The altered olivine grains incorporated a small amount of Al in a style of alteration that looks like a hybrid of alteration products in *Séítah* and *Máaz*, but closer to *Séítah* than to *Máaz*.

Table 1 | **Chemical Compositions: PIXL XRF.**

	Novarupta2 Bulk Abraded Sol 570		*Novarupta2* 'Least Altered Olivine' Sol 570		*Dourbes* Bulk Abraded Sols 257 & 270	
Wt %	N=3333	Stdev 1σ	N=15	Stdev 1σ	N=5670	Stdev 1σ
Na_2O	1.0	0.9	0.6	0.6	1.9	0.5
MgO	19.1	1.1	19.7	1.5	19.2	1.0
Al_2O_3	1.8	0.5	1.6	0.3	2.4	0.2
SiO_2	30.8	1.6	29.4	1.9	39.4	3.1
P_2O_5	0.1	0.4	0.0	0.1	0.5	0.1
SO_3	3.8	0.5	3.2	1.2	0.8	0.1
Cl	2.0	0.5	2.0	0.2	0.7	0.1
K_2O	**0.0**	**0.0**	0.0	0.0	0.4	0.1
CaO	3.3	0.4	2.0	1.1	2.9	1.6
TiO_2	0.7	0.2	0.5	0.4	0.2	0.1
Cr_2O_3	1.9	0.3	3.3	1.0	0.3	0.1
MnO	0.4	0.2	0.3	0.1	0.7	0.1
FeO-T	28.0	1.5	32.4	2.8	30.1	1.7
NiO	0.06	0.03	0.06	0.02	-	-
ZnO	nd	nd	nd	nd	-	-
Sum %	93.0		95.0		99.4	
Mg#	55		52		54	

'Least Altered Olivine' was identified by analysis spots with diffraction peaks not attributable to spinel or phosphate minerals and having molar (Mg + Fe)/Si from 1.3-2.0.
N is number of analyses averaged.
Stdev is 1σ uncertainty from calibration and counting statistics**.**
Mg# is molar Mg/(Mg+Fe), in percent.

Figure 13 shows the chemical analyses of *Novarupta2* in the Mangold et al. (2017) classification for Gale crater rocks, and the common TAS classification diagram for volcanic rocks. In the Mangold scheme, *Novarupta2* would be classified as Fe-rich, Si-poor, K-poor, and Na-poor. In the TAS diagram, the spot and bulk compositions of *Novarupta2* are unlike typical igneous rock, and more akin to an Al-depleted komatiite. In the TAS projection, the *Novarupta2* compositions are close to that of olivine, and are like the average composition of the *Brac/Dourbes* rock of the *Séítah* formation (**Table 1)**.

Figure 13 | **Chemical classification of *Novarupta2*.** Blue dots are individual PIXL analyses, red circle is the average composition (**Table 1**). Figures **13a** and **13b** follow the classification scheme of Mangold et al. (2017). **(b)** nearly all the individual analyses are on the X-axis, i.e., have no detectable potassium (**Figure 14f**). See text for explanations.

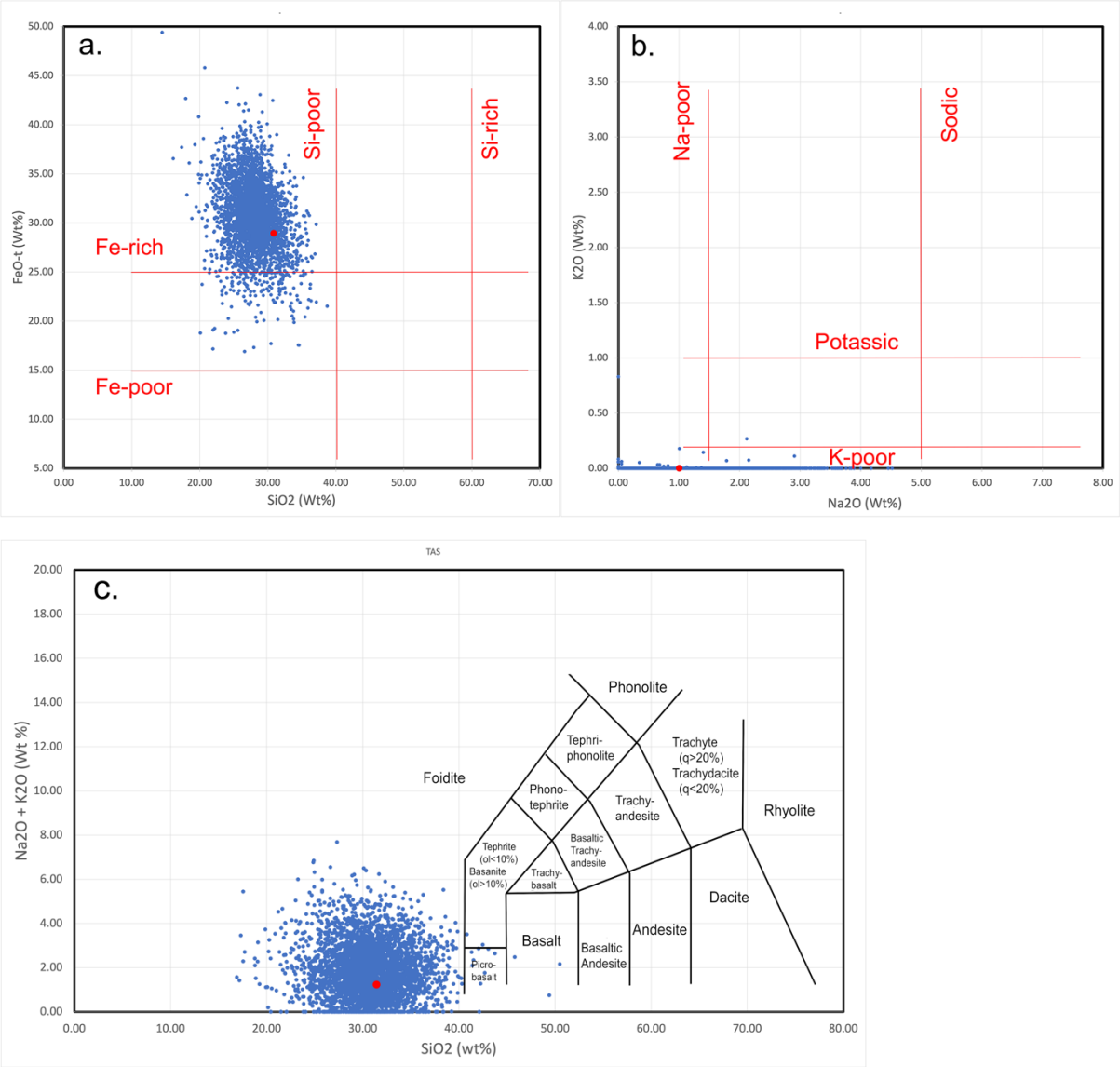

Figure 14 shows multi-element color images from the PIXL map of *Novarupta*2. The most important feature in **Figure 14** is that the *Novarupta2* rock is layered, apparent in **Figures 14a, b, d,** and **f**. The layers are most prominent in **Figure 14d**, where they are marked by enrichments in chromite (yellow) and ilmenite (magenta) that alternate with layers poor in those phases (dark red). The chromite-rich layers also contain most of the scan area's apatite (**Figure 14e**) and are enriched in Na-chlorine salts (orange in **Figure 14f**). The intervening layers (poor in chromite & ilmenite) are also poorer in Fe and Ca (**Figures 13a, 13c**) and richer in Mg and Al (**Figures 14a, 14b**), and in Cl unassociated with alkali elements (green in **Figure 14f**). The chromite-rich layers can be interpreted as sedimentary concentrations of

heavy minerals. The intervening layers could be interpreted as containing phyllosilicate minerals (from their elevated Al contents).

The *Novarupta* abrasion surface is parallel to the rock's bedding plane, but the abrasion tool randomly removed large chunks of material from the surface, producing windows into an underlying layer. The mineralogical and compositional variation visible in **Figure 14** largely reflects this division into a thin, flat surface layer rich in heavy mineral grains (chromites, ilmenites, phosphates, and a zircon/baddeleyite) and an underlying layer rich in altered olivine grains. The windows into the underlying layer are especially visible in the MCC NIR/UV band-ratio image (**Figure 18**), likely reflecting partial oxidation of the altered olivine.

The *Novarupta2* map scan area contains little evidence of sulfate minerals, as only a few spot analyses contain SO_3 > 3 % (**Figure 14c**). These few high-S spots are associated with Ca (magenta on **Figure 14c**; see **Figure 15c**). There is little to no Mg-sulfate (which would be yellow on **Figure 14c**; see **Figure 4c**). The map does contain some Na-chlorine associations (orange on **Figure 14g**), and a few spots with a K-chlorine association (light blue on **Figure 14g**). These likely represent chlorides or oxychlorine salts.

The mapped area shows a single analysis spot with significant zirconium, the green pixel in **Figure 14e**. This is considered a detection of zirconium, rather than a diffraction effect, because the X-ray energy mapped here is exactly that of ZrKα (**Figure 14h**), the energy peak is shaped properly for ZrKα, and the peak height is significantly above background. Quantitation of that spot analysis gives only 1.5% ZrO_2, while the mineral zircon contains 67% ZrO_2. Either zircon is a very small proportion of the analysis area or (more likely) a larger zircon grain is beneath the abrasion scan surface.

Of special note is that the *Novarupta2* rock contains almost no potassium. The map's only spots with significant potassium, at the bottom left and right of **Figure 14g**, are associated with Cl. Few of the other PIXL analysis spots had detectable K (**Figure 13b**).

Figure 14 | **PIXL multi-element maps from the *Novarupta2* abrasion, Sol 570.** Legends indicate which element is assigned to which color, the full range of abundances of that element or oxide (numbers) and the distribution of element abundances in the scan (black bars & histograms left of the color bars). **(a)** FeO-MgO-SiO_2. **(b)** FeO_T-Al_2O_3-CaO. **(c)** SO_3-MgO-CaO, emphasizing sulfates. **(d)** FeO-TiO_2-Cr_2O_3, emphasizing oxide minerals. **(e)** P_2O_5-ZrO_2-ZnO, emphasizing minor minerals. **(f)** Na_2O-Cl-K_2O, emphasizing chlorine phases. **(g)** A portion of the PIXL X-ray spectrum of the zirconium-bearing spot (green in **(e)**). X-ray peaks for Fe are on the left – the X-ray counts at the ZrKa peak, at 15.73 keV, are ~5 times the background.

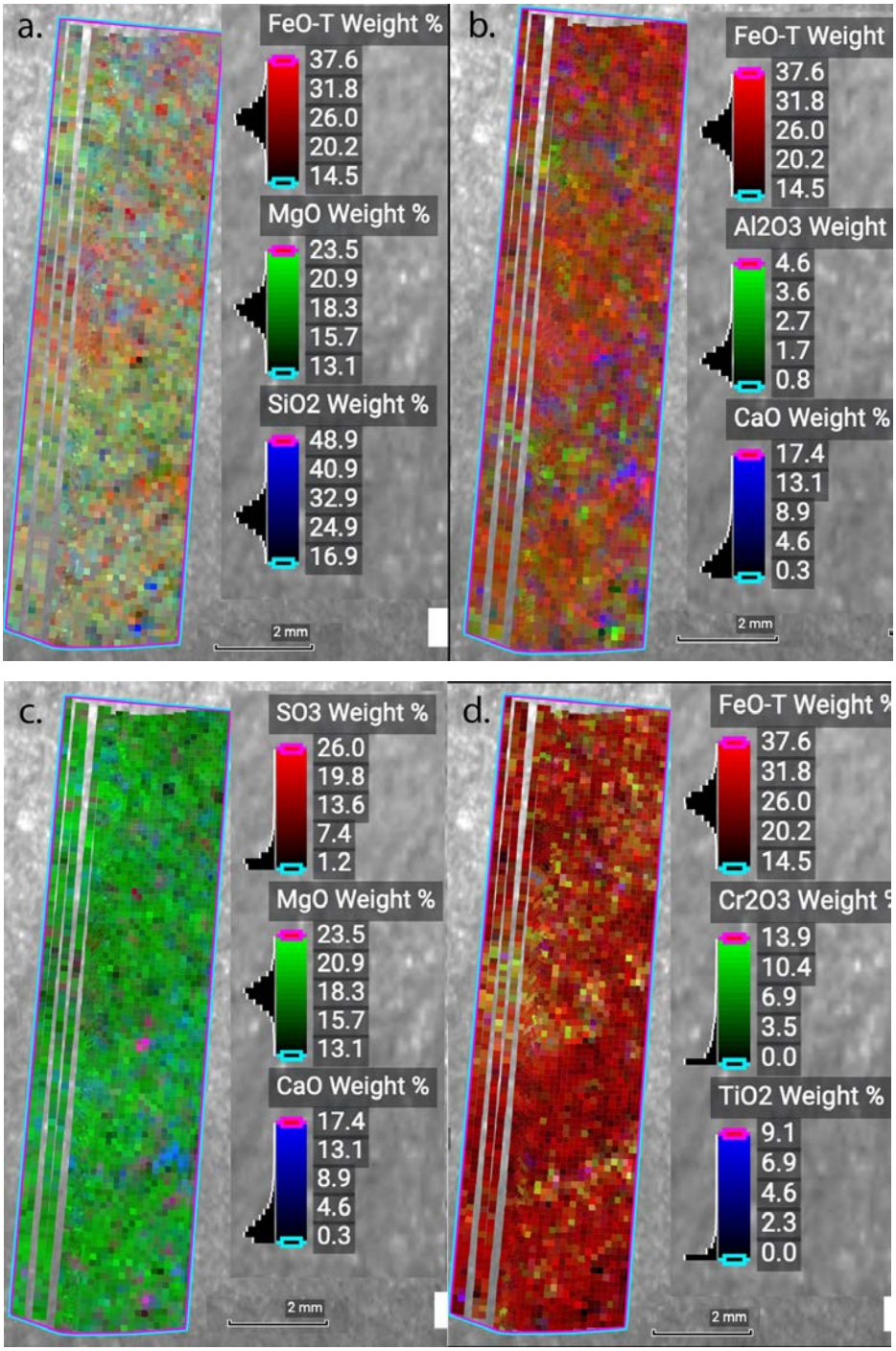

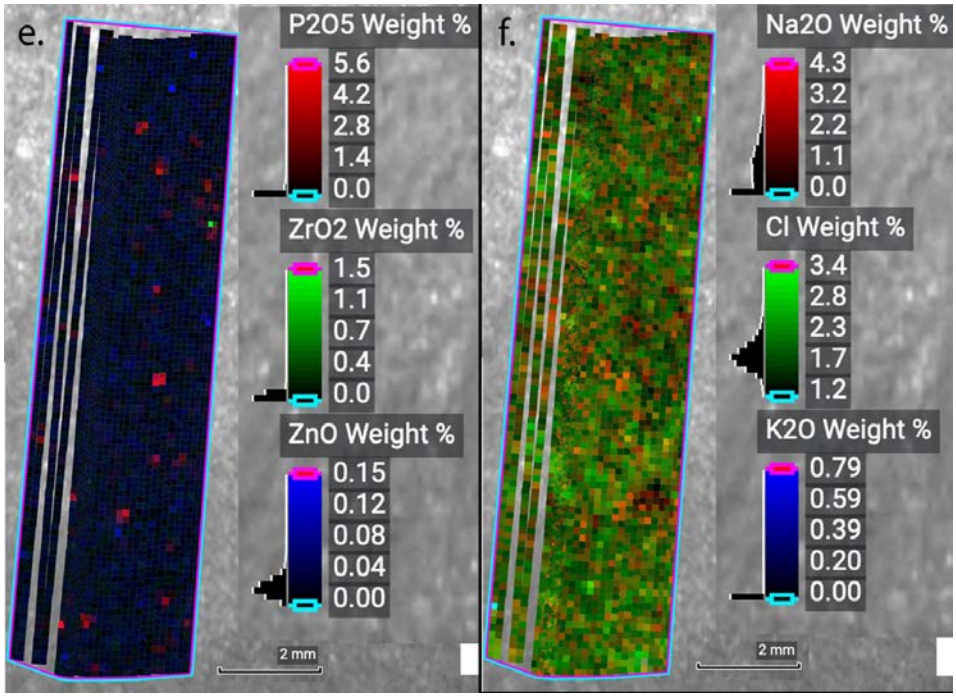
e.
P2O5 Weight %
5.6
4.2
2.8
1.4
0.0
ZrO2 Weight %
1.5
1.1
0.7
0.4
0.0
ZnO Weight %
0.15
0.12
0.08
0.04
0.00
2 mm
f.
Na2O Weight %
4.3
3.2
2.2
1.1
0.0
Cl Weight %
3.4
2.8
2.3
1.7
1.2
K2O Weight %
0.79
0.59
0.39
0.20
0.00
2 mm

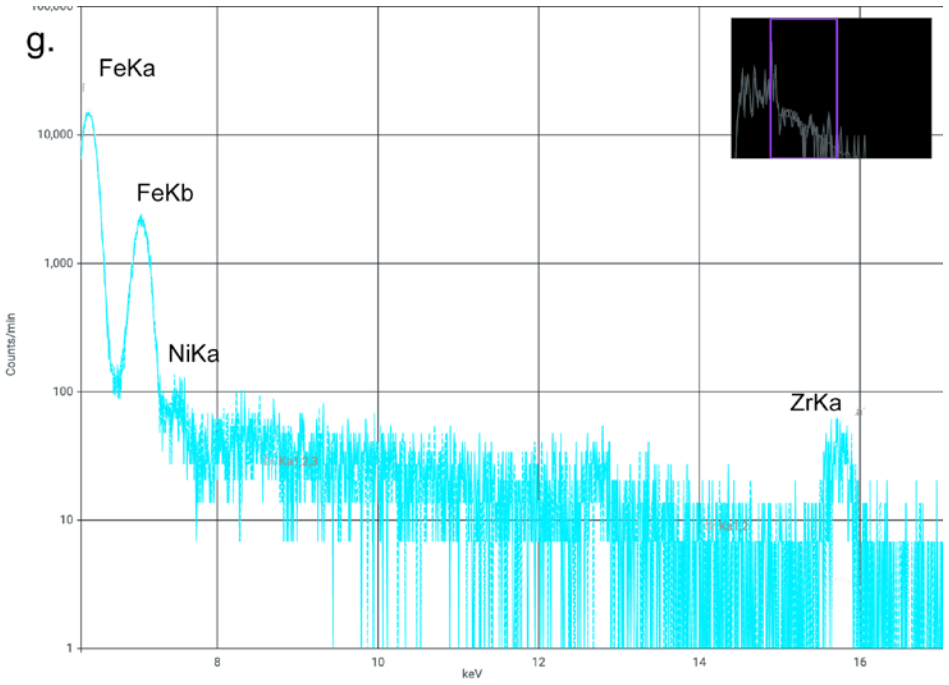
g.
FeKa
FeKb
NiKa
ZrKa
Counts/min
10,000
1,000
100
10
1
8
10
12
14
16
keV

Figure 15 shows ternary plots of elemental chemistry for the PIXL scan of *Novarupta2*. In its most abundant elements (Mg, Fe, Ca, Si), the *Novarupta2* composition is consistent with a mixture of olivine, its aqueous alteration products (e.g., serpentine), dolomite [$Ca(Mg,Fe)(CO_3)_2$], and silica (**Figure 15a**). The presence of carbonate in the sample is confirmed by the strength of the rhodium X-ray scattering peaks in PIXL spectra. The red line on **Figure 15a** is a mixing line between olivine and dolomite. *Novarupta2* contains a little Al, but no indication of Al-enrichment via loss of Ca and alkalis (**Figure 15b**). The rock contains little evidence for Mg-Fe sulfates, **Figure 15c**, as few of the spot analyses trend from the diagram's Fe-Mg apex toward the S apex. Instead, arrays of points trend toward both the Ca apex and the Ca-S join at molar 1:1. These arrays suggest mixtures of Fe-Mg silicate minerals with Ca sulfate and dolomitic carbonate. Finally, the oxide minerals in *Novarupta2* are dominated by chromite with a little Ti, as shown in Figure **15d** by the trend at Cr_2O_3/TiO_2 ~8. Chromite of this composition is present in *Dourbes/Brac* but is not its dominant Fe-Cr-Ti oxide. A few points on that figure appear to define a trend at Cr_2O_3/TiO_2 ~1.5, which is also present in *Dourbes/Brac*. The few points near the x-axis of **Figure 15d** are consistent with ilmenite (or rutile).

The bulk chemical analysis of the *Novarupta*1 natural surface is given in **Table 2.** Chemically, that surface is relatively homogeneous (see **Figure 15**). Beyond what is in the Table, the *Novarupta1* analysis includes Sr and Zr at or below 1σ detection. Also included in **Table 2** are analyses of similar natural surfaces analyzed by PIXL in Jezero Crater. *Chiniak_Offset2* is near *Novarupta1*, and the dust crust in *Beaujeu2* is from early in the mission, on a *Máaz* basalt.

The *Novarupta1* map scan is of the natural surface of the rock, in an area where SuperCam-LIBS shots cleared away some of the surface dust. The differences shown in **Tables 1**-**2** and the element maps of **Figures 14** and **16** indicate the natural surface is chemically distinct from the abraded surface, ~8 mm into the rock. The natural surface is inferred to be a coating or crust on the rock, immobile in the local shock waves of the SuperCam-LIBS shots. WATSON images suggest that the coating or crust is less than a millimeter thick. PIXL diffraction data indicate that the crust/coating is very fine-grained (<50 μm), or amorphous.

The crust or coating is homogeneous across the *Novarupta1* map area, as evidenced by the limited ranges of element abundances across the maps (**Figure 16**) and the small uncertainties on the bulk analysis in **Table 2**. Sulfate in the dust crust seems to be mostly associated with Ca (pink and magenta in **Figure 16c**), and there is some indication that Ca-sulfate is concentrated in linear features, i.e., veinlets. There is no evidence for Mg sulfate (**Figure 16c**). Chlorine is distributed evenly in the crust (**Figure 16f**) with little indication of discrete Na- or K- chlorine salts.

Only a few distinct mineral grains are apparent in the natural surface, and these are interpreted as being beneath the coating or exposed where the coating was removed. There are a few grains of Fe and Fe-Ti oxides (**Figure 16d**), but the maximum TiO_2 value is only 4%, so PIXL is detecting either very small grains or those beneath the coating (or both). A single grain of chromite is suggested in **Figure 16d** by a value of Cr_2O_3=4%, and a single grain of zircon or baddeleyite is suggested in **Figure 16e** by a value of ZrO_2=0.4%.

Figure 15 | Plots of PIXL element analyses of the *Novarupta2* abrasion, Sol 570. **(a)** Molar proportions of Ca+Na+K, Si, & Fe+Mg. Common minerals that plot at the Fe+Mg apex include oxides, Fe-Mg carbonate, and Fe-Mg sulfates. **(b)** Molar proportions of Ca+Na+K, Al2, & Fe+Mg. 'Ol' at Fe+Mg corner includes minerals olivine, orthopyroxene, Fe oxides, and Fe-Mg carbonates & sulfates. **(c)** Molar proportions of SO_3, MgO, and CaO, emphasizing sulfates. **(d)** Weight percent of Cr_2O_3 vs. TiO_2, showing compositions of Cr-Ti oxides.

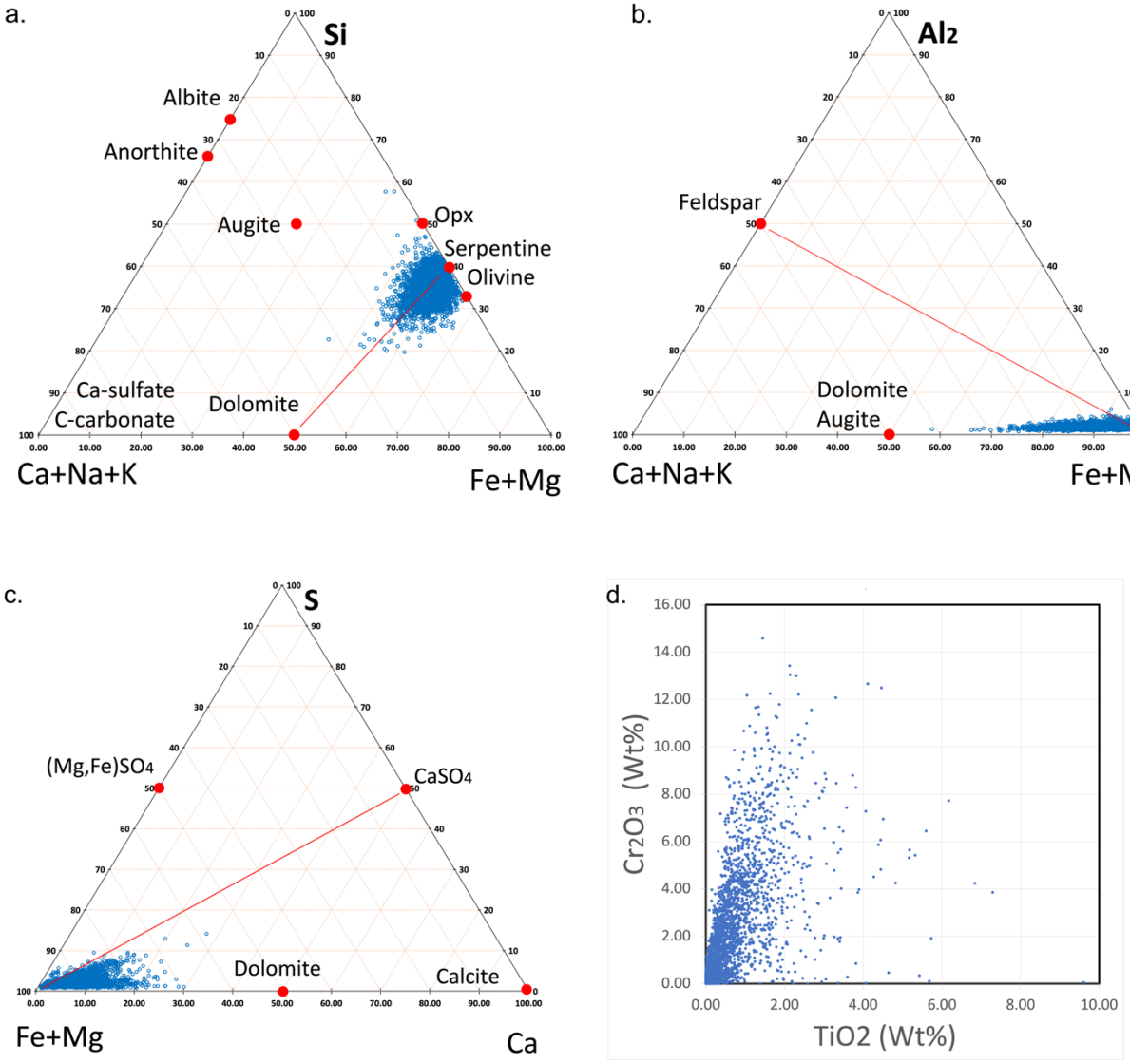

Table 2 | **Natural Surface Preliminary Chemical Compositions: PIXL XRF.**

	Novarupta1 Map Sol 567		*Chiniak_Offset2* Map Sol 560		*Beaujeu2* Dust Crust Map Sol 139	
Wt %	N=3306	Stdev 1σ	N=3306	Stdev 1σ	N=144	Sddev 1σ
Na_2O	3.2	1.2	3.0	1.2	4.0	0.7
MgO	6.9	0.5	7.3	0.5	7.3	0.4
Al_2O_3	7.5	0.4	7.4	0.4	7.9	0.4
SiO_2	37.3	1.9	38.2	1.9	37.5	1.9
P_2O_5	1.6	0.5	1.7	0.5	1.6	0.5
SO_3	9.2	0.5	9.9	0.5	10.9	0.6
Cl	3.0	0.1	3.0	0.6	3.4	0.5
K_2O	0.5	0.2	0.5	0.2	0.6	0.2
CaO	6.7	0.6	7.2	0.4	7.3	0.4
TiO_2	0.7	0.3	0.7	0.3	0.9	0.3
Cr_2O_3	0.1	0.1	0.5	0.3	0.2	0.2
MnO	0.2	0.2	0.3	0.2	0.4	0.2
FeO-T	21.2	1.1	21.5	1.1	18.8	0.9
NiO	0.05	0.02	0.06	0.03	0.07	0.04
ZnO	**0.09**	**0.04**	**0.07**	**0.03**	**0.09**	**0.04**
Sum %	98.4		101.4		100.8	
Mg#	37		38		41	

N is number of analyses averaged.

Stdev is uncertainty (1σ) from calibration and counting statistics**.**

Mg# is molar Mg/(Mg+Fe), in percent.

Figure 16 | PIXL multi-element maps of the *Novarupta1* natural surface on Sol 567. Legend (right on each frame) shows which element is mapped to which color, the full range of abundances of that element or oxide (numbers), and the distribution of element abundances in the scan (black bars & histograms left of the color bars). **(a)** FeO-MgO-SiO_2. **(b)** FeO_T-Al_2O_3-CaO. **(c)** SO_3-MgO-CaO, emphasizing sulfates. **(d)** FeO-TiO_2-Cr_2O_3, emphasizing oxide minerals. **(e)** P_2O_5-ZrO_2-ZnO, emphasizing minor minerals. **(f)** Na_2O-Cl-K_2O, emphasizing chlorine phases.

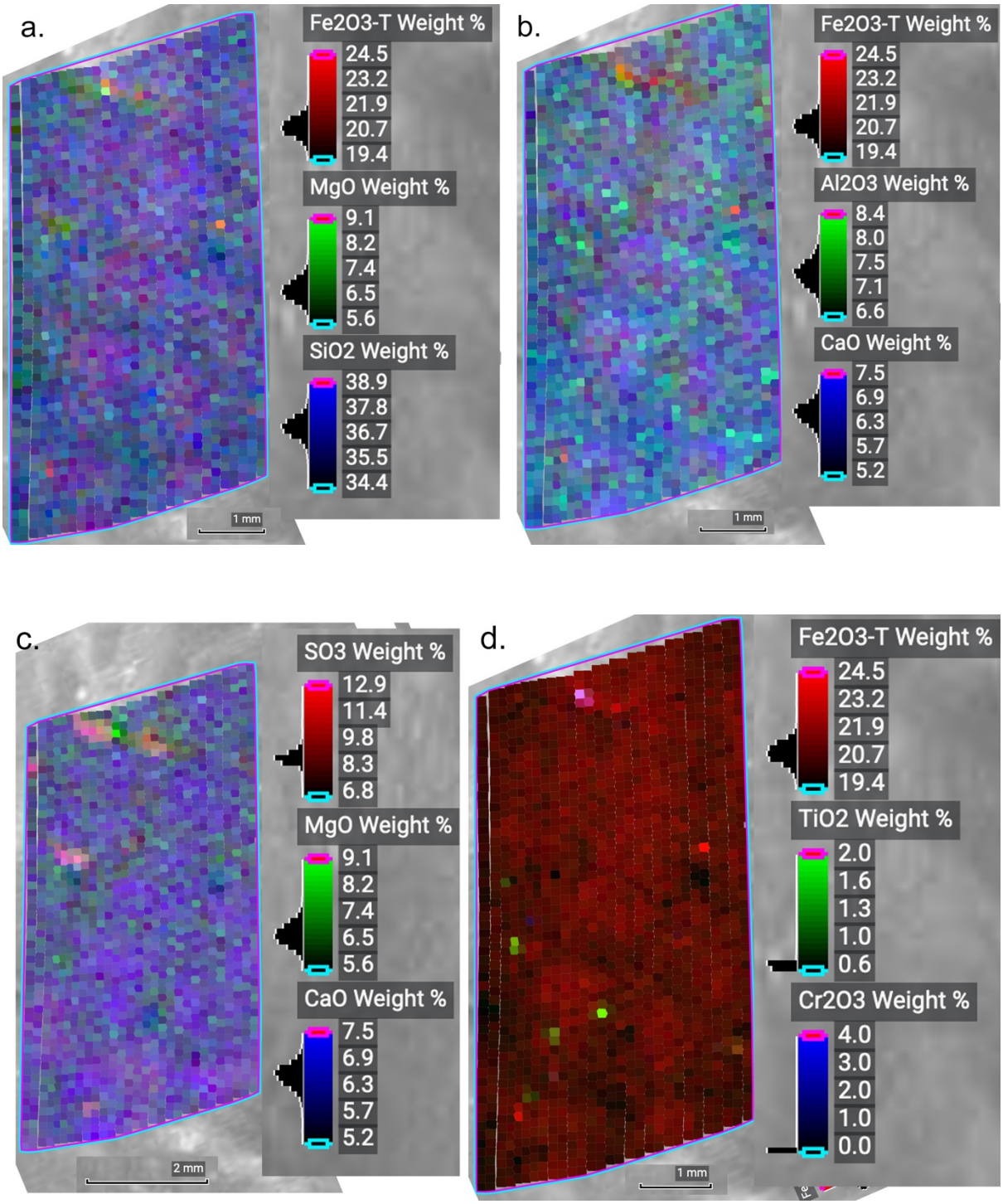

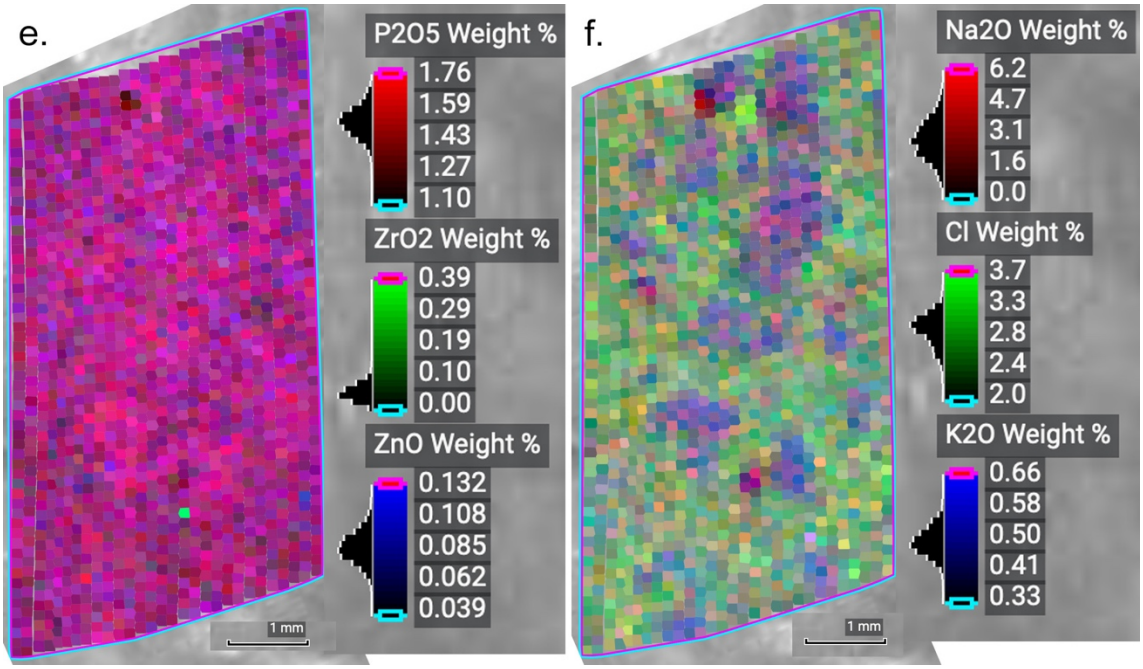

The *Novarupta1* bulk is similar chemically to other natural surfaces analyzed on the nearby *Chiniak_Offset* (sol 558) and the distant *Beaujeu2* (sol 139); see **Table 2** and **Figure 17a**. The compositions of these natural surfaces are consistent with global martian dust plus sulfate and chlorine salts (**Figure 17a**) and have been interpreted as being windblown dust deposited on rock surfaces and cemented by S-Cl salts. It is noteworthy that the crusts are enriched in the volatile S and Cl; but their analytical totals are near 100% (**Table 2**). This fact suggesting that the crusts contain little hydrogen (in hydrous minerals) and carbon (in carbonate minerals). In comparison, analytical totals for the *Novarupta* rock interior and its constituents (**Table 1**) are lower than 100%, suggesting that they contain significant hydrogen (in hydrous minerals) and/or carbon (in carbonate minerals).

Figure 17 | Comparisons of the *Novarupta1* crust to *Beaujeu2* crust and *Novarupta* interior rock. **Figure 17a** – a 'spider' diagram comparing the average composition of Jezero crusts, normalized to the composition of air-fall dust analyzed in Gale crater (Berger et al., 2016). **Figures 17b-f** compare the analyzed composition of crust at *Novarupta1* and *Beaujeu2* with those of the underlying rock in the *Novarupta2* and *3* scans. The crusts at *Novarupta1* and *Beaujeu2* are homogeneous and similar to each other, possibly identical within analytical uncertainties. Both crusts are very distinct from the *Novarupta* interior rock exposed in the abrasion.

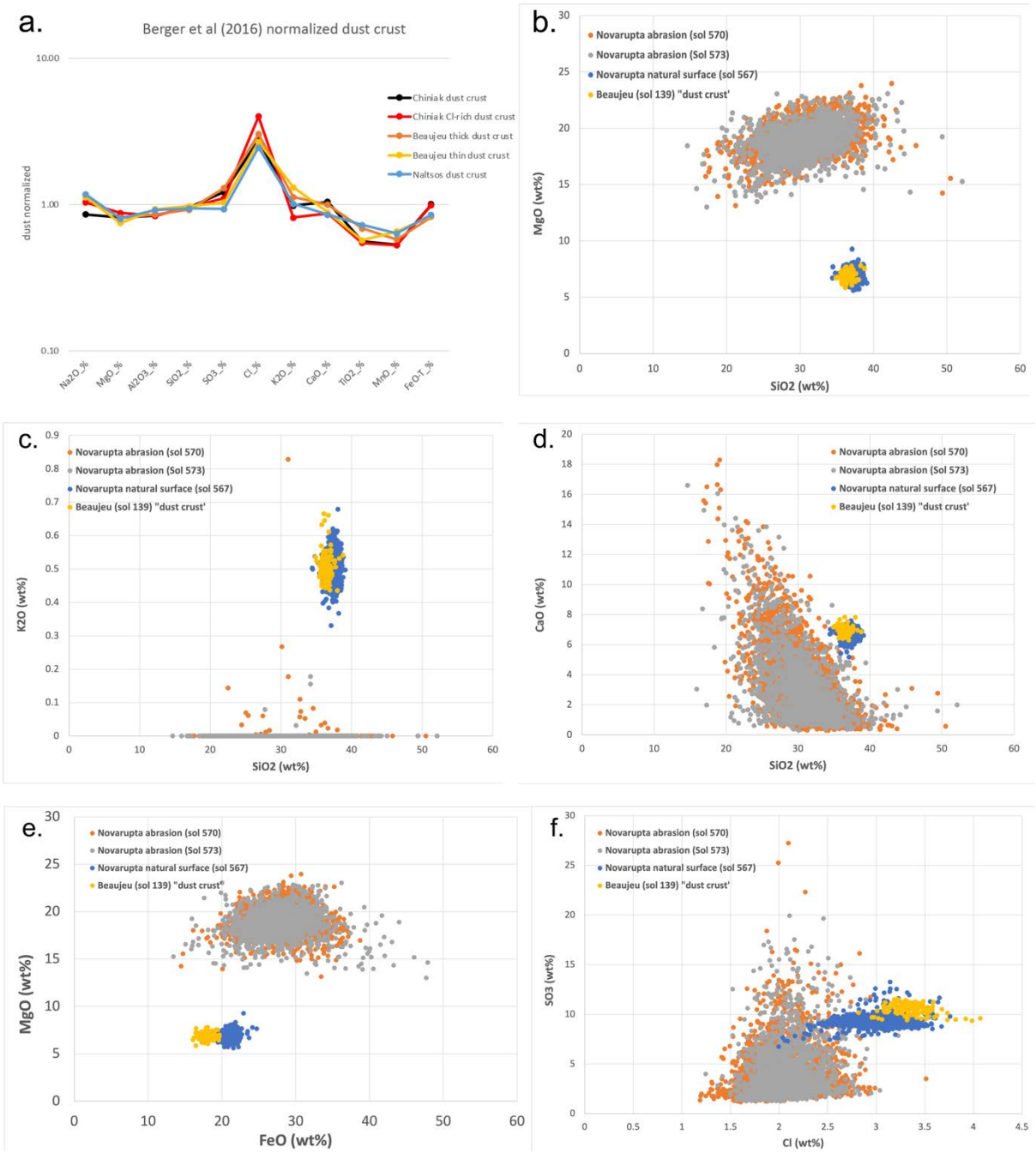

The *Novarupta1* natural surface is strikingly different from the underlying *Novarupta2* rock (**Figure 17**). Texturally, the crust is chemically much more homogeneous than the rock, shows none of its layered structure, lacks its abundant grains of chromite, and has a significantly different composition (**Figures 14d, 16d**). Compared to the underlying rock, the dust crust is significantly enriched in Al_2O_3, K_2O, Na_2O, and ZnO, and significantly depleted in MgO which leads to a much lower Mg-number (**Figure 17b, e; Tables 1, 2)**. The crust and underlying rock are also distinct in some element ratios, like Ca/Si and Cl/SO_3 (**Figures 17d, f**). The crust appears to have derived little or no chemical signatures from the underlying rock.

PIXL Micro-Context Camera (MCC) images of the *Novarupta2* abrasion patch (**Figure 18**) show more of the abrasion area than the XRF scans (**Figure 12**). The MCC image of NIR-G-B (**Figure 18b**), analogous to WATSON visible RGB images, shows that the chromite-ilmenite layers are relatively red (higher NIR reflectance) and the layers richer in olivine (and its alteration products) are relatively green. The difference between these layer types is emphasized in the NIR/G ratio image, **Figure 18c.** In NIR/G images, Fe^{3+}-bearing minerals tend to have high values, and Fe^{2+}-bearing phases tend to have low values. These relationships can be quantified in a graph of UV, G, & NIR reflectances, **Figure 18d**.

Figure 18 | **PIXL MCC data for the *Novarupta2* abrasion of sol 570**. **(a)** Raw green image, grayscale of a portion of the *Novarupta2* abrasion, showing the location of the PIXL scan (**Figures 12, 14**). **(b)** MCC false color of abrasion area (Red = MCC Near-IR; Green = MCC Green; Blue = MCC Blue), flat-fielded and enhanced. Note that the layers rich in chromite & magnetite appear red, and layers rich in olivine (and alteration products) appear greenish. **(c)** MCC ratio image of Near-IR/Green reflectances. **(d)** Graph of MCC reflectance ratios.

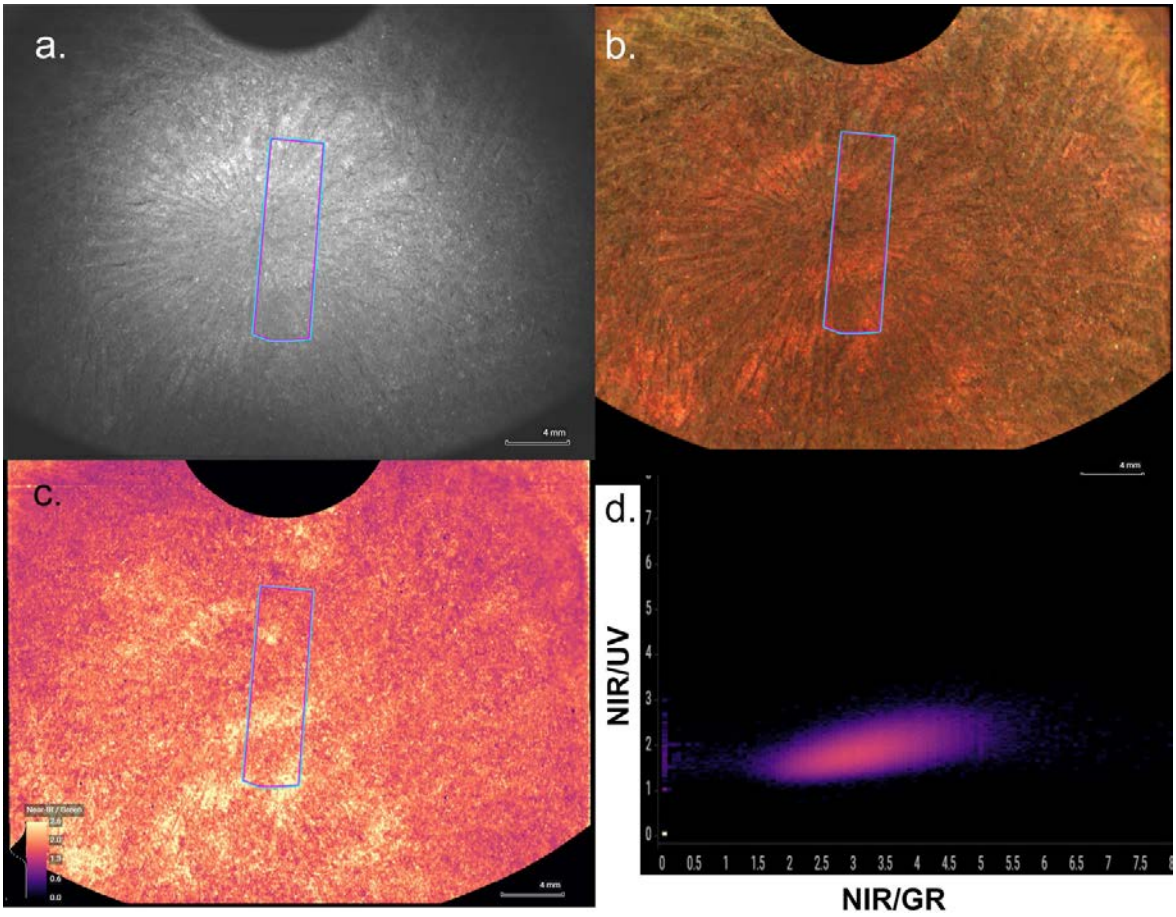

PIXL MCC images of the *Novarupta1* natural surface (**Figure 19**) show that the PIXL map area (**Figure 12, 16**) is on a relatively dark portion of the surface. The PIXL map was, in fact, targeted on an area where bright-toned dust was cleared away by SCAM-LIBS shots. Within the PIXL map area, relatively brighter spots in the NIR/G image (**Figure 19c**) and dark in the NIR-G-B image (**Figure 19b**), may represent places where the underlying *Novarupta* rock is exposed. Note that maximum NIR/GR values on **Figure 19d** are far higher than that of the abraded surface, **Figure 18d**; this difference arises from the high NIR/GR value for the windblown dust outside the PIXL map area.

Figure 19 | **PIXL MCC data for the *Novarupta1* natural surface sol 567**. **(a)** Raw grayscale RGB image of the *Novarupta1* site. **(b)** MCC false color of abrasion area (Red = MCC Near-IR; Green = MCC Green; Blue = MCC Blue), flat-fielded and enhanced. Shows the location of the PIXL scan (**Figure 12, 16**). **(c)** MCC ratio image of Near-IR/Green reflectances. Dust is very bright. **(d)** Graph of MCC reflectance ratios. Note that the NIR/GR scale is far larger than for the abraded surface (**Figure 18d**).

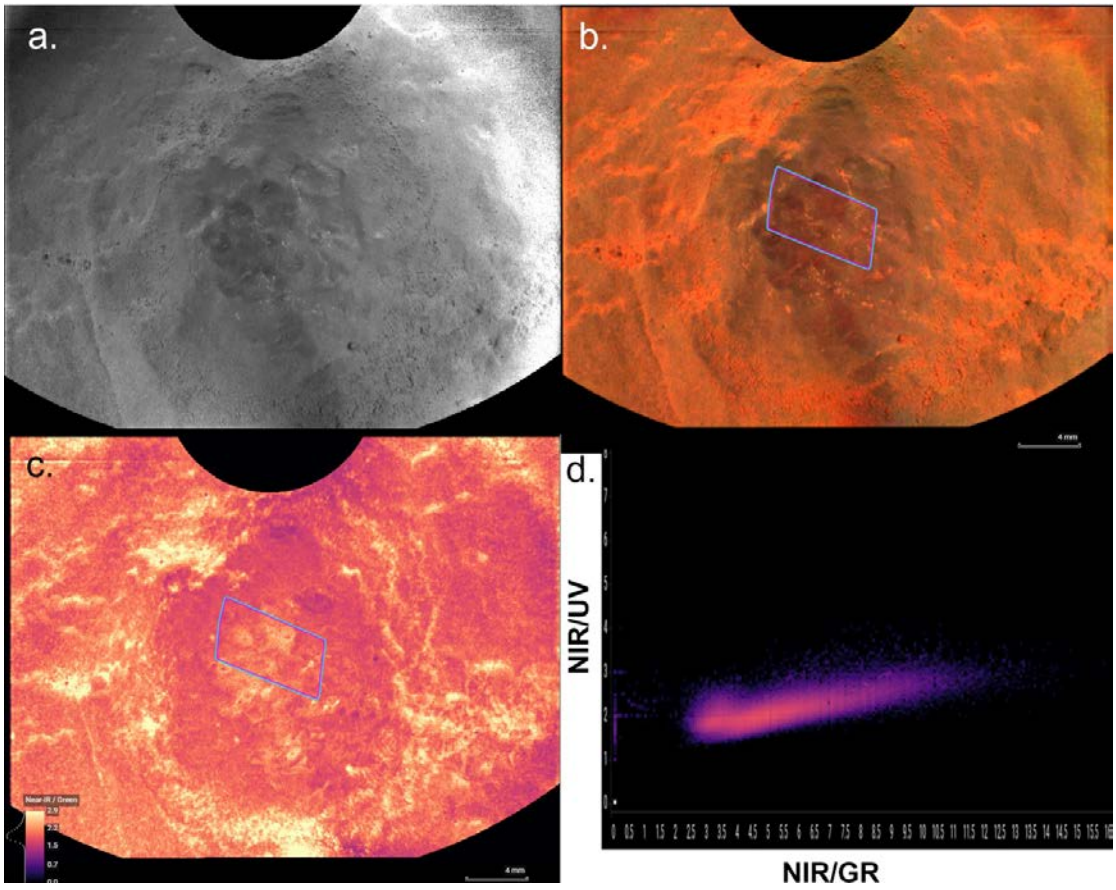

Mineralogy and Organics-SHERLOC

SHERLOC DUV Raman and fluorescence spectra were obtained from two different areas of the abraded patch on sols 570 and 573, respectively. The scans included one HDR scan (7x7 mm, 100 points, 780 µm spacing, 500 pulses per point), two survey scans (5x5 mm, 1296 points, 144 µm spacing, 15 pulses per point) and two detailed scans (1x1 mm, 100 points, 144 µm spacing, 500 pulses per point).

The Raman spectra from scans on sol 570 and 573 contain peaks that can be assigned to carbonates (1093 cm^{-1}), sulfates (~1019 cm^{-1}, no hydration feature detected) and possible phosphate (980 cm^{-1}) (**Figure 20** and **Table 3**). The fluorescence signals are dominated by a relatively weak fluorescence feature at 340 nm, which was only detected in a few pixels and is consistent with a double ring aromatic (**Figure 20**). The low fluorescence signal and the absence of organic signals in the Raman spectra suggest that any organic compounds present are in generally low abundance. No correlation is evident between spectral features and textures in the abrasion patch.

SHERLOC mineral identifications are shown in **Table 3**.

Table 3 | SHERLOC Raman spectra mineral ID.

Sample	Certain	Possible (not confirmed)	We looked for these, but cannot find them
Novarupta	Carbonate Sulfate (possible anhydrite)	Phosphate	-

Figure 20 | **Sol 573 SHERLOC fluorescence and Raman spectral results for *Novarupta.* (a)** Colorized ACI image of the *Novarupta* abraded patch; blue rectangle indicates the detailed scan area and white circle indicates regions of interest (ROIs) correlating to the fluorescence data presented in panels **b** and **c**. **(b)** Detailed scan map showing the possible presence of organics. Upper panel shows an RGB map indicating the main regions of fluorescence. The lower panel is blank for this abrasion patch because no Raman features have been identified that would indicate the presence of organic materials. **(c)** Fluorescence spectra. The upper panel shows the average fluorescence spectrum for the whole area of analysis and the lower panel includes spectra from selected fluorescence ROI (see **a** and **b**). **(d)** Map showing the results of the Raman detail scan. The grid of open red circles indicates the points analyzed (cf. Panel **a**). The blue, purple and red points indicate presence of different minerals. The right panel includes Raman spectra from the detail scan. The upper spectrum is the median of the whole scan area. The other three spectra are medians of the blue, purple, and red points.

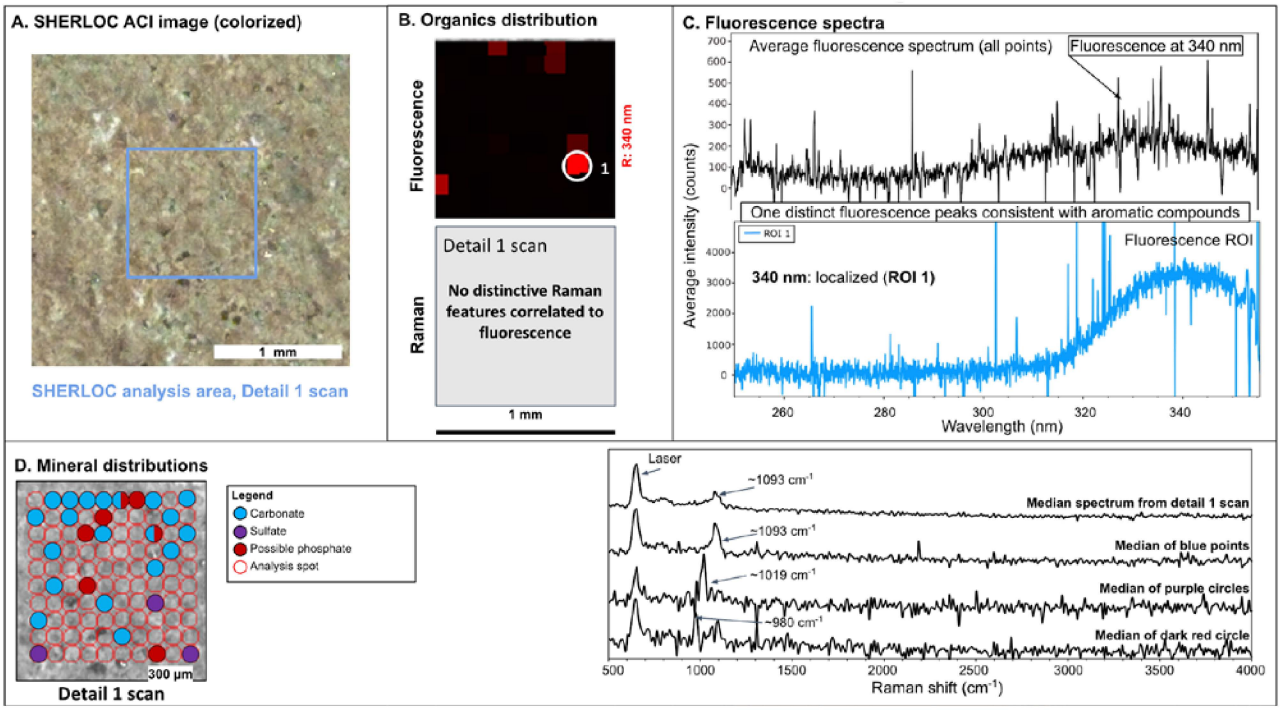

Elemental Geochemistry and Mineralogy – SuperCam.

SuperCam LIBS observations of targets at *Amalik* show that the rocks are compositionally heterogeneous on the scale of RMI images (**Figure 6**) and LIBS raster spacing (generally a few mm; **Figure 21**). The compositional spread at *Amalik* falls within the range observed previously on the Jezero delta front; the variance is greater than the fine-grained rocks at *Wildcat Ridge*, and smaller than the compositional range at *Skinner Ridge* due to the absence of points enriched in FeOT+MgO and depleted in SiO_2 and Al_2O_3 (i.e., *Wildcat Ridge* is comparatively richer in Mg,Fe sulfates) The compositions of individual LIBS spots on the natural surfaces and the abrasion patch are consistent with a possible mixture of olivine, pyroxene and feldspar (though the latter two minerals were not detected by PIXL), with additional phases such as serpentine and other phases produced by the alteration of primary igneous minerals (**Figures 21, 22**). The compositional diversity of spots analyzed on the abraded patch *Novarupta* is representative of the overall compositional diversity of the *Amalik* outcrop (**Figure 22**). Between 33% and 50% of the points analyzed by LIBS on *Novarupta* abraded patch (**Figure 6**) have a total oxide content between 66 and 85 wt%, indicating the presence of elements that are not quantified

by SuperCam such as H, O, C, S and Cl. The natural surfaces, particularly in points on shiny patches illustrated in **Figure 6**, also contain low total oxide contents. These include all points on the shiny patch of target *Novarupta* analyzed on Sol 567 before abrasion, 90% of the points on the shiny natural surface of the target *Swikshak*, 60% of the points on the target *Walatka* and 50% of the points on the natural surface targets *Chiniak* (Figure 6) and *Kelez*. These compositional and visual features of the shiny patches (**Figure 6**) indicated the presence of extensive surface coatings that are enriched in CaO, depleted in MgO+FeOT (**Figure 22**), and, by comparison with PIXL natural surface data, rich in S and Cl undetected by LIBS. All analyzed points on natural and abraded surfaces presented evidence of hydration, but points on the abraded patch exhibit a lower hydrogen ICA score (Clegg et al., 2017) (1.4±0.2, N=9) relative to the points on the coatings (2.0 ± 0.3, N=10), supporting more pronounced hydration underneath the coatings.

Figure 21| SuperCam LIBS major element oxide (MOC) analyses of *Amalik* rocks. Solid solution fields for olivine, pyroxene, and feldspar compositions are included. Black spots show the delta rocks analyzed from Sols 420-588.

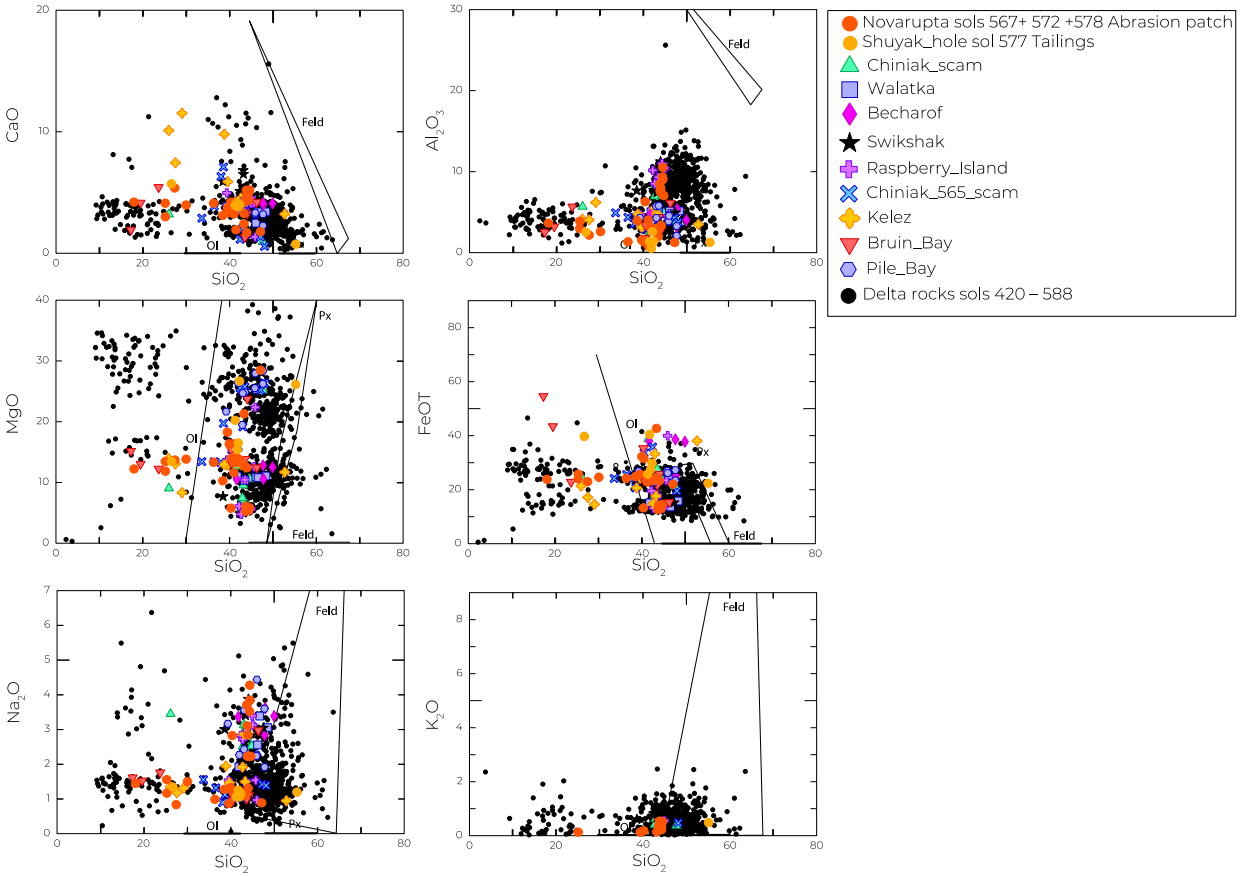

Figure 22| Molar compositions of the points in the LIBS rasters of *Amalik* from Sols 558, 561, 563, 565-567, 572, 577 and 578 compared to various minerals and on-board calibration standards. Analyzed points are shown by the yellow, orange, red, fuchsia, dark blue and purple circles. Purple and fuchsia circles show points analyzed on the abraded patch *Novarupta* from sols 572 and 578. Dark blue and dark and bright red circles, respectively, show the natural surfaces of *Novarupta* target from Sol 567 and *Chiniak* target from Sol 558 and 565, respectively. Dark and light orange circles, respectively, show the natural surfaces of *Swikshak* target from Sol 563 and *Walatka* target from Sol 561, respectively. Lemon yellow circles show the natural target *Raspberry_Island* analyzed on Sol 565. Marigold circles show the composition of the tailings from *Shuyak* drillhole analyzed on Sol 577. Turquoise circle surrounds the points analyzed on the shiny surface coatings. The legend presents a range of standards from igneous calibration targets (Ca-pyroxene, pyroxene, olivine) to other minerals (calcite, ankerite, siderite, serpentine, gypsum). The green cloud shows all data points acquired up to Sol 588.

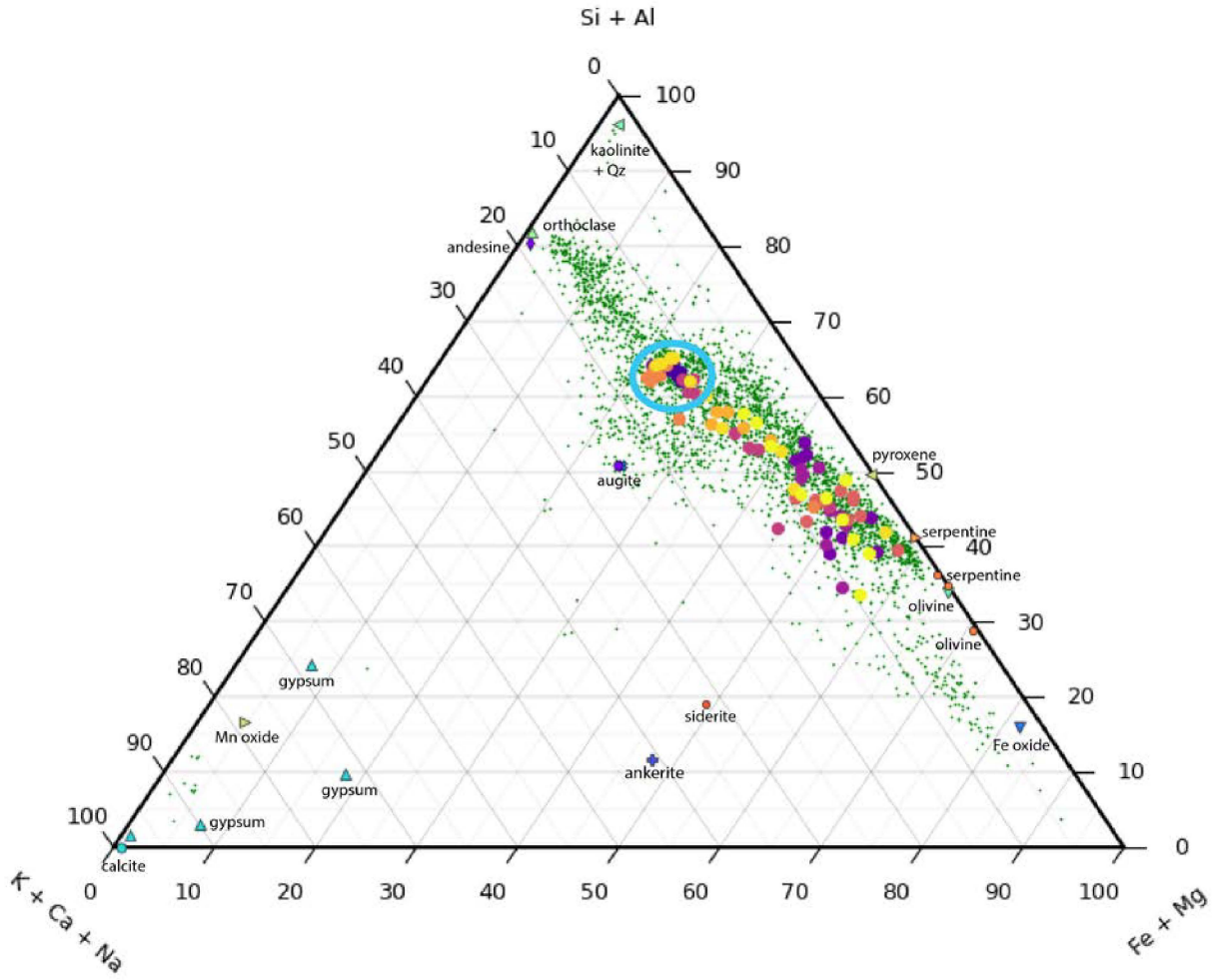

SuperCam VISIR rasters on the natural and abraded surface targets and tailings from the coring activity at *Enchanted Lake* (**Figure 23**) reveal the presence of compositionally diverse materials, hydration, clay minerals and coatings. The SCAM VISIR technique is highly sensitive to hydrated minerals, so the signatures of hydration are present in the spectra even when these minerals are a minor proportion of the rock. Red slope in the 1.3-1.8 µm range in **Figure 23** is consistent with the presence of ferrous phyllosilicates or olivine. **Figure 23** also shows the absorption bands that indicate the presence of hydrated minerals. The main signals of hydration, indicated by grey bars, are present at 1.94 µm and 1.42 µm in abraded targets. The band at 1.9 µm and the band centered at 2.33 µm are

consistent with a magnesium phyllosilicate, likely a serpentine species. The spectrum in the visible range is flat relative to the spectra of other delta front units. This suggests less overall oxidation, except for the reddish material exposed in the *Bruin Bay* fractured rock. The signature of the purplish rock coating on *Novarupta* unabraded surface is like the VISIR signatures of the purple and brown coatings observed on the crater floor. These coatings exhibit weaker hydration features at 1.42 and 1.94 µm relative to the abraded rock, in keeping with the lower hydrogen ICA scores from LIBS analyses of the coatings. The thin grey bar centered at 0.43 µm indicates absorption that is attributed to ferric sulfate minerals, although this identification awaits confirmation. The VISIR spectra are greatly affected by the grain size, contributing to the differences in the tailings and rock spectra. Based on the observed hydration, compositional diversity, spectral properties and the presence of phases that likely originated during aqueous alteration, the *Shuyak* and *Mageik* cores can be interpreted as a coarse mudstone that was subaqueously deposited and altered.

Figure 23| Mean reflectance spectra of the SuperCam VISIR rasters at *Amalik*. These spectra show the natural surface of the *Hook Glacier* target observed on Sol 424, the abraded surface of *Novarupta* target from Sol 572 and tailings created by the coring of *Shuyak*. Also shown is the spectrum of the coating around the abraded surface at *Novarupta* analyzed on Sol 567. Lighter spectrum lines near 2 µm indicate the spectral range possibly affected by the CO_2 absorption features that could remain after the atmospheric correction. The UV region was smoothed using a savgol filter. Note that owing to temperature sensitivities in the IRS instrument, the calibration is still uncertain for wavelength longer than ~2.55 µm. The absorption centers are indicated with arrows and their positions at 1.94 and 2.33 µm point towards the presence of hydrated magnesium phyllosilicates, likely serpentine. Other arrows indicate additional absorption centers attributed to hydrated phases.

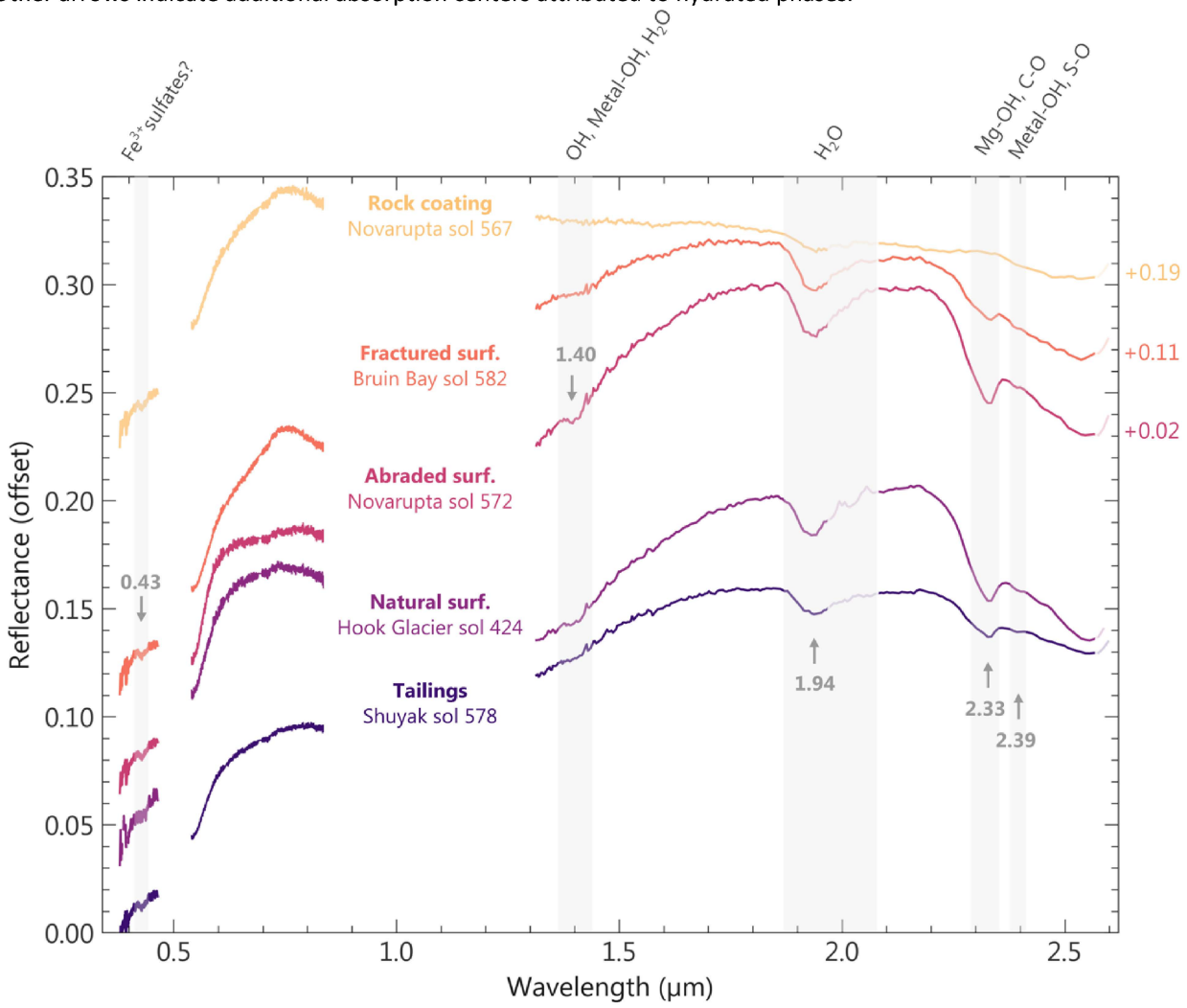

Subsurface Structure

The subsurface structure of the delta front near the *Amalik* outcrop south of *Cape Nukshak* is revealed by RIMFAX radargrams. The radargram was acquired on sol 556 during a traverse headed from east to west, then south to north, then east to west (see red line in **Figure 24a** ending near the area labeled *Amalik*). *Amalik* and adjacent units are in general horizontally stratified as seen in both outcrop and in the subsurface as illustrated by RIMFAX radargrams (**Figure 24b**). The *Amalik* samples were acquired near the base delta unconformity capping the underlying *Séítah* Formation strata, at depth -2529 to -2530 m. Depths have been calculated from two-way travel times using 0.10 m/ns.

Figure 24 | Geological context and RIMFAX-derived subsurface stratigraphy of the delta front south of *Cape Nukshak*. (a) Location of the *Amalik* outcrop, from which the samples *Shuyak* and *Mageik* were collected, within the delta front. The red line indicates the traverse on sol 556 during which RIMFAX radargrams were collected. **(b)** Radargram of the three-leg traverse acquired on sol 556 ending near the *Amalik* outcrop (yellow star). The radargram shows strata with largely horizontal geometries above the *Séítah* Fm.

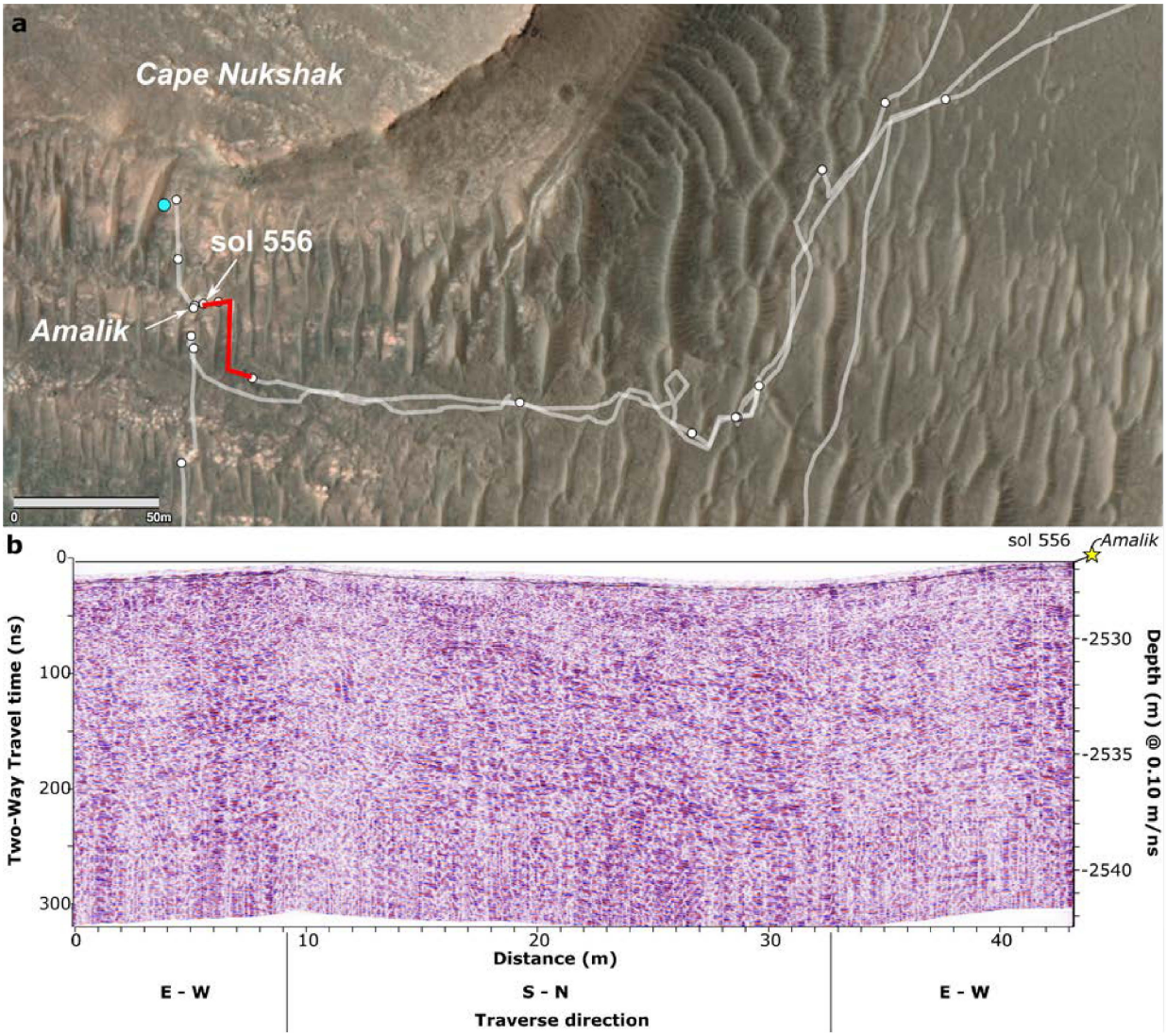

Core orientation

At the time of drilling and 6.8-cm pre-drilling WATSON imaging, the rover, Coring Drill, and WATSON had the following characteristics:

1. Rover orientation quaternion just after drilling but before unloading the stabilizers (transferring from RMECH to SITE frame): **bQll1** = (0.08126, 0.03658, 0.01394, -0.99592)
2. Coring Drill orientation quaternion just after drilling but before unloading the stabilizers (transferring from CORING DRILL to RMECH frame): **cdQb** = (0.73384, 0.22246, -0.58608, 0.26174)
3. Rover orientation quaternion at time of acquisition of WATSON image SIF_0570_0717551784_765FDR_N0290000SRLC00750_0000LMJ01: (transferring from RMECH to SITE frame): **bQll2** = (0.08124, 0.03472, 0.0139, -0.99599)
4. WATSON orientation quaternion at time of acquisition of WATSON image SIF_0570_0717551784_765FDR_N0290000SRLC00750_0000LMJ01: (transferring from WATSON to RMECH frame): **wQb** = (0.73651, 0.22871, -0.58195, 0.25802)

Items 1 and 2 give a coring drill pointing vector estimate of

hade = 16.72°
azimuth = **219.48°**

Items 3 and 4 give an estimate of the angle between the WATSON y-axis and the Core y-axis projected into the WATSON image plane (**Figure 25**) of:

core roll, α = **259.41°**

Figure 25 | Core orientation. 6.8-cm standoff WATSON image of *Shuyak* core target on sol 570. WATSON image SIF_0570_0717551784_765FDR_N0290000SRLC00750_0000LMJ01. Image scale is 32.6 µm pixel^{-1}. Orientation compass gives WATSON frame (**wx**, **wy**, **wz**). Core roll is α = 259.41°. Projection of Martian geographic north onto WATSON image plane is noted (clockwise angle of 38.80° from **wy**).

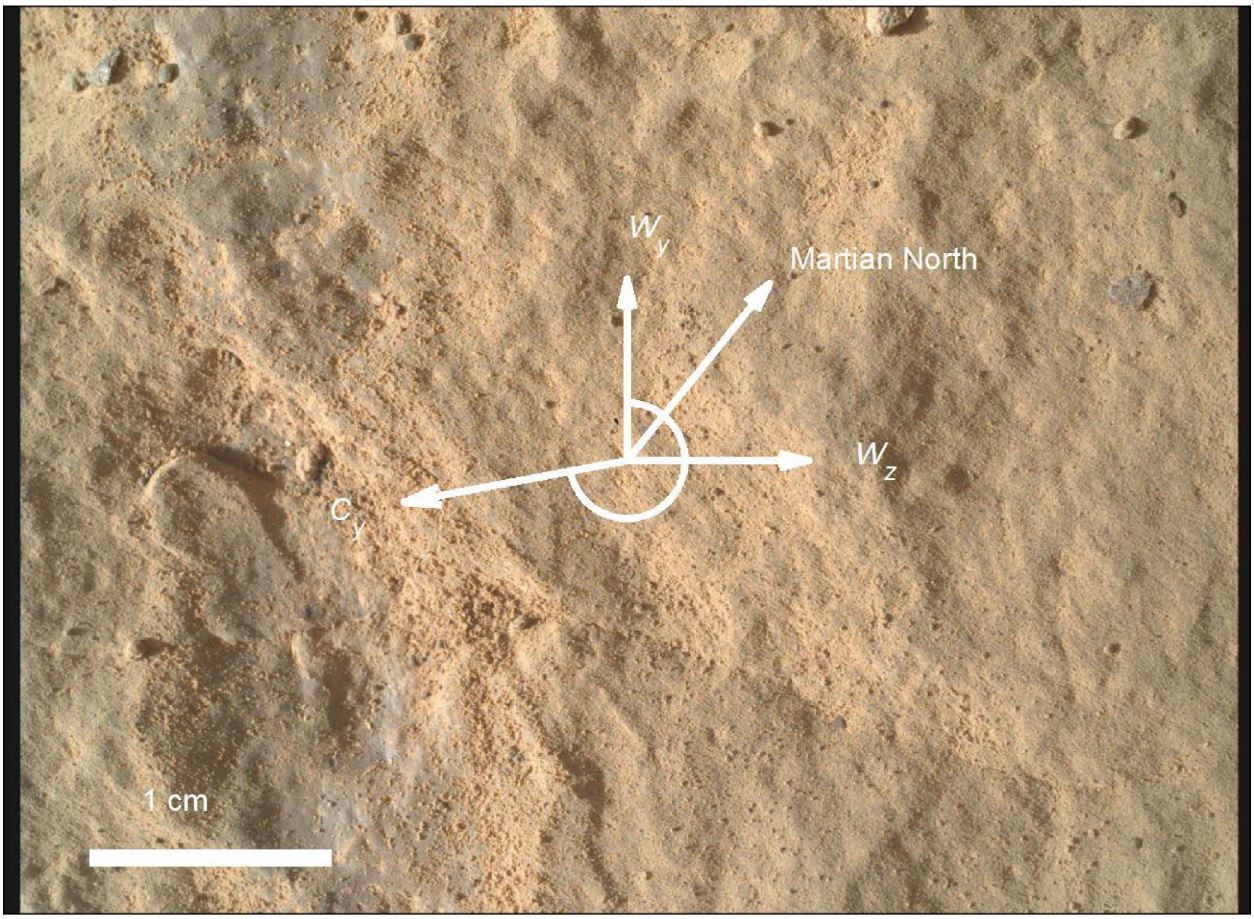

Preliminary Scientific Assessment

Synthetic sample description and preliminary interpretation

Sample type: **Fine-grained, well-sorted sedimentary rock; an olivine-bearing coarse mudstone.**

1. **Relationship with surrounding rocks**
    a. *Shuyak* and *Mageik* were obtained from a position relatively low in the accessible stratigraphy of Jezero Delta within the *Amalik* member, roughly 1-2 m above the lowest exposed delta outcrop in the *Cape Nukshak* region, *Kaguyyak*, within the *Shenandoah* formation.
    b. Based on its appearance and concordance with surrounding outcrops in overall color and composition, the *Amalik* outcrop and its paired cores are interpreted to be an in-place portion of *the Amalik* member.
2. **Texture and fabric**
    a. Grain size: <0.02–0.094 mm
    b. Rock fabric (natural surface): the exposed surface is fractured, dusty, and light toned. Individual grains are not commonly visible on the surfaces. Abundant coating.
    c. Rock fabric (abrasion patch): grains are silt sized (50 μm), with a unimodal size distribution and are typically subrounded; the largest observed grains do not exceed 100 μm. The grain size distribution is well sorted.
    d. The rock appears to be a well sorted, coarse mudstone.
3. **Mineralogy and chemistry**
    a. Minerals present: the rock has compositional heterogeneity among the clasts and the matrix. Igneous minerals were detected in the clasts, primarily olivine, with very little, if any, pyroxene or feldspar. Minor phase detections include chromite, ilmenite, apatite, and zircon or baddeleyite; heavy minerals appear to be co-located and enriched in individual layers. Other detections include carbonates and sulfates.
    b. The natural surface is chemically and texturally different from the interior; it is homogeneous, enriched in Al_2O_3, K_2O, Na_2O, SO3, Cl, and ZnO, and significantly depleted in MgO. It is a coating less than 1 mm thick.
    c. The rock appears to be a coarse mudstone, rich in olivine and its alteration products (e.g., serpentine).
4. **Alteration/secondary characteristics**
    a. Evidence for hydration and alteration(s) exists as aqueous alteration products of olivine (e.g., serpentine), phyllosilicates, dolomite and silica.
    b. Secondary phases may include hydrated minerals and phyllosilicates, likely including a serpentine species, Ca sulfate and dolomitic carbonate.

Returned Sample Science Considerations

Since before landing, the delta stratigraphy and the western Jezero delta front have been the primary astrobiologically relevant mission sampling targets, i.e., sediments deposited into an ancient lake on Mars. Jezero Lake was likely present during the valley network-forming late Noachian to early Hesperian period of early Mars, and therefore delta sedimentary rock samples provide a potential record of the environmental conditions during that period. On Earth, early deltaic bottomset deposits often contain relatively fine-grained, organic-rich material, and can preserve ancient biosignatures. Coarser-grained (> mm) deltaic sedimentary units contain detritus that reveal the catchment source lithology and can be used to constrain delta deposition timing. Collectively, a set of coarse-grained *and* fine-grained sedimentary rock samples collected from the delta front in proximity provides a sample suite for addressing key goals of MSR.

The *Shuyak* and *Mageik* samples are the second set of fine-grained (~50 μm) sedimentary rock samples collected by the Perseverance Rover. These samples partially fulfill the objective of collecting 2 paired samples of fine-grained material with biosignature preservation potential prior to placement of the contingency cache. The *Amalik* outcrop was chosen for sampling because it possessed several desired sample characteristics for a fine-grained sedimentary rock including: (1) grains <100 μm; (2) siliciclastic and carbonate components; (3) a low delta/stratigraphic position; (4) deposition associated with the delta; (5) detrital grains appear aqueously altered.

Compared to the previously collected sandstone cores from *Skinner Ridge*, *Shuyak* and *Mageik* are substantially finer grained and richer in olivine. Compared to the coarse mudstones from *Wildcat Ridge*, these cores have far less sulfate and possibly-organic-induced fluorescence. *Shuyak* and *Mageik* are also thought to be stratigraphically lower than these other cores.

Amalik is a fine-grained sedimentary rock that was likely deposited in a sub-aqueous environment within a lacustrine basin. Thus, the *Shuyak* and *Mageik* cores record paleoenvironmental and paleoclimatic conditions of a formerly habitable environment. Laboratory-based investigations of these samples would enable reconstruction of chemical conditions in a subaqueous paleoenvironment, and interpretation of a sedimentary system in which aqueous processes occurred in Mars's past. These analyses will also enable characterization of the distribution and chemical diversity of organic molecules and the search for morphological and chemical biosignatures. The samples from *Amalik* can be used to address multiple science questions and objectives of the MSR sampling campaign:

Geochronology: The observed mineralogy and fine grain sizes observed in *Amalik* are not well-suited for existing methods of isotopic geochronology. PIXL detected a single point with elevated zirconium which may be indicative of the presence of a larger zircon grain in the subsurface. If so, igneous phase geochronology may provide an upper bound of timing of delta sediment deposition. It may also be possible for existing methods of isotopic geochronology to be applied (or developed and/or refined) to constrain the timing of any cement or salt precipitation, if present. In addition to quantifying the timing of late-stage aqueous activity, such information would place a *lower* bound on the timing of sediment/delta deposition. Observations of stable cosmogenic nuclides (e.g., ^{3}He, ^{21}Ne, ^{36}Ar, ^{38}Ar) in bulk *Shuyak* and *Mageik* samples could quantify the material's integrated cosmic ray exposure duration, thereby helping to constrain the latest-stage erosional history of the delta and the most recent cosmic ray exposure of the rocks in this vicinity.

Paleomagnetism: The sedimentary lithologies of the *Shuyak*/*Mageik* cores may enable relative measurements of the paleointensity of the Martian dynamo. In combination with geochronology, this could constrain the timing of the martian paleomagnetic field to test the hypothesis that martian atmospheric loss was driven by the cessation of an early dynamo. The orientations of the samples (**Figure 25)**, combined with paleohorizontal indicators from the outcrop and sample, may enable measurements of the absolute paleodirection of the ancient field during or after deposition. This could constrain the dynamo's geometry, establish if the dynamo exhibited secular variation and polarity reversals, and constrain tectonic processes. Because the host rocks form the lowest sampled layer of the delta, these samples may provide the oldest sedimentary records of the dynamo obtainable from the delta. Paleomagnetic investigations would also constrain the aqueous and thermal alteration history of the samples and, by implication, the preservation state of any potential biosignatures.

Texture: A key component of understanding fine-grained sedimentary rocks and the diagenetic processes that have acted upon them, is the ability to distinguish between authigenic and allogenic minerals. The fine-grained nature of *Shuyak* and *Mageik* cores precludes making this distinction using Perseverance's in-situ instrumentation. Only returning samples for microscopic investigations would enable this level of understanding. This distinction is key to understanding what can be discerned about primary/catchment processes vs post-depositional processes experienced by these rocks.

Geochemistry: Elemental and mineralogical data from the *Novarupta* abrasion patch and the *Shuyak* borehole reveal an Fe- and Mg-rich rock. LIBS analyses are consistent with a possible mixture of olivine with minor pyroxene and feldspar, with additional secondary phases such as serpentine. Distinct planar concentrations of heavy minerals like chromite, ilmenite, and apatite suggest enrichment of these minor phases during sedimentary deposition. VISIR data is consistent with the presence of olivine and/or ferrous phyllosilicates and Mg-phyllosliicates and reveals a strong hydration signal. This is consistent with hydration of the *Novarupta* abrasion patch indicated from LIBS H scores. PIXL data confirms the presence of minimally altered olivine with intergrown alteration products and suggests the presence of carbonate (dolomite). SHERLOC Raman data is also consistent with the presence of carbonates. These chemical and mineralogical signatures are similar to those of the *Dourbes* abrasion patch and may indicate that *Amalik* consists of reworked *Séítah* material.

Purplish rock coatings, similar in appearance to those observed on Crater Floor rocks, are prevalent on the natural surfaces of the *Amalik* outcrop. These coatings are visually observed by RMI and chemically unique from the abraded patch. VISIR signatures of the coatings are consistent with those from Crater Floor rocks and are less hydrated then abraded surfaces. The presence of ferric sulfate is suggested by VISIR data but not yet confirmed. PIXL data suggests global dust, sulfates, and chlorine salts as components of the coating material.

Laboratory-based microscopic imaging and chemical mapping of the grains and grain boundaries at resolutions higher than Perseverance's in-situ instrumentation would enable distinction between authigenic, allogenic, and diagenetic solid phases. Chemical mapping at similarly high resolution can also determine whether organic compounds are preferentially distributed in and around particular solid phases (i.e., phyllosilicate grains). Subsequent high-resolution elemental and mineralogical analyses can also be used to link the component materials to either (1) geochemical conditions in the environment where *Amalik* was deposited or (2) the post-depositional diagenetic processes that acted upon the

sediments. The elemental composition and redox state of secondary phases may document paleoenvironmental geochemical conditions including temperature, redox state, and water/rock ratio.

Habitability and Biosignature potential: The *Shuyak* and *Mageik* cores were deposited in a subaqueous paleoenvironment that, due to the presence of liquid water, is interpreted as formerly habitable. Carbonates and phyllosilicates have a recognized biosignature preservation potential. SHERLOC fluorescence data from the *Novarupta* abrasion patch indicate a weak signal consistent with double-ring aromatic organic molecules. An organic signature is absent in Raman spectra. These observations suggest a low abundance of organic compounds in these rocks. Yet, these rocks possess characteristics suggestive of biosignature preservation potential. Therefore, laboratory based, high resolution microscopic mapping of the mineral and organic distribution in the cores, along with analyses of organics extracted from these cores, may still reveal a greater presence of organic material and provide more detailed information on the organic signals and any associations with solid phases. Analyses that characterize the compositional, structural, and isotopic diversity of organic compounds found to be present in the *Shuyak* and *Mageik* cores can also help distinguish possible organics produced by prebiotic or abiotic processes from organics delivered from space.

Due to the small mineral grain sizes, constraints on the environmental conditions during the deposition of *Amalik* require textural analyses, identification of the coexisting primary mineral phases, and chemical modeling. These analyses will test whether the fluids were acidic or circum-neutral, oxidizing or reducing, and whether and how the original minerals were altered during diagenesis. These constraints will help establish whether this formerly habitable environment was extreme (e.g., acidic or hypersaline) or more amenable to microbial life. In either case, sediments deposited in the Delta may have provided a habitat for active microorganisms and may have preserved microbial life that was present in the water column of Lake Jezero. There is a geochemical and mineralogical similarity of *Amalik* rocks to *Séítah* rocks and the team has previously noted that low-temperature hydrothermal, serpentinizing and carbonation reactions may have sustained microbial life, particularly chemoautotrophs/chemolithotrophs that have been suggested as likely inhabitants of Martian biotopes. Alteration of olivine bearing-sediments may provide an even more habitable environment relative to olivine-bearing igneous rocks due to the relatively higher porosity and permeability. As such, it is possible that organic materials and/or biosignatures have been preserved within some alteration phases within the *Amalik* outcrop. Cells and/or other organic materials could have been trapped in precipitated carbonates or phyllosilicates during lithification and diagenesis. Microscopic analyses of thin sections of the cores from *Amalik* could contain organic inclusions or even body fossils encapsulated within or preserved by these mineral phases detected in the *Novarupta* abrasion patch. Sample return and detailed analyses are required to search for these types of biosignatures.

References

Berger, J. A., Schmidt, M. E., Gellert, R., Campbell, J. L., King, P. L., Flemming, R. L., ... & Desouza, E. (2016). A global Mars dust composition refined by the Alpha-Particle X-ray Spectrometer in Gale Crater. *Geophysical Research Letters*, *43*(1), 67-75.

Clegg, S. M., Wiens, R. C., Anderson, R., Forni, O., Frydenvang, J., Lasue, J., ... & Maurice, S. (2017). Recalibration of the Mars Science Laboratory ChemCam instrument with an expanded geochemical database. *Spectrochimica Acta Part B: Atomic Spectroscopy*, *129*, 64-85

Lazar, O. R., Bohacs, K. M., Macquaker, J. H., Schieber, J., & Demko, T. M. (2015). Capturing Key Attributes of Fine-Grained Sedimentary Rocks In Outcrops, Cores, and Thin Sections: Nomenclature and Description GuidelinesMUDSTONES: NOMENCLATURE AND DESCRIPTION GUIDELINES. *Journal of Sedimentary Research*, *85*(3), 230-246.

Mangold, N., Schmidt, M. E., Fisk, M. R., Forni, O., McLennan, S. M., Ming, D. W., ... & Wiens, R. C. (2017). Classification scheme for sedimentary and igneous rocks in Gale crater, Mars. *Icarus*, *284*, 1-17.

Stack, K. M., Williams, N. R., Calef, F., Sun, V. Z., Williford, K. H., Farley, K. A., ... & Aileen Yingst, R. (2020). Photogeologic map of the perseverance rover field site in Jezero Crater constructed by the Mars 2020 Science Team. *Space Science Reviews*, *216*(8), 1-47.

INITIAL REPORT

M2020-579-17 *Mageik*

Sample Designation: M2020-579-17 *Mageik*

Date of Coring: 6-Oct-2022

Mars Time of Sample Core Sealing: 19:53 LMST, Sol 619, Ls 339.96

Latitude (N), Longitude (E), Elevation: 18.45068664˚, 77.40143554˚, -2526.292311 m

Campaign: Delta Front

Region of Interest: *Cape Nukshak*

Lithology: Fine-grained, well-sorted sedimentary rock likely deposited in a lacustrine setting; an olivine-bearing coarse mudstone. The rock primarily contains detrital olivine and aqueous alteration products of olivine (e.g., serpentine) plus minor salts. Minor phases detected may include chromite, ilmenite, apatite, and zircon/baddeleyite. No clear evidence of sand-sized pyroxene or feldspar was observed. The rock contains little, if any, evidence of sulfate minerals, and a possible/weak fluorescence signal potentially arising from aromatic organic compounds.

Estimated Volume Recovered: 10.4 cm^3

Coring Bit Number: 4

Core Orientation: hade = 26.11°; azimuth = 198.38°; core roll = 91.18°

Sample Serial Numbers: Tube SN184; Seal SN587; Ferrule SN030

ACA Temperature at Time of Sealing: 40^{o}C

Estimated Rover-Ambient Pressure and Temperature at Time of Sealing: 725 Pa, 225 K

Estimated Amount of Martian Atmosphere Headspace Gas: 0.63×10^{-6} mol

Anomalous Behavior: 40 sols between coring and sealing.

Abrasion Patch Name and Depth: *Novarupta*, 8 mm

January 15, 2023

D. L. Shuster, K. A. Farley, T. Bosak, A. D. Czaja, E. M. Hausrath, L. E. Mayhew, M. E. Minitti, S. Siljeström, J. I. Simon, K. M. Stack, A. Treiman, B. P. Weiss, B. V. Wogsland, M.-P. Zorzano, A.C. Allwood, H.E.F. Amundsen, F. J. Calef III, B.C. Clark III, D. Flannery, J.A. Hurowitz, T. Kizovski, A. Knight, L. Mandon, E. N. Mansbach, D.A.K. Pedersen, M.E. Schmidt, M.M. Tice, A. Udry, S. Van Bommel, K. Williford, and the Mars 2020 Team

Summary Description

This sample is paired with M2020-575-16 *Shuyak*. Only the core orientation for *Mageik* is described below. See the Initial Report for M2020-575-16 *Shuyak* for sample details.

Core orientation

At the time of drilling and 7.1-cm pre-drilling WATSON imaging, the rover, Coring Drill, and WATSON had the following characteristics:

1. Rover orientation quaternion just after drilling but before unloading the stabilizers (transferring from RMECH to SITE frame): **bQll1** = (0.08125, 0.03583, 0.01391, -0.99595)
2. Coring Drill orientation quaternion just after drilling but before unloading the stabilizers (transferring from CORING DRILL to RMECH frame): **cdQb** = (0.04047, -0.82581, -0.05719, -0.55958)
3. Rover orientation quaternion at time of acquisition of WATSON image SIF_0577_0718170754_562FDR_N0290000SRLC00701_0000LMJ01: (transferring from RMECH to SITE frame): **bQll2** = (0.08123, 0.03403, 0.01377, -0.99602)
4. WATSON orientation quaternion at time of acquisition of WATSON image SIF_0577_0718170754_562FDR_N0290000SRLC00701_0000LMJ01: (transferring from WATSON to RMECH frame): **wQb** = (0.03947, -0.8272, -0.05783, -0.55752)

Items 1 and 2 give a coring drill pointing vector estimate of

hade = 26.11°
azimuth = **198.38°**

Items 3 and 4 give an estimate of the angle between the WATSON y-axis and the Core y-axis projected into the WATSON image plane (**Figure 1**):

core roll, α = **91.18°**

Figure 1 | Core orientation. 7.1-cm standoff WATSON image of *Mageik* core target on sol 577. WATSON image SIF_0577_0718170754_562FDR_N0290000SRLC00701_0000LMJ01. Image scale is 32.6 µm pixel^{-1}. Orientation compass gives WATSON frame (**wx**, **wy**, **wz**). Core roll is α = 91.18°. Projection of Martian geographic north onto WATSON image plane is noted (clockwise angle of 250.81° from **wy**).

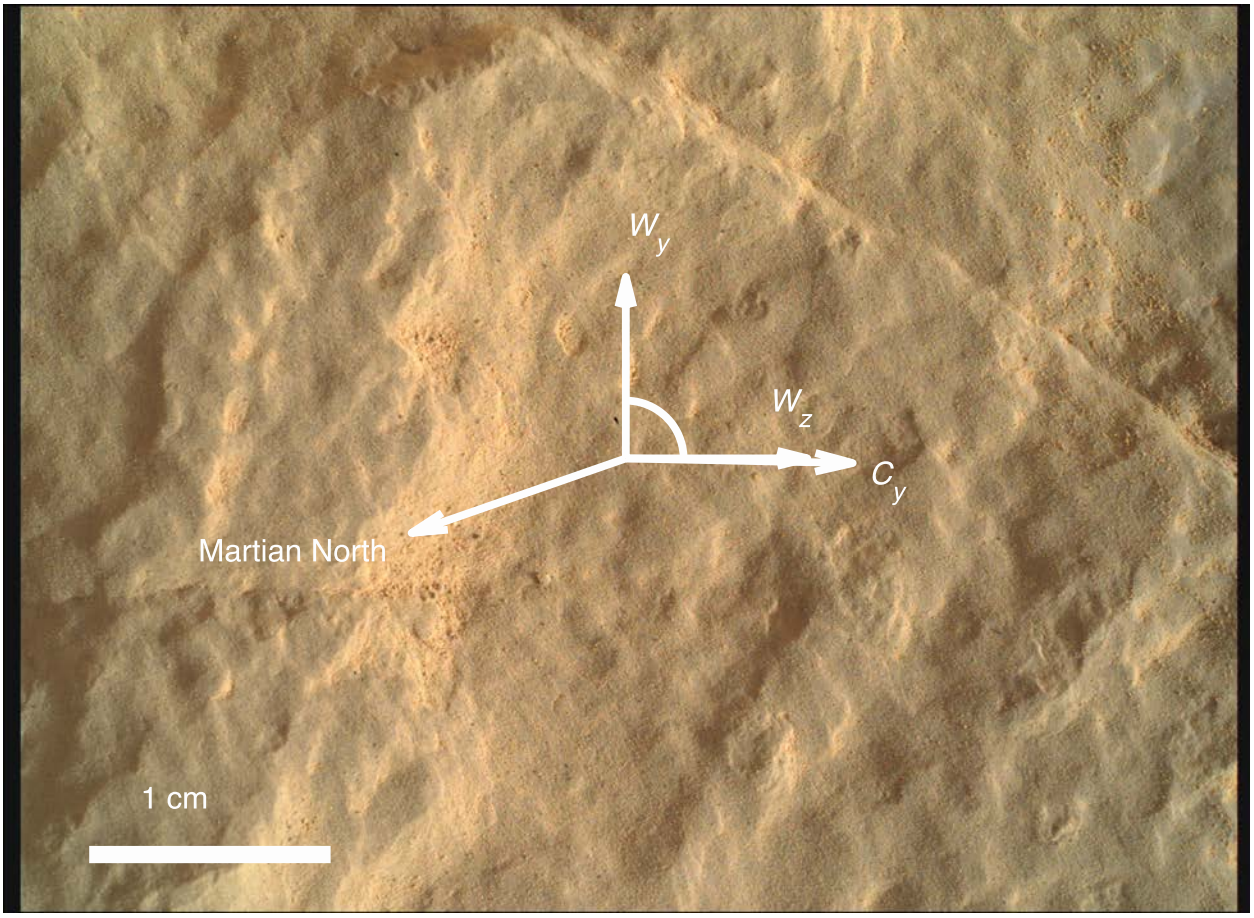

INITIAL REPORT

M2020-586-18 WB3

Witness Tube Designation: M2020-586-18 WB3

Date of Initial Witness Exposure: 10-October-2022

Date of Activation: 10-October-2022

Date of Sealing: 12-Octber-2022

Mars Time of Witness Tube Sealing: 19:16:40 LMST, Sol 586, Ls 321.03

Latitude (N), Longitude (E), Elevation: 18.45069082, 77.40142933, -2526.326886

Sample Serial Numbers: Tube SN188; Seal SN153; Ferrule SN073

ACA Temperature at Time of Sealing: 40° C

Estimated Rover-Ambient Pressure and Temperature at Time of Sealing: 722 Pa, 226 K

Estimated Amount of Martian Atmosphere Headspace Gas: 2.31×10^{-6} mol

Anomalous Behavior: Faults during acquisition and sealing

August 15, 2022

S. Siljeström, M.-P. Zorzano, Y. Goreva, K. A. Farley, R. Moeller and the Mars 2020 Team

Summary Description

Perseverance carries 5 Witness Tube Assemblies (WTA's) which will be used to document the evolving rover contamination environment (organic, inorganic and particulates) over the course of the mission (Moeller et al., 2020). Four of these "witness tubes" are identical and located in sheaths just like sample tubes within the ACA (ACA WTA). The main purpose of the ACA WTAs is to record potential contaminants from the rover to which the rock cores might have been exposed during the several hours of handling needed to acquire and process a sample. The four witness tubes are protected from particle accumulation by fluid mechanical particle barriers and are isolated from volatile organic molecules by a tortuous path of gettering surfaces (Moeller et al., 2020) until activation. To activate the WTA the seal is punctured using the volume probe inside the ACA. Thereafter, they are processed in the same way as the rock cores except there is no contact between drill bit and rock.

To capture the evolving contamination throughout the whole mission, it was decided to process two ACA WTAs early in the mission when the largest outgassing from the rover is expected. The earliest opportunity, considering engineering constraints, came during the Delta Campaign.

WB3, the second of the ACA WTA to be processed, was processed beside the outcrop called *Amalik* at *Cape Nukshak* after sampling of *Shuyak* and *Mageik* (Figure 1). It was processed on sols 584-586 after coring of *Mageik* on sol 579, cleaning of the drill chuck, and abrade bit pick-up on sol 581. WB3 was activated on sol 584, and simulated motions of coring occurred while the corer was positioned directly over the *Novarupta* abrasion patch (**Figure 1)**.

During the processing of the WTA, two faults occurred. On sol 584 there was a fault during the simulated coring which resulted in only 5 of the normally 7 spindle/percuss motions being performed, and no percuss-to-ingest motion was executed. While anomaly recovery was being undertaken, the tube remained in the corer and exposed to the Martian environment about 10 times longer than normal WTA/sample exposure time. A second fault occurred after the sealing of the tube on sol 586, and left the hermetically sealed WTA sitting in the sealing station at an elevated temperature (up to 40° C) until sol 591.

Operations

1. This witness tube was activated by the volume probe inside ACA on 14:39:29 LMST, sol 584.

2. It was then moved through a simulated sampling path (with fewer than normal percuss motions and no PTI), and remained exposed for two sols during anomaly recovery.

3. It was sealed at 19:16:40 LMST, sol 586.

4. It was moved from sealing station and stored in ACA at 17:31:14 LMST, sol 591.

Figure 1 | **Navcam left sol 579 mosaic showing *Amalik* with abrasion patch *Novarupta* and drill holes of *Shuyak* and *Mageik*.** During simulated coring the drill was positioned directly above the white circle.

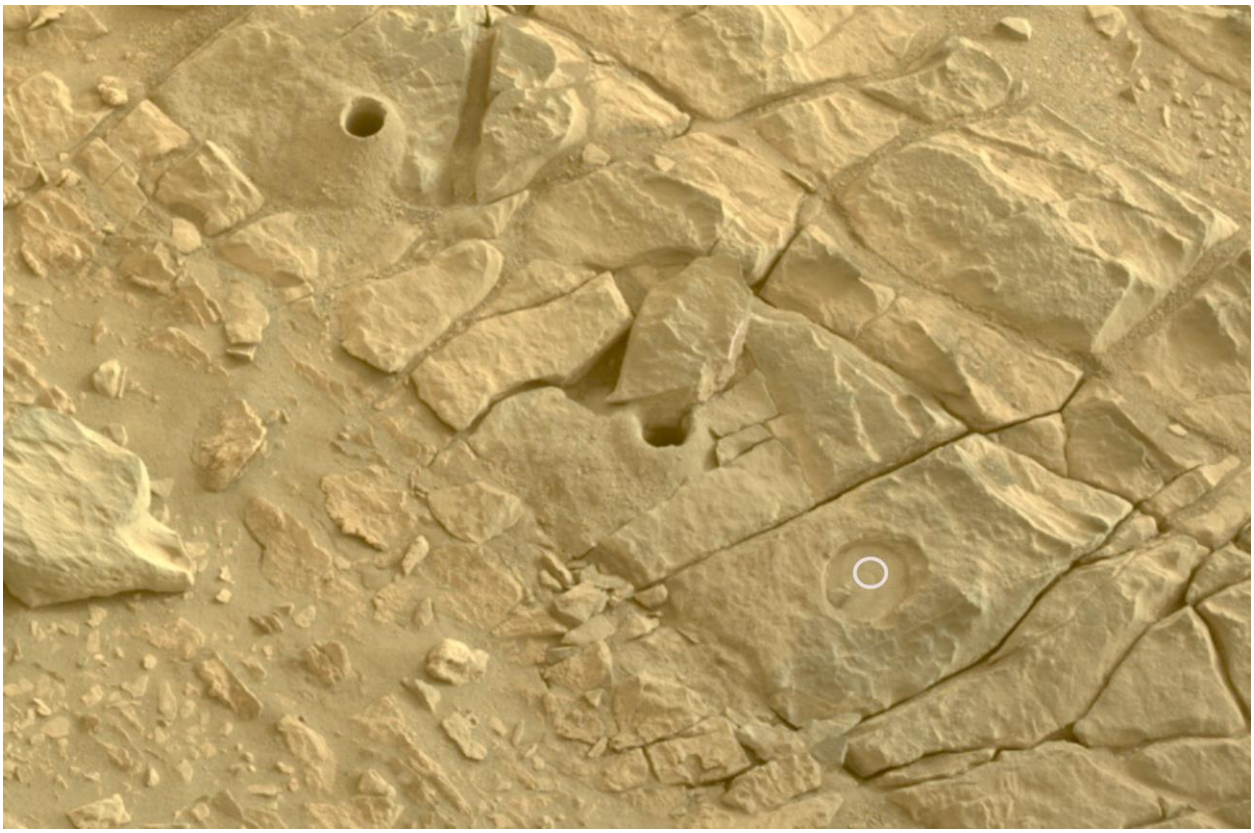

INITIAL REPORT

M2020-623-19 *Kukaklek*

Sample Designation: M2020-623-19 *Kukaklek*

Date of Coring: 20-Nov-2022

Mars Time of Sample Core Sealing: 18:16 LMST, Sol 631, Ls 346.15

Latitude (N), Longitude (E), Elevation: 18.45363597˚, 77.39911421˚, -2517.093594 m

Campaign: Delta Front

Region of Interest: *Cape Nukshak*

Lithology: Fine-grained, moderately sorted sedimentary rock likely deposited in a lacustrine setting; a sulfate-bearing fine sandstone. The rock is rich in weakly-hydrated Mg-Fe sulfate. Small amounts of Fe-Mg-clay minerals, possible carbonates, and hydrated silica or Al-clay minerals were also detected. The rock is cut by scattered veins and patches of Ca sulfate, likely anhydrite, whereas the sulfate in the rock matrix is more magnesian. Fluorescence signals are consistent with a mix of aromatic compounds, and are associated with the calcium sulfate patches.

Estimated Volume Recovered: 7.0 cm^3

Coring Bit Number: 5

Core Orientation: hade = 6.15°; azimuth = 289.36°; core roll = 265.10°

Sample Serial Numbers: Tube SN242; Seal SN151; Ferrule SN113

ACA Temperature at Time of Sealing: 40°C

Estimated Rover-Ambient Pressure and Temperature at Time of Sealing: 701 Pa, 237 K

Estimated Amount of Martian Atmosphere Headspace Gas: 1.78×10^{-6} mol

Anomalous Behavior: 8 sols between coring and sealing

Abrasion Patch Name and Depth: *Uganik Island*, 8 mm

January 15, 2023

D. L. Shuster, K. A. Farley, T. Bosak, A. D. Czaja, E. M. Hausrath, L. E. Mayhew, M. E. Minitti, S. Siljeström, J. I. Simon, K. M. Stack, A. Treiman, B. P. Weiss, B. V. Wogsland, M.-P. Zorzano, A.C. Allwood, *H.E.F. Amundsen, F. J. Calef III, B.C. Clark III, D. Flannery, J.A. Hurowitz, T. Kizovski, A. Knight, L. Mandon, E. N. Mansbach, D.A.K. Pedersen, M.E. Schmidt, M.M. Tice, A. Udry, S. Van Bommel, K. Williford,* M.J. Zawaski *and the Mars 2020 Team*

Summary Description

Kukaklek, the core representing the eighth sample target of the Mars 2020 mission, was collected from *Hidden Harbor*, an outcrop of the *Yori Pass* member of the *Cape Nukshak* region of the western Jezero delta front. *Hidden Harbor* lies above the exposed delta sedimentary rocks in the *Cape Nukshak* region, is ~15 vertical meters below the break in slope that defines the base of *Whale Mountain* (**Figures 1 - 5**) and is likely to be in place. The outcrop is a horizontally layered, fine-grained, and moderately sorted sedimentary rock; a sulfate-bearing fine sandstone (**Figures 3, 5**). We sampled this sedimentary rock because it is from a low stratigraphic position within the western Jezero delta and contains a fine-grained texture, likely deposited on to the floor of a lake. The rock contains abundant weakly hydrated Mg-Fe sulfate with evidence of small amounts of Fe-Mg-clay minerals, possible carbonates, hydrated silica or Al-clay minerals, and sulfate veins and patches likely of diagenetic origin. Thus, this rock has high potential for biosignature preservation.

The *Uganik Island* abrasion patch, acquired at *Hidden Harbor*, has a matrix that appears homogeneous in its color, composition, and grain size, with observable grains ranging from <0.03 to ~1.2 mm, and a fine-grained cement and/or secondary chemical weathering phases. The rock also contains lighter colored, mm-scale polycrystalline masses of anhydrite that crosscut the matrix and appear to have precipitated within fractures. *Uganik Island* is Fe- and Mg-rich. Sulfates and Fe/Mg-phyllosilicates are present, and, potentially, carbonates and hydrated silica as well. Phyllosilicates potentially include kaolinitic and montmorillonitic clays. Strong fluorescence consistent with the presence of both single- and double-ring aromatic compounds is associated with anhydrite. This fluorescence could alternatively arise from inorganic constituents.

Uganik Island is compositionally similar to the fine-grained sedimentary rock analyzed in the abrasion patch *Berry Hollow* (at *Hogwallow Flats*), but has more (Fe,Mg) sulfate, much larger anhydrite masses, and is more chemically weathered. Thus, *Kukaklek* has a strong potential to provide geochemical information on past aqueous and habitable environments distinct from earlier samples. Open system weathering is suspected at this location, and possible veins indicate the transport of fluid through the rock. The potential presence of clay minerals, along with fluorescence associated with the sulfate minerals, indicate this sample has a strong potential for biosignatures.

In contrast to previous samples, the *Kukaklek* core was collected through the *Uganik Island* abrasion patch rather than from an undisturbed outcrop surface. A ~5 mm patch of anhydrite was targeted for coring to ensure its presence in the sample. The *Kukaklek* core was collected on Sol 623, has a core length of 49.7 mm, and based on Cachecam and ZCAM images appears to be a coherent piece of rock, also containing a broken fragment. Due to faults during sample processing, the *Kukaklek* core was not sealed until Sol 631. Between coring and sealing, the sample was stored within the adaptive caching assembly, behind a fluid mechanical particle barrier.

The *Kukaklek* core originates from a subaqueous paleoenvironment that, due to the presence of liquid water, is interpreted as formerly habitable. The returned sample science objectives of the *Kukaklek* core include combined microscopic textural, geochemical, and isotopic analyses of a sample with high potential for biosignature preservation, paleomagnetism, the history of water and water–rock interactions during sedimentary deposition and in the delta sediments after deposition, and possibly geochronology. High spatial resolution elemental and mineralogical analyses can be used to link the

component materials to (1) geochemical conditions of the sediment source/catchment lithology, (2) geochemical conditions in the environment where *Hidden Harbor*/*Yori Pass* was deposited and/or (3) the post-depositional diagenetic processes that acted upon the sediments.

Stratigraphic and Geologic Context

The *Yori Pass* member of the *Shenandoah* formation, which contains the *Hidden Harbor* outcrop, is stratigraphically above the cliff forming *Alagnak* member and *Cape Nukshak* plateau and below the higher delta units of nearby *Whale Mountain* in the *Cape Nukshak* region of the western Jezero delta front (**Figures 1 - 4**). *Hidden Harbor* is stratigraphically ~8 meters above the base of the *Alagnak* member, and ~10 meters above the light toned, laminated *Kaguyak* sandstone, which defines the base of the *Shenandoah* formation in the *Cape Nukshak* region (**Figure 4**). Based on orbital mapping, *Kaguyak* lies at the contact between the Crater floor fractured rough (*Cf-f-2*) and the Delta thinly layered (*D-tnl*) photogeologic units mapped in orbiter images (Stack et al., 2020). *Hidden Harbor* is ~54 vertical meters below the top of nearby *Whale Mountain* ~0.18 km to the northwest, and ~124 vertical meters below the highest exposed delta surfaces ~3.0 km to the northwest.

The *Yori Pass* member contains low relief, light-toned outcrops within the slopes above *Cape Nukshak*. Within this member, the *Hidden Harbor* outcrop appears light toned on its natural surface (**Figure 3**). Alternating light-dark layered units observed in the *Yori Pass* member can be traced laterally in orbiter images at least ~0.5 km along the delta front to the northwest and ~0.2 km to the northeast. *Yori Pass*, including the light-toned *Hidden Harbor* outcrop, is similar to, and may correlate with, the *Hogwallow Flats* member found at *Hawksbill Gap* (**Figure 4**). *Hidden Harbor* lies below cliff-forming units of *Whale Mountain* (**Figure 3**), and above the *Cape Nukshak* plateau capping the *Alagnak* member (**Figure 1-2**). Below *Alagnak* are the *Amalik* and *Kaguyak* members, which overlie a broadly recessive zone that likely includes the contact between the delta and the crater floor (**Figure 4**).

This stratigraphy appears to be representative of the base of the delta but could include some pre-delta units. Unlike the stratigraphy at *Hawksbill Gap,* the lower delta front at *Cape Nukshak* is not significantly covered by regolith, and therefore likely includes the earliest units deposited on the crater floor basement rocks. Overall, these different horizontal layers indicate that the explored stratigraphy of the delta front is comprised of several distinct units and facies, that are largely, if not entirely, sedimentary in origin. *Hidden Harbor* is from a relatively low stratigraphic position within the exposed delta, but higher than *Amalik*, which yielded the *Mageik* and *Shuyak* cores.

Operations

Sampling objectives of the *Delta Front Campaign* included the collection of both fine-grained (<0.06 mm) sedimentary rocks, ideally rich in clay minerals, and coarse-grained sedimentary rocks containing lithologically diverse clasts. The *Kukaklek* singleton core was collected as a sample of opportunity to help fulfill the fine-grained sedimentary rock sampling objectives of the campaign.

The Delta Front Campaign planning process occurred during February and March of 2022 and identified four paired samples to be collected from relatively low stratigraphic positions within the western Jezero delta, and prior to depositing the initial cache: (1 & 2) two different samples of lacustrine sediments with potential for biosignature preservation (ideally fine-grained mudstone and/or fine sandstone containing clay minerals and reduced phases indicative of anoxic preservation conditions), (3)

one relatively coarse-grained sediment sample (ideally containing medium sand size particles, >250 μm, with a lithologic diversity of detrital material) for delta deposition geochronology and Jezero catchment provenance studies, and (4) one regolith sample.

On Sol 424, Perseverance encountered the first delta rock outcrops of the mission at a site called *Enchanted Lake* at the base of *Cape Nukshak* (**Figure 1**). *Enchanted Lake* contained the *Kaguyak* sandstone and overlying *Amalik* fine-grained, gray rocks. SCAM RMI observations at *Cape Gull* (on *Kaguyak*) and *Hook Glacier* (on *Amalik*) revealed sedimentary facies consistent with distal subaqueous deposition. The team then decided to explore a laterally equivalent section of the lower delta exposure in the *Hawksbill Gap* region with the intention to execute proximity science and sampling activities (**Figure 1**). From Sols 426-441, Perseverance drove ~700 m from *Cape Nukshak* to *Hawksbill Gap*, arriving at the lowest exposed delta deposits of *Devils Tanyard* on Sol 441. Between Sols 441 and 474, Perseverance drove up-section through the following delta members while collecting remote sensing data and seeking outcrops suitable for potential proximity science and sampling: *Devils Tanyard*, *Hughes River Gap, Boston Knob*, *Hogwallow Flats*, and *Rockytop* (**Figure 1**).

From Sols 463 to 516, Perseverance collected sedimentary rock cores from *Skinner Ridge* (the relatively coarse-grained *Swift Run* and *Skyland* cores), processed a Witness Tube (M2020-499-13 WB2), and collected sedimentary rock cores from *Wildcat Ridge* (the relatively fine-grained and sulfate-rich *Hazeltop* and *Bearwallow* cores). On Sol 535, Perseverance began a multi-Sol drive back to the *Amalik* outcrop (**Figure 1**). On Sol 557, Perseverance arrived at the *Amalik* outcrop and completed collecting the *Shuyak* and *Mageik* cores on Sol 579, although the *Mageik* sample tube initially failed to seal. On Sol 592, Perseverance drove to the *Observation Mountain* bedform and conducted a wheel scuff (Sol 593) in preparation for regolith sampling. However, because the engineering team did not wish to attempt regolith sampling until the issue with *Mageik* sealing was resolved, Perseverance then drove to the *Hidden Harbor* outcrop at *Yori Pass* for opportunistic proximity science activities while *Mageik* sealing attempts continued.

On Sol 611, we selected potential targets for abrasion and acquired natural surface WATSON images of *Hidden Harbor*. We conducted an abrasion at *Uganik Island* on Sol 612, followed by abrasion proximity science activities (consistent with the STOP list) from Sols 614 to 621. (During this time, the opportunistic science activities were interspersed with *Mageik* sealing attempts; *Mageik* was finally sealed on Sol 619). Initial images of the *Uganik Island* abrasion patch revealed fine particle sizes (<100 μm) displaying a narrow range of both size and color, like the *Hogwallow Flats* abrasion (*Berry Hollow*), but also including mm-scale, light-colored polycrystalline masses/veins. PIXL and SHERLOC data were acquired on *Uganik Island* between Sols 614 and 618. Remote-sensing and abraded proximity science observations revealed that *Hidden Harbor* possessed multiple desired characteristics for a fine-grained sedimentary rock sample with potential for biosignature preservation, including: (1) clay- or silt-sized particles, <63 μm (2) the presence of cements or authigenic minerals; (3) the presence of clay minerals; (4) sediment associated with delta deposition; and (5) a relatively low stratigraphic position in the delta (see above). It also hosts coarse diagenetic sulfates. Thus, the team decided to move forward with collecting a single core and completing the STOP list activities.

We drilled the *Kukaklek* core from the *Uganik Island* abrasion patch (targeting one of the light-colored, polycrystalline veins of anhydrite to ensure their presence in the core) on Sol 623, but the core did not initially break from the rock. Coring resumed and successfully broke from the *Hidden Harbor*

rock on Sol 626, but the sample tube did not seal. The *Kukaklek* core was sealed during a reattempt on Sol 631. The *Kukaklek* core is the fourth sedimentary rock sample collected by the Perseverance Rover and the first single-core sample collected in the mission (i.e., not intended to be duplicated and included in the *Three Forks* Depot). Interpreted to be a sulfate-rich, fine sandstone that has experienced aqueous alteration(s), this sample helps fulfill the desired characteristics for a delta front fine-grained sedimentary rock sample with biosignature preservation potential.

Figure 1 | Regional context of Perseverance rover operations. (a) Geologic map with topography showing Jezero crater floor and western delta units, as defined by Stack et al. 2020. (b) Inset map showing the Delta Front Campaign regions of interest, *Cape Nukshak* and *Hawksbill Gap*, the *Kukaklek* core location (red point), and rover drive route (white lines). Elevation contours are meters relative to the Mars aeroid.

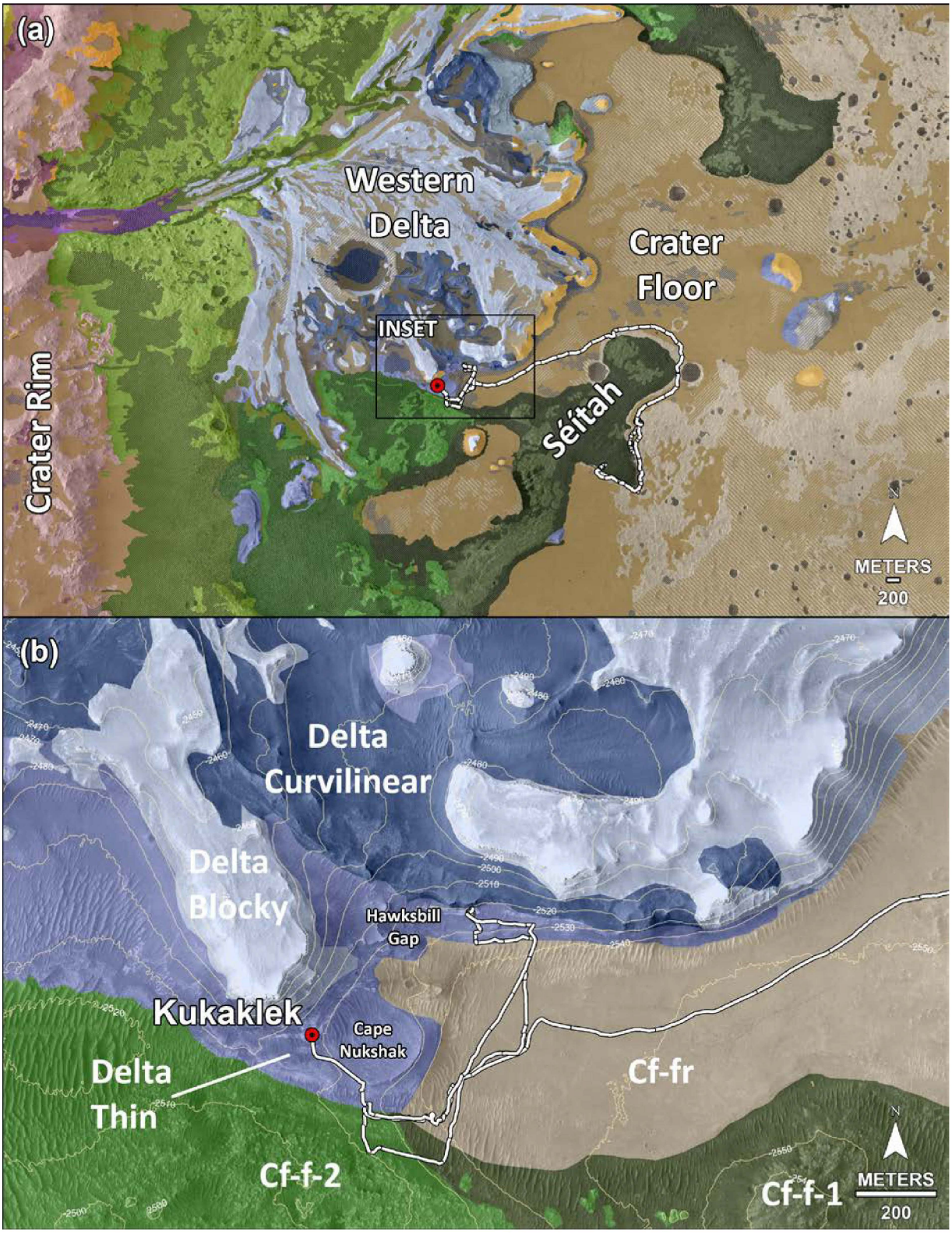

Figure 2 | Local context of Perseverance rover operations during *Kukaklek* sampling. HIRISE image showing the location of sample collection together with other notable outcrops investigated during the sol path leading to *Hidden Harbor*, a rock out crop of the *Yori Pass* member. Location of the *Kukaklek* core is indicated with a red circle.

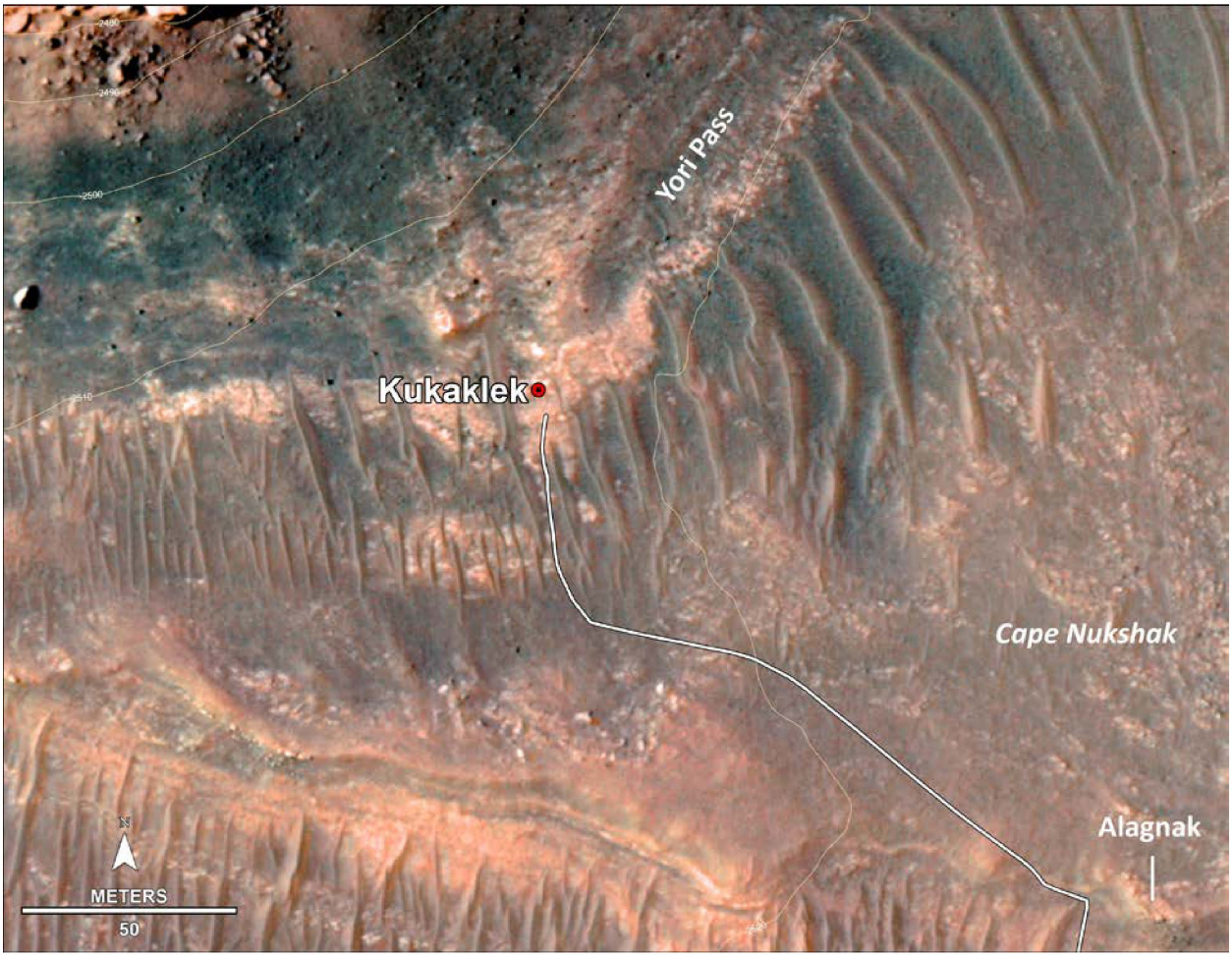

Figure 3 | View of *Hidden Harbor* and *Yori Pass* at the base of *Whale Mountain* within the *Cape Nukshak* delta front stratigraphy. (a) The *Hidden Harbor* outcrop is located near the base of the exposed *Yori Pass* member. *Whale Mountain* (upper right) is comprised of stratigraphically higher delta units. Lower stratigraphic units and crater floor lie below the bottom of the image. The *Hidden Harbor* outcrop is ~5 m across; the vertical distance from *Hidden Harbor* to the break in slope that defines the base of *Whale Mountain* seen in this image is ~15 m. View is to the W; Sol 619, zcam08623, Z110 enhanced color. The *Uganik Island* abrasion (and *Kukaklek* coring location) is indicated with white arrow. UPDATE WITH HIGHER RES FIGURE AND IMPROVE JUSTIN LABELS?

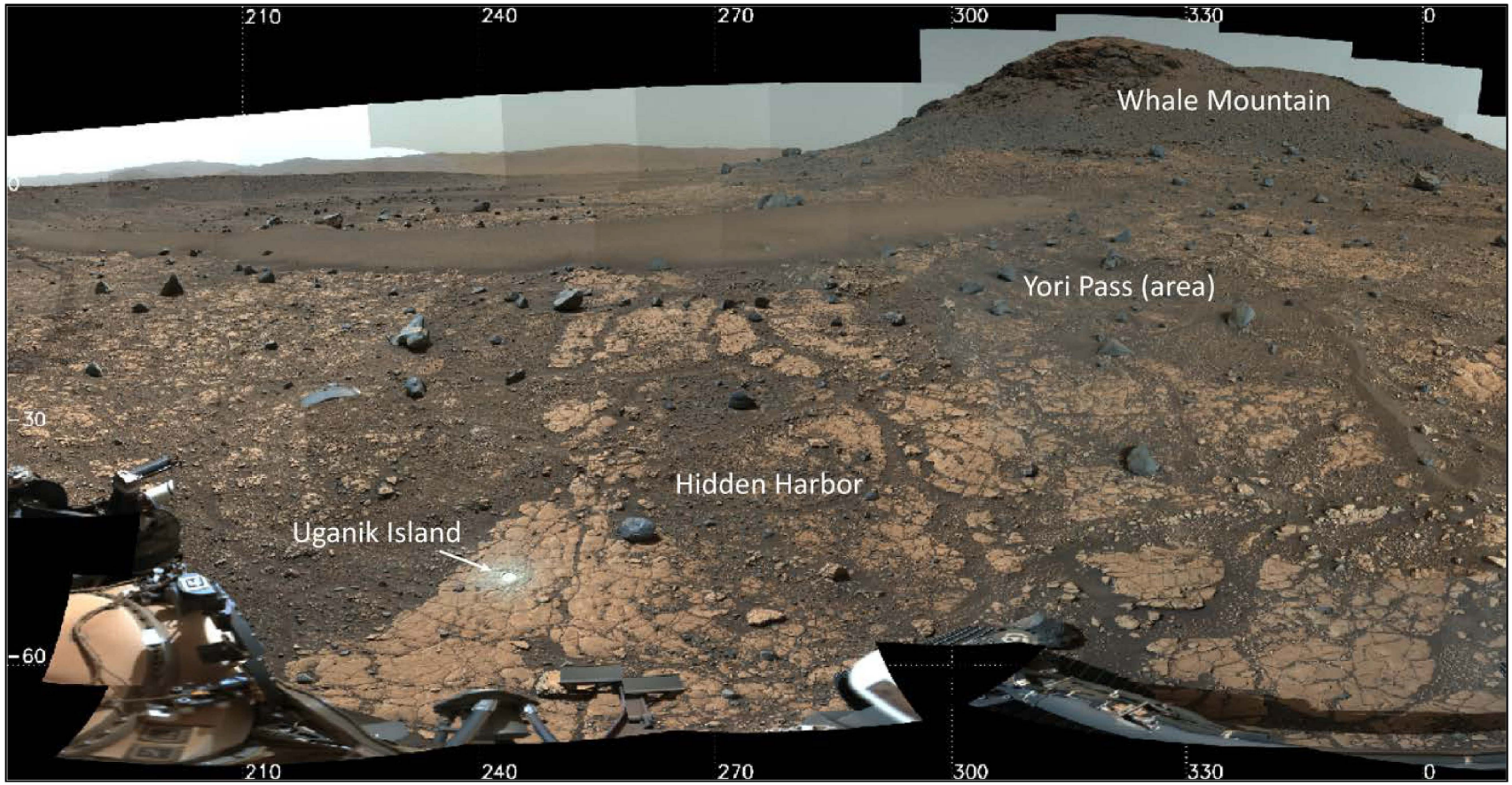

Figure 4 | Stratigraphic column of the *Shenandoah* formation explored at *Hawksbill Gap* between sols 439 and 538 and *Cape Nukshak* primarily between sols 556 and 643. c/si/vf = clay/siltstone/very fine sandstone; f = fine sandstone; m = medium sandstone; C = coarse sandstone; vC = very coarse sandstone; gr = granule; pb = pebble.

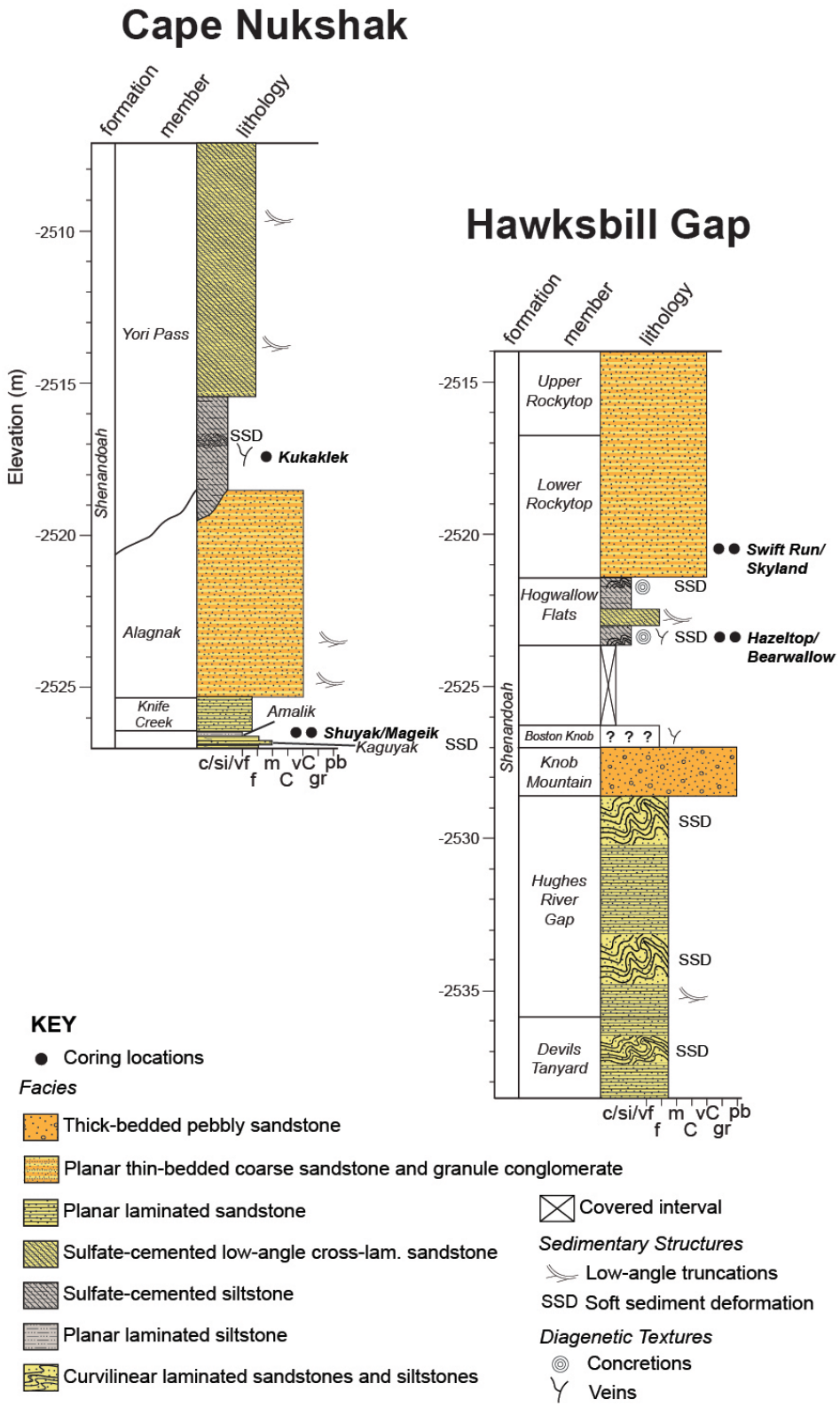

Sample-Related Observations

Workspace Images

Figure 3 shows Mastcam-Z context images for the *Hidden Harbor* workspace. Images were taken on approach to, and positioned at, the workspace prior to sampling *Kukaklek*. The decimeter-scale outcrop from which the sample was taken is semi-continuous with adjacent outcrop patches that have similar appearance.

The surface of the outcrop is light toned, fractured and dusty in a similar manner to *Wildcat Ridge*. Diagenetic features are visible, including light-colored veins that crosscut the outcrop. Possible bedding planes are visible within ~30 cm of the abrasion patch, to the right and slightly towards the rover in **Figure 3**. The outcrop is interpreted to be in place, in which case the *Uganik Island* abrasion patch is subparallel to bedding, and the *Kukaklek* sample was cored perpendicular to bedding. No significant changes in outcrop position were noted after abrasion and sampling. Dust from the abrasion is light-colored, like that produced during abrasion and sampling at *Wildcat Ridge*.

Bed surfaces at *Hidden Harbor* are light-toned, with millimeter-scale layers and 5-10 mm wide light toned veins, e.g., as seen in RMIs acquired on Sols 613 and 620 (**Figure 6**). The bed surfaces also contain millimeter scale fractures filled with dark, loose sand grains (**Figure 6**). The RMI image of the abraded patch (*Uganik Island*) shows interspersed brown and grey areas with difficult-to-discern individual grains. Grey regions larger than ~200 μm, and a tan, mm-scale rounded area suggest the presence of compositionally diverse sand grains and/or cements. Prominent white veins that are less than 1 millimeter wide, and <5 mm-wide masses filled with similarly bright material, are distributed irregularly throughout the abraded patch (**Figure 6**). Larger, ~5 mm wide bright veins composed of larger crystals can be seen protruding millimeters above the bed surface at *Hidden Harbor* (targets *Kupreanof_Strait* and *Gorge_Creek*), indicating that the veins contain material that is more resistant thanthe surrounding matrix. There is a morphological similarity between *Hidden Harbor and Wildcat Ridge,* but the former has a higher abundance of bright veins and somewhat coarser grains.

Figure 5 | Mastcam-Z context images for *Hidden Harbor*. (a) Approach to *Yori Pass* on Sol 607; zcam08616 L0 enhanced color mosaic at a focal length of 110 mm. **(b)** The *Hidden Harbor* workspace, just off the right side of the image, at ~az240; zcam08622 R0 enhanced color mosaic at a focal length of 34 mm. **(c)** The *Hidden Harbor* workspace on Sol 610 prior to abrasion and sampling; zcam07101 R0 enhanced color mosaic at a focal length of 110 mm. The location of the *Uganik Island* abrasion and *Kukaklek* sampling target is shown with arrow.

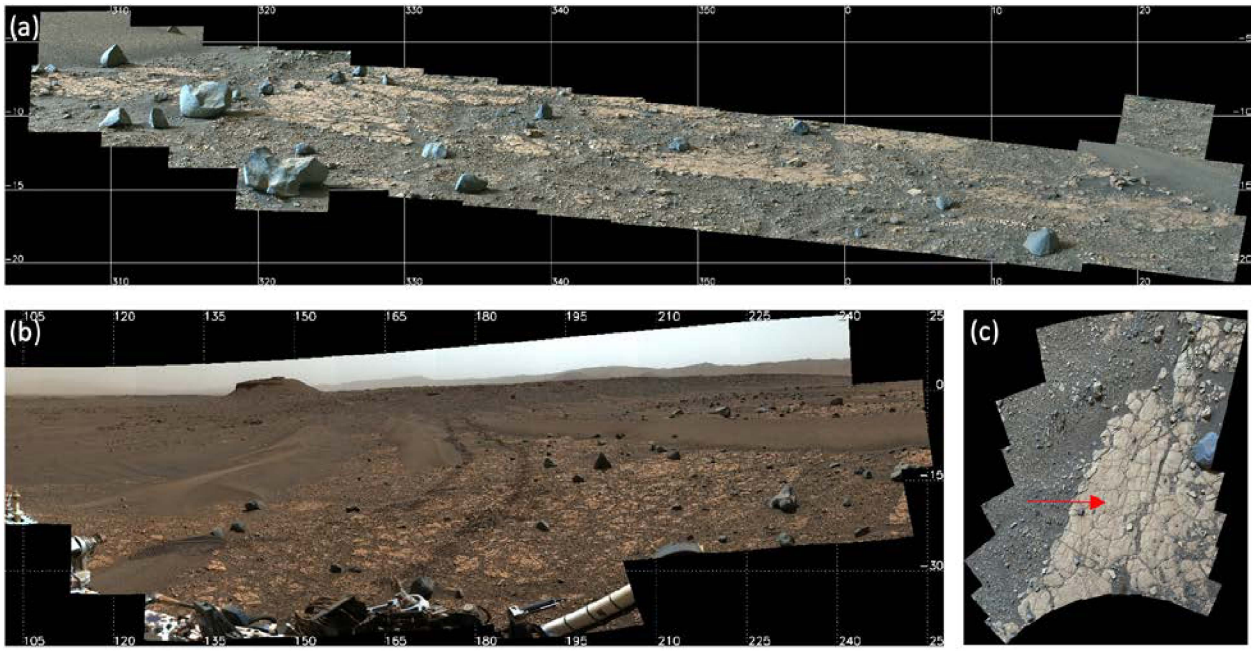

Figure 6 | SuperCam RMI images of rocks in the *Hidden Harbor* area. (a) Large, smooth, bright crystals that protrude above the surface of the bedrock at target *Kupreanof_Strait* imaged on Sol 620. **(b)** Grey, brown and darker grey grains in the abraded patch *Uganik Island* imaged on Sol 619. Bright veins and patches are distributed throughout the abrasion. **(c)** Unabraded surface of *Valley_of_Ten_Thousand_Smokes* target imaged on Sol 613. Thin layers are visible in the left and center parts of the image. Red crosses in all RMI images show spots analyzed by LIBS.

Pre and Post Coring/Abrasion Images

The *Hidden Harbor* workspace is comprised of bedrock slab segments separated by linear and arcuate fractures that in some instances are filled with material more resistant than the bedrock itself (**Figure 7a**). The fill is generally 1-5 mm wide, with a single irregularly shaped example up to ~1 cm wide. Raised features with a variety of shapes and sizes are also present within the bedrock slab segments. The closest-approach images of the natural surface of the target selected for abrasion, *Uganik Island*, highlight some of these resistant features (e.g., **Figure 7b**). They have the same color as the host bedrock but a generally smoother texture. Some occurrences of the resistant features have flat facets and sharp edges. The grain size of the host bedrock is difficult to discern due to dust cover and loose sand grains covering the surface.

The *Uganik Island* abrasion achieved a depth of 8 mm. The bottom of the patch is free of prominent tool marks from the abrasion bit (**Figure 7c**). Under sunlight illumination, the bulk bedrock is a uniform grey color and contains a homogenous distribution of matrix-supported black, grey, brown, and orange grains. Rare, medium to coarse sand-sized grains are present, but most visible grains fall between silt and fine sand (**Figures 7c, 8a**). The rare grains large enough to evaluate morphologically are subrounded. The shape of most of the grains cannot be evaluated, but most appear to be equant (**Figure 8a**).

Uganik Island is notable relative to previous abrasions in the abundance and distribution of textures distinct from the host bedrock. These features were the focus of multiple SHERLOC and PIXL scans (**Figure 8b**). The white material present within the abrasion does not incorporate host bedrock material, varies in color and luster within individual patches (matte white to translucent grey), and assumes a variety of shapes from equant to elongate (**Figures 7c, 8a**). The similarity of shapes and distributions of resistant features present on the pre-abrasion surface (**Figure 8c**) to white material visible post-abrasion (**Figure 8d**) suggests these are manifestations of the same material, likely interconnected throughout the bedrock. We interpret the white material to be veins. In addition to the vein material, there is a rounded feature, ~2 mm in diameter, that stands out from the host bedrock (**Figure 7c**). The feature is yellow relative to the host bedrock, and gray, medium sand-sized grains mark part of the perimeter of the feature. While some fine sand-sized grains are visible within the feature, its texture is less granular than the host bedrock (**Figure 7c**).

Figure 7 | **Natural surface WATSON images from the *Hidden Harbor* workspace**. **(a)** Mosaic of full frame images acquired from 40 cm standoff over candidate abrasion and sampling targets. Illumination is a mix of full and partial sunlight. **(b)** Full frame image of the *Uganik Island* target acquired at 7 cm standoff. Target is in full shadow. **(c)** Focus merge of the *Uganik Island* abrasion from 7 cm standoff. Most of the abrasion is in full sun illumination.

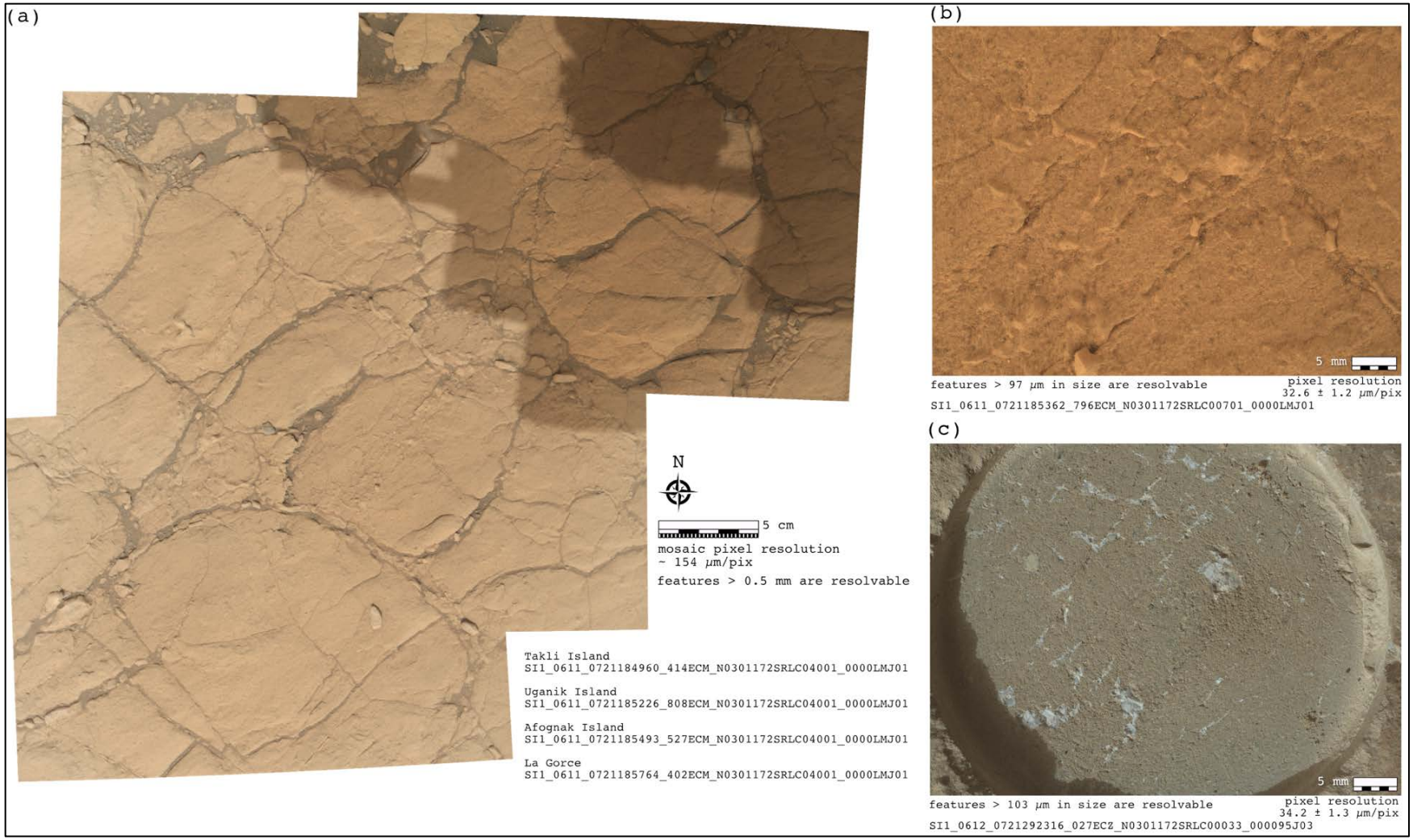

Figure 8 | **(a)** WATSON post-abrasion focus merge from 4.1 cm standoff, the highest resolution WATSON image of the *Uganik Island* abrasion. Field of view is in full shadow. **(b)** WATSON post-abrasion focus merge from 7 cm standoff with all SHERLOC and PIXL footprints indicated. Same image as **Figure 7c**. **(c)** Cropped field of view within the WATSON pre-abrasion full frame image from 40 cm standoff (subset of **Figure 7a**). Image field of view is for comparison to **(d)** WATSON post-abrasion focus merge from 10 cm standoff.

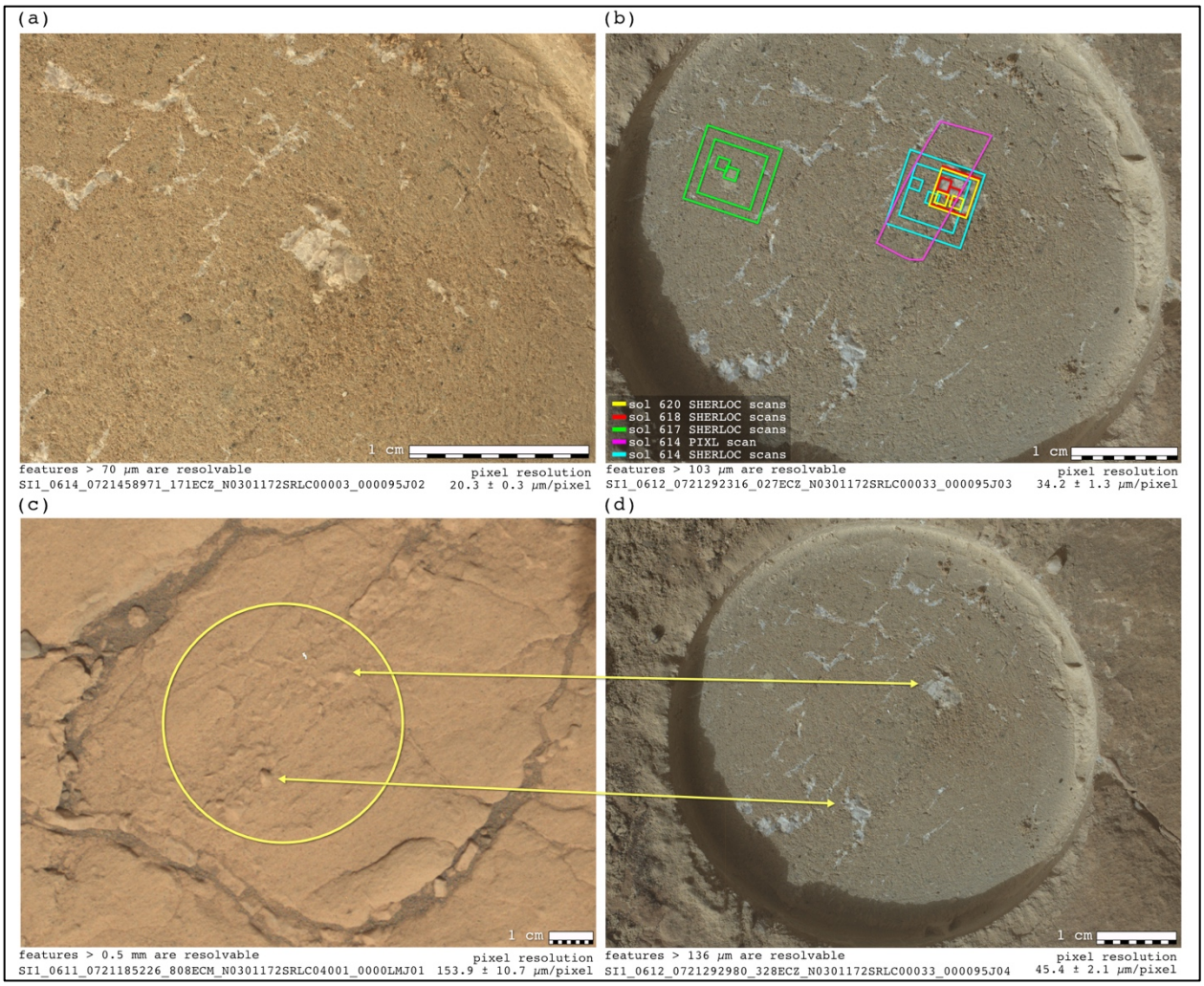

Figure 9 | Grain size distribution of *Uganik Island*.

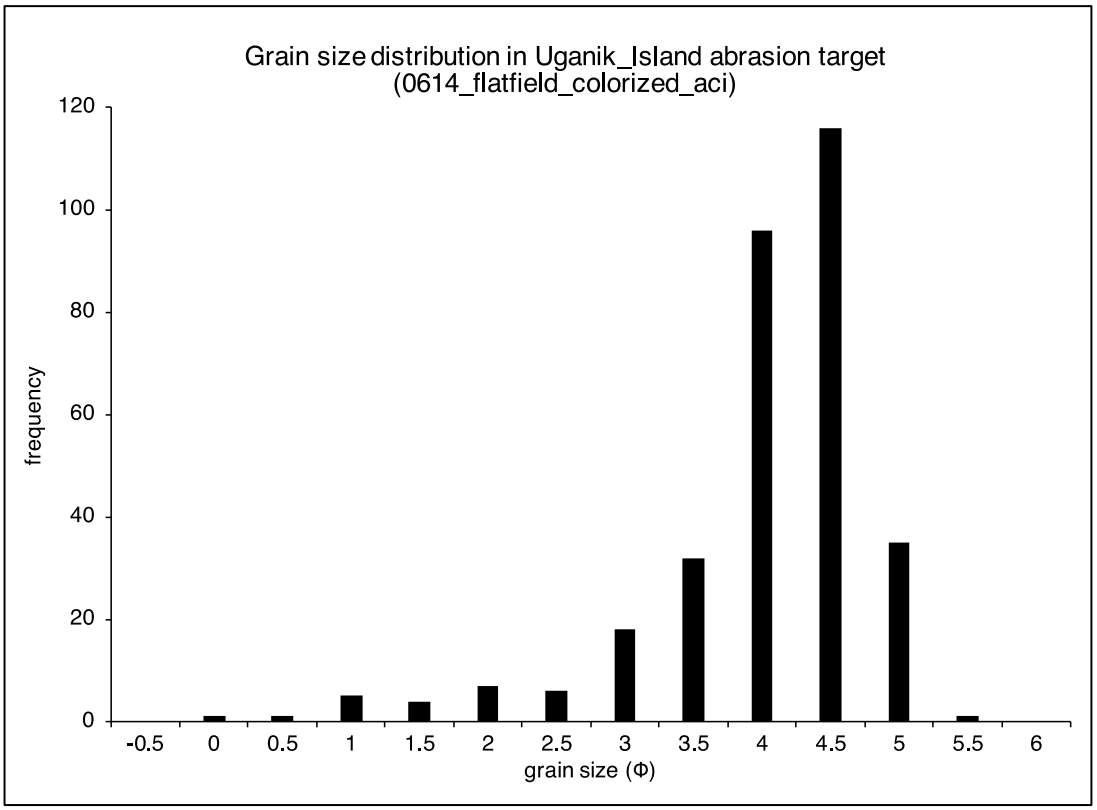

Figure 9 shows the distribution of grain sizes in *Uganik Island*. Equivalent diameters of 322 grains were measured at intersection points of a grid with 0.5 mm spacing, projected on a mosaic of SHERLOC ACI images of the abrasion patch. Grains in *Uganik Island* show a broad, but unimodal distribution, with the mode at φ=3.9 (very fine sand, 67 μm), mean grain size of φ =3.8 (very fine sand, 73 μm), and standard deviation of φ=0.74 (moderately-sorted). [$\varphi = -\log_2(D)$, where D is the diameter of a grain in millimeters.] Measured grains range in size from 1209 μm down to the limit of ACI resolution (10.1 μm/pixel, enabling objects of >30 μm to be resolved). Grains are generally equant (**Figure 8**). Using the textural classifications defined by Lazar et al. (2015), this rock is a very fine sandstone.

The *Kukaklek* core was acquired over the largest patch of vein material within the abrasion patch. The Cachecam image of the freshly fractured bottom face of the core emphasizes the clastic nature of the rock (**Figure 10**). Silt to very fine sand-sized grains with the same range of colors present in the abrasion patch are resolvable across the face of the sample. Whether the white material is as abundant on this face as in the abrasion patch surface is difficult to discern. The RMI image of the dust-covered borehole (**Figure 11**) sheds no light on the question of how deeply the white veins penetrate.

Figure 10 | (**a**) Color-stretched Cachecam and (**b**) ZCAM images of the *Kukaklek* core. The core length is 49.7 mm; note that the rock fragment in the mouth of the bit seen in (b) was ejected by the percuss-to-ingest step prior to tube sealing. The core diameter is 13 mm.

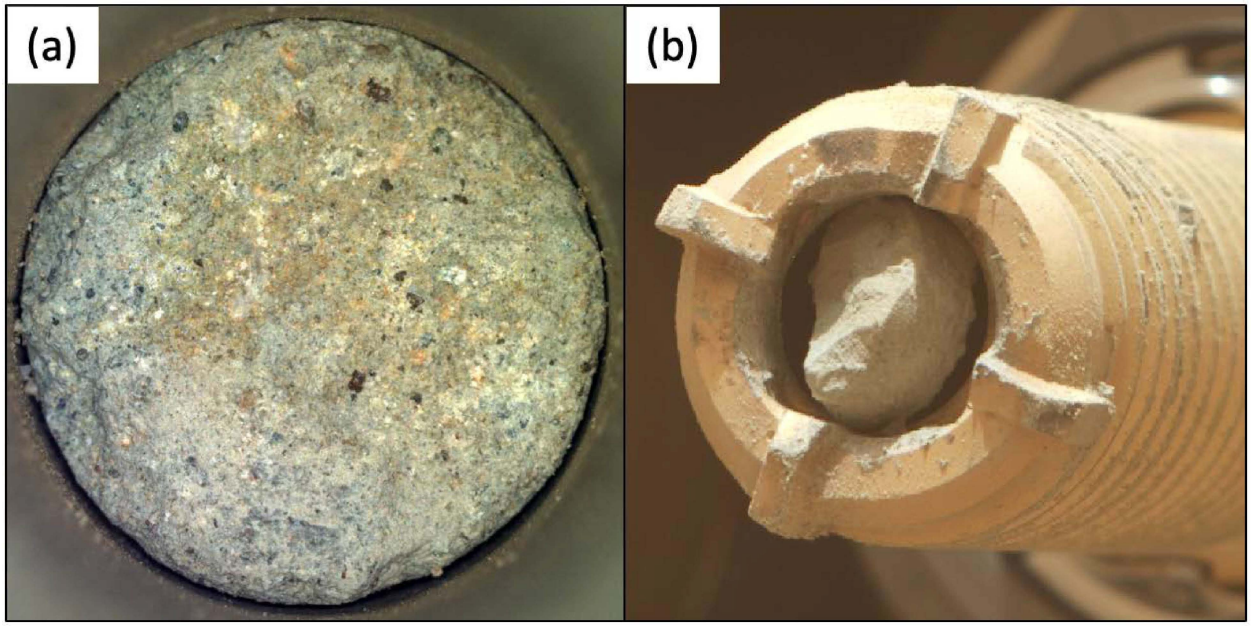

Figure 11 | SCAM RMI borehole image after *Kukaklek* core extraction (Sol 628).

Elemental Geochemistry - PIXL

Elemental chemistry for the *Kukaklek* core comes from the co-located abrasion site, *Uganik Island.* *Uganik Island* exposes a fine-grained sandstone, consisting primarily of grains (<120 µm) of Mg-Fe^{2+} sulfate and Mg-Fe^{2+} silicate (possibly a montmorillonitic clay). *Uganik Island* is chemically and mineralogically similar to *Wildcat Ridge*/*Berry Hollow*. The presence of a mixed Mg-Fe^{2+} sulfate mineral, which would be soluble in water, suggests that *Uganik Island* formed under highly saline (possibly evaporitic) conditions. The similarity in Mg/Fe^{2+} ratio of the sulfate and silicate phases suggests the rock was not deposited under oxidizing or sulfidic conditions; under either condition, iron would have been fractionated from magnesium through the formation of insoluble Fe-oxides or Fe-sulfides. *Uganik Island* also contains masses, interpreted as detrital rock fragments, that are consistent with being rich in clay minerals, both Al-rich and Mg-rich. The Al-rich fragments consist primarily of Al and Si oxides and could be kaolinite or montmorillonite clay. The Mg-rich fragment is significantly enriched in chromium. *Uganik Island* is cut by scattered veins and patches of calcium sulfate, likely anhydrite (based on their high analytical totals). Overall, the high analytical total for *Uganik Island* (~95%) suggests that the rock is only modestly hydrated.

The abraded surface was mapped by PIXL on Sol 614 (*Uganik_Island*), Sol 617 (*Uganik_Island2*), and again on 618 (*Uganik_Island_Line*), **Figure 12**. **Table 1** gives the parameters for the three PIXL scans on *Uganik_Island* (**Figure 12c**). This Initial report emphasizes the *Uganik_Island* map scan; data on the other two scans will be reported elsewhere.

Table 1. PIXL Scans on *Uganik_Island*.

Sol	Name	Scan Size mm	Point Spacing mm	Purpose/Target
614	*Uganik_Island*	12.5 x 4	0.125	General, white 'fish'
617	*Uganik_Island2*	5 x 5	0.125	Tan blob/fragment
618	*Uganik_Island_Line*	12.5	0.125	Support SHERLOC observation.

The bulk chemical composition of the *Uganik_Island* map scan is given in **Table 2**, along with compositions of two distinctive objects in that scan. The X-ray spectra from which the analyses are derived were corrected for scattering and diffraction effects where possible. Due to the potential effects of diffraction, abundances of Na and Cl are likely to be significantly lower than reported.

Figure 12 | **PIXL raster scans on the *Uganik Island* abrasion, sols 614, 617, and 618. (a)** Pre-abrasion (ZCAM image ZRF_0612_0721272628_348FDR_N0301172ZCAM03480_1100LMJ01). **(b)** Post-abrasion, abrasion is 5 cm diameter (ZCAM ZLF_0613_0721362736_818FDR_N0301172ZCAM03483_1100LMJ01). **(c)** Detail of abrasion, rotated slightly from part (b). PIXL scan locations & Sol annotated onto WATSON image SIF_0612_0721282138_906FDR_N0301172SRLC00746_0000LMJ01.

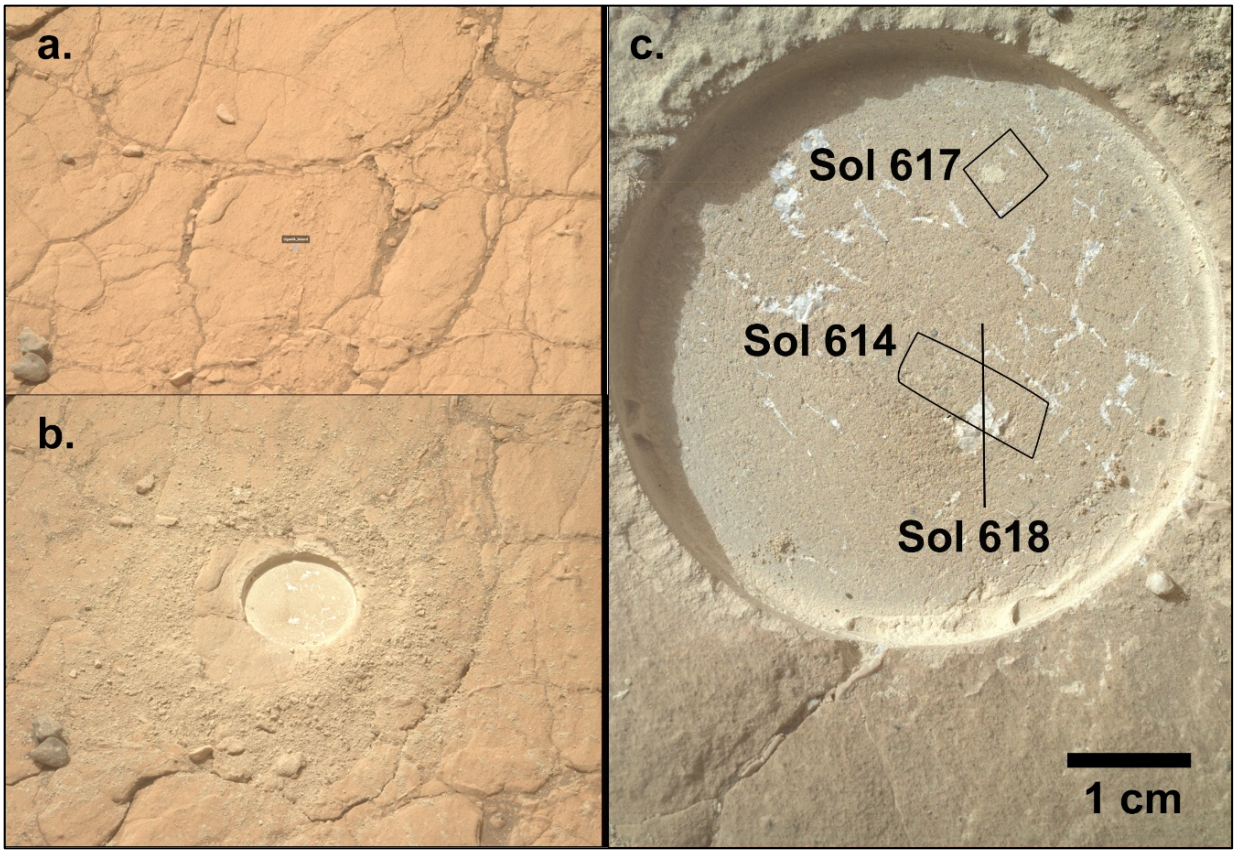

Table 2 | ***Uganik Island*** **Chemical Compositions: PIXL XRF.**

	Bulk Abrasion Sol 614		'UI Blob 1' Sol 614		'UI Blob 2' Sol 614	
Wt %	N=3333	Stdev 1σ	N=22	Stdev 1σ	N=27	Stdev 1σ
Na_2O	2.1	1.04	0.7	0.68	0.65	0.74
MgO	12.44	0.77	11.25	0.68	18.18	1.03
Al_2O_3	5.32	0.38	10.91	0.59	5.022	0.37
SiO_2	31.36	1.60	46.61	2.35	51.12	0.28
P_2O_5	0.57	0.22	0.57	0.22	0.15	0.03
SO_3	21.53	1.15	8.00	0.49	0.45	0.49
Cl	1.14	0.36	2.04	0.51	1.55	0.46
K_2O	0.19	0.17	0.48	0.21	0.17	0.17
CaO	5.72	0.57	0.54	0.22	0.26	0.17
TiO_2	0.64	0.24	0.23	0.14	0.77	0.27
Cr_2O_3	0.11	0.04	0.03	0.02	2.88	0.46
MnO	0.13	0.14	0.15	0.16	0.19	0.19
FeO-T	14.35	0.74	8.62	0.43	12.10	0.61
NiO	0.03	0.03	0.01	0.07	0.03	0.03
ZnO	0.02	0.03	0.03	0.03	0.03	0.03
Sum %	95.75		90.0		97.7	
Mg#	61		70		73	

'UI Blob 1' is a distinctive area on the Sol 614 scan with high Al and Si (**Figure 14**).
'UI Blob 2' is another distinctive area with high Cr and high Mg + Si (**Figure 14**).
Stdev is 1σ uncertainty from calibration and counting statistics**.**
Mg# is molar Mg/(Mg+Fe), in percent.

The bulk composition from the 614 scan is consistent with a mixture mostly of Fe-Mg silicate, Fe-Mg sulfate, and Ca sulfate. Like the *Wildcat Ridge/Berry Hollow* samples, the *Uganik_Island* bulk composition is dominated by Fe-Mg silicates and sulfates, with post-depositional masses of Ca-sulfate. In *Uganik Island*, the Ca-sulfate component corresponds to the white-colored inclusions, veins, and lensoid areas. The silica content of the rock (**Table 2**) is consistent with that of olivine+pyroxene (**Figure 13c**), suggesting derivation from an olivine-rich rock something like *Dourbes* in *Séítah.* The Fe-Mg silicate and sulfate are intimately mixed (at the scale of PIXL analysis spots). The *Uganik Island* abrasion bulk composition is like that of *Berry Hollow* (**Table 2**). This similarity suggests that the *Kukaklek* rock was formed in the same manner as *Wildcat Ridge* – it is possible that they are correlative or represent recurrences of the same depositional environment(s).

Figure 13 shows the chemical classifications of the spot analyses in the *Uganik Island* map scan, and the average (as in **Table 2**). In the Mangold et al. (2017) classification (**Figure 13a, b**), *Uganik Island* would be classified as Fe-poor, Si-poor, K-poor, and Na-poor (again, note that reported Na abundances may be far higher than actuality). In the TAS diagram (**Figure 14c**), the spot and bulk compositions of *Uganik Island* are unlike typical igneous rock, and more akin to that of a dunite or serpentinite. Most

point analyses are consistent with olivine (± other minerals), as might arise from hydrodynamic sorting of minerals from an ultramafic rock like *Dourbes*. No spot analyses consistent with plagioclase or pyroxene are apparent. The points at low SiO_2 are interpreted as sulfate minerals. The high Na+K and low SiO_2 contents do not match known likely minerals (other possibly than sulfates); their high alkali sums are from the aforementioned apparent excess of Na arising from mineral diffraction peaks at the same energy as characteristic NaKα X-rays.

Figure 13 | **Chemical classification of *Uganik Island*.** Blue dots are individual PIXL analyses, red circle is average composition (**Table 2**). **(a)** and **(b)** follow the classification scheme of Mangold et al. (2017). **(c)** is the standard TAS classification for igneous rocks.

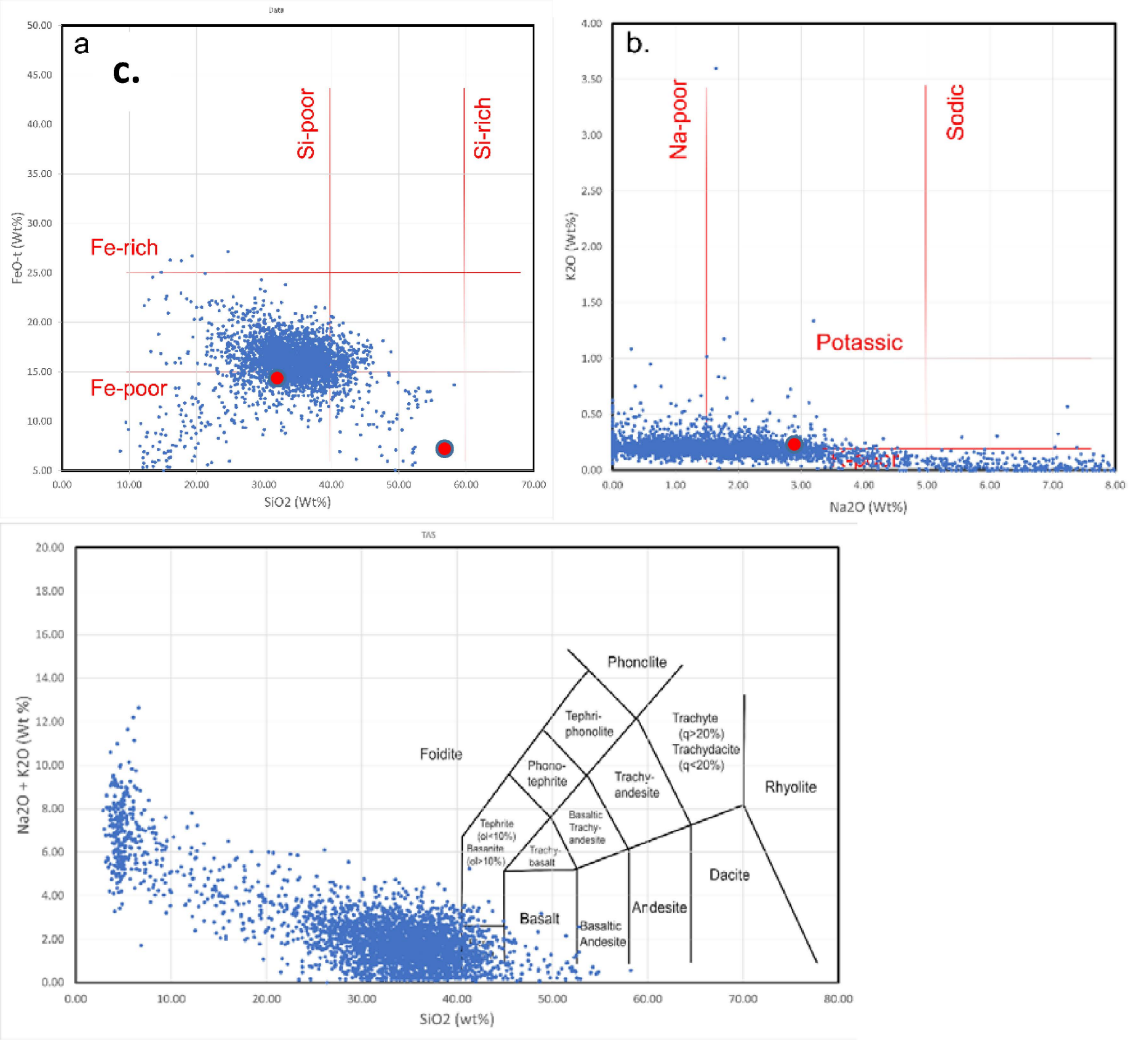

Figure 14 shows multi-element color images from the PIXL map scans of *Uganik Island*. The bulk of *Uganik Island* is silicate and sulfate material rich in Fe and Mg. The silicate portion is consistent with an igneous origin or protolith (**Figures 13c, 14**, **Table 2**), possibly related to the relatively magnesian olivine cumulate rocks of the *Séítah* Formation. The presence of Fe-Mg sulfate (hydrated according to SHERLOC data) is almost identical to that in the *Wildcat Ridge/Berry Hollow* rock.

Important features in **Figure 14** include the largest, irregular white object (~5 mm long), informally dubbed the 'fish' on account of its distinctive shape (see **Figure 12c**). This object has abundant SO_3 and CaO (**Figure 14c**) suggesting that it is $CaSO_4$, anhydrite. It's apparent high abundances of Na_2O are likely illusory, an effect of mineral X-ray diffractions. Likewise, there are small patches of Ca-sulfate in the scan. Similar, white zig-zag areas are abundant elsewhere in the abrasion patch that appear to radiate in some cases, with wider centers than edges (**Figure 12c**). These sulfate-filled areas could be syneresis cracks, although other origins are possible.

The *Uganik Island* abrasion area includes two patches with color and chemistry quite distinct from the main mass of the rock, see **Figure 14**. The first, 'UI-Blob 1,' dark blue in **Figure 14a**, is rich in Al and Si, and has a low analytical total, see **Table 2**). This is likely a grain of phyllosilicate mineral(s), possibly of kaolinitic or montmorillonitic clay. Considering its composition and size relative to other grains in the rock, Blob 1 is likely detrital rather than formed in situ.

'UI Blob 2,' light blue in **Figure 14a**, is rich in Si, Mg, and Fe, with some Al, and with a Cr-enriched rim, **Figure 14d** and **Table 2**. Its bulk composition is more magnesian than the surrounding matrix (**Figure 14c**), has an average of nearly 3% Cr_2O_3, and spot analyses of the rim contain up to 8% Cr_2O_3 (**Figure 14d**). Overall, the Blob 2 composition is consistent with a phyllosilicate (clay) mineral, possibly dehydroxylated given its high analytical total. The abundance of Cr is unusual and noteworthy. Chromium clays are known on Earth, e.g., the mineral volkonskoite (Foord et al. 1987) in which chromium is Cr^{3+}. The origin of this Cr-bearing phyllosilicate is not clear. Cr-bearing phyllosilicates can form by hydrothermal alteration of igneous chromite (Morata et al. 2001), but that mechanism might not apply here. Considering its composition and size relative to other grains in the rock, Blob 1 is likely detrital rather than formed in situ.

The *Uganik Island* scan shows limited evidence for 'heavy minerals' (in a sedimentological sense). **Figure 14d** shows only a few spots consistent with chromite (high Fe and Cr, appearing yellow), and only a few spots that could be consistent with ilmenite (high Fe and Ti, appearing magenta). **Figure 14e** shows two analysis spots that apparently contain small proportions of zirconium (<0.3% ZrO_2), the green pixels. These show X-ray peaks at the proper energy for ZrKα but are barely above background noise level. **Figure 14e** also shows a few spots rich in P_2O_5 (to ~10%), which likely represent apatite or merrillite. There is no evidence of Zn-rich or K-rich phases (**Figure 14f).**

From **Figure 14f**, *Uganik Island* appears to contain moderate abundances of both Na and Cl, especially in the Ca-sulfate masses. As noted above, the PIXL team is concerned that these apparent abundances represent X-ray diffraction peaks, and not actual elemental abundances.

Figure 15 plots the elemental chemistry from the PIXL scan of *Uganik Island* on Sol 614. In its most abundant elements (Mg, Fe, Ca, Si, S), the *Uganik Island* composition is very similar to that of *Berry Hollow*. In **Figure 15a**, it is apparent that *Uganik Island* consists of Fe-Mg materials (e.g., silicates and sulfates) mixed with $CaSO_4$ (the veinlets and the 'fish'). The Fe-Mg materials have relatively too much silica for them to be olivine or serpentines; the ratio (Fe+Mg)/Si is more consistent with orthopyroxene or clay minerals. There is minimal evidence for calcic pyroxene or feldspars. **Figure 15b**, confirms this absence of feldspar, in the modest proportions of Al in any of the spot analyses. It is important to note that the material rich in Fe+Mg also contains significant Al, again consistent with its identification as clay. **Figure 15c** emphasizes the importance of Ca sulfate in the *Uganik Island* rock, with a distinct array

of analyses trending toward a point with equimolar Ca and S, i.e., $CaSO_4$. In The *Uganik Island* scans, Fe-Ti-Cr minerals (**Figure 15d**) are not abundant, and where present in PIXL spots, these elements are diluted by the surrounding sulfates and silicates. Only a few points are consistent with ilmenite (Fe+Ti, magenta), and a few are consistent with chromite (Fe+Cr, yellow). The points on the plot with high Cr and low Ti come from the Cr-bearing clay fragment, UI Blob2. **Figure 15e** demonstrates the intimate mixture of silicate and sulfate materials at the scale of a PIXL analytical volume. From that array on **Figure 15e**, the silicate component contains ~50% SiO_2, and the sulfate component contains ~50-60% SO_3. **Figure 15f**, comparable to a similar figure in the *Berry Hollow* Initial Report, shows that compositions are consistent with a mixture of a $(Fe,Mg)SO_4$ component, a CaSO4 component, and a Fe-Mg silicate component. The silicate component has excess silica compared to olivine and to orthopyroxene; it has a molar ratio (Mg+Fe)/Si of ~0.35. For comparison, typical smectite & saponite clays would have this ratio at ~0.42.

Figure 16 provides PIXL MCC images of the Sol 614 scan of *Uganik Island.*

Figure 14 | **PIXL multi-element maps from the *Uganik Island* map scan, Sol 614.** The legend for each panel indicates which element is assigned to which color, the full range of abundances of that element or oxide (in numbers) and the distribution of element abundances in the scan (black bars & histograms left of the color bars). **(a)** FeO-MgO-SiO_2. Note that the two 'blobs' are distinctly richer in Si than the bulk of the rock. **(b)** FeO_T-Al_2O_3-CaO. Note that Blob 1 is strongly enriched in Al, and that the 'fish' is rich in Ca. **(c)** SO_3-MgO-CaO, emphasizing sulfates. Note that the fish is enriched in S, and that the rock matrix has significant S and little Ca. **(d)** FeO-TiO_2-Cr_2O_3, emphasizing oxide minerals. **(e)** P_2O_5-ZrO_2-ZnO, emphasizing minor minerals. The points 'rich' in Zr (green) contain <0.3% ZrO_2 and could represent noise in the spectra. **(f)** Na_2O-Cl-K_2O, emphasizing chlorine phases. Much of the apparent enrichments in Cl and Na could be from diffraction peaks mimicking Cl$K\alpha$ and Na$K\alpha$ X-rays.

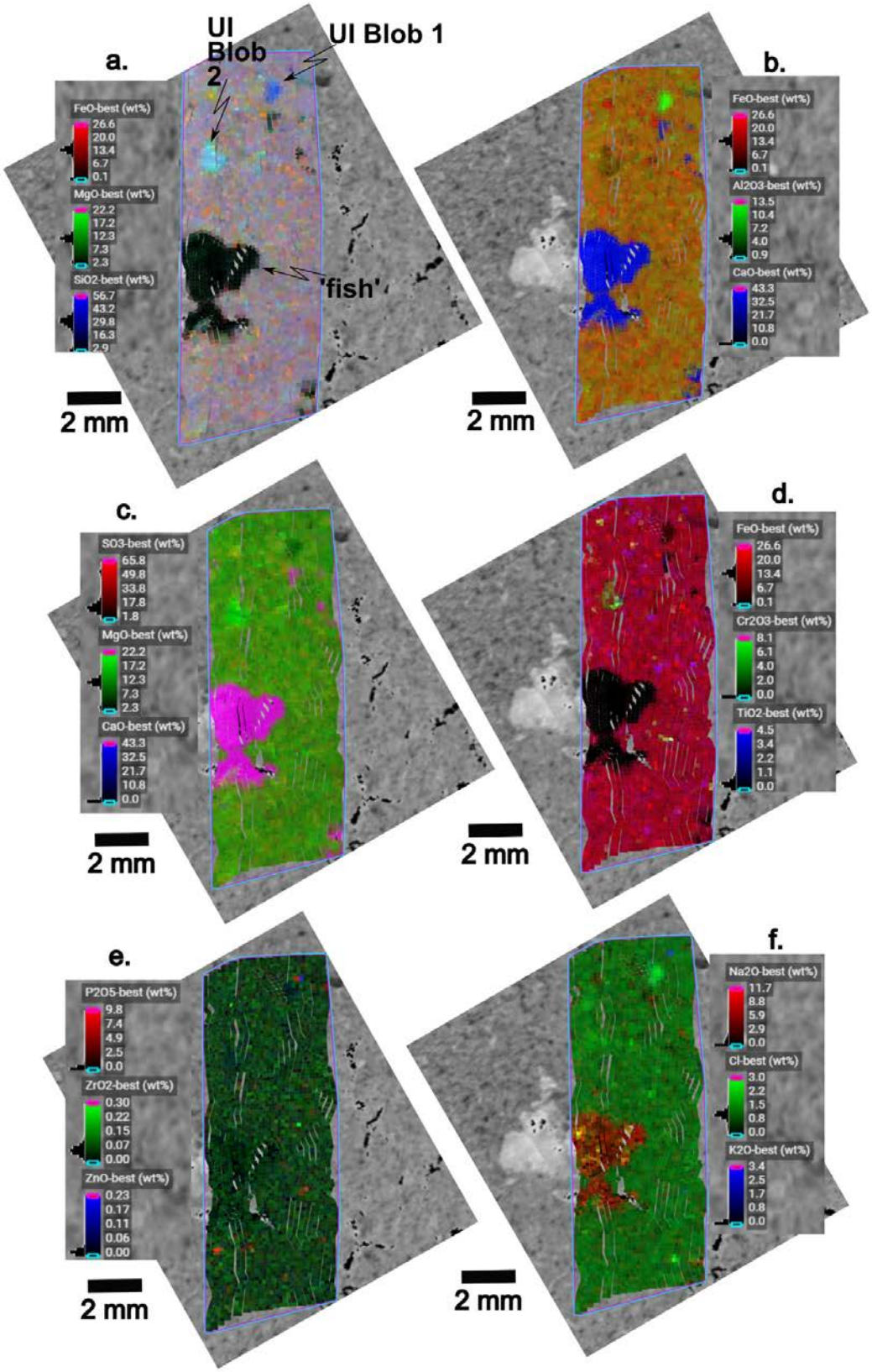
a.
UI Blob 2
UI Blob 1
'fish'
FeO-best (wt%)
26.6
20.0
13.4
6.7
0.1
MgO-best (wt%)
22.2
17.2
12.3
7.3
2.3
SiO2-best (wt%)
56.7
43.2
29.8
16.3
2.9
2 mm
b.
FeO-best (wt%)
26.6
20.0
13.4
6.7
0.1
Al2O3-best (wt%)
13.5
10.4
7.2
4.0
0.9
CaO-best (wt%)
43.3
32.5
21.7
10.8
0.0
2 mm
c.
SO3-best (wt%)
65.8
49.8
33.8
17.8
1.8
MgO-best (wt%)
22.2
17.2
12.3
7.3
2.3
CaO-best (wt%)
43.3
32.5
21.7
10.8
0.0
2 mm
d.
FeO-best (wt%)
26.6
20.0
13.4
6.7
0.1
Cr2O3-best (wt%)
8.1
6.1
4.0
2.0
0.0
TiO2-best (wt%)
4.5
3.4
2.2
1.1
0.0
2 mm
e.
P2O5-best (wt%)
9.8
7.4
4.9
2.5
0.0
ZrO2-best (wt%)
0.30
0.22
0.15
0.07
0.00
ZnO-best (wt%)
0.23
0.17
0.11
0.06
0.00
2 mm
f.
Na2O-best (wt%)
11.7
8.8
5.9
2.9
0.0
Cl-best (wt%)
3.0
2.2
1.5
0.8
0.0
K2O-best (wt%)
3.4
2.5
1.7
0.8
0.0
2 mm

Figure 15 | Plots of PIXL element analyses of the *Uganik Island* map scan, Sol 614. **(a)** Molar proportions of Ca+Na+K, Si, & Fe+Mg. Common minerals that plot at the Fe+Mg apex include oxides, Fe-Mg carbonate, and Fe-Mg sulfates. **(b)** Molar proportions of Ca+Na+K, Al, & Fe+Mg. 'Ol' at Fe+Mg corner includes minerals olivine, orthopyroxene, Fe oxides, and Fe-Mg carbonates & sulfates. **(c)** Molar proportions of SO_3, MgO, and CaO, emphasizing sulfates. **(d)** Weight percent of Cr_2O_3 vs. TiO_2. The points are consistent with variable small proportions of a low-Ti chromite, and possibly a very small proportion of ilmenite (or rutile). There is minimal evidence for higher-Ti chromite as is observed in rocks of the *Séítah f*ormation. **(e)** Weight percent of SiO_2 vs SO_3. **(f)** Molar proportions of S, Si, & Fe+Mg.

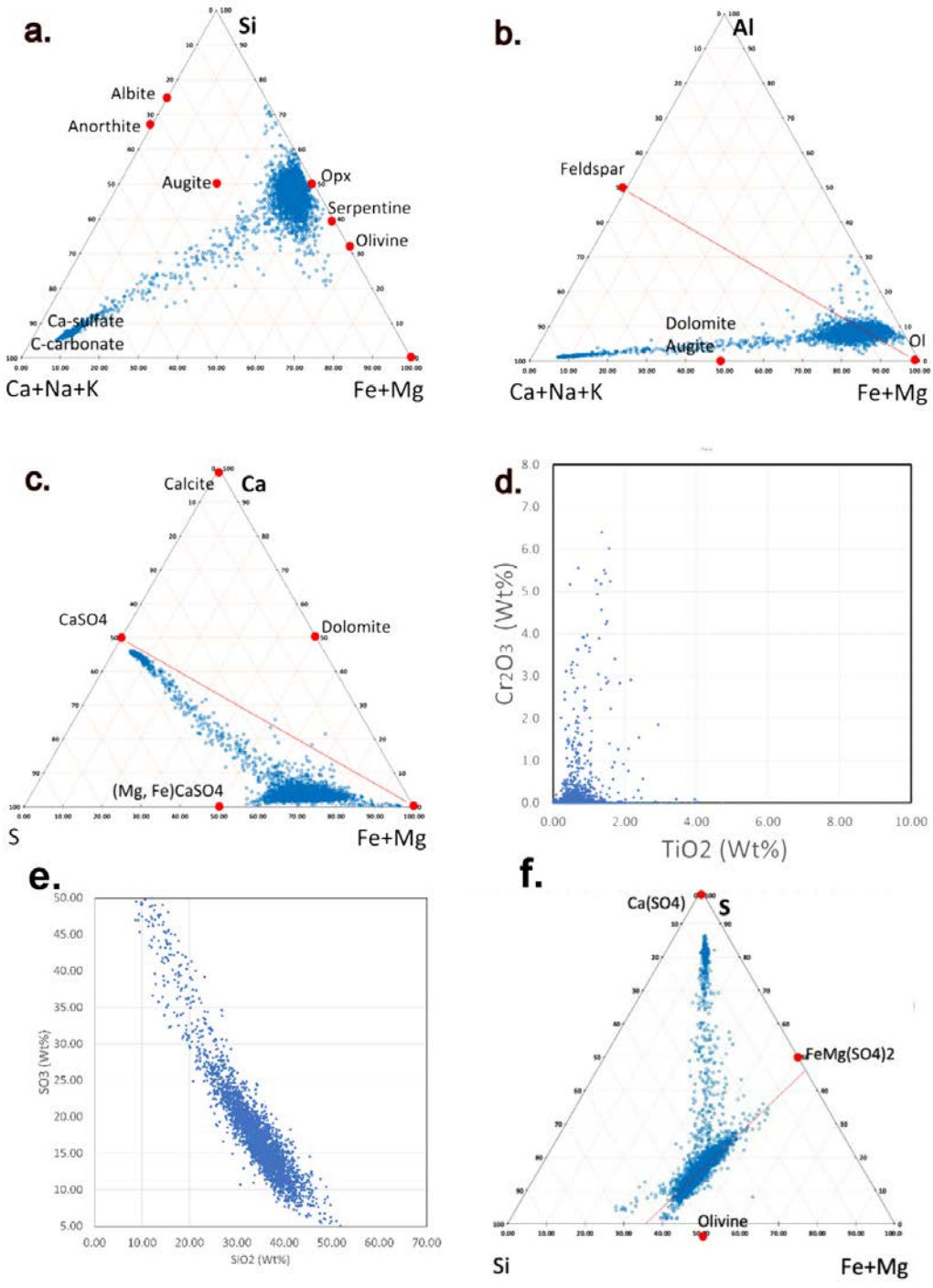

Figure 16 | **PIXL MCC (Micro-context camera) images for the *Uganik Island* abrasion of Sol 614 (scan area outlined)**. **(a)** MCC grayscale image, a portion of the ***Uganik Island*** abrasion. **(b)** MCC false color of abrasion area; Red = MCC Near-IR; Green = MCC Green; Blue = MCC Blue. **(c)** MCC ratio image of Green/Near-IR reflectances. **(d)** Graph of MCC reflectance ratios.

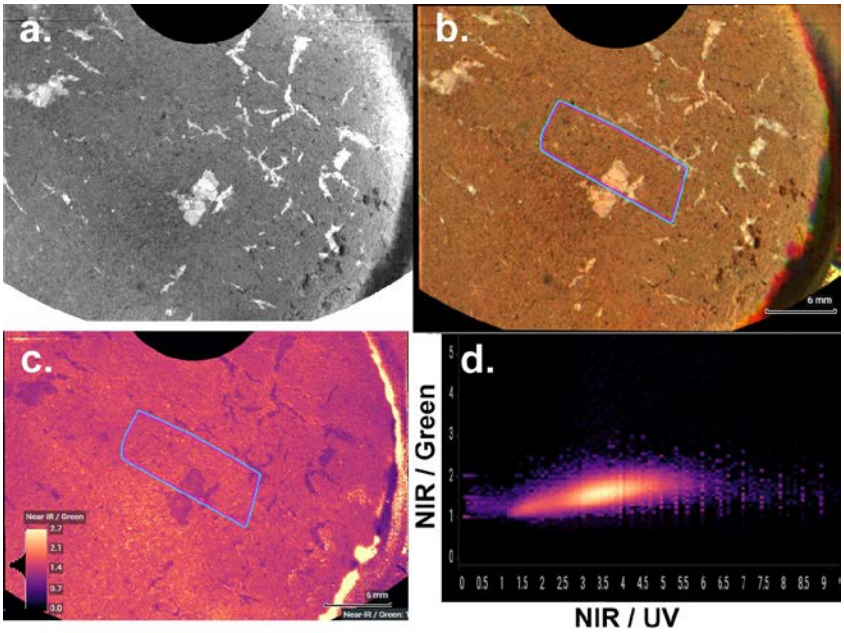

Mineralogy and Organics-SHERLOC

SHERLOC Raman and fluorescence spectra were obtained from two different areas of the abraded patch on Sols 614, 617, 618 and 620, respectively. The scans on Sols 614, 618 and 620 targeted a large white crystal while the scan on Sol 617 targeted a tan feature. The observations included two HDR scans (7x7 mm, 100 points, 780 µm spacing, 500 pulses per point), 4 survey scans (5x 5 mm, 1296 points, 144 µm spacing, 15 pulses per point) and 8 detailed scans (1x1 mm, 100 points, 144 µm spacing, 500 pulses per point or 900 pulses per point). This intense coverage was designed to better inform the distribution and origin of fluorescence detected by SHERLOC in this abrasion patch and in several previous rocks.

The Raman spectra from all scans contain peaks that can be assigned to sulfates (~1014-1018 cm^{-1}) (**Figures 17, 18, 19** and **Table 3**). The most intense sulfate spectra (~1016-1018 cm^{-1} and 1125 cm^{-1}) are typically associated with the white crystals observed in the abrasion patch and contain no or minor hydration peaks (~3400 cm^{-1}), indicating a minimally hydrated sulfate such as anhydrite. PIXL data shows that Ca and S are associated with the white crystals, confirming this assignment. The spectra from the tan feature show lower intensity sulfate peaks (~1016-1017 cm^{-1}) but relatively more-intense hydration peaks (~3400 cm^{-1}) indicating the presence of more-hydrated sulfates (**Figures 18 and 19**). PIXL data shows Mg/Fe associated with this feature. The fluorescence signals are dominated by a doublet fluorescence feature at 303 and 325 nm, which is most intense in the white sulfate crystals in both scan areas and is consistent with a mix of aromatic compounds but may also be consistent with an inorganic origin. In the Sol 614 survey scan this fluorescence is most intense in the boundary between the 'fish' white sulfate crystals and the matrix (**Figure 17**). In addition, there is a fluorescence feature at 340 nm,

which is consistent with a double ring aromatic, and is only detected in a few of points of the scans (**Figures 17 and 18**). The low fluorescence signal and the absence of any obvious organic signals in the Raman spectra suggest that any organic compounds present are in generally low abundance.

SHERLOC mineral identifications are shown in **Table 3**.

Table 3 | SHERLOC Raman spectra mineral ID.

Sample	Certain	Possible (not confirmed)	We looked for these, but cannot find them
Uganik Island	Sulfate (likely anhydrite) Sulfate (more hydrated, possible Mg/Fe-sulfate)		

Figure 17| Sol 614 SHERLOC fluorescence and Raman spectral results for *Uganik Island.* (a) Colorized ACI image of the *Uganik Island* abraded patch; blue rectangle indicates the detailed scan area and white circle indicate regions of interest (ROIs) correlating to the fluorescence data presented in (b) and (c). **(b)** Survey scan map showing the possible presence of organics. Upper panel shows an RGB map indicating the main regions of fluorescence. The lower panel is blank for this abrasion patch because no Raman features have been identified that would indicate the presence of organic materials. **(c)** Fluorescence spectra. The upper panel shows the average fluorescence spectrum for the whole area of analysis and the lower panel includes spectra from selected fluorescence ROI [see (a) and (b)]. **(d)** Map showing the results of the Raman survey scan. The left panel shows a map of intensity of spectra at ~1018 cm^{-1}, interpreted as sulfate. The yellow and white circles indicate regions of the scan deemed to represent the rock matrix (yellow) and the sulfate grain(s) (white). The right panel includes Raman spectra from the survey scan. The upper spectrum is the median of the spectra within the white circle and the lower spectrum is the median of spectra within the yellow circle.

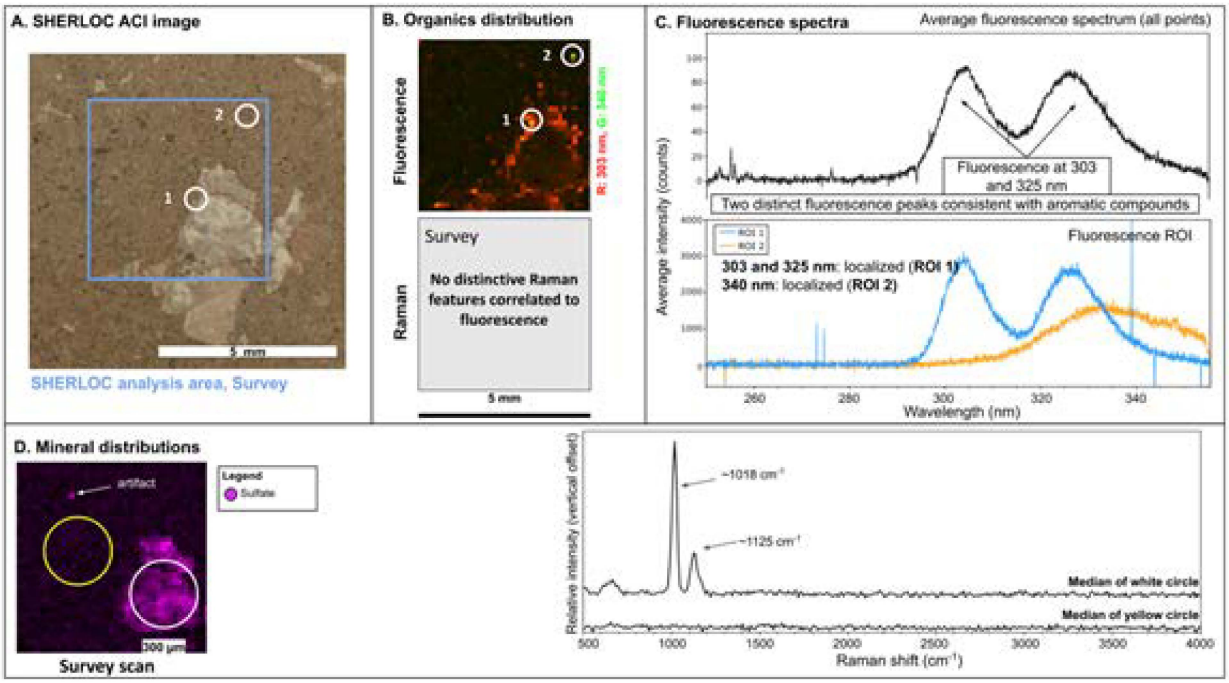

Figure 18 | **Sol 617 SHERLOC fluorescence and Raman spectral results for *Uganik Island*. (a)** Colorized ACI image of the *Uganik Island* abraded patch; blue rectangle indicates the HDR scan area and white circle indicate regions of interest (ROIs) correlating to the fluorescence data presented in (b) and (c). **(b)** HDR scan map showing the possible presence of organics. Upper panel shows an RGB map indicating the main regions of fluorescence. The lower panel is blank for this abrasion patch because no Raman features have been identified that would indicate the presence of organic materials. **(c)** Fluorescence spectra. The upper panel shows the average fluorescence spectrum for the whole area of analysis and the lower panel includes spectra from selected fluorescence ROI (see (a) and (b). **(d)** Map and spectra showing the results of the Raman HDR scan. The left panel shows a grid of open red circles that indicate the points analyzed superimposed on the grayscale ACI image of the scan area [cf. Panel (a)]. The circles represent the size of the analysis spots. The purple circles indicate points where spectra showing sulfates were detected. The numbers in certain circles refer to spectra called out in the middle panel. The middle panel includes Raman median spectra. The upper spectrum is the median of points 12, 15, 86, and 99, which have intensities that are 1–2 orders of magnitude stronger than the other spectra and are associated with the white crystals observed in panel A and the most intense fluorescence in panel B. This spectrum was reduced in intensity by a factor of 25 in order to compare it to the other two spectra. The lower spectrum is the median spectrum of points 44, 45, and 56, three of the points on the tan feature in the middle of the ACI image. The middle spectrum is the median of the unnumbered purple circles. The rightmost panel shows the same three spectra as the middle panel, in the same order, except the upper spectrum is shown at full intensity. This panel highlights the presence of weak broad peaks centered between ~3200 and 3400 cm^{-1}, which is interpreted to indicate the presence of hydration.

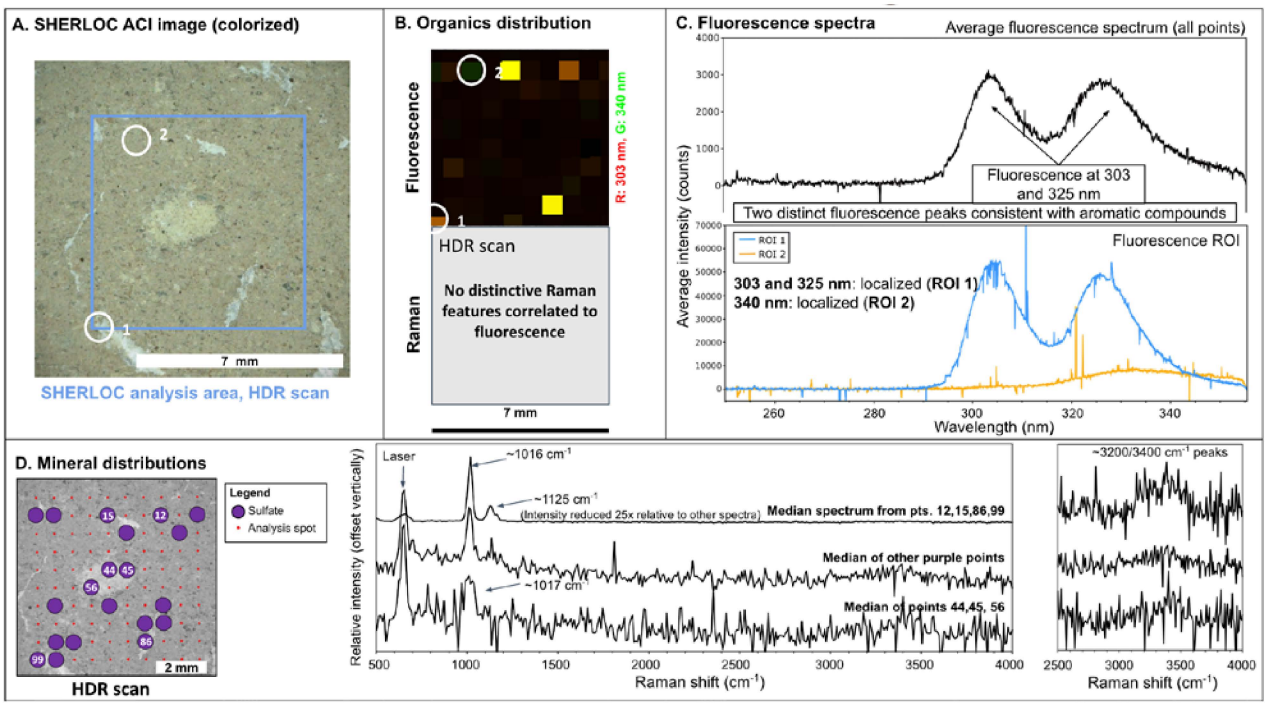

Figure 19 | **Sol 617 SHERLOC fluorescence and Raman spectral results for *Uganik Island*. (a)** Colorized ACI image of the *Uganik Island* abraded patch; blue rectangle indicates the detailed scan area and white circle indicate regions of interest (ROIs) correlating to the fluorescence data presented in (b) and (c). **(b)** Detailed scan map showing the possible presence of organics. Upper panel shows an RGB map indicating the main regions of fluorescence. The lower panel is blank for this abrasion patch because no Raman features have been identified that would indicate the presence of organic materials. **(c)** Fluorescence spectra. The upper panel shows the average fluorescence spectrum for the whole area of analysis and the lower panel includes spectra from selected fluorescence ROI [see (a) and (b)]. **(d)** Map and spectra showing the results of the Raman detail scan. The left panel shows a grid of open red circles that indicate the points analyzed superimposed on the grayscale ACI image of the scan area [cf. Panel (a)]. The circles represent the size of the analysis spots. The purple numbers in certain circles refer to spectra with much greater than average signal intensity. The right panel includes Raman median spectra. The lower spectrum is the median of points 2, 3, and 17 (note that these points are associated with the white crystal observed within the tan feature in panel (a) and the most intense fluorescence in panel B). The upper spectrum is the median of all of the other points. The intensity of this spectrum was increased by 75x to better compare the features. All spectra also contain a broad band centered at ~3400 cm^{-1}, interpreted to indicate the presence of hydration.

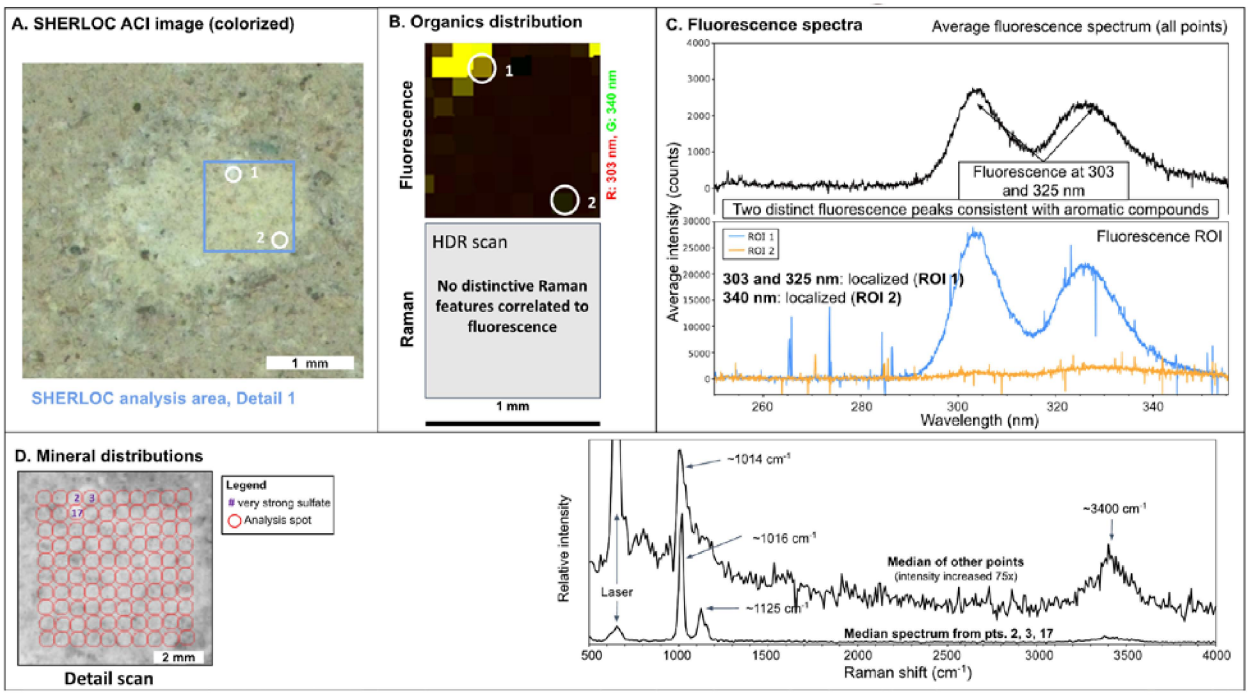

Elemental Geochemistry and Mineralogy – SuperCam.

SuperCam LIBS observations of *Hidden Harbor* (**Figures 20, 21**) show that the rocks are compositionally heterogeneous on the scale of RMI images (**Figure 6**) and LIBS raster spacing (generally a few mm). The points analyzed by LIBS compositionally group with pyroxene minerals (**Figures 20, 21**), although none seem to match pyroxene calibration standards and on-board calibration targets (**Figure 21**). None of the points from *Hidden Harbor* group with olivine or serpentine (**Figure 20**), but the ternary diagram shows a larger compositional spread towards both Si+Al and Fe+Mg relative to the finer-grained rocks at *Wildcat Ridge*, where the previous two cores of sulfate-rich sedimentary rocks were acquired.

The compositions of individual LIBS spots on the natural surfaces and on the abrasion patch *Uganik Island* are consistent with a mixture of low-Ca pyroxene and additional unrecognized phases. Three out of ten points that were analyzed by LIBS on *Hidden Harbor* abrasion patch had a total oxide content lower than 85 wt%, indicating the presence of elements that are not quantified by SuperCam such as H, C, S and Cl. Based on PIXL data the most abundant undetected element is S. All points presented evidence of hydration, but points in veins and bright areas exhibited lower H scores. These points are also enriched in calcium and exhibit low total oxide wt% values (**Figure 21**), consistent with the post-depositional formation of calcium sulfate minerals at *Hidden Harbor*. In fact, the Raman spectra of points on the vein in *Kupreanof_Strait* and points on the white material in *Uganik Island* (not shown) confirm the presence of anhydrite in the bright veins and areas. In combination, these observations support the interpretation of *Kukaklek* as a sample of subaqueously deposited sedimentary sandstone that was altered by later fluid flow that delivered calcium cations and enabled the precipitation of calcium sulfate minerals.

Figure 20| SuperCam LIBS major element oxide (MOC) analyses of *Hidden Harbor* rocks. Solid solution fields for olivine, pyroxene, and feldspar compositions are included. Black points indicate delta rocks analyzed from Sols 420-643.

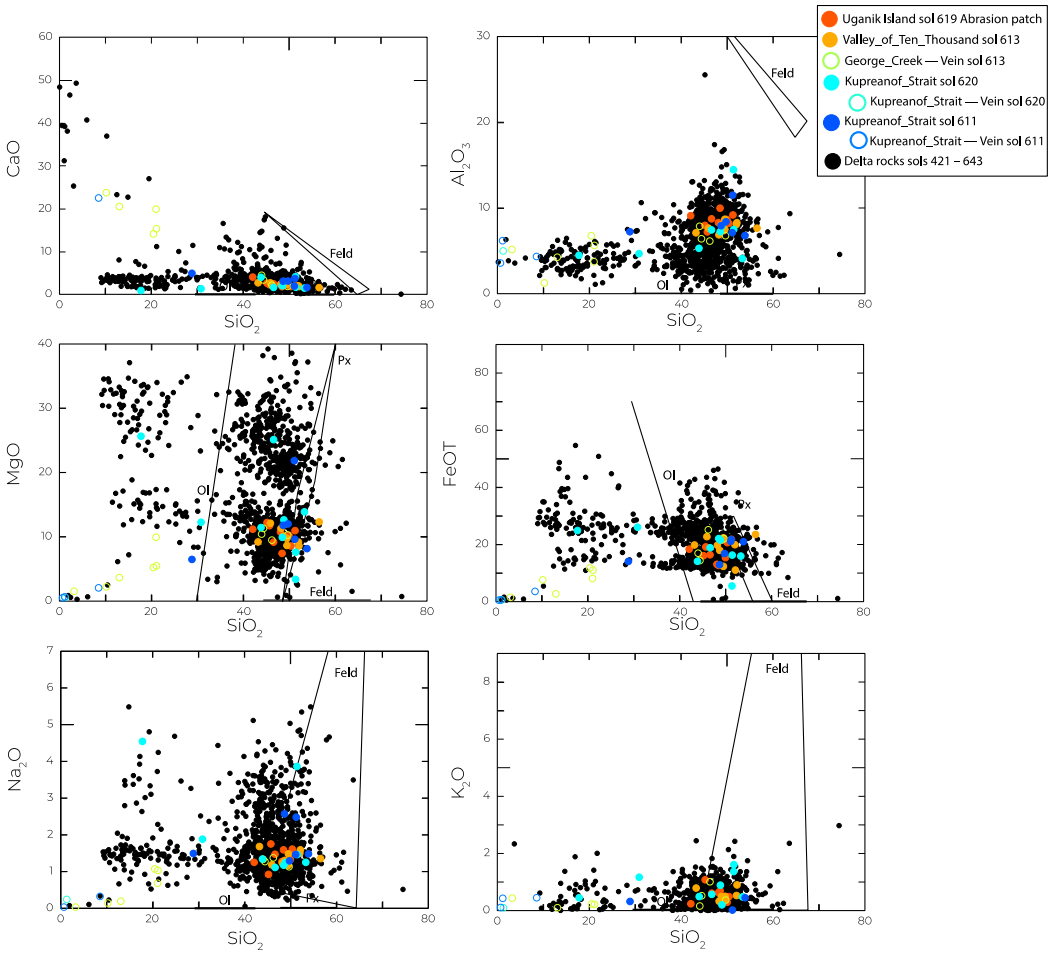

Figure 21| Molar compositions of the points in the LIBS raster of *Hidden Harbor* from Sols 611, 613, 619 and 620 compared to various minerals and on-board calibration standards. Analyzed points are shown by the yellow, orange, red and purple circles. Yellow and orange circles show points analyzed on the natural surface of the target *Kupreanof_Strait* on Sols 611 and 620. Red circles show points analyzed on the natural surface of the target *Valley_Of_Ten_Thousand_Smokes* on Sol 613. Purple circles show points analyzed on the abraded patch *Uganik_Island* on Sol 619. *Kupreanof_Strait* from Sol 620 contained a vein enriched in calcium, points analyzed in this vein cluster with gypsum in the left lower corner of the ternary diagram. One point from the abraded patch that was analyzed on a white area, where the Raman spectra indicated anhydrite, exhibits the same compositional grouping with gypsum. The legend presents a range of standards from igneous calibration targets (Ca-pyroxene, pyroxene, olivine) to other minerals (calcite, ankerite, siderite, serpentine, gypsum). The green cloud shows all data points acquired up to Sol 622.

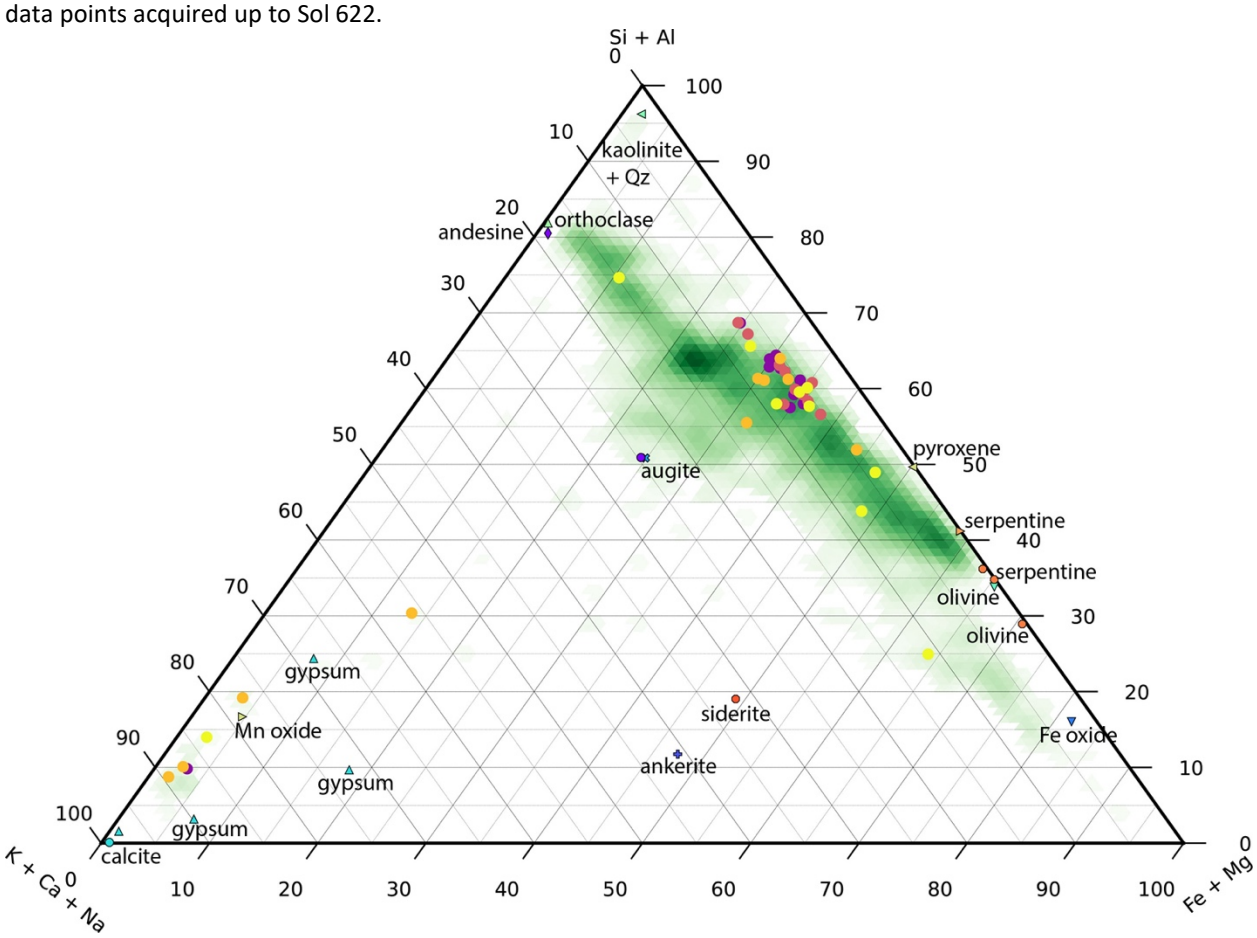

SuperCam VISIR rasters on the *Hidden Harbor* natural and abraded surface targets and tailings from the coring activity (**Figure 22**) reveal the presence of hydration and phases produced during aqueous alteration. SCAM VISIR technique is highly sensitive to hydrated minerals, so the signatures of hydration are present in the spectra even when these minerals are a minor proportion of the rock. **Figure 22** shows the absorption bands that indicate the presence of hydrated minerals. The main signals of hydration are present at 1.94 µm and 1.42 µm in abraded targets. The weak absorptions in the 2.1-2.5 µm range indicate small amounts of Fe/Mg-clay minerals, possible carbonates (2.53 µm band) and sulfate at 2.39 µm. Sulfate absorption is present both in and outside of the veins and is particularly prominent in the abraded patch. The absorption at 0.43 µm, attributed to ferric sulfate minerals, is present in *Uganik Island* at *Hidden Harbor*. The VISIR spectra are greatly affected by the grain size, contributing to the differences in the tailings and rock spectra, but all support the presence of hydrated, sulfate-rich, subaqueously deposited and aqueously altered sandstones at *Hidden Harbor*.

Figure 22| Mean reflectance spectra of the SuperCam VISIR rasters at *Hidden Harbor* outcrop. Mean reflectance spectra of the SuperCam VISIR rasters at *Hidden Harbor* (natural and abraded surface, tailings from coring activity and vein). Lighter line segments near 2 µm indicate the spectral range possibly affected by the CO_2 absorption features that could remain after the atmospheric correction. The UV region was smoothed using a Savitsky-Golay filter with a window length of 51. Note that owing to temperature sensitivities in the IRS instrument, the calibration is still uncertain for wavelength longer than ~2.55 µm. For the *Kupreanof_Strait* target that contained a vein, points #4-6 from Sol 611 and #1 from Sol 620 were averaged for the vein; for the natural surface, points #1, 8, 9 and 10 from Sol 611 and #3-10 from Sol 620 were averaged. The absorption centers are indicated with arrows and their positions point towards the presence of hydrated minerals: sulfates (including ferric sulfates), and Fe/Mg-phyllosilicates and/or carbonates.

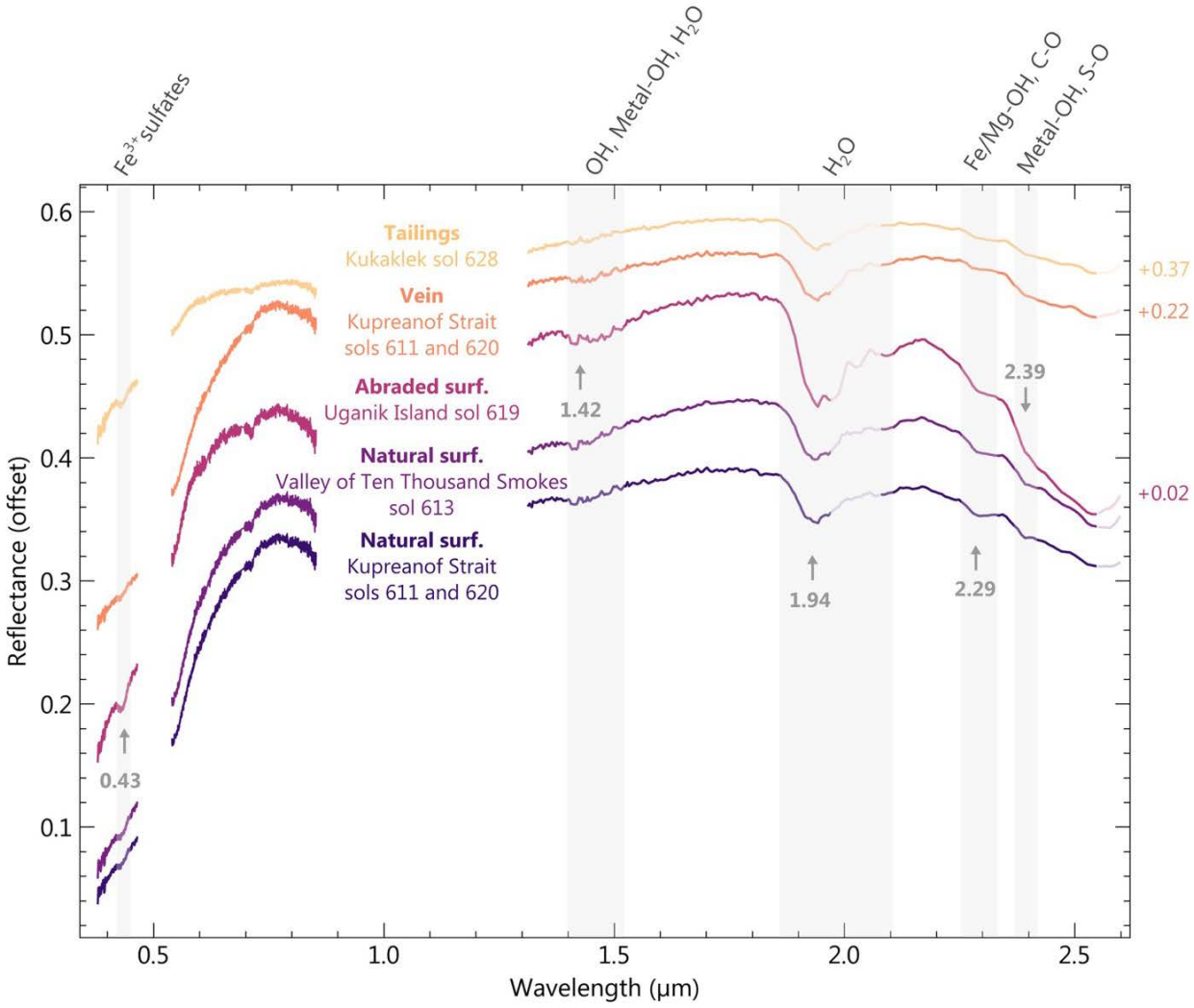

Subsurface Structure

The subsurface structure of the delta front near the *Hidden Harbor* outcrop on the western side of *Cape Nukshak* (**Figure 23**) is revealed by RIMFAX radargrams. The radargram was acquired on Sol 629 during a traverse headed south then east (see red line in **Figure 23a** beginning near the area labeled *Hidden Harbor*). The *Hidden Harbor* outcrop and adjacent units are generally horizontally stratified as seen in both outcrop and in the subsurface as illustrated by RIMFAX radargrams (**Figure 23b**). The *Hidden Harbor* samples were acquired near the base delta unconformity capping the underlying *Séítah* Formation strata, at depth -2535 to -2536 m. Depths have been calculated from two-way travel times using 0.125 m/ns.

Figure 23 | **Geological context and RIXFAX-derived subsurface stratigraphy of the delta front on the western side of *Cape Nukshak*. (a)** Location of the *Hidden Harbor* outcrop, from which the samples *Kukaklek* was collected, within the delta front. The inset shows the broader context of the sample location. The red line indicates the beginning of the traverse on Sol 629 during which RIMFAX radargrams were collected. **(b)** Radargram of the multileg traverse acquired on Sol 629 beginning near the *Hidden Harbor* outcrop. The radargram shows strata with largely horizontal geometries above the Séítah Fm.

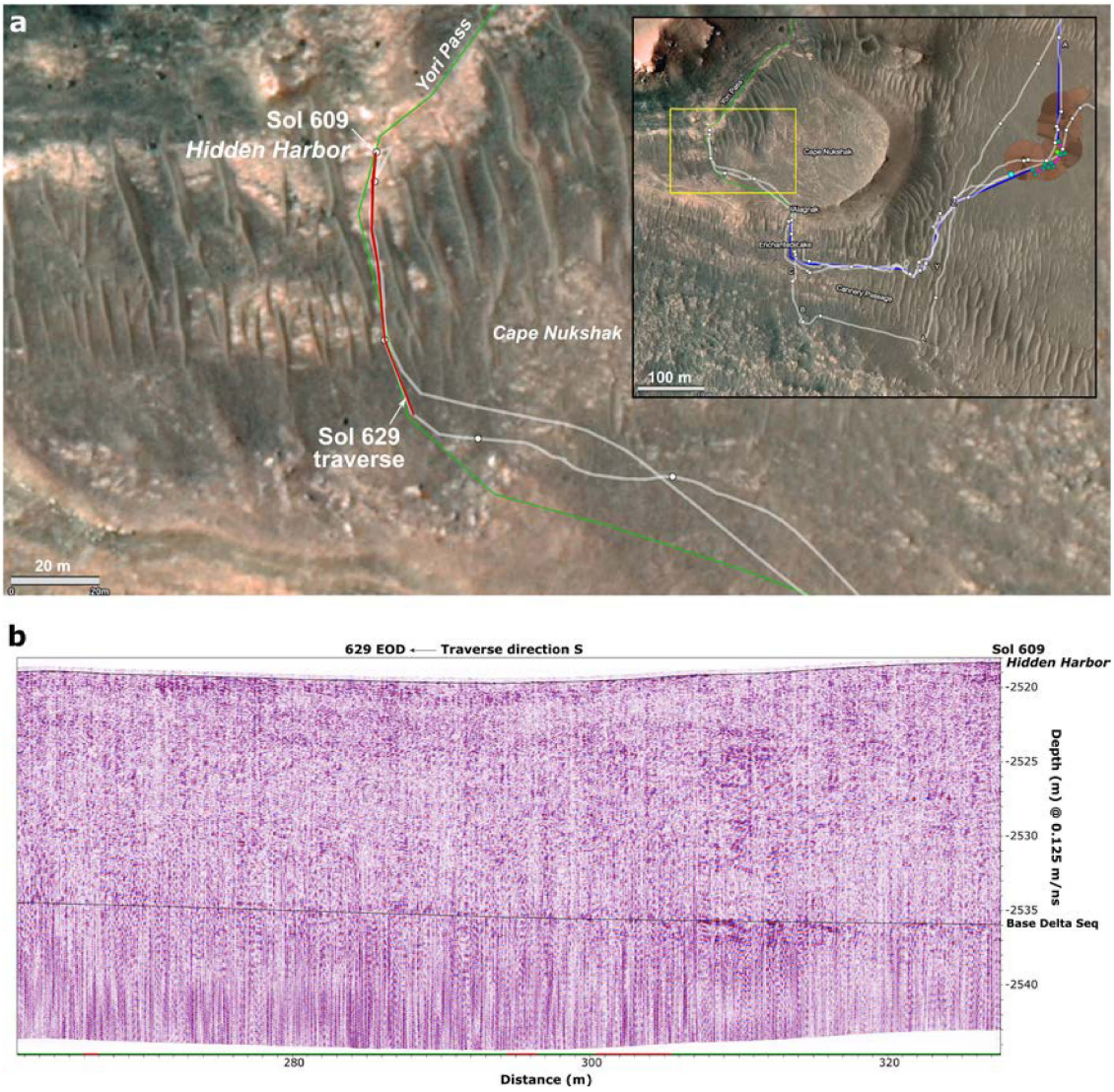

Core orientation

At the time of drilling and 5.7-cm pre-drilling WATSON imaging, the rover, Coring Drill, and WATSON had the following characteristics:

1. Rover orientation quaternion just after drilling but before unloading the stabilizers (transferring from RMECH to SITE frame): **bQll1** = (0.599375, 0.0166575, 0.0456629, -0.798991)
2. Coring Drill orientation quaternion just after drilling but before unloading the stabilizers (transferring from CORING DRILL to RMECH frame): **cdQb** = (0.666485, 0.242253, -0.660351, 0.247076)
3. Rover orientation quaternion at time of acquisition of WATSON image SIF_0614_0721455441_734FDR_N0301172SRLC00643_0000LMJ01: (transferring from RMECH to SITE frame): **bQll2** = (0.599385, 0.0143712, 0.0438615, -0.799129)
4. WATSON orientation quaternion at time of acquisition of WATSON image SIF_0614_0721455441_734FDR_N0301172SRLC00643_0000LMJ01: (transferring from WATSON to RMECH frame): **wQb** = (0.668613, 0.246199, -0.658112, 0.243375)

Items 1 and 2 give a coring drill pointing vector estimate of

hade = 6.15°
azimuth = **289.36°**

Items 3 and 4 give an estimate of the angle between the WATSON y-axis and the Core y-axis projected into the WATSON image plane (**Figure 24**) of:

core roll, α = **265.10°**

Figure 24 | Core orientation . 5.7-cm standoff WATSON image of *Kukaklek* core target on Sol 614. WATSON image SIF_0614_0721455441_734FDR_N0301172SRLC00643_0000LMJ01. Image scale is 27.4 µm pixel^{-1}. Orientation compass gives WATSON frame (**wx**, **wy**, **wz**). Core roll is **α** = 265.10°. Projection of Martian geographic north onto WATSON image plane is noted (clockwise angle of 335.85° from **wy**).

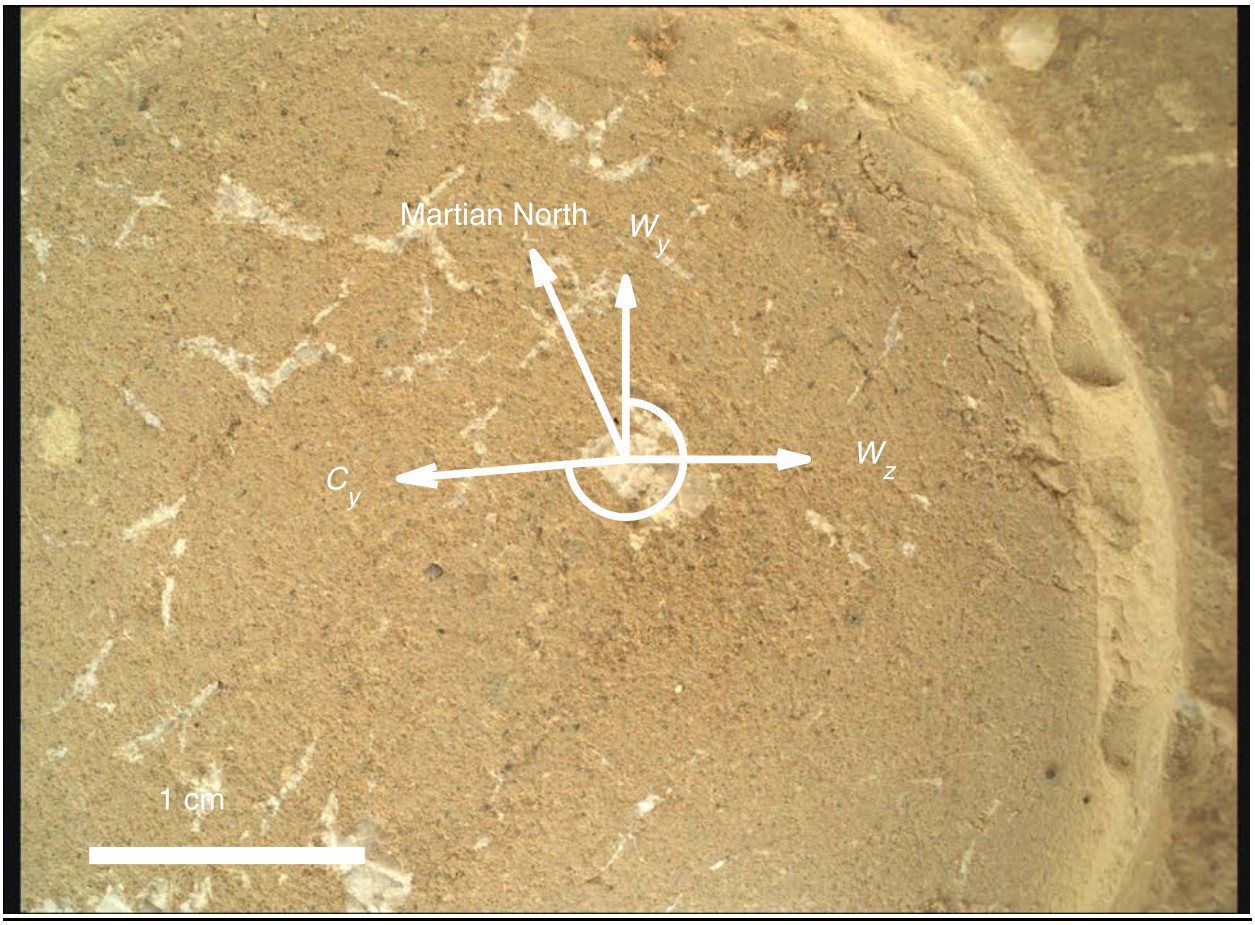

Preliminary Scientific Assessment

Synthetic sample description and preliminary interpretation

Sample type: **Fine-grained, moderately sorted sedimentary rock; a sulfate-bearing very fine sandstone.**

1. **Relationship with surrounding rocks**
    a. *Kukaklek* was obtained from a position relatively low in the accessible stratigraphy of Jezero Delta near the base of the *Yori Pass* member, roughly 10 m vertically above the lowest exposed delta outcrop in the *Cape Nukshak* region, *Kaguyak*, within the *Shenandoah* formation.
    b. Based on its appearance and concordance with surrounding outcrops in overall color and composition, the *Hidden Harbor* outcrop is interpreted to be an in-place portion of *the Yori Pass* member.
2. **Texture and fabric**
    a. Grain size: <0.03–1.2 mm
    b. Rock fabric (natural surface): the exposed surface is fractured, dusty, and light toned. Individual grains are not commonly visible on the surfaces, but raised, resistant features with a variety of shapes and sizes are present.
    c. Rock fabric (abrasion patch): a distribution of matrix-supported, very fine sand-sized (~70 μm) grains have a diversity in color, with a few individual grains as large as 1.2 mm in diameter. The grain size distribution is moderately sorted. The rock matrix is cut by small (mm-scale) veins and polycrystalline masses.
    d. The rock appears to be a moderately sorted, very fine sandstone.
3. **Mineralogy and chemistry**
    a. Minerals present: the rock matrix is compositionally diverse but spatially uniform and is cut by small veins and polycrystalline masses. Minerals detected in the matrix include weakly hydrated Mg-Fe sulfates and Mg-Fe silicates (possibly smectite); detrital fragment compositions are consistent with both Al-rich (e.g., kaolinite or montmorillonite) and Mg-rich clay minerals. The small veins and polycrystalline masses are composed of Ca sulfate (likely anhydrite). Minor materials detected also include possible carbonates, chromite, hydrated silica, and ilmenite.
    b. The rock appears to be minimally hydrated sulfate-bearing sandstone.
4. **Alteration/secondary characteristics**
    a. The presence of hydrated phases, the Ca-sulfate veins and polycrystalline anhydrite masses likely indicate diagenetic alteration.
    b. Secondary phases and/or cements indicative of aqueous alteration include small amounts of Fe-Mg-clay minerals, possible carbonates, and Al-clay minerals and/or hydrated silica.

Returned Sample Science Considerations

Since before landing, the delta stratigraphy and the western Jezero delta front have been the primary astrobiologically relevant mission sampling targets, *i.e*., sediments deposited into an ancient lake on Mars. Jezero Lake was likely present during the valley network-forming late Noachian to early Hesperian period of early Mars, and therefore delta sedimentary rock samples provide a potential record of the environmental conditions during that period. On Earth, early deltaic bottomset deposits often contain relatively fine-grained, organic-rich material, and can preserve ancient biosignatures. Coarser-grained (> mm) deltaic sedimentary units contain detrital materials that reveal the catchment source lithology and can be used to constrain delta deposition timing. Collectively, a set of coarse-grained *and* fine-grained sedimentary rock samples collected from the delta front in proximity provides a sample suite for addressing key goals of MSR.

The *Kukaklek* core is a fine-grained (up to ~200 um) sedimentary rock sample collected by the Perseverance Rover. The *Uganik Island* abrasion patch revealed white veins and patches composed of anhydrite. The *Kukaklek* core was taken through these prominent features to sample them. Thus, this sample partially fulfills the objective of collecting samples of fine-grained material with biosignature preservation potential. *Hidden Harbor* was chosen for sampling because it possessed several desired sample characteristics for a fine-grained sedimentary rock including: (1) grains ~70 μm (<30 μm up ~1200 μm); (2) siliciclastic and sulfate components; (3) a low delta/stratigraphic position; and (4) deposition associated with the delta. It additionally includes diagenetic sulfate materials, of potential astrobiological relevance.

Compared to the previously collected sandstone cores from *Skinner Ridge*, *Hidden Harbor is* substantially finer grained and richer in sulfate. *Hidden Harbor* is very similar in composition and grain size to the coarse mudstones from *Wildcat Ridge,* with which it may be correlative. Compared to *Bearwallow* and *Hazeltop* (the two cores from *Wildcat Ridge*), *Kukaklek* may be more chemically altered, and clearly has a greater abundance of diagenetic sulfate features.

Hidden Harbor is a very fine-grained sandstone that was deposited in a sub-aqueous environment within a lacustrine basin, and later altered by fluid flow that precipitated calcium sulfate minerals. Thus, the *Kukaklek* core records paleoenvironmental and paleoclimatic conditions of a formerly habitable environment. Laboratory-based investigations of this sample will enable reconstruction of chemical conditions in a subaqueous paleoenvironment, and interpretation of a sedimentary system in which aqueous processes occurred in Mars's past. These analyses will also enable characterization of the distribution and chemical diversity of organic molecules and the search for morphological and chemical biosignatures. The sample from *Hidden Harbor* can be used to address multiple science questions and objectives:

Geochronology: The observed mineralogy and fine grain scales observed in *Hidden Harbor* are not well-suited for existing methods of isotopic geochronology. However, it may be possible for existing methods of isotopic geochronology to be applied (or developed and/or refined) to constrain the timing of sulfate precipitation. In addition to quantifying the timing of late-stage aqueous activity, such information would place a *lower* bound on the timing of sediment/delta deposition. Observations of stable cosmogenic nuclides (e.g., ^{3}He, ^{21}Ne, ^{36}Ar, ^{38}Ar) in the bulk *Kukaklek* sample could quantify the

material's integrated cosmic ray exposure duration, thereby helping to constrain the latest-stage erosional history of the delta and the most recent cosmic ray exposure of the rocks in this vicinity.

Paleomagnetism: The sedimentary lithology of the *Kukaklek* sample may enable relative measurements of the paleointensity of the martian dynamo. In combination with radiometric dating, this could constrain the timing of the martian paleomagnetic field to test the hypothesis that martian atmospheric loss was driven by the cessation of an early dynamo. The orientation of the sample (**Figure 24**), combined with paleohorizontal indicators from the outcrop and sample, may enable measurements of the absolute paleodirection of the ancient field during or after deposition. This could constrain the dynamo's geometry, determine if the dynamo exhibited secular variation and polarity reversals, and constrain tectonic processes. Paleomagnetic investigations would also constrain the aqueous and thermal alteration history of the samples and, by implication, the preservation state of any potential biosignatures.

Texture: A key component of understanding fine-grained sedimentary rocks and the diagenetic processes that have acted upon them, is the ability to distinguish between authigenic and allogenic minerals. The fine-grained nature of the bulk/matrix material of the *Kukaklek* cores precludes making this distinction using Perseverance's in-situ instrumentation. Only returning samples for microscopic investigations would enable this level of understanding. This distinction is key to understanding what can be discerned about primary/catchment processes vs post-depositional processes experienced by these rocks.

Geochemistry: Elemental and mineralogical data from the *Uganik Island* abrasion patch reveal the presence of hydrated phases in the bulk/matrix material. LIBS analyses are consistent with a possible mixture of low-Ca pyroxene with other unrecognized phases. VISIR data is consistent with mineral phases including small amounts of Fe/Mg-phyllosilicates, possible carbonates, hydrated silica or Al-phyllosilicates, and sulfate. The sulfate signal occurs in both the bulk rock and veins and bright-appearing, polycrystalline masses. Raman spectra of veins in the area indicate anhydrite as the dominant sulfate phase. Ferric sulfate is indicated in the VISIR data of the bulk rock material. PIXL data confirms the presence of Fe/Mg-phyllosilicates and sulfates in the matrix. Matrix sulfate appears dominated by Mg-Fe^{2+} sulfates and confirms that the secondary veins and bright masses are composed of Ca-sulfate. PIXL data also indicates Al-rich and Mg-rich compositions of rock fragments with enrichments in Si and Cr, respectively.

Laboratory-based microscopic imaging and chemical mapping of the grains and grain boundaries at resolutions higher than Perseverance's in-situ instrumentation would enable distinction between authigenic, allogenic, and diagenetic solid phases. Chemical mapping at similarly high resolution can also determine whether organic compounds are preferentially distributed within the vein/bright area-filling anhydrite or are concentrated at the boundaries between those grains and the matrix.

Habitability and Biosignature potential: The *Kukaklek*/*Hidden Harbor* rock was deposited in a subaqueous paleoenvironment that, due to the presence of liquid water, is interpreted as formerly habitable. Sulfates have a recognized biosignature preservation potential. SHERLOC fluorescence data from the *Uganik Island* abrasion patch indicate a doublet fluorescence feature that is most intense in the sulfate-rich areas and at the boundaries between the sulfate crystals and the matrix. This signal is consistent with a mixture of aromatic compounds. A single peak fluorescence feature suggestive of a double ring aromatic was detected in only a few points. There is no organic signature present in Raman

spectra. These observations suggest a low abundance of organic compounds in these rocks. Yet, these rocks possess characteristics suggestive of biosignature preservation potential. Therefore, laboratory based, high resolution microscopic mapping of the mineral and organic distribution in the cores, along with analyses of organics extracted from these cores, may still reveal a greater presence of organic material and provide more detailed information on the organic signals and any associations with solid phases. Analyses that characterize the compositional, structural, and isotopic diversity of organic compounds found to be present in the *Kukaklek* core can also help distinguish any organics produced by prebiotic or abiotic processes from organics delivered from space.

Due to the small mineral grain sizes, constraints on the environmental conditions during the deposition of *Hidden Harbor* require textural analyses, identification of the coexisting primary mineral phases, and chemical modeling. These analyses will test whether the fluids were acidic or circum-neutral, oxidizing or reducing, and whether and how the original minerals were altered during diagenesis. These constraints will help establish whether this formerly habitable environment was extreme (e.g., acidic, hypersaline, or reducing) or more amenable to microbial life. In either case, sediments deposited in the Delta may have provided a habitat for active microorganisms and may have preserved microbial life that was present in the water column of Lake Jezero. As such, it is possible that organic materials and/or biosignatures have been preserved within sulfate phases within the *Hidden Harbor* outcrop. Cells and/or other organic materials could have been trapped in precipitated sulfates during deposition. Microscopic analyses of thin sections of the *Kukaklek* core from *Hidden Harbor* could contain organic inclusions or even body fossils encapsulated within or preserved by the mineral phases detected in the *Uganik Island* abrasion patch. Sample return and detailed analyses are required to search for these types of biosignatures.

References

Foord, E.E., Starkey, H.C., Taggart, J.E. *et al.* (1987) Reassessment of the volkonskoite-chromian smectite nomenclature problem. *Clays Clay Miner.* **35**, 139–149.

Lazar, O. R., Bohacs, K. M., Macquaker, J. H., Schieber, J., & Demko, T. M. (2015). Capturing Key Attributes of Fine-Grained Sedimentary Rocks In Outcrops, Cores, and Thin Sections: Nomenclature and Description Guidelines in MUDSTONES: NOMENCLATURE AND DESCRIPTION GUIDELINES. *Journal of Sedimentary Research*, *85*(3), 230-246.

Morata, D., Higueras, P., Dominguez-Bella, S., Parras, J., Velasco, F., & Aparicio, P. (2001). Fuchsite and other Cr-rich phyllosilicates in ultramafic enclaves from the Almadén mercury mining district, Spain. *Clay minerals*, *36*(3), 345-354.

Mangold, N., Schmidt, M. E., Fisk, M. R., Forni, O., McLennan, S. M., Ming, D. W., ... & Wiens, R. C. (2017). Classification scheme for sedimentary and igneous rocks in Gale crater, Mars. *Icarus*, *284*, 1-17.

Stack, K. M., Williams, N. R., Calef, F., Sun, V. Z., Williford, K. H., Farley, K. A., ... & Aileen Yingst, R. (2020). Photogeologic map of the perseverance rover field site in Jezero Crater constructed by the Mars 2020 Science Team. *Space Science Reviews*, *216*(8), 1-47.

INITIAL REPORT

M2020-634-20 *Atmo Mountain*

Sample Designation: M2020-634-20 *Atmo Mountain*

Date of Coring: 02-Dec-2022

Mars Time of Sample Core Sealing: 22:16 LMST, Sol 634, Ls 347.85

Latitude (N), Longitude (E), Elevation: 18.45131442, 77.40121811, -2525.061741 m

Campaign: Delta Front

Region of Interest: *Observation Mountain*

Lithology: Regolith sample consists of a mixture of coarse grains up to ~ 5 mm diameter, finer sand of various grades, silt, and likely (not directly resolved) atmospheric dust. Primary (igneous) minerals include variably altered olivine, pyroxene, Fe- and Ti-oxides, and possibly quartz. Secondary phases include sulfates and carbonates and possibly Fe-Mg phyllosilicates. Phosphates and aluminosilicates may be primary or secondary or both.

Estimated Volume Recovered: 7.47 cm^3

Coring Bit Number: Regolith

Core Orientation: NA

Sample Serial Numbers: Tube SN059; Seal SN098; Ferrule SN063

ACA Temperature at Time of Sealing: 40^o C

Estimated Rover-Ambient Pressure and Temperature at Time of Sealing: 722 Pa, 210 K

Estimated Amount of Martian Atmosphere Headspace Gas: $1.87x10^{-6}$ mol

Subsurface Regolith Targets: *Topographers Peak* (wheel scuff tailings pile), *Geographers Harbor* (wheel scuff tailings pile), *Fultons Falls* (wheel scuff wall), *Funnel Creek* (wheel scuff cavity floor)

Anomalous Behavior: Regolith assessment and sampling occurred in two separate phases (sols 593-606, and sols 632-641).

February 7, 2023

E.M. Hausrath, K.A. Farley, R. Sullivan, Y. Goreva, T. V. Kizovski, A. O. Shumway, A.H. Treiman, M.M. Tice, S. VanBommel, S. Siljeström, S. Sharma, E. Cardarelli, L. Mandon, A. Udry, A. Cousin, T. Bosak, R. Wiens, A. Vaughan, H. Amundsen, S-E. Hamran, A. Czaja, M-P. Zorzano, G. Martinez, C.T. Adcock, J. Simon, C. Herd, L. Mayhew, J.M. Madariaga, K. Williford, J. Johnson, D. Shuster, F. Calef, the PIXL team, the RSSWG, the Regolith WG, and the Mars 2020 Team

Summary Description

The *Atmo Mountain* and *Crosswind Lake* regolith samples were collected from the megaripple *Observation Mountain* (**Figure 1, 2**). *Observation Mountain* was selected for sampling because it is a large megaripple with sufficient size to allow sample acquisition and workspace analyses, and because it was thought to be less mobile than other potential sampling targets, allowing investigation of a surface likely impacted by martian surface processes such as crust formation. The rover's wheel was used to scuff the megaripple to expose material beneath the surface; this subsurface material likely dominates the regolith samples. The wheel scuff wall (*Fultons Falls*) (**Figure 2**) provided an in situ exposure of subsurface material for observations by Mastcam-Z, Supercam, and, at moderate standoff, WATSON. The wheel scuff tailings pile provided a positive-relief accumulation of sub-surface material that was large enough to be approached closely by PIXL, SHERLOC, and WATSON (target *Topographers Peak*) to compare with Mastcam-Z multispectral observations and Supercam observations (*Geographic Harbor*). The floor of the wheel scuff cavity (the wheel track) also was analyzed with Supercam and Mastcam-Z (target *Funnel Creek*). These multiple observations of the subsurface material help place the returned material, which was unavoidably mixed during collection, into context.

Grain size analysis indicates coarse grains on the surface, fine-grained material exposed beneath the surface, as well as likely atmospheric dust (not directly resolved). CacheCam images of *Atmo Mountain* show both coarse and fine-grained material present in the sample; *Crosswind Lake* shows only the presence of fine-grained particles but coarser particles are inferred to be present. Observed igneous minerals include pyroxene, Fe-Ti oxides, heavily altered olivine, and possibly quartz. Secondary minerals include sulfates and carbonates and possibly Fe-Mg phyllosilicates. Detected phosphates and aluminosilicates may be either primary or secondary or both. SuperCam observations are interpreted to indicate hydration of the regolith. The presence of fluorescence signatures, but no Raman signatures, suggest the presence of low concentrations of single and double ring aromatic compounds in the samples.

Atmo Mountain and *Crosswind Lake* are the first two regolith samples collected from the Mars2020 Perseverance landing site, and therefore increase the diversity of the sample cache. They provide information about the aeolian processes that currently dominate the surface of Mars, including fine-grained likely wind-blown material that may be common to many locations on Mars. In addition, they contain larger grains, likely from local outcrops. These larger grains may include material more friable than was collected in outcrop core samples. Some grains are heavily aqueously altered, and the sample may contain low concentrations of organic compounds. The collection of modern sediments thus complements the sedimentary and igneous samples already cored, and in addition will be useful for questions related to human health and in situ resource utilization.

Figure 1 | Regional context of Observation Mountain sampling site. (a) Bedrock and surficial geology and unit names from Stack et al. 2020. Black square is inset for (b).

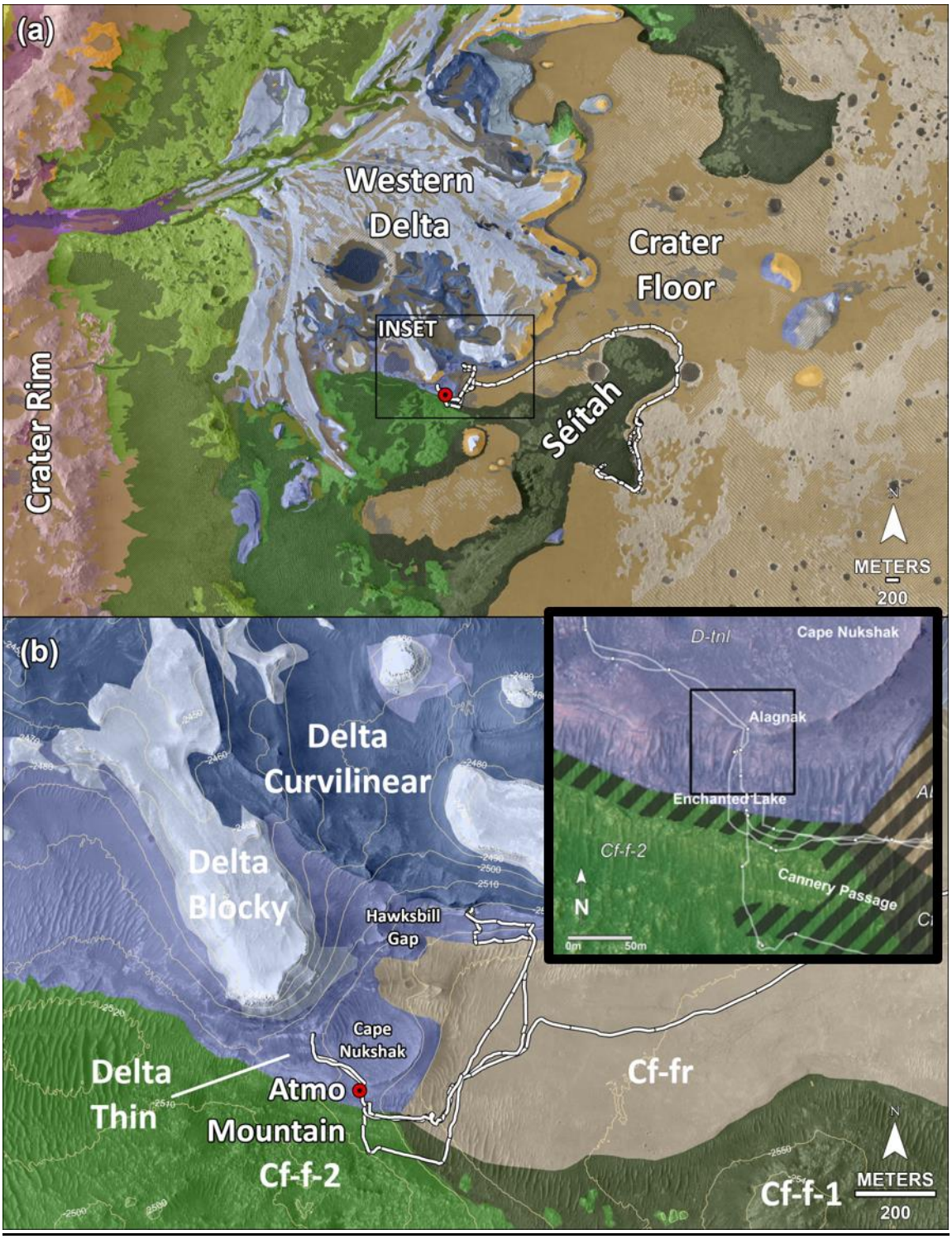

Figure 2 | ***Observation Mountain* images.** (a) HiRise image map and (b) Labelled locations of samples *Atmo Mountain* and *Crosswind Lake* and instrumental observations (*Granite Peak, Marmot Bay, Topographers Peak, Fultons Falls, Geographic Harbor,* and *Funnel Creek* (FHAZ image FRF 0593 0719593428 996CWS N0300000FHAZ02008 0A0095J01).

a)

b)

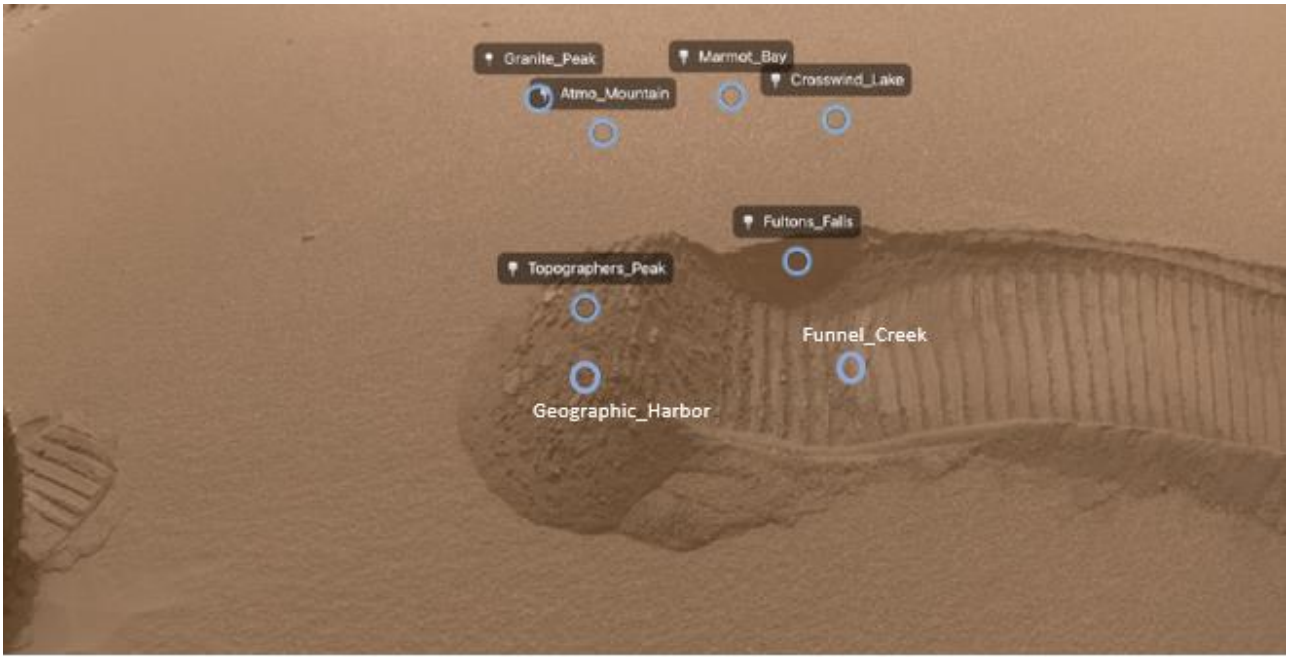

Stratigraphic and Geologic Context

The *Atmo Mountain* and *Crosswind Lake* regolith sample tubes were filled with material collected at *Observation Mountain*, a megaripple that is part of a field of broadly north-south trending aeolian bedforms lying on stratigraphy exposed on the southern slope of *Cape Nukshak* (**Figures 2, 3**). The regolith sample tubes may contain locally derived materials, e.g., the stratigraphic units explored and sampled by Perseverance, and material sourced more broadly including global dust. The nearby stratigraphic units include those found up section that comprise the eastern shoulder of the cliff-forming units of *Whale Mountain* as well as the low relief outcrop *Hidden Harbor* from which the *Kukaklek* core was obtained, see **Figure 4**. *Hidden Harbor* contains the light-dark layers of *Yori Pass* that likely correlate to the *Hogwallow Flats* unit found in the *Hawksbill Gap* area. Below *Hidden Harbor* and the *Alagnak* ledge-forming unit is *Knife Creek*, a low relief slope-forming unit. At the base of *Cape Nukshak* is *Enchanted Lake* and the outcrop *Amalik* from which the *Mageik* and *Shuyak* cores were acquired. The regolith samples could also include material that has migrated up-slope from the Jezero Crater Floor.

Figure 3 | Geologic setting of the *Observation Mountain* megaripple. The megaripple is one of a family of such features on the slope of the region shown in this image, called *Cape Nukshak*. Labelled units in this image are thought to be sedimentary, and associated with the Jezero western delta. The crater floor is stratigraphically lower and lies about 100 meters to the south of the sampling site.

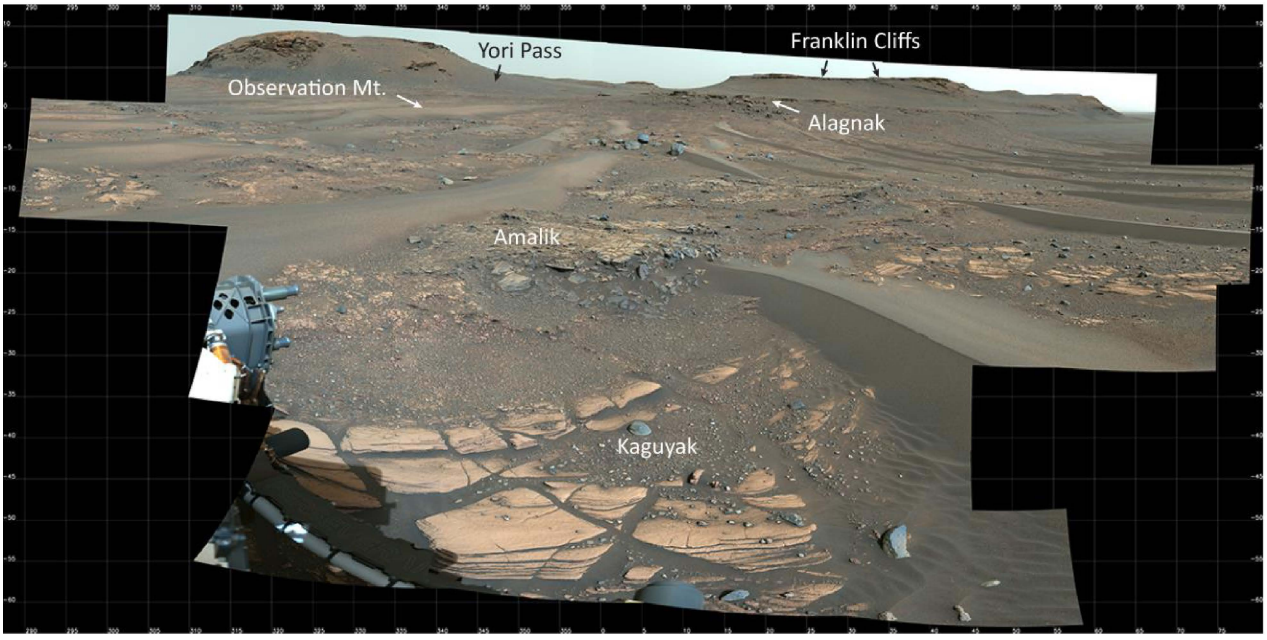

Figure 4 | **View upslope from *Observation Mountain.*** Labelled units are sufficiently close-by that they may have sourced some of the grains within the regolith samples. *Uganik Island* is the abrasion patch associated with the *Kukaklek* core.

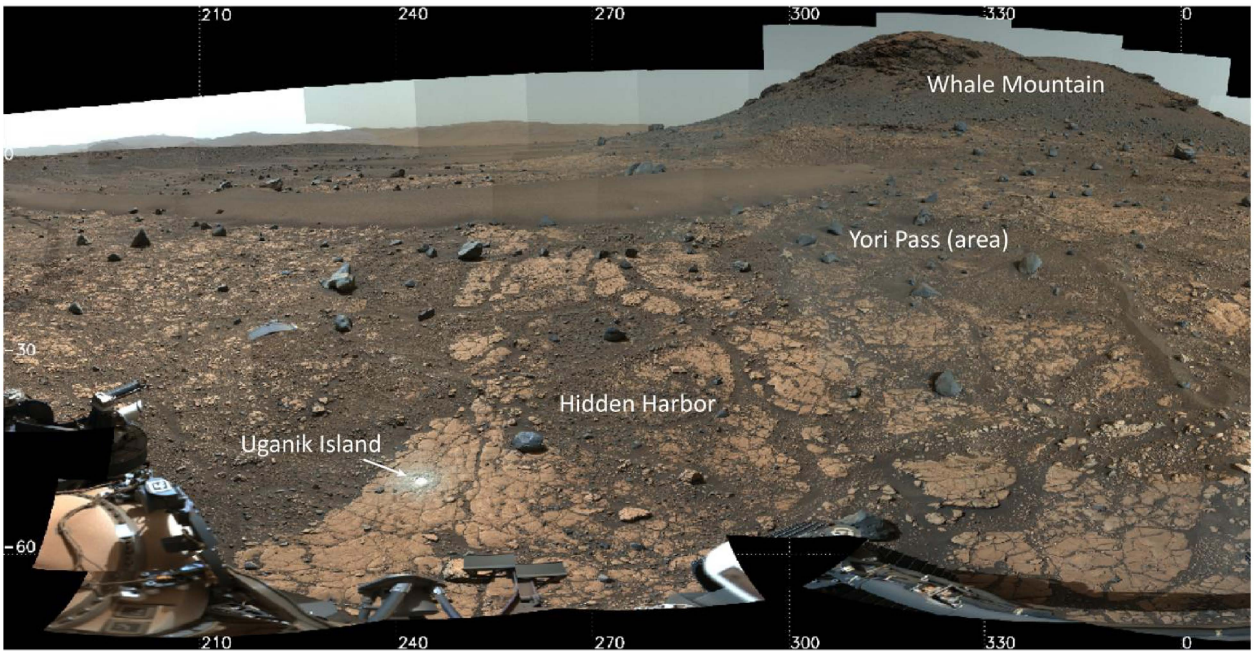

Operations

Mars 2020 rock samples have been chosen for their potential to reveal the history of Mars and especially of the Jezero fluviolacustrine system that might preserve ancient habitable environments (Farley et al., 2020). These same goals apply to sampled regolith to be returned to Earth. It was therefore desirable that the sampled regolith include both locally-sourced materials as well as components representative of the regolith mantle that covers much of the martian surface. Such regolith components include a broad range of grain sizes, which reflect different maximum potential aeolian transport distances from source rocks during the arid last half of martian history: (1) dust particles <4 µm, small enough to be suspended in the atmosphere by wind, and sourced from around the planet; (2) silt and sand-sized grains capable of saltation and perhaps short-term suspension, capable of traveling relatively long distances from various source regions, with <150 µm grains sharing similar compositions at widely dispersed locations across the planet (e.g., Clark et al., 1982; Rieder et al., 1997; Yen et al., 2005; Brückner et al., 2008, Cousin et al., 2017); and (3) coarser grains capable only of short, creep-like motion (driven by high-speed impacts of finer, saltating grains) that are likely sourced from local materials, possibly including the *Séítah* and *Máaz* crater floor units (Farley et al., 2022) as well as delta rock units that in turn were sourced from throughout the watershed of the delta (e.g., Goudge et al., 2015). Experience during previous rover missions (MER-A, MER-B, MSL) revealed that megaripples—aeolian bedforms mostly covered with coarse grains, but with finer-grained interiors—would likely allow collection of all three desired components. Experience also revealed the ubiquitous presence of cohesion within regolith (e.g., Moore et al., 1987; Sullivan et al., 2011), a characteristic also

displayed by regolith crusts in Jezero. For this reason a relatively inactive megaripple with surface crust development was desired for regolith sampling. Finally, the choice of an inactive megaripple was desirable for technical reasons, to avoid subsurface rocks interfering with the regolith collection process during the lateral motions of the bit while it is sweeps through the regolith. A megaripple located near the delta, to maximize the potential collection of material that differs from the crater floor, and potentially includes material from outside the crater, was chosen.

The rover arrived near *Observation Mountain* on sol 592, then executed a precision approach and wheel scuff on sol 593 to create a workspace that included exposures of undisturbed megaripple surface (dominated by coarse grains >1 mm), as well as much-finer subsurface material exposed in the wheel scuff tailings pile, scuff wall, and scuff floor. Analyses of the undisturbed surface, the tailings pile resulting from the scuff, and the edge of the scuff were completed through sol 606. Due to problems with sealing the *Mageik* core that temporarily precluded regolith core acquisition, the rover left *Observation Mountain* on sol 606 and drove to *Hidden Harbor* in *Yori Pass*. Once there the *Kukaklek* core was acquired and the *Mageik* tube was sealed. On Sol 633, the rover returned to *Observation Mountain*, arriving within mm of its original location. The rover then completed the regolith STOP list, including sampling of *Atmo Mountain* on sol 634 and *Crosswind Lake* on Sol 639, and post sampling STOP list analyses.

The regolith collection process involves a hollow drill bit with access windows (**Figure 5**). The bit is pushed into the surface while spinning, then tilted back and forth as the bit continues to spin while embedded in the regolith (Moeller et al., 2020). These actions force regolith materials extending from the surface down to a depth range of 4-6 cm through the access windows and into the hollow collection area within the bit (Moeller et al., 2020). The bit is then inverted causing the sample to slide into the sample tube inside the bit. This process mixes the constituents of the regolith, likely destroying any regolith stratigraphy. The regolith sample tubes are identical to the tubes used for rock cores, only the bit differs.

This procedure at both sampling sites (*Atmo Mountain* and *Crosswind Lake*) disturbed only relatively small areas of the megaripple surface.

On sol 641 the rover drove away from *Observation Mountain*, towards the *Three Forks* Sample Depot location.

Figure 5 | **Regolith sampling bit.** The bit contains two windows that are each 8 mm tall x 7.4 mm wide.

Sample-Related Observations

Workspace Images

Figure 6 shows context images of the *Observation Mountain* workspace. Images were taken on approach to, and positioned at, the workspace, and after sampling of *Atmo Mountain* and *Crosswind Lake*. The decimeter-scale bedform from which the samples were taken is continuous over several meters and is similar in size, shape, and appearance to nearby bedforms. The size of the bedform at this location is ~4 m wide and 1.1 m tall. The megaripple surface appears to be dominated by coarse (>1 mm) grains, with intervening much-finer material that is more common lower on the megaripple's flank.

Multispectral images of *Observation Mountain* included the natural surface of the megaripple at a target called *Granite Peak*, the tailings pile created by the wheel scuff activity at the target *Topographers Peak*, the scuff wall and wheel track at the target *Fulton Falls*, and tailings created by the *Crosswind Lake* sampling event. These data reveal at least two populations of coarse grains forming an apparent surface armor on the bedform (**Figure 7**), and spectral differences between the finer-grained regolith exposed on natural surfaces and material that is disturbed or initially below the bedform surface (**Figures 7, 8**).

The surface of the megaripple is covered mostly with relatively coarse grains. These include rounded dark-toned grains commonly 1-2 mm across, and larger 3-5 mm light-toned, platy, partly rounded, polygonal grains. The light-toned fragments have more ferric iron spectral features including peak reflectance at 800 nm and 528 nm and 866 nm absorptions. Spectra have flat slopes between 978-1022 nm. The smaller, darker-toned grains have more mafic (pyroxene-dominated) spectral signatures with reflectance peaks at 677 to 754 nm and broader 900 nm absorptions (**Figure 7d**).

Relative reflectance of fine-grained surface material is similar to the dark-toned grains. The 866 nm absorption band associated with ferric iron is narrower in the undisturbed region, and exhibits a positive slope between 866 and 1022 nm, consistent with hematite. In the LIBS dust-cleared area, the 866 nm absorption is more broad, and the material is darker (**Figure 7c**). This is consistent with the removal of ferric dust by the LIBS laser, revealing more-mafic materials. Disturbed fine-grained regolith exposed in the wheel trench and by sampling is dark-toned. It does not have the 866 nm absorption center associated with ferric iron. This observation suggests material at depth is less oxidized (poorer in hematite) than surface material (**Figure 8**). The wheel track and the scuff tailings have broader 900 nm absorptions, consistent with the ferrous iron absorption in some pyroxenes. The *Crosswind Lake* sample tailings have a narrower absorption at 900 nm, suggesting possible mixing of more ferric-rich surface and more mafic subsurface materials.

Figure 6 | Context images for *Observation Mountain*. A) was taken on approach to the bedform on sol 593, prior to the wheel scuff, looking approximately west. The sample locations are indicated by the red circles (*Atmo Mountain* = left, *Crosswind Lake* = right) (QZCAM SOL0593 ZCAM08608 L0 Z034 OBSERVATION MOUNTAIN REGOLITH SAMPLE CONTEXT E01). B) was taken on sol 639, after returning from *Yori Pass*, and after both regolith samples were acquired. Scale bar applies to the surface sampled. Locations of sampling targets *Atmo Mountain* and *Crosswind Lake* are indicated. Note the wheel scuff approximately 40 cm below the sample holes. (NLF 0639 0723682394 977RAS N0310000NCAM00709 0M0095J01). C) and D) were taken on sols 638 and 641, respectively, and show the holes after sampling. QZCAM SOL0638 ZCAM03496 L0 Z110 ATMO MOUNTAIN REGOLITH SAMPLE HOLE TAILINGS RETAKE PINHOLE E01); (QZCAM SOL0641 ZCAM03499 L0 Z110 CROSSWIND LAKE REGOLITH SAMPLE HOLE TAILINGS PP E01).

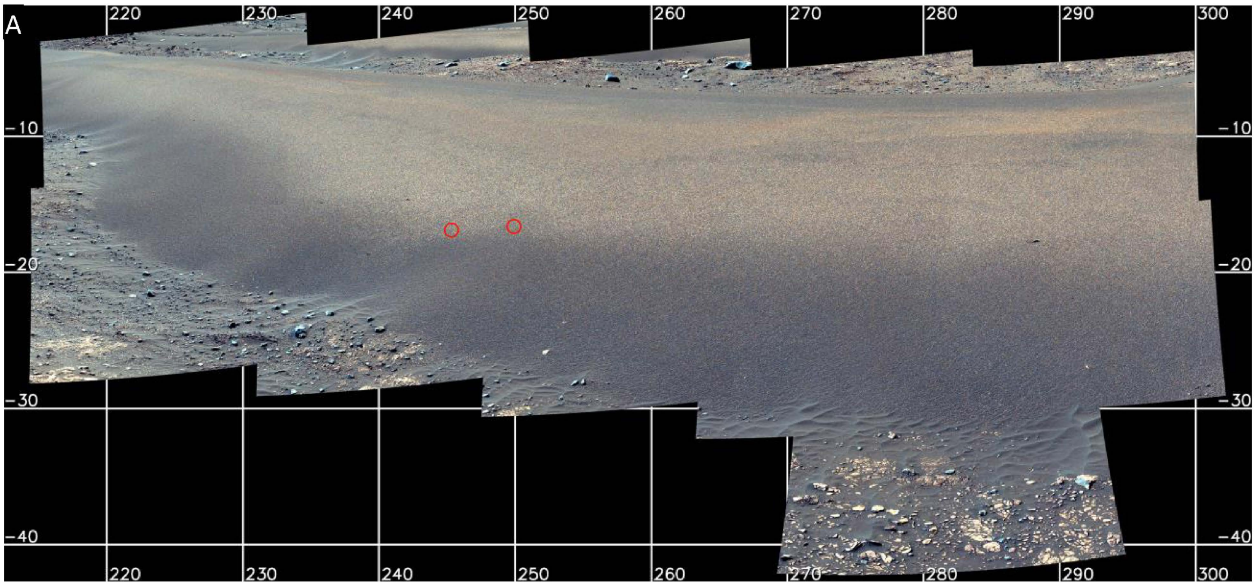

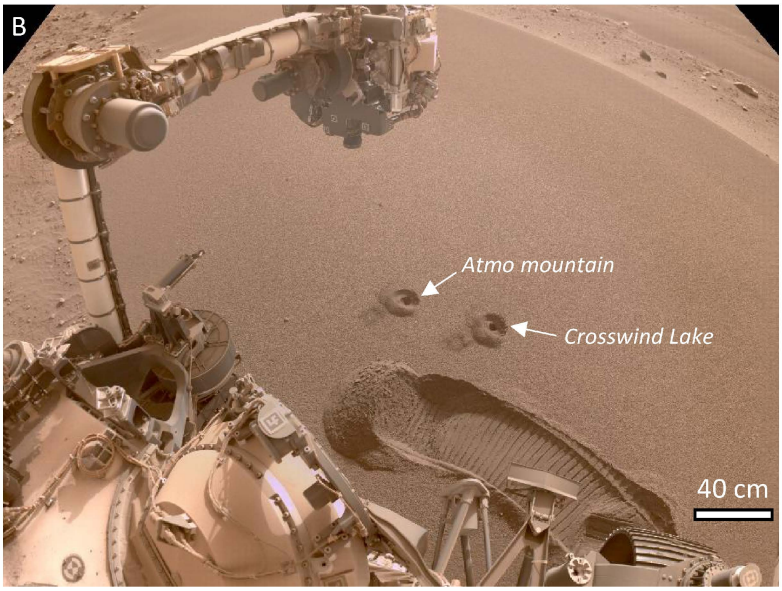

Figure 7| **Mastcam-Z *Granite Peak* multispectral data.** (a) Mastcam-Z enhanced color left-eye image of the *Granite Peak* target on the surface of the *Observation Mountain* mega-ripple taken at 110 mm focal length. The top brightly-colored box outlines the area cleared of surface dust by SuperCam LIBS laser shots, filled in with left-eye decorrelation stretch data (754 nm, 528 nm, 442 nm) to highlight the color diversity of the materials present. (b) Left-eye decorrelation stretch data showing representative examples of the finer-grained material, the larger light-toned fragments, and smaller, darker-toned, rounded grains. (c) Mastcam-Z spectra of undisturbed and LIBS dust-cleared finer-grained material. (d) Mastcam-Z spectra of the coarser grains on the surface (undisturbed and LIBS dust-cleared examples).

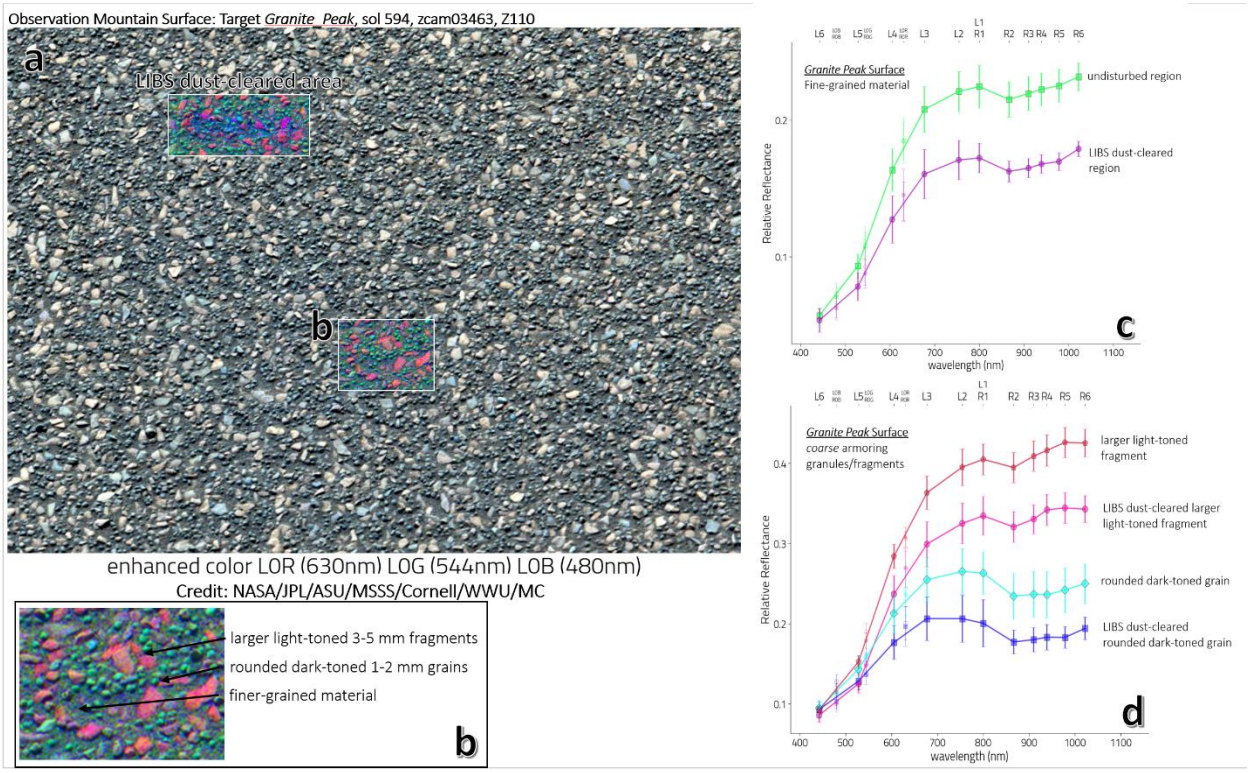

Figure 8 | **Mastcam-Z multispectral data and images of disturbed fine-grained regolith targets.** (a) Multispectral data obtained from areas marked by arrows in images in panels b-c-d. (b) Mastcam-Z enhanced color left-eye (L0: 630 nm, 544 nm, 480 nm) images taken at focal length 110mm of *Crosswind Lake* sample tailings (c) *Fultons Falls* scuff wall and wheel track, and (d) *Topographers Peak* scuff tailings.

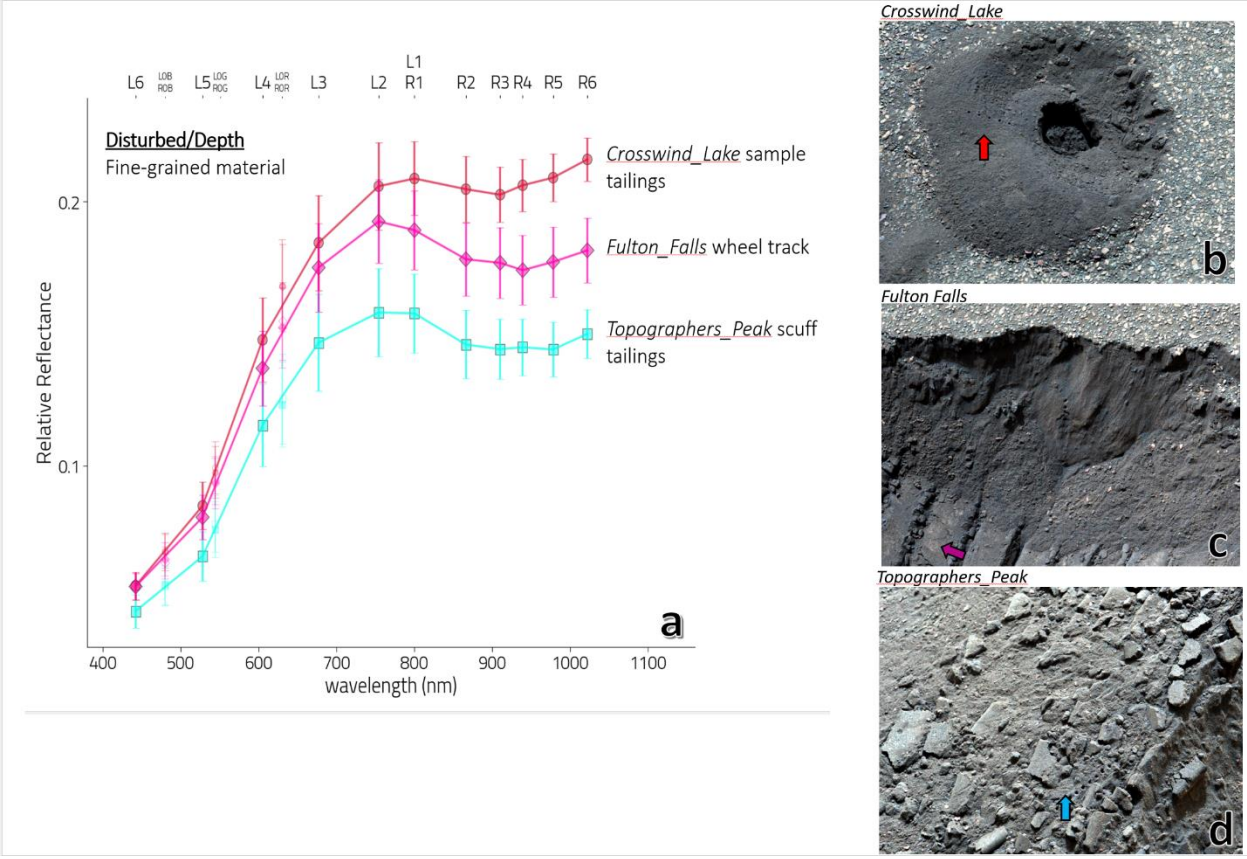

Environmental Observations

On the sampling sols (634 and 639), environmental measurements by MEDA were obtained during the first 15 minutes of each hour, with three additional 15-min-long floating sessions that were used to document conditions during sample sealing and sunrise and sunset. Of particular interest for the regolith samples are measurements of ground temperature and relative humidity. **Figure 9** shows the field of view of the MEDA ground temperature sensor and the location of the regolith samples. While the sampling sites were not within MEDA's field of view, measurements of ground temperature should be representative of those sites because they were acquired at similar positions part way up the flank of the megaripple.

Figure 9 | **Temperature measurement location and sampling sites on *Observation Mountain*.** The green shaded area indicates the MEDA ground temperature sensor field of view, which covers an ellipsoid of approximately 3–4 m^2 centered ~3.75 m away from the rover's Radioisotope Thermoelectric Generator to avoid thermal contamination. The white arrows point to the regolith sample sites, which are ~50 cm apart. The attitude of the rover during sampling was: roll = -5.635 deg, pitch 2.371 deg, yaw = -107.390 deg and tilt = 6.112 deg. Sol 639 Navcam mosaic.

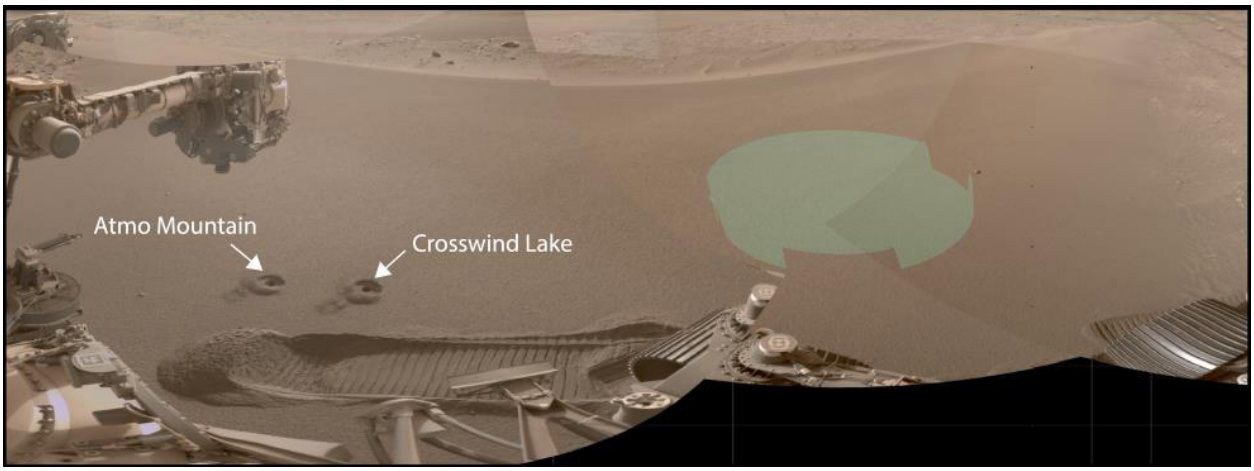

Figure 10 shows MEDA measurements of ground temperature and relative humidity (RH) at 1.5 m height on sols 634 and 639. Also included are estimates of RH at the ground assuming that water vapor content is constant within 1.5 m above the surface. At the time of sampling, the ground temperature was ~255 K while the RH at both 1.5 m and the ground surface were virtually 0%. Interestingly, estimated values of RH at the ground surface show supersaturation (> 100%) during early a.m. hours (blue region in **Figure 10**, bottom). However, these values represent an upper limit because adsorption of water vapor onto the ground is likely occurring at night, which would reduce the water content at the ground compared to that at 1.5 m and therefore the actual RH values at the ground. Consequently, it is uncertain whether frost formed on the regolith sampling area overnight.

Figure 10 | **Environmental conditions during regolith sampling.** (Top) Ground temperature measurements at 1 Hz on sols 634 and 639. Regolith sample collection activities started at 15:54 on sol 634 and at 15:52 LMST on sol 639 (vertical dashed line), and lasted for about 43 minutes in both cases. The ground temperature is measured with an accuracy of 0.75 K and a resolution of 0.08 K. Differences in ground temperature between sols are likely due to different atmospheric aerosol content and hence opacity, which was retrieved from Mastcam-Z images on sol 634 at 12:32 LTST, and on sol 639 at 13:25 LTST, with values at 0.88 μm of 0.916 and 0.797, respectively. (Bottom) MEDA's relative humidity measurements at 1.5 m on sols 634 and 639. Their uncertainty is <4.5% for sensor temperatures above 203 K, and <6% down to 190 K. Also shown are estimated values of relative humidity at the ground (squares) assuming a constant vertical profile in the first 1.5 m. The blue region indicates the period in which saturation at the ground may have been reached on both sols, between ~04:00 and ~07:30 LMST.

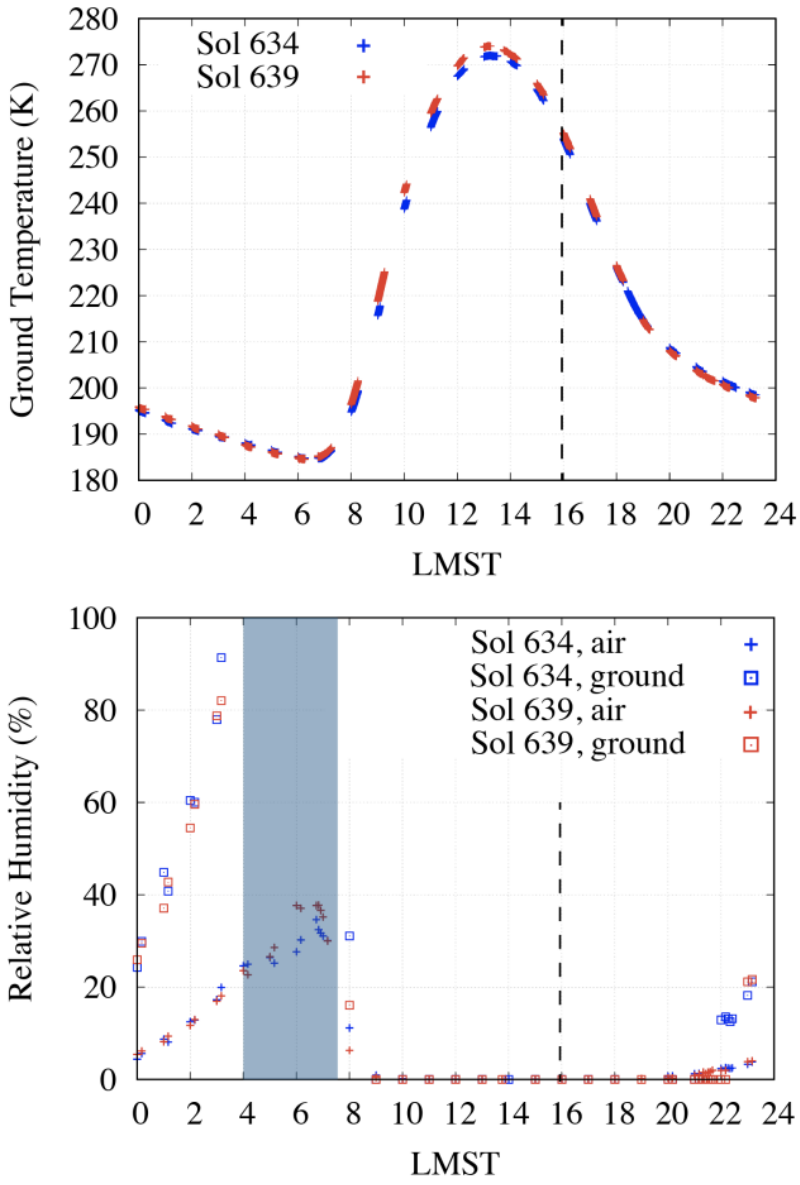

Figure 11|Regolith sampled from the *Observation Mountain* workspace imaged pre- and post-sampling. Navcam images document the (A) wheel-scuffed *Observation Mountain* workspace before regolith sampling (A) and after (F). Mastcam-Z images document the sampling sites after acquisition (*Atmo Mountain*, left borehole (B) with pre-sampling context (C); *Crosswind Lake*, right borehole (G) with pre-sampling context (H). WATSON imaging of *Atmo Mountain* (D, E) and *Crosswind Lake* (I, J) at multiple standoffs (~40 cm (D, I), ~7 cm (E, J) detail the heterogeneous grains sampled from the megaripple surface.

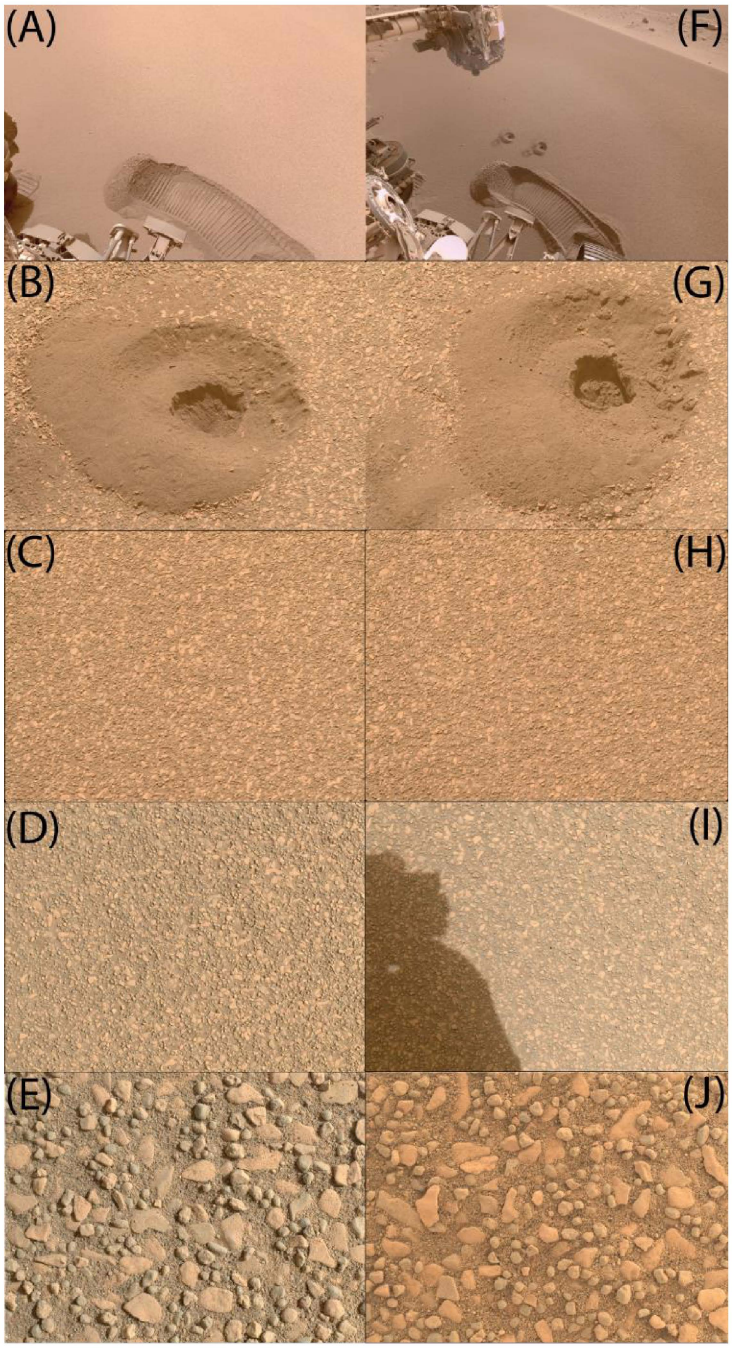

Figure 12 | **Wheel-scuff documentation images and areas of analysis.** WATSON image at (A) ~25 cm standoff and (B) ~9 cm standoff images of the surface-scarp interface. (C) ZCAM image of the surface-scarp interface and (D) of the wheel track. (E) Excavated regolith imaged with WATSON at ~ 7 cm standoff (*Topographers Peak*). Gaussian stretched RMI of (F) post LIBS analysis of *Fultons Falls*, (G) *Funnel Creek* and (H) *Geographic Harbor*.

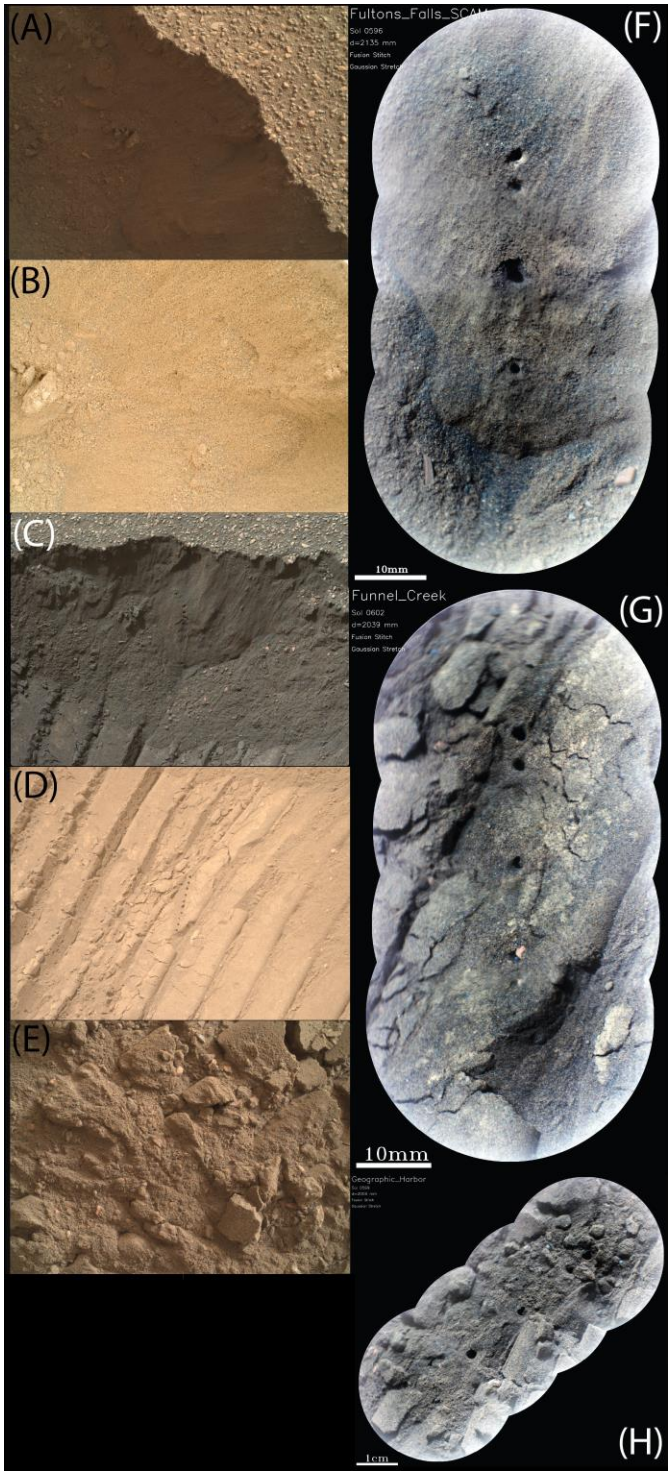

Pre and Post Coring/Abrasion Images

WATSON images (e.g., **Figure 11, 12**) provide evidence of grains ranging in size from ~80 microns to ~5.5 mm. For the closest approach WATSON images, the pixel size is ~ 20 µm (17.5 µm/pixel for *Atmo Mountain* and 18.1 µm/pixel for *Crosswind Lake*), so the finest grain that can be resolved from WATSON images is ~50 micron. Within this measurable grain size range, a bimodal distribution was observed at both sampling sites. One peak occurs from approximately 0.7 mm to 4 mm, with the greatest frequency at around 1.4-2 mm, and the other from approximately 80 to 500 microns, with the greatest frequency around 250 to 350 µm in diameter (**Figures 13 and 14**).

Figure 13 |**Grain size distribution for *Atmo Mountain*.** Distribution based on a 875 µm x 875 µm spacing grid analysis of a 3.2 cm approach WATSON image of the undisturbed regolith surface before sampling. Grain size in ϕ units: ϕ=-log2D, where D is the diameter of the grain in mm, i.e., ϕ =3 indicates a grain diameter of 125µm.

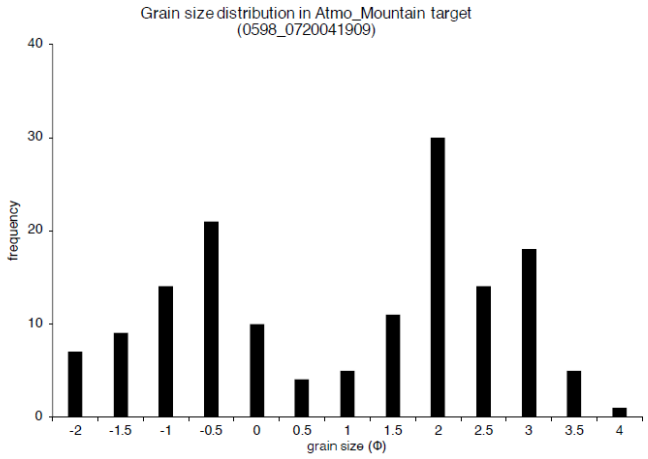

Figure 14 | **Grain size distribution for *Crosswind Lake*.** Distribution based on a 905 µm x 905 µm spacing grid analysis of a 3.2 cm approach WATSON image of the undisturbed regolith surface before sampling.

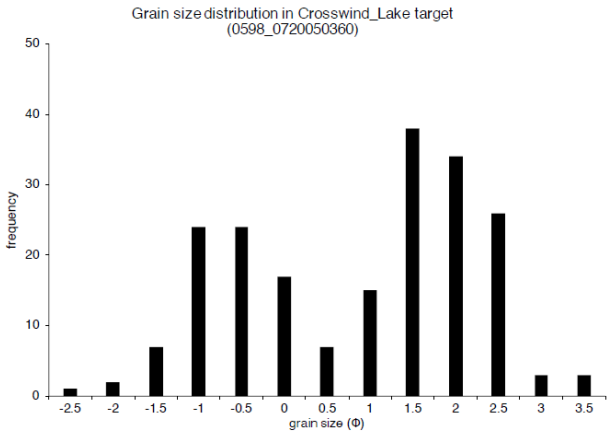

The finer-grained material imaged on the undisturbed megaripple surface was also observed in the area disturbed by sampling, the scuff face, the material excavated by the scuff, and in the wheel track (**Figures 11 and 12**).

The Cachecam images (**Figure 15**) show both coarser and finer grains in the *Atmo Mountain* sample, whereas only finer grains are seen in the *Crosswind Lake* sample. Because the undisturbed surfaces where the samples were acquired both had coarse grains (**Figures 13, 14**), it seems likely that coarse grains are nevertheless present in the *Crosswind Lake* sample.

Figure 15 | **Cachecam images of regolith samples.** (left) *Atmo Mountain* (right) *Crosswind Lake*. *Atmo Mountain* clearly contains large grains (multiple mm across), whereas *Crosswind Lake* contains no evidence of such grains on the exposed surface of the sample. Samples are ~13 mm diameter.

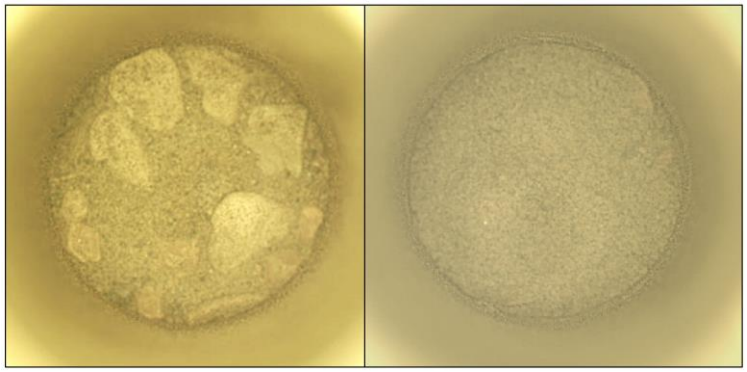

Elemental Geochemistry - PIXL

PIXL observations associated with *Atmo Mountain* and *Crosswind Lake* include a grid scan and a map scan of the undisturbed regolith surface (target *Marmot Bay*; sols 600 and 601), and a map scan of the regolith churned up by the wheel scuff (target *Topographers Peak*; sol 598). The PIXL scans varied in size from 5 x 5 mm to 21 x 21 mm, with 0.125 mm spacing used for the maps, and 1.5 mm spacing used for the grid scan, see **Figure 16** and **Table 1** for scan details.

The PIXL scans of *Marmot Bay* show that the undisturbed regolith surface consists predominantly of pebbles of altered olivine of several types. The altered olivine can be broadly divided into two groups – Al-rich olivines, and Al-poor olivines with varying amounts of Fe-Mg carbonates and dust cover (see **Table 2** for compositions).

The undisturbed regolith surface also includes abundant fine grains, composed of aluminosilicates, Ca-rich pyroxene, Ca-phosphate minerals, and Fe-Ti-Cr oxides (see **Table 2** for compositions). The PIXL scan of the disturbed regolith pile (*Topographers Peak*) is dominated by the fine-grained regolith component, with a bulk composition similar to fine grains observed on the *Marmot Bay* undisturbed surface.

Figure 16 | **PIXL scans on the *Observation Mountain* megaripple.** a) Close-up of *Marmot Bay*, with the PIXL grid footprint of sol 600 (large square) and map location of sol 601 (small rectangle) (WATSON SIF 0594 0719685996 250RAS N0300000SRLC00704 0000LMJ02). b. Close-up of the *Topographers Peak* area, with the PIXL map location of sol 598 (WATSON image SI1 0598 0720049360 660FDR N0300000SRLC00071 000090J01).

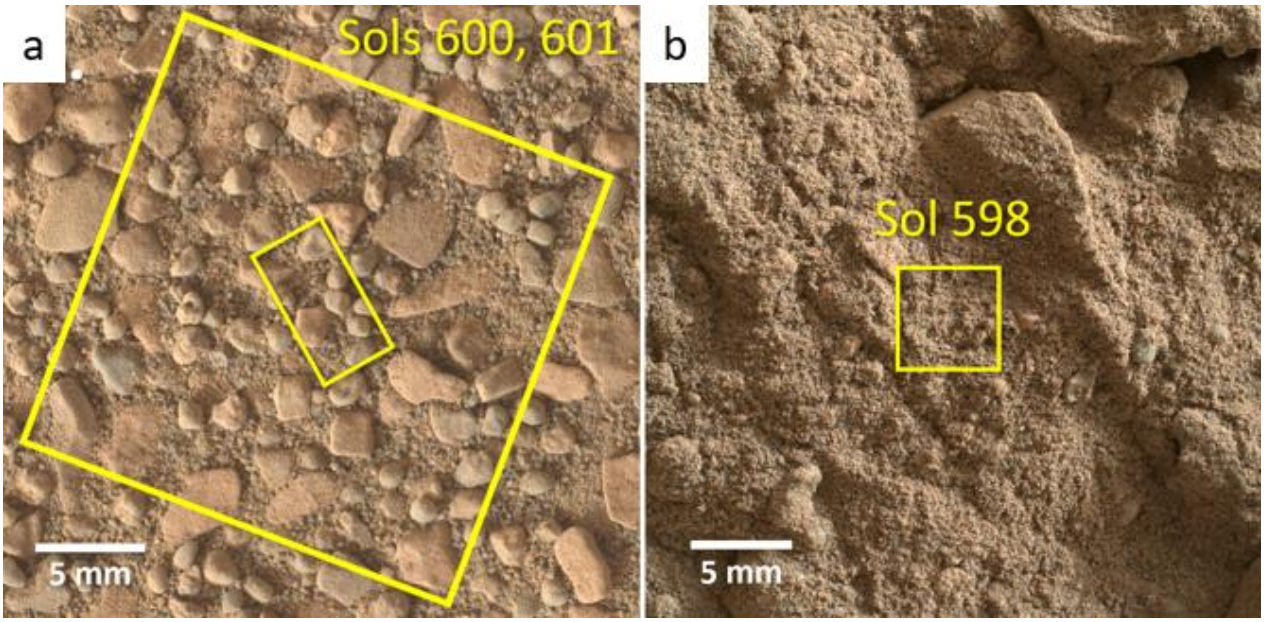

Table 1. Details of PIXL scans on *Observation Mountain*.

Sol	Name	Scan Size (mm)	Point Spacing (mm)	Purpose/Target
598	*Topographers Peak*	5 x 5	0.125	General
600	*Marmot Bay*	21 x 21	1.50	Capture wider diversity of grains in the regolith
601	*Marmot Bay*	3.5 x 7	0.125	General

The PIXL Micro Context Camera (MCC) imaged the areas surrounding the PIXL map and grid scans on the undisturbed surface and regolith tailings pile in four bands: near-infrared (NIR), green, blue, and ultraviolet (UV) (Allwood et al., 2020) (**Figures 17** and **18**). On the undisturbed surface the dark-toned pebbles in **Figure 17a** correspond to Al-poor altered olivines in the XRF data, and the light-toned pebbles correspond to Al-rich olivines (see compositions in **Table 2**). The differences between distinct populations of pebbles and the finer-grained regolith material are emphasized in the NIR/Green ratio image, **Figure 17c**. The MCC images of the regolith tailings pile (**Figure 18**) are more uniform in color due to the mix of

fine-grained regolith scraped up in the wheel scuff, however, some pebbles are distinguishable outside of the PIXL scan area.

Figure 17 | **PIXL MCC data for the *Marmot Bay* scans on sols 600 and 601**. a) Grayscale NIR image showing the location of each PIXL scan. b) MCC false color image of the scan area (Red = MCC NIR; Green = MCC Green; Blue = MCC Blue), flat-fielded and enhanced. c) MCC ratio image of NIR/Green reflectances. Note that distinct populations of pebbles with similar spectral signatures are distinguishable within the regolith. d) Graph of MCC reflectance ratios.

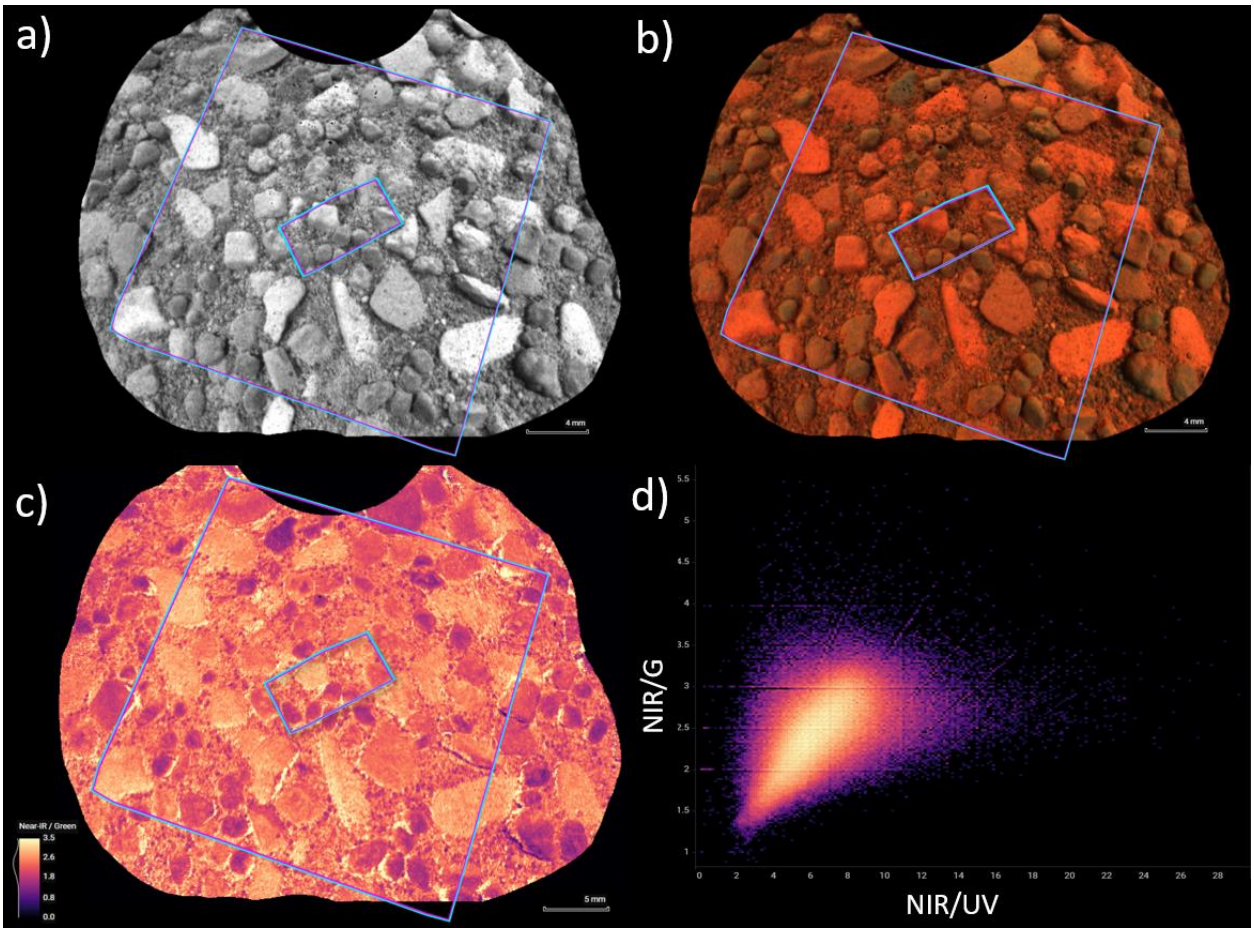

Figure 18 | **PIXL MCC data for the *Topographers Peak* scan on sol 598**. **a)** Grayscale NIR image showing the location of the PIXL scan. b) MCC false color image of the scan area (Red = MCC NIR; Green = MCC Green; Blue = MCC Blue), flat-fielded and enhanced. c) MCC ratio image of NIR/Green reflectances. Note that some pebbles are distinguishable within the regolith. d) Graph of MCC reflectance ratios.

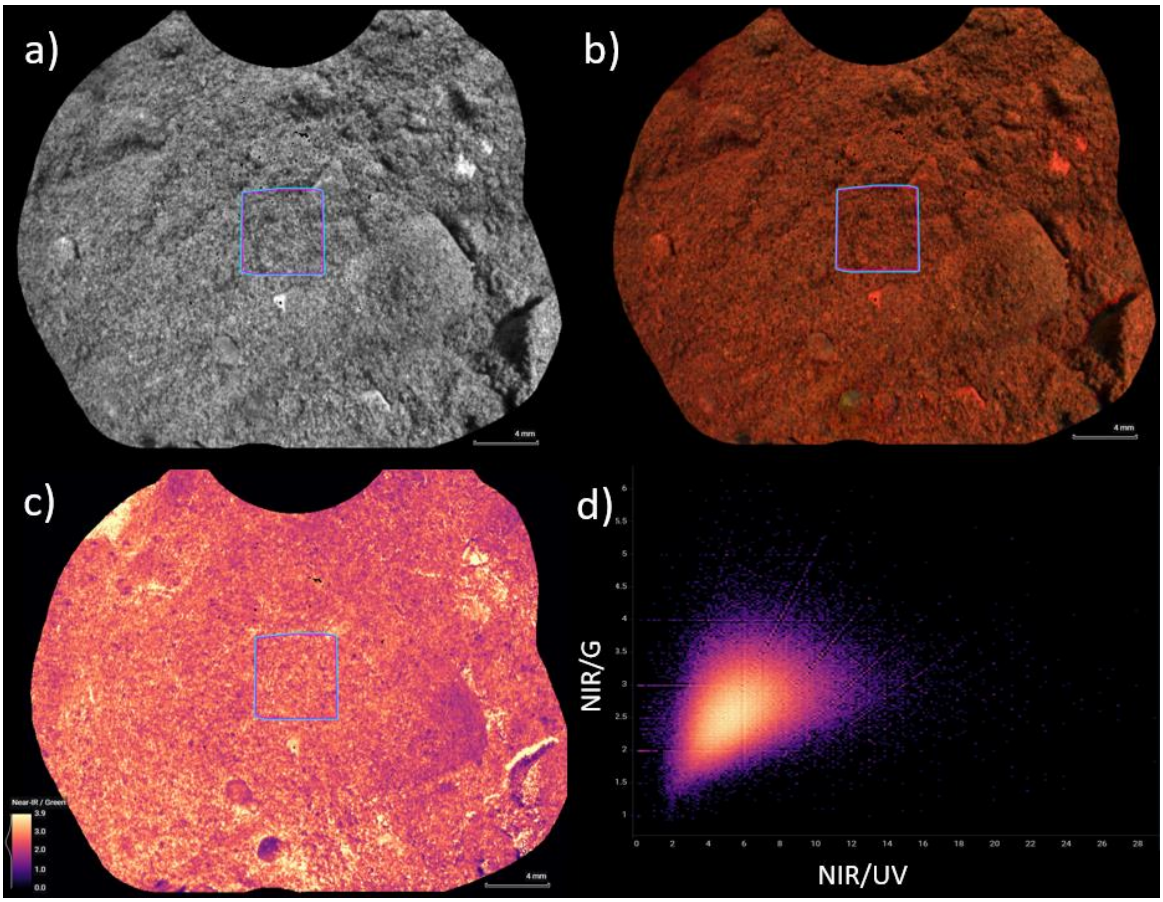

Figure 19 | **PIXL scans of the undisturbed regolith surface *Marmot Bay* and tailings *Topographers Peak*** *(next page)***.** Legends indicate element assigned to which color, range of abundances of that element or oxide (in numbers) and the distribution of element abundances in the scan (white bars & histograms). The "best" label after each element refers to a refinement of XRF data used to remove diffraction and roughness effects, however, for all multi-element maps, high or low concentrations observed on grain edges should be interpreted with caution due to the effects of topography. A) FeO_T-Al_2O_3-CaO, emphasizing the two main types of olivine alteration in the pebbles (high and low-Al). B) FeO_T-MgO-SiO_2, further classifying the pebbles based on the presence of dust and/or carbonate. C) P_2O_5-TiO_2-Cr_2O_3, emphasizing minor minerals (phosphate and Cr-Ti oxide minerals). D) Br-Cl-SO_3. E) Contiguous diffraction maps. In these maps, different diffraction patterns observed by PIXL's two detectors are converted into unique integers that encode the presence or absence of diffraction peaks in the regions 0.8-3.8 keV, 3.8-6.8 keV, 6.8-9.8 keV, and 9.8-12.8 keV. Note that, in this coding, brighter colors do not necessarily indicate more diffraction; however, black points indicate spots with no identified diffraction peaks. Because diffraction patterns reflect a combination of mineral identity, crystalline domain size, and crystallographic orientation, detection of the same pattern over multiple contiguous PIXL spots generally indicates a large monomineralic crystalline domain. Thus, in these maps, single-color grains correspond to monocrystalline minerals.

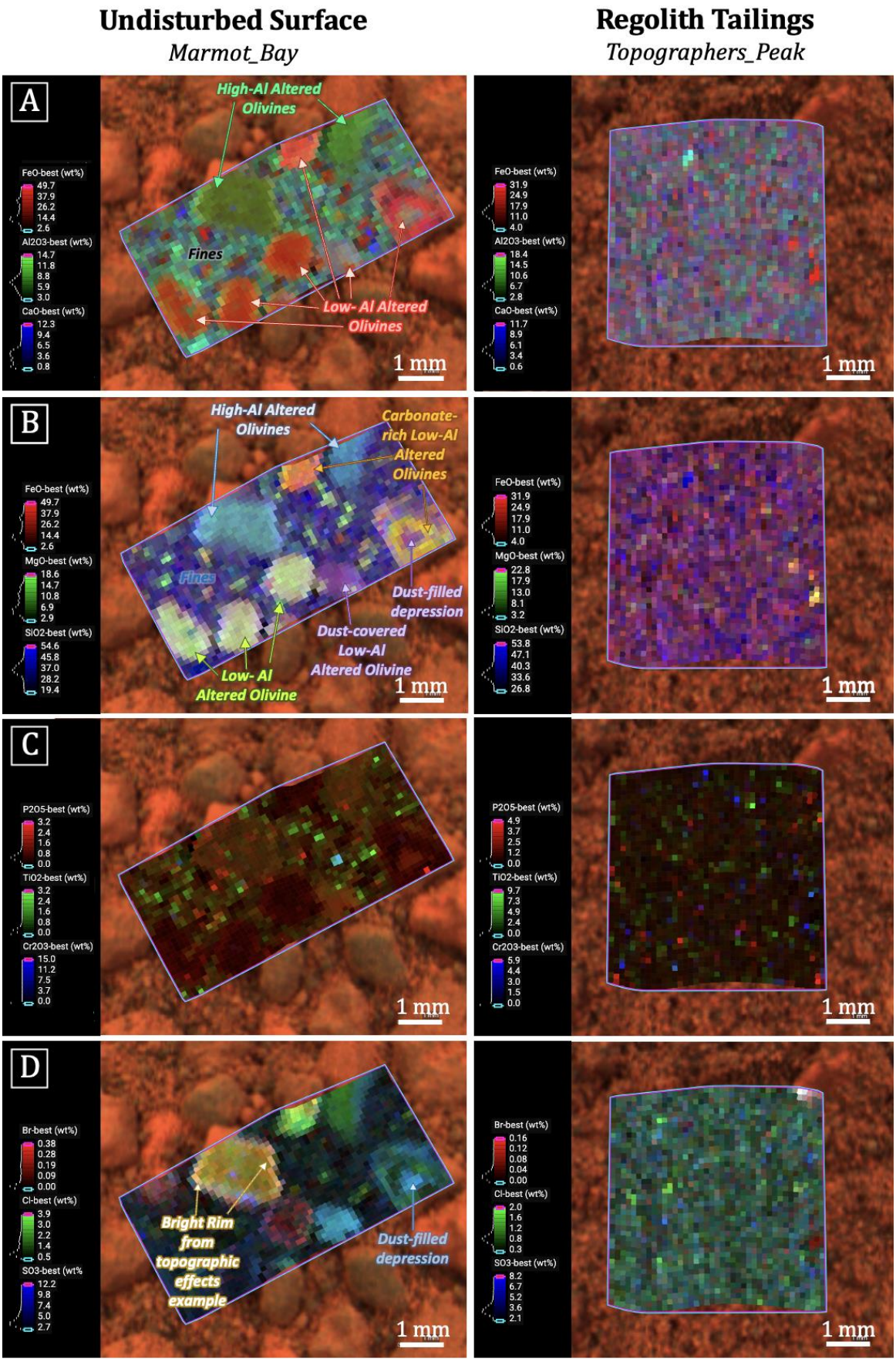
Undisturbed Surface
Marmot_Bay
Regolith Tailings
Topographers_Peak
A
High-Al Altered Olivines
Fines
Low- Al Altered Olivines
FeO-best (wt%)
49.7
37.9
26.2
14.4
2.6
Al2O3-best (wt%)
14.7
11.8
8.8
5.9
3.0
CaO-best (wt%)
12.3
9.4
6.5
3.6
0.8
1 mm
FeO-best (wt%)
31.9
24.9
17.9
11.0
4.0
Al2O3-best (wt%)
18.4
14.5
10.6
6.7
2.8
CaO-best (wt%)
11.7
8.9
6.1
3.4
0.6
1 mm
B
High-Al Altered Olivines
Carbonate-rich Low-Al Altered Olivines
Fines
Dust-filled depression
Dust-covered Low-Al Altered Olivine
Low- Al Altered Olivine
FeO-best (wt%)
49.7
37.9
26.2
14.4
2.6
MgO-best (wt%)
18.6
14.7
10.8
6.9
2.9
SiO2-best (wt%)
54.6
45.8
37.0
28.2
19.4
1 mm
FeO-best (wt%)
31.9
24.9
17.9
11.0
4.0
MgO-best (wt%)
22.8
17.9
13.0
8.1
3.2
SiO2-best (wt%)
53.8
47.1
40.3
33.6
26.8
1 mm
C
P2O5-best (wt%)
3.2
2.4
1.6
0.8
0.0
TiO2-best (wt%)
3.2
2.4
1.6
0.8
0.0
Cr2O3-best (wt%)
15.0
11.2
7.5
3.7
0.0
1 mm
P2O5-best (wt%)
4.9
3.7
2.5
1.2
0.0
TiO2-best (wt%)
9.7
7.3
4.9
2.4
0.0
Cr2O3-best (wt%)
5.9
4.4
3.0
1.5
0.0
1 mm
D
Br-best (wt%)
0.38
0.28
0.19
0.09
0.00
Cl-best (wt%)
3.9
3.0
2.2
1.4
0.5
SO3-best (wt%
12.2
9.8
7.4
5.0
2.7
Bright Rim from topographic effects example
Dust-filled depression
1 mm
Br-best (wt%)
0.16
0.12
0.08
0.04
0.00
Cl-best (wt%)
2.0
1.6
1.2
0.8
0.3
SO3-best (wt%)
8.2
6.7
5.2
3.6
2.1
1 mm

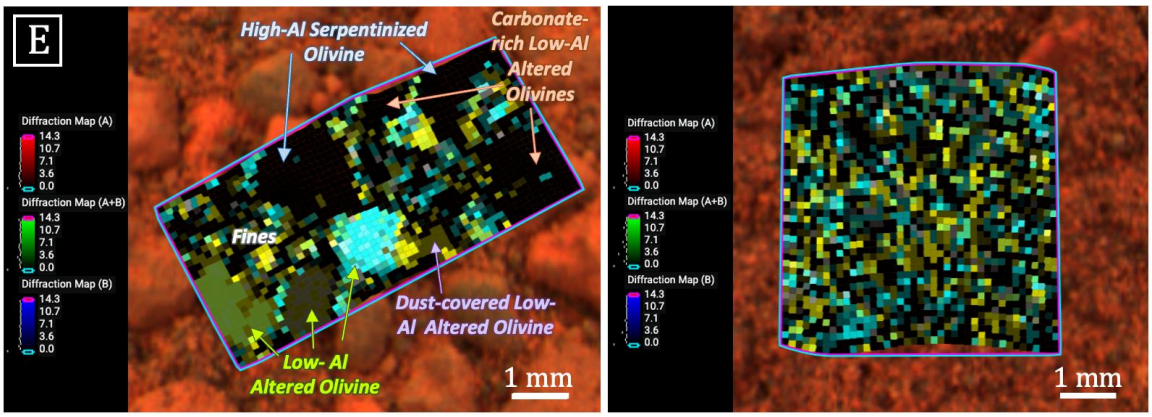

Figure 19 shows multi-element color images from the PIXL maps of the undisturbed regolith surface (*Marmot Bay*, Sol 601), and disturbed regolith tailings (*Topographers Peak*, Sol 598). These maps highlight the compositional variety of pebbles on the undisturbed surface and the more-uniform distribution of elements in the tailings. In the undisturbed surface map scan (*Marmot Bay*), the coarse-grained (pebbles) and fine-grained components are readily differentiated in all multi-element color images. The pebbles can be broadly divided into Al-rich altered olivines, and Al-poor altered olivines with varying amounts of Fe-Mg carbonates and dust cover (**Figure 19**). The high-Al olivine pebbles are relatively Mg-rich and have varying amounts of Fe (Mg# 55, **Table 2**). These high-Al grains do not yield strong diffraction peaks detectable by comparing spectra from PIXL's two detectors (**Figure 19E**), implying that they do not contain coherent crystalline domains larger than ~40-50 µm (Tice et al., 2022). They are likely heavily altered to amorphous or microcrystalline materials. The low-Al altered olivines are comparatively Fe-rich (Mg# 39, **Table 2**). The carbonate-bearing low-Al altered olivine grains have the highest Fe concentrations, and are low in Si (orange in **Figure 19B**). The diffraction patterns observed in the low-Al pebbles vary (**Figure 19E**). While the Fe-Mg carbonate-bearing grains are non-diffracting (indicating heavy alteration), the diffraction patterns in the low-Al altered olivines are strong and consistent with minimal or surface alteration of monocrystalline olivine.

As shown in **Table 2 and Figure 19**, the fine grains are rich in Ca, K, Al, P, Ti, and Cr, and are relatively depleted in Fe and Mg in comparison to the altered olivine pebbles. As the PIXL spot size is ~120 µm, this means that the majority of the XRF analyses in the fines are mixtures of minerals, making it more difficult to delineate mineral end-members. However, the multi-element images and mineral mixing trends of **Figure 21** suggest that fines in the undisturbed surface contain altered Fe-Mg silicates (green in **Figure 19B**), aluminosilicates (green in **Figure 19A**), Ca-phosphates (red in **Figure 19C**), and Cr-Ti-Fe oxides (blue and green in **Figure 19C**).

The disturbed regolith (*Topographers Peak*) appears to contain similar minerals, but these minerals are harder to identify because the material is so fine-grained. However, a few distinct grains of altered olivine (yellow in **Figure 19B**, and red in **19A**), as well as aluminosilicates (turquoise in **Figure 19A**), Ca-phosphates (red in **Figure 19C**), and Cr-Ti-Fe oxides (blue and green in **Figure 19C**) can be identified.

Fine-grained material in both *Marmot Bay* and *Topographers Peak* includes abundant diffracting grains (**Figure 19E**), but contiguous PIXL spots do not typically contain identical diffraction patterns. This is consistent with fine-grained crystalline minerals with ~40-100 µm domains. Combined with visual

observations of fine grains containing particles <100 µm in diameter, this suggests that most grains are monomineralic and monocrystalline, or comprise only a small number of distinct minerals or crystalline domains.

Figure 19D highlights the distribution of S, Cl, and Br on the undisturbed regolith surface and the fine-grained regolith pile. High S concentrations (blue in **Figure 19D**) are inferred to be associated with dust-rich areas. It should be noted that the S-rich region within the center of one of the carbonate-bearing pebbles is interpreted as dust accumulated in a depression, not zoning. Chlorine (green in **Figure 19D**) is elevated in the pebbles in comparison to the fine grains, and is typically associated with the low-Al carbonate-bearing olivines and high-Al olivines. Substantial Br concentrations are also associated with some low-Al altered olivine grains, and one of the high-Al olivine grains (red and orange grains in **Figure 19D**).

Table 2 gives the average normalized chemical compositions of the *Marmot Bay* map and grid scans, and the *Topographers Peak* map scan of the regolith tailings scuff. Table 2 also includes the average compositions of the main pebble "types" observed on the undisturbed surface. As noted in the section above, the composition of the pebbles is generally consistent with altered olivines with varying amounts of Al, S, and Cl (**Figure 19**). Notably, the composition of the fines on the undisturbed surface is most similar to the regolith tailings included in the *Topographers Peak* target map scan.

As noted in **Figure 19**, the uneven and rough surfaces on these targets produced unreliable absolute element abundances and analytical totals in many PIXL measurement spots (e.g., on fine-grained regolith and on the surfaces of larger grains sloped toward or away from either detector). In order to account for this, all analyses in **Table 2** were re-normalized to 100%; therefore, absolute element abundances should be interpreted with caution while ratios and relative abundances are still reliable. This is especially important to consider for the low-Al altered olivines included in **Table 2**. These carbonate-bearing grains should contain a significant non-detectable component (i.e., carbon, which is not detectable by PIXL) that is not shown here.

Table 2. PIXL chemical compositions from *Observation Mountain*

	Marmot Bay		***Marmot Bay* Components (Sol 601 Map)**						***Topographers Peak Map***	
	Map & Grid Scans		**Low-Al Altered Olivine Pebbles**		**High-Al Altered Olivine Pebbles**		**Fines**			
wt%	N=1878	Error	N=288	Error	N=191	Error	N=553	Error	N=1681	Error
Na2O	1.5	1.2	0.3	0.3	1.2	1.4	2.2	1.7	2.2	1.7
MgO	10.3	0.6	12.3	0.7	13.1	0.7	8.1	0.5	7.7	0.5
Al2O3	8.6	0.4	5.9	0.3	8.8	0.4	10.3	0.5	10.1	0.5
SiO2	42.2	1.5	35.5	1.3	46.5	1.7	45.3	1.7	45.0	1.6
P2O5	0.9	0.2	0.7	0.2	1.1	0.3	1.0	0.2	0.9	0.2
SO3	5.3	0.4	5.3	0.3	4.6	0.4	5.1	0.4	4.6	0.5
Cl	1.5	0.3	1.5	0.3	2.3	0.4	1.2	0.3	1.1	0.3
K2O	0.19	0.12	0.06	0.04	0.12	0.10	0.31	0.17	0.32	0.17
CaO	4.5	0.4	2.7	0.3	2.2	0.4	6.7	0.3	6.9	0.3
TiO2	0.40	0.15	0.08	0.03	0.49	0.17	0.61	0.22	0.86	0.25
Cr2O3	0.11	0.04	0.01	0.00	0.17	0.10	0.14	0.05	0.18	0.07
MnO	0.25	0.13	0.47	0.16	0.04	0.04	0.19	0.14	0.21	0.15
FeO-T	24.0	0.9	34.8	1.2	19.1	0.7	18.6	0.7	19.6	0.7
NiO	0.03	0.03	0.02	0.02	0.03	0.03	0.03	0.03	0.02	0.02
ZnO	0.04	0.03	0.04	0.03	0.03	0.03	0.03	0.03	0.04	0.03
Br	0.07	0.05	0.05	0.04	0.20	0.07	0.04	0.05	0.03	0.05
SrO	0.06	0.06	0.06	0.07	0.05	0.05	0.07	0.06	0.07	0.06
TOTAL	**100**		**100**		**100**		**100**		**100**	
Mg#	**43.4**		**38.7**		**55.0**		**43.7**		**41.1**	

Notes: All columns represent averages that have been renormalized to 100% to account for topography and roughness effects on X-ray intensities (spuriously high or low totals). N = number of analyses averaged. Error is the uncertainty from calibration and counting statistics. Mg# is molar Mg/(Mg+Fe), in percent.

Figure 20 shows the chemical analyses of *Marmot Bay* and *Topographers Peak* in the Mangold et al. (2017) classification for Gale crater rocks, and the common TAS classification diagram for volcanic rocks. In the Mangold scheme, Fe-rich, Si-poor points are more common on the undisturbed surface (*Marmot Bay*) than the disturbed regolith (*Topographers Peak).* These points likely represent Fe-Mg carbonates, an inference based on their low Si abundances, and their positions on mixing trends (**Figure 22A).** These carbonate detections are concentrated in high-Fe olivine grains. Abundances of K_2O and Na_2O show less difference between the undisturbed and disturbed regolith surfaces (**Figure 20B**). This similarity may be because the K_2O- and Na_2O-bearing phases are concentrated in the fine-grained portions of the regolith, which are present in both the undisturbed and disturbed surfaces. In the TAS diagram, the compositions of *Marmot Bay* and *Topographers Peak* plot within the picro-basalt and basalt fields. Some points with high SiO_2 (up to 75%) were hit in the grid scan, typically associated with grains of altered olivine. However, these high-SiO_2 points should be interpreted with caution, because of potential effects of topography and roughness.

Figure 21 plots elemental abundances for the PIXL scans of the undisturbed regolith surface (*Marmot Bay*, Sols 600-601), and regolith churned up in the wheel scuff (*Topographers Peak,* Sol 598). **Figure 21A** shows that the undisturbed regolith surface likely comprises a mixture of altered olivines, Fe-Mg carbonates, aluminosilicates, and augite. **Figure 21B** shows the variety of altered pebbles observed on the regolith surface.

As noted above, the presence of carbonate on the undisturbed surface is inferred by the low Si concentrations in carbonate regions, and compositional mixing lines between altered olivine (moderate Fe+Mg relative to Si) and Fe-Mg carbonates (high Fe+Mg relative to Si) (See **Figure 21A**). However, the carbonate-altered olivine mixing trend is only observed in the high-resolution map scan of the undisturbed surface (*Marmot Bay* Sol 601). Carbonates are absent in the *Marmot Bay* grid scan (Sol 600 - 21 x 21 mm, **Figure 21C**), and are also absent from the regolith scuff (*Topographers Peak* scan, Sol 598, **Figure 21D**). This may indicate that the carbonate is less abundant in the regolith than indicated by the *Marmot Bay* map scan.

Figure 21E shows that there is abundant chlorine (>1 wt%) throughout the regolith. Higher Cl concentrations are noted in the high-Al altered olivine grains, the dust-rich areas, and the carbonate-bearing grains when compared to the fines and altered olivines. Dust on Mars is commonly enriched in Cl (Berger et al., 2016). Finally, the oxide minerals in the *Observation Mountain* megaripple have a range of Cr and Ti compositions, with Cr-rich oxides comprising the dominant trend (**Figure 21F)**.

Figure 20 | **Chemical classification of the *Observation Mountain* megaripple including scans of the undisturbed regolith surface (*Marmot Bay*, Sols 600 and 601), and disturbed regolith (*Topographers Peak*, Sol 598).** All points have been normalized to 100% to account for topography and roughness effects. The points correspond to individual PIXL analysis points across the grid and map scan areas. The legend in (C) indicates which scan corresponds to each color. (A) and (B) follow the classification scheme of Mangold et al. (2017). The analysis points from the regolith scuff (*Topographers Peak*), show a smaller range of compositions than the undisturbed regolith scans.

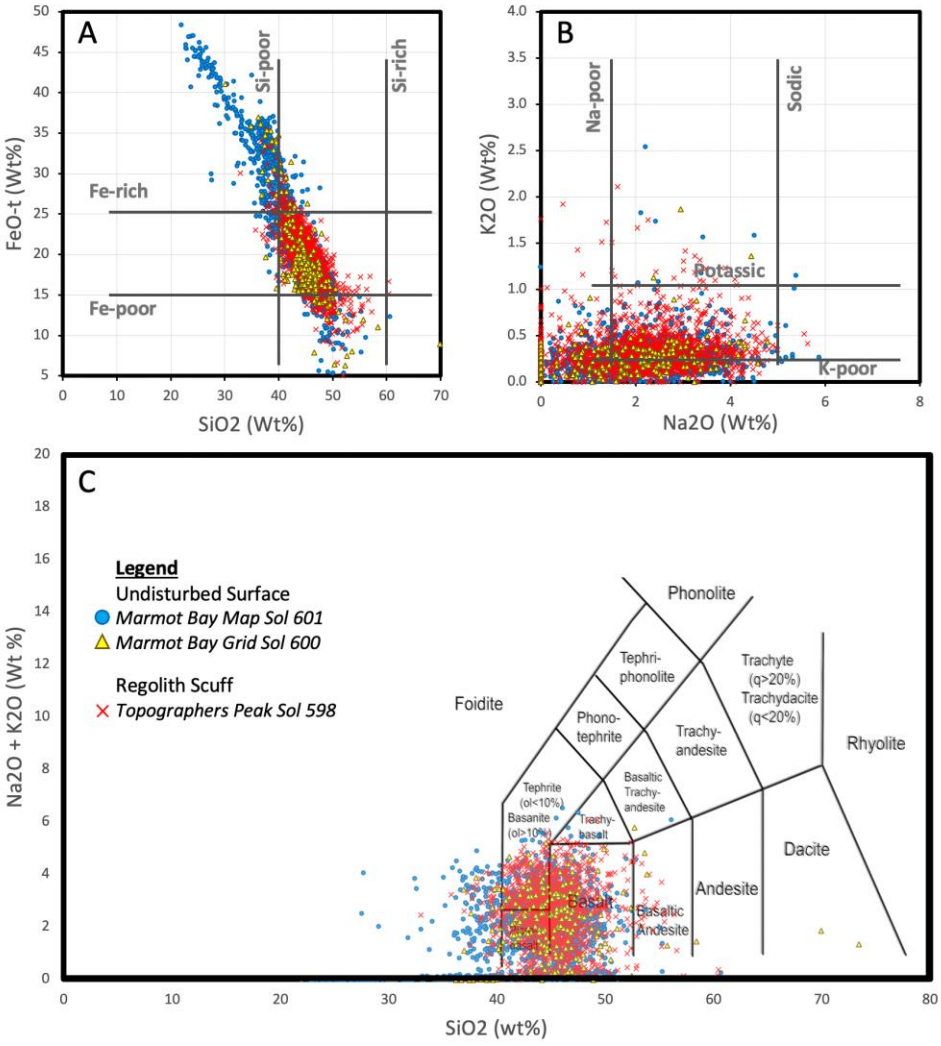

Figure 21 | **Elemental compositions of the undisturbed regolith surface *Marmot Ba*and disturbed regolith *Topographers Peak*** *(next page)* A) Molar proportions of Ca+Na+K, Si, & Fe+Mg for the *Marmot Bay* map scan (Sol 601). All XRF points are in grey, and the different components are colored and labeled according to the Fe-Mg-Si multi-element map shown in (B),(C),(D): Molar proportions of Ca+Na+K, Si, & Fe+Mg for the *Marmot Bay* grid scan (Sol 600), and regolith scuff scan (*Topographers Peak*, Sol 598), respectively with all XRF points in grey (separate components are not delineated). Notably the carbonate mixing trend clearly delineated in (A) for the *Marmot Bay* map is missing from the grid scan and regolith scuff scan. (E) Weight percent of FeO_T vs. Cl, showing the distribution of Cl across the various major pebble types, and fines in the regolith for the *Marmot Bay* map scan (Sol 601). All XRF points are in grey, and the different components are colored and labeled according to the Fe-Mg-Si multi-element map shown in (B). (F) Weight percent of Cr_2O_3 vs. TiO_2, showing compositions of Cr-Ti oxides, which are relatively Cr-rich in this sample.

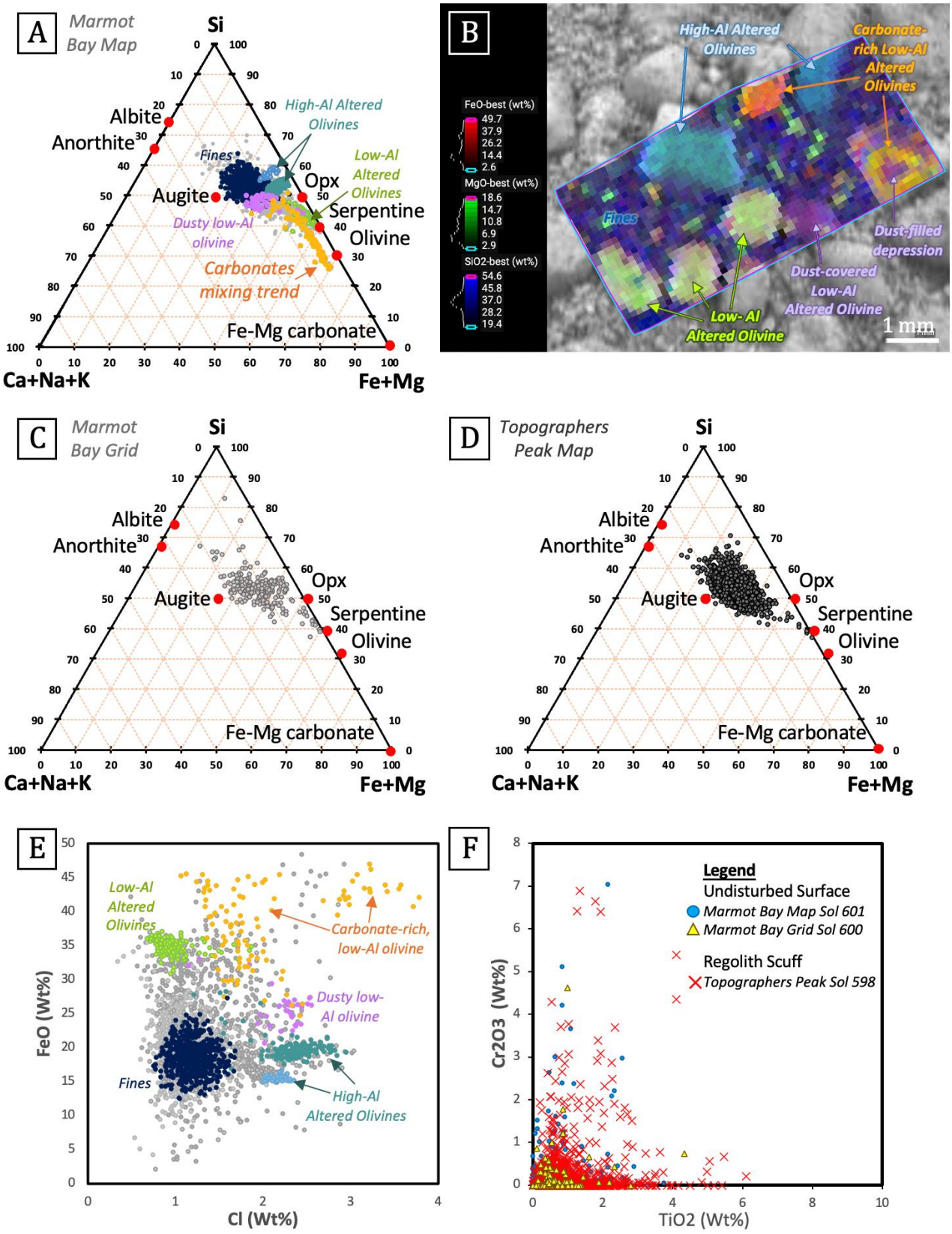
A
Marmot Bay Map
Si
Albite
Anorthite
Augite
Opx
Serpentine
Olivine
Fe-Mg carbonate
High-Al Altered Olivines
Low-Al Altered Olivines
Fines
Dusty low-Al olivine
Carbonates mixing trend
Ca+Na+K
Fe+Mg
B
FeO-best (wt%)
MgO-best (wt%)
SiO2-best (wt%)
High-Al Altered Olivines
Carbonate-rich Low-Al Altered Olivines
Fines
Dust-filled depression
Dust-covered Low-Al Altered Olivine
Low- Al Altered Olivine
1 mm
C
Marmot Bay Grid
D
Topographers Peak Map
E
FeO (Wt%)
Cl (Wt%)
Low-Al Altered Olivines
Carbonate-rich, low-Al olivine
Dusty low-Al olivine
Fines
High-Al Altered Olivines
F
Cr2O3 (Wt%)
TiO2 (Wt%)
Legend
Undisturbed Surface
Marmot Bay Map Sol 601
Marmot Bay Grid Sol 600
Regolith Scuff
Topographers Peak Sol 598

Figure 22 | Comparisons of composition across the three regolith scans. A) A "spider" diagram comparing the average composition of regolith targets, normalized to the composition of air-fall dust analyzed in Gale crater (Berger et al., 2016). This normalization is useful to identify so-called "dust crusts," which PIXL has observed on several other rocks (e.g., *Novarupta, Beaujeu*, and *Chiniak* targets. Panels B) through D) compare the composition of surface (red and blue points) and excavated regolith (yellow points).

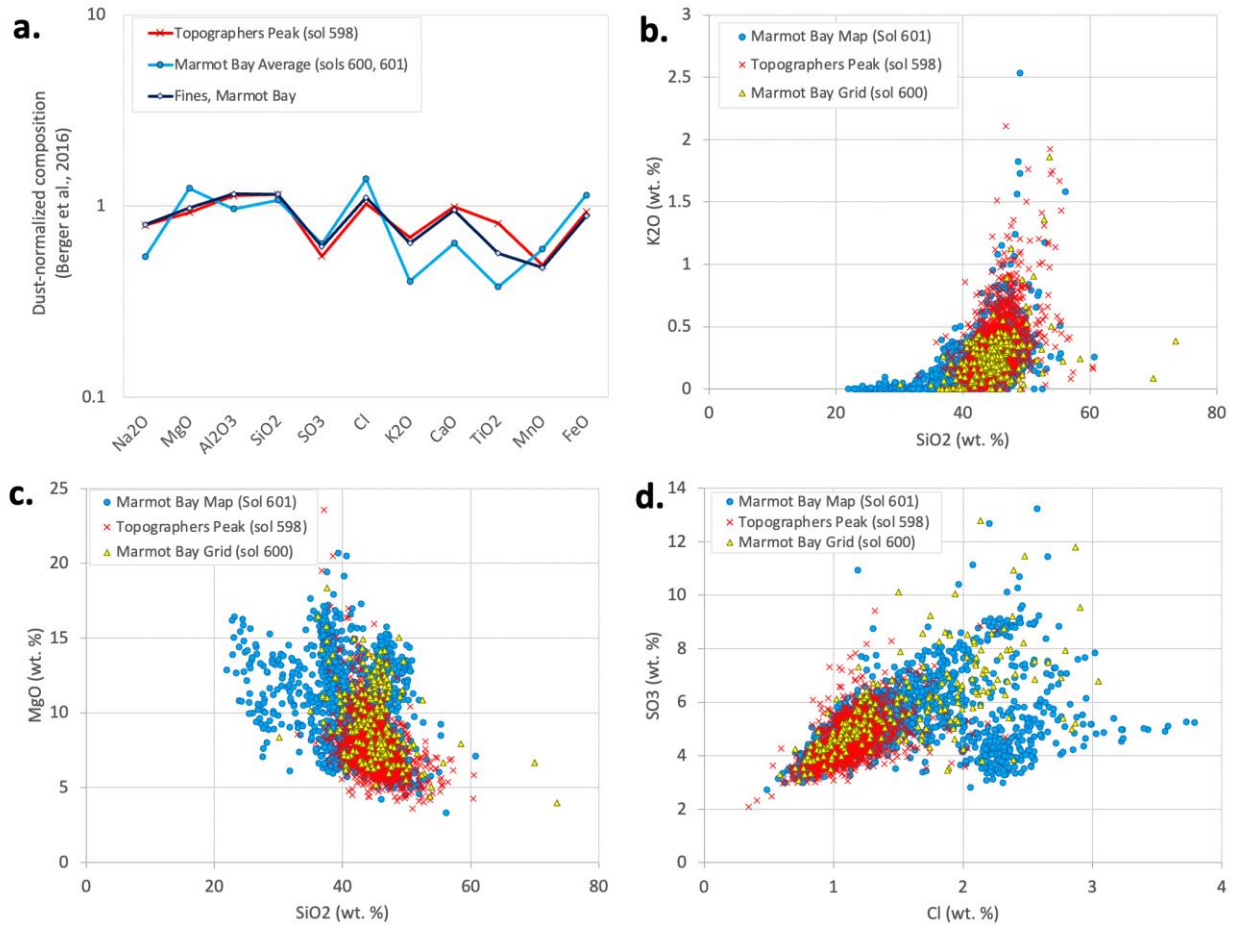

The major compositional differences between the undisturbed megaripple surface and tailings pile seen in **Figure 22** are due to the coarse pebbles at *Marmot Bay* as the finer-grained material is compositionally similar at both targets (**Figure 22A**). The average composition at *Marmot Bay* does not seem to be related to "dust crusts" previously observed on natural rock surfaces, although one dust-covered pebble does have a composition that closely resembles a dust crust (**Figures 19B** and **22a**). Typically, dust crusts are enriched in potassium compared to the interior rock, which is not a trend we observe between the surface and excavated regolith (**Figure 22B**). Differences in the magnesium/silicon ratio between the two targets can be explained by the pebbles at *Marmot Bay*, which were not included in the regolith scuff scan (**Figure 22C**).

Notably, the surface is enriched in Cl compared to the excavated regolith (**Figure 22D**)**.** This trend has also been observed in other martian soils (Yen et al., 2005), and may be related to oxychlorine salts. In *Marmot Bay*, the overall Cl enrichment is mainly due to the presence of Cl-enriched pebbles: the high-Al altered olivines, the low-Al carbonate-rich altered olivines, and the dusty grains (**Figure 19D**). Meanwhile, finer-grain material had similar salt content (SO_3 and Cl) at both *Marmot Bay* and *Topographers Peak.*

Mineralogy and Organics-SHERLOC

SHERLOC Raman and fluorescence spectra were obtained from a tailings pile (*Topographers Peak*) and undisturbed surface (*Marmot Bay*) on *Observation Mountain* on sols 598 and 600, respectively. The scans included two HDR (High Dynamic Range) scans (7x7 mm, 100 points, 780 µm spacing, 500 pulses per point) and 2 survey scans (5x 5 mm, 1296 points, 144 µm spacing, 15 pulses per point). ACIs included in this report were not colorized, as the automated process is optimized for abrasion surfaces. In addition, the signals from these samples were weak due to dust and a large amount of topography, which particularly affected the undisturbed surface. Other things that might have affected the signal strength are luster, grain size and temperature of the instrument at the time of the measurement.

The Raman spectra from scans on *Topographers Peak* contain peaks that can be assigned to phosphates (~960 cm^{-1}), carbonates (~1090 cm^{-1}), olivine (~815 cm^{-1}), possible sulfates (~1005 cm^{-1}), and possibly quartz (~465 cm^{-1}) (**Figure 23 and Table 3**). The sulfate spectra contain no hydration feature though this might be due to the weak Raman signal. Three different fluorescence features were observed at 270, 285 and 340 nm, which are consistent with single and double ring aromatic compounds. The 340 nm feature is associated with phosphate in one point and the only detection of the 270 nm feature is associated with possible quartz (Figure 23). The low fluorescence signal and the absence of any obvious organic signals in the Raman spectra suggest that any organic compounds present are in generally low abundance.

The median Raman spectrum (median spectrum is a sum of all spectra from the scan and was used for this target as the signals in the individual point spectra in the scan were too weak to identify any Raman peaks) from the HDR scan on *Marmot Bay* contains peaks that can be assigned to olivine (~815 cm^{-1}) and tentative silicates (~1100 cm^{-1}) (**Figure 24 and Table 3**). Two different fluorescence features were observed at 285 and 340 nm, which are consistent with single and double ring aromatic compounds (**Figure 24**). No fluorescence-mineral associations could be discerned for this target as the signal in individual point spectra were too weak to identify Raman mineral features that could be matched with identified fluorescence signals.

Figure 23 | Sol 598 SHERLOC fluorescence and Raman spectral results for *Topographers Peak.* A) ACI image of the *Topographers Peak* tailings pile; the blue rectangle indicates the HDR scan area and white circles indicate regions of interest (ROIs) correlating to the fluorescence data presented in B and C. B) HDR map showing the possible presence of organics. Upper panel shows an RGB map indicating the main regions of fluorescence. The lower panel is blank because no Raman features have been identified that would indicate the presence of organic materials. C) Fluorescence spectra. The upper panel shows the average fluorescence spectrum for the whole area of analysis and the lower panel includes spectra from selected fluorescence ROIs (see A and B). D) Map showing the results of the Raman HDR scan. The left panel shows a map of identified minerals indicated by large colored circles on top of a grid of small red circles that indicate the points analyzed (the small red circles are scaled to the size of the analysis spots). These points are superimposed on the grayscale ACI image of the scan area (cf. Panel A). Spectra from the points indicated with white numbers are shown in the panels to the right. In the middle panel, the lower spectrum is the median of all of the spectra in the scan. In general, the Raman signal strength is very low compared to analyses of abraded and dust-fee patches.

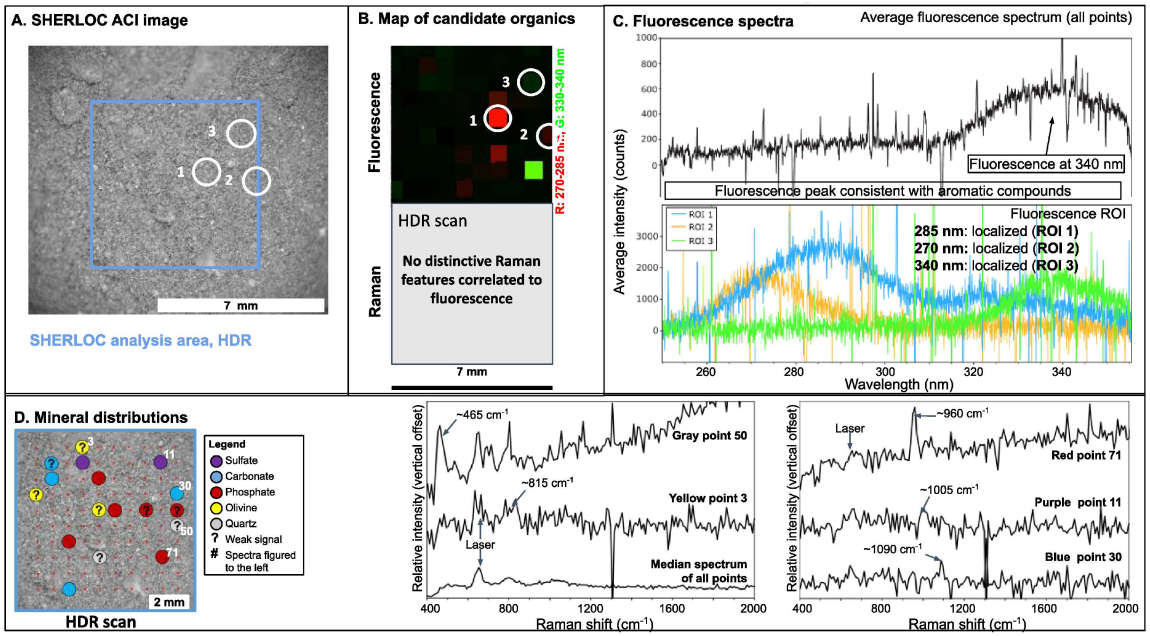

Figure 24 | Sol 600 SHERLOC fluorescence and Raman spectral results for *Marmot Bay*. A) ACI image of the *Marmot Bay* undisturbed surface; the blue rectangle indicates the HDR area and white circles indicate regions of interest (ROIs) correlating to the fluorescence data presented in B and C. B) HDR scan map showing the possible presence of organics. Upper panel shows an RGB map indicating the main regions of fluorescence. The lower panel is blank because no Raman features have been identified that would indicate the presence of organic materials. C) Fluorescence spectra. The upper panel shows the average fluorescence spectrum for the whole area of analysis and the lower panel includes spectra from selected fluorescence ROIs (see A and B). D) Map and spectra showing the results of the Raman HDR scan. The left panel shows a grid of red circles that indicate the points analyzed superimposed on the grayscale ACI image of the scan area (cf. Panel A). The circles are scaled to the size of the analysis spots. The right panel shows the median spectrum of all of the analysis points in the HDR scan. In general, the Raman signal strength is very low compared to analyses of abraded and dust-free patches, and unlike the HDR scan of *Topographers Peak* (sol 598, see Figure 24), there were no mineral detections deemed significant in the individual points though there are some possible detections in the median spectra of all points.

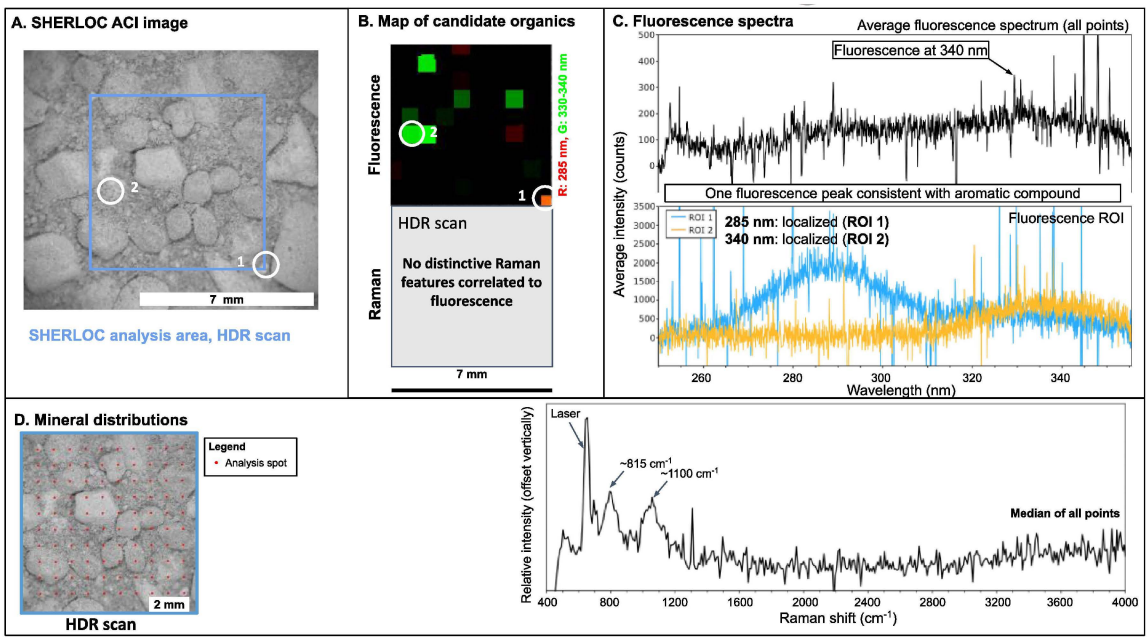

Table 3 SHERLOC Raman spectra mineral ID.

Sample	Certain	Possible (not confirmed)	We looked for these, but cannot find them
Topographers peak	Phosphate Carbonate Olivine	Sulfate Quartz	
Marmot Bay	Olivine	Silicate	

Elemental Geochemistry and Mineralogy - SuperCam

SuperCam remote micro-imaging (RMI, **Figure 25**) of the ripple at *Observation Mountain* shows diverse grains on the undisturbed surface of the regolith (target *Granite Peak* on Sol 594), the sides of the rover wheel scuff (*Fultons Falls* on Sols 596 and 600), in the rover wheel track (*Funnel Creek* on Sol 602), and in the tailings pile (*Geographic Harbor*, Sol 599). The RMI of the undisturbed regolith shows tan to red, angular, flat 2-6 mm long pebbles, round, dark grey 1-3 mm wide grains and brown grains smaller than 1 mm. These sand- and pebble-sized grains are visible in the wheel scuff, whereas the steep sides of the > 5 cm deep scuff are covered by brownish red grains smaller than 0.5 mm. A small overhang containing pebbles suggests a 2-3 mm thick cohesive surface. The RMI of the tailings (*Geographic Harbor*) shows the presence of some flat pebbles and round grains, all coated by the < 0.5 mm brown or grey-brown grains. The two regolith samples (*Atmo Mountain* and *Crosswind Lake*) include compositionally and morphologically diverse sand grains, pebbles and smaller grains that are not well resolved by the RMIs. The surface and subsurface of the regolith at *Observation Mountain* show similarities to the regolith in the previously explored areas of Jezero Crater.

Figure 25 | **SuperCam RMI images of regolith at *Observation Mountain*.** Top left: undisturbed surface of target *Granite Peak* imaged on Sol 594. Middle: Side view of angular tan pebbles, dark rounded sand grains and smaller brownish red grains on the surface and brownish red grains at the sides of the wheel scuff *Fultons Falls* imaged on Sol 600. Left bottom: Surface of the tailings pile (*Geographic Harbor*) shows larger sand grains and pebbles covered by the finer brownish red grains. Red and yellow circles and red crosshairs indicate spots analyzed by SuperCam VISIR and LIBS. Right: Disturbed rover track (*Funnel Creek*).

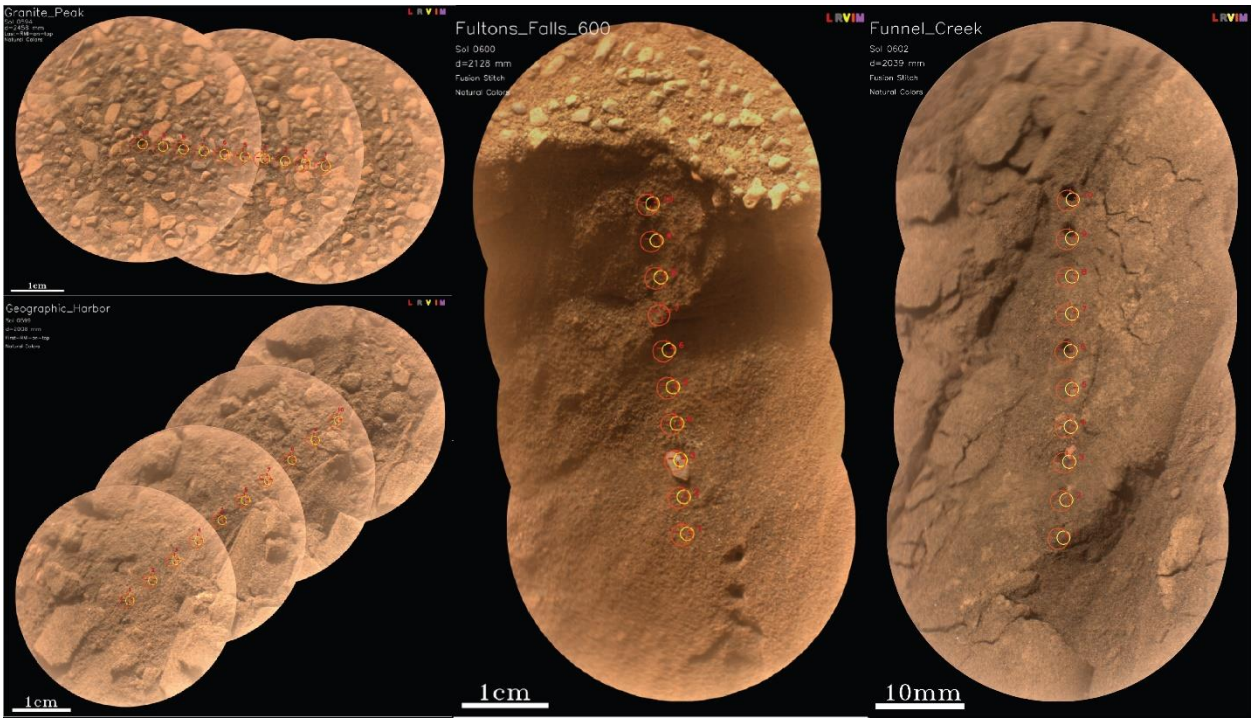

SuperCam LIBS observations at *Observation Mountain* (**Figures 26 , 27**) indicate that the compositions of the particles are in general similar to previous fine grains observed along the rover traverse. Because fine-grained soils can be transported long distances, whereas larger grains are more likely to have a local origin, the LIBS points from *Observation Mountain* are compared separately to fine and coarse grains from the mission (**Figure 27**). Both fine and coarse grains are similar to grains previously observed along the traverse, although some coarse grains observed in the sample were not common along the traverse, and may be from the delta front rocks. Harker Oxide diagrams suggest the presence of olivine and pyroxene, and that grains show similarities with *Máaz*, *Séitah*, and Delta front rocks. Half of the points that were analyzed by LIBS on the wheel scuff and 60% of points in the LIBS rasters on the wheel track and the tailings had a total oxide content lower than 85 wt%, indicating the presence of elements that are not quantified by SuperCam such as H, C, S and Cl. All points presented evidence of hydration. These observations indicate that the regolith samples of *Atmo Mountain* and *Crosswind Lake* contain a mixture of igneous grains and aqueous alteration phases that include elements not quantified by SuperCam.

Figure 26 | **SuperCam LIBS major element oxide (MOC) analyses of regolith at *Observation Mountain*.** Solid solution fields for olivine, pyroxene, and feldspar compositions are included. Black circles show the delta rocks analyzed from Sols 420-643, gray circles the *Máaz* rocks from sols 15-201 and 343-379, and white circles the *Séitah* rocks sols 202-379.

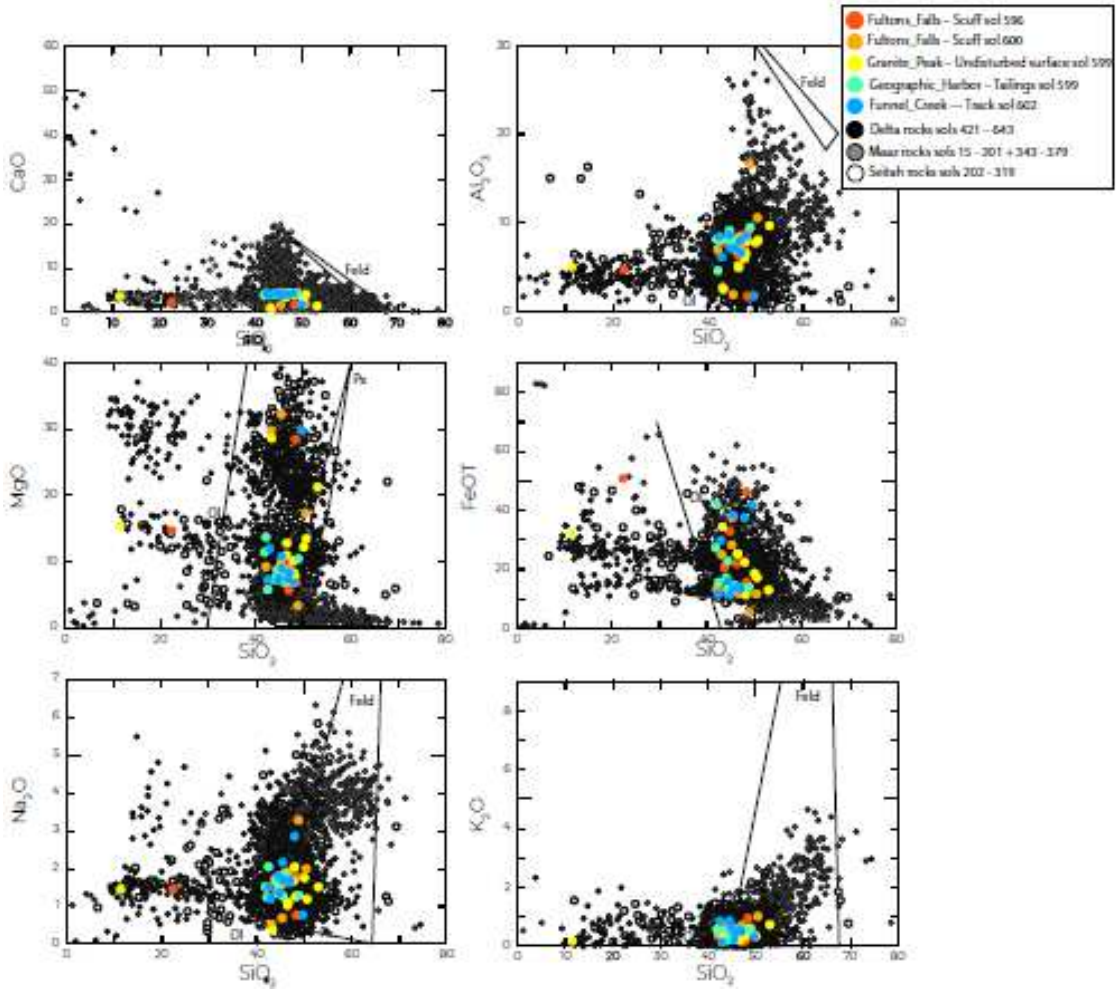

Figure 27 | **Molar compositions of the points in the LIBS rasters at *Observation Mountain* compared to various minerals, previous coarse- (blue – left) and fine- (orange -right) grained compositions, and on-board calibration standards.** Analyzed points are shown by the yellow, orange, red, fuchsia and purple circles. Orange circles show the composition of points on the tailings (*Geographic Harbor*). Red circles show wheel track (*Funnel Creek*). Yellow circles show the undisturbed surface of the ripple (*Granite Peak*). Triangles and circles with black borders present a range of standards from igneous calibration targets (Ca-pyroxene, pyroxene, olivine) to other minerals (calcite, ankerite, siderite, serpentine, gypsum).

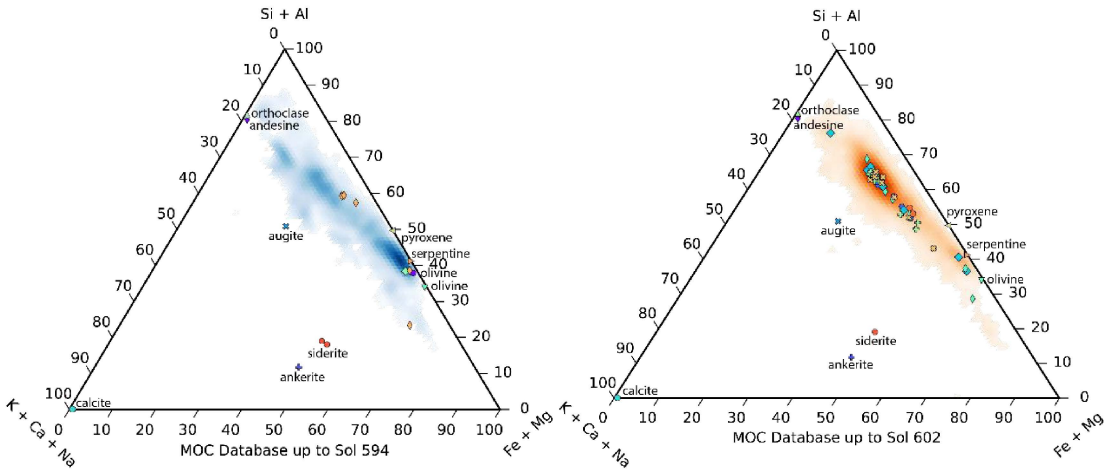

SuperCam VISIR rasters on the undisturbed and disturbed soil (**Figure 28**) reveal a mixture of olivine and pyroxene in all the soils (feldspars are mostly featureless in VISIR), some weak water-related features, including the signatures of hydrated minerals (Fe/Mg-phyllosilicates; possibly a minor contribution of carbonates). The stronger 1.94, 2.3 and 2.4 µm bands in the undisturbed regolith are likely caused by the small pebbles sitting on the surface. The physical weathering of these materials and mixing into the fine soils might cause the faint 2.3 and 2.4 µm bands observed in the fine soils within the tailings, scuff and rover track. These absorption bands are centered at the same wavelength in the spectrum of the nearby rock target *Knife Creek*, suggesting the presence of similar hydrated minerals. The SCAM VISIR technique is highly sensitive to hydrated minerals, so the signatures of hydration are present in the spectra even when these minerals are a minor proportion of the regolith. The VISIR spectra are greatly affected by grain size, contributing to the differences in the tailings, undisturbed and disturbed regolith targets.

Figure 28 | **Mean reflectance spectra of the SuperCam VISIR rasters of the disturbed and undisturbed regolith at *Observation Mountain*.** Lighter lines near 2 µm indicate the spectral range possibly affected by the CO_2 absorption features that could remain after the atmospheric correction. The UV region was smoothed using a Savitsky-Golay filter with a window length of 51. Note that owing to temperature sensitivities in the IRS instrument, the calibration is still uncertain for wavelength longer than ~2.55 µm. The absorption centers are indicated with arrows and their positions point towards the presence of hydration and hydrated minerals, Fe/Mg-phyllosilicates and/or carbonates.

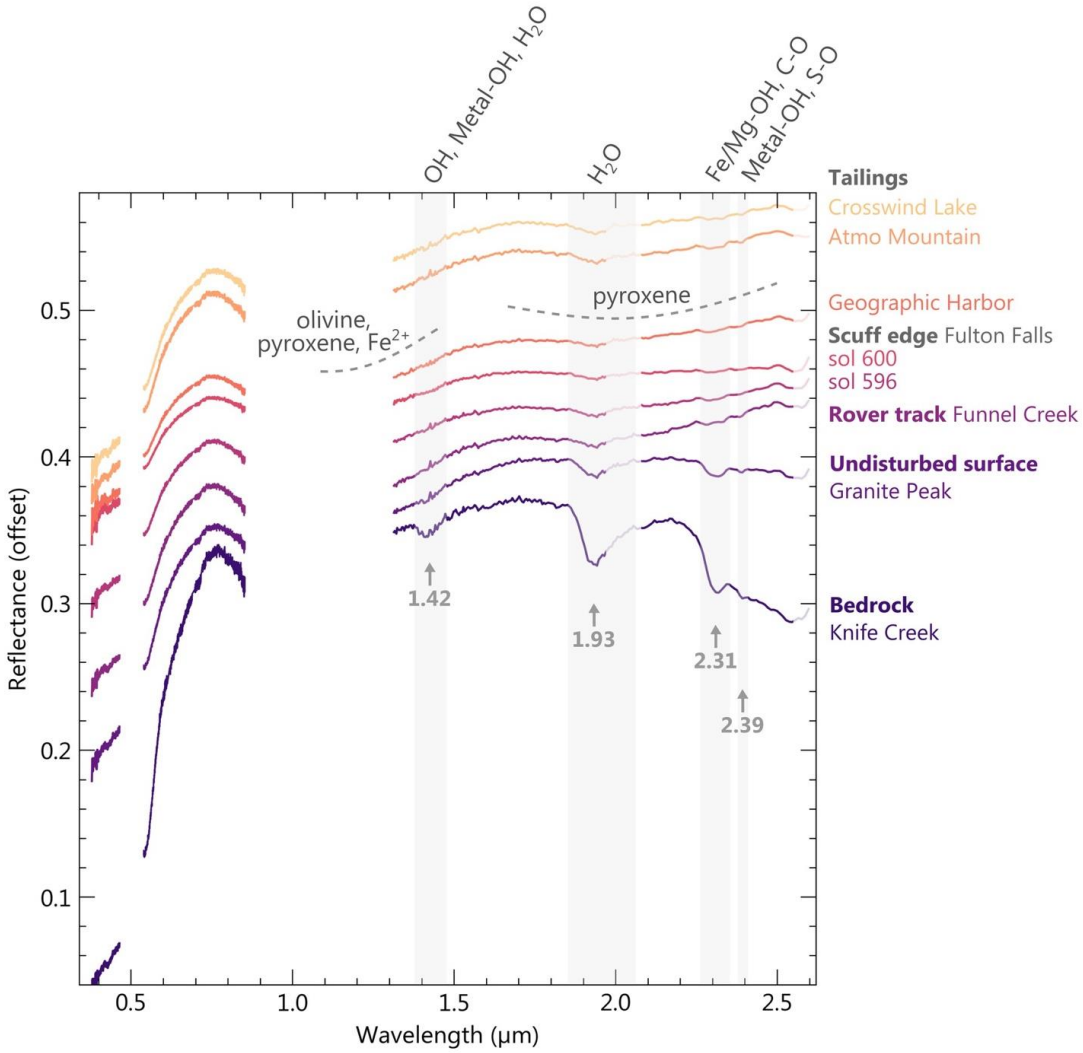

Subsurface Structure

The subsurface structure of the delta front, near the *Observation Mountain* megaripple just south of *Cape Nukshak* (**Figure 29**), is revealed by RIMFAX radargrams. Perseverance did not traverse over the bedform, so no RIMFAX data were collected for the bedform itself. The radargram was acquired on sols 632 and 641 during a traverse headed southwest toward *Observation Mountain* and then further south away from the bedform (see red line in **Figure 29a**). The units beneath the *Observation Mountain* and adjacent bedforms are generally horizontally stratified as seen in both outcrop and in the subsurface (**Figure 29b**). The *Observation Mountain* regolith samples were acquired from aeolian material 6 to 7

meters above the base delta unconformity, which caps the underlying *Séítah* Formation strata, at depth -2535 to -2536 m. Depths have been calculated from two-way travel times using 0.1 m/ns.

Figure 29. Geologic context and RIMFAX-derived subsurface stratigraphy of the delta front south of *Cape Nukshak*. (a) Location of the *Observation Mountain* megaripple. The inset shows detail of the sample location. The red line indicates the portions of the traverses on sols 632 and 641 during which RIMFAX radargrams were collected. (b) Radargram of the traverses shown by the red line in panel (a), leading to and away from the *Observation Mountain* megaripple.

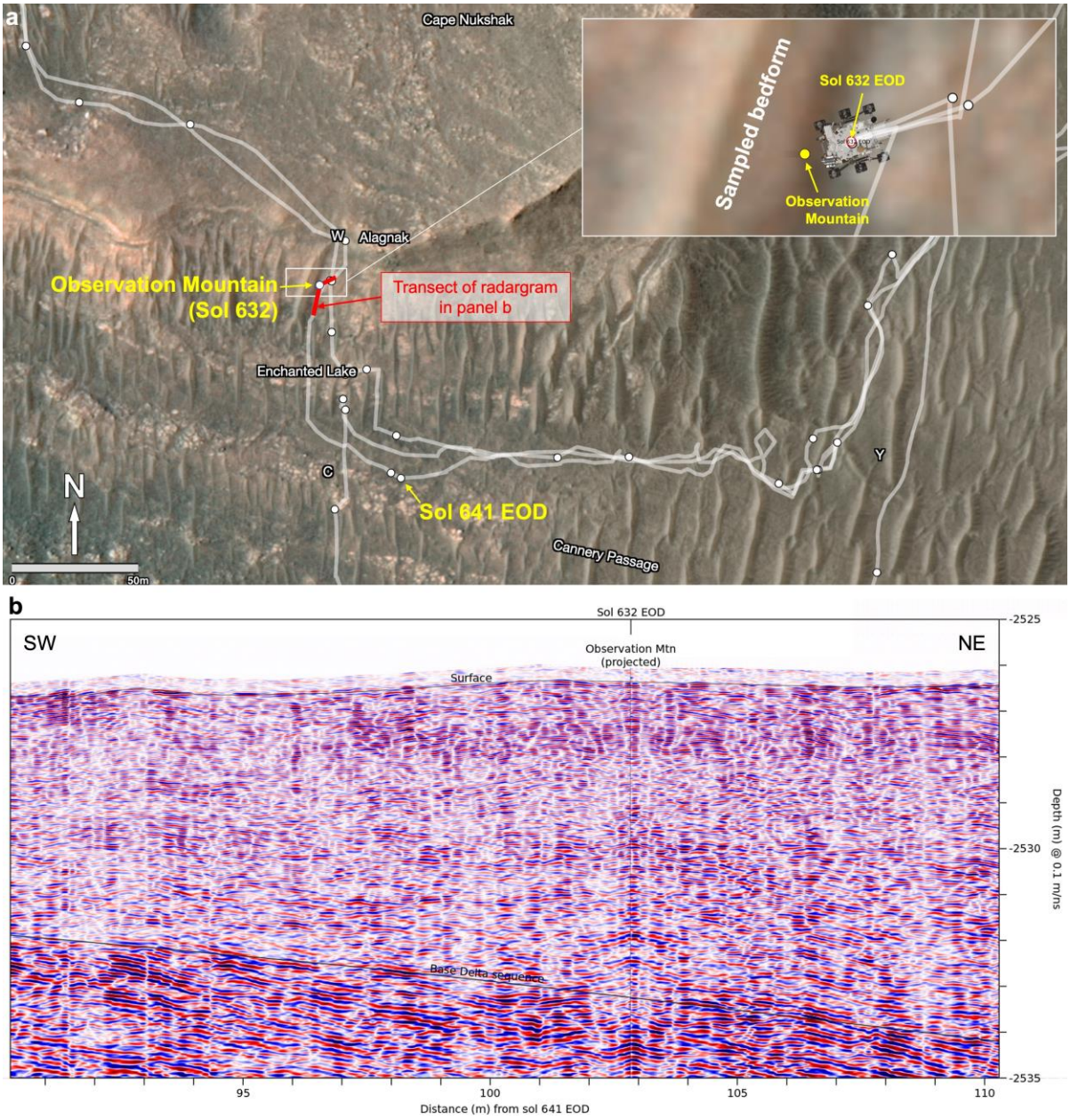

Core orientation

Not Applicable

Preliminary Scientific Assessment

Synthetic sample description and preliminary interpretation

Sample type: **Regolith**

1. **Relationship with surrounding rocks**
    a. Measurement by Mastcam-Z, SuperCam, PIXL, and SHERLOC suggest the presence of regolith material that is similar to material observed along Perseverance's ongoing traverse, as well as material that may be from local outcrops.
2. **Texture and fabric**
    a. Grain size: The megaripple contains a range of sizes, including coarser grains up to ~ 5mm in size, finer sand of various grades, silt, and likely (not directly resolved) atmospheric dust.
    b. Overall, the sample is consistent with collection of a bulk fine-grained material, larger grains on top, and atmospheric dust.
    c. Images indicate evidence for cohesion of the surface, including soil crusts.
3. **Mineralogy and chemistry**
    a. Primary minerals present include altered olivine, pyroxene, Fe- and Ti-oxides, and possibly quartz.
    b. Secondary mineralogy includes sulfates and carbonates, possible Fe-Mg phyllosilicates.
    c. Alteration features include evidence of hydration.
    d. Phosphates and aluminosilicates may be primary or secondary or both.
    e. Low concentrations of aromatic organics may be present, both localized and distributed in the rock.
4. **Atmospheric measurements**
    a. The temperature of the surface at the time of sampling was ~ 255 K and the ground relative humidity was ~0.
    b. The ground may have reached saturation during the early morning previous to each sampling, potentially affecting the hydration state of minerals in the sample.

Returned Sample Science Considerations

The *Crosswind Lake* and *Atmo Mountain* regolith samples fulfill the objective of collecting paired regolith samples prior to placement of the first depot. *Observation Mountain* was chosen for sampling because it is a megaripple that possessed several desired characteristics for the regolith sample including: (1) presence of airfall dust (inferred in this case); (2) presence of "global" fine-grained silt and sand <150um; (3) presence of diverse coarser materials; and (4) the megaripple itself appears relatively inactive. The surface and subsurface of the regolith at *Observation Mountain* appear similar to the regolith in the previously explored areas of Jezero Crater. The two regolith samples (*Atmo Mountain* and *Crosswind Lake*) sample compositionally and morphologically diverse sand grains, pebbles and smaller grains.

Observation Mountain is an aeolian bedform. Thus, the *Crosswind Lake and Atmo Mountain* samples record the potentially complex history of fluvial and aeolian transport within/upon the delta. Laboratory-based investigations of this sample will enable reconstruction of sediment transport processes that occurred in Mars's past. The samples from *Observation Mountain* can be used to address multiple science questions and objectives of the mission sampling campaign including:

Geochronology: Samples of regolith can be used to measure the isotopic composition of nuclides that will help to elucidate the exposure history of Martian surface materials, e.g., stable cosmogenic noble gases such as ^{3}He and ^{21}Ne in olivine (e.g. iMOST objective 3: Quantitatively determine the evolutionary timeline of Mars).

Geochemistry: Laboratory-based microscopic imaging and chemical mapping of the grains and alteration phases at resolutions higher than Perseverance's in-situ instruments will enrich our understanding of the primary minerals and relationships with secondary phases. This may help to elucidate the provenance of the individual pebbles as well as the geochemical conditions and processes to which they were subjected. Such information will add to our understanding of the Jezero watershed and sediment transport processes. Understanding these relationships concurrent with the atmospheric conditions will also help link kinetic and equilibrium isotope fractionation patterns to near-surface processes including the paleoclimate record of Mars (e.g. iMOST object 4 – Martian volatiles: Inventory, history, and interactions). Measurements of SO_4, CO_3, oxygen isotopes, and noble gases in regolith and dust samples will help to reveal how atmospheric chemical reactions and gases are preserved in minerals (iMOST 4B). If possible, measurement of oxidizing compounds in returned regolith samples would establish the amount and availability of oxidizing compounds on the surface of Mars, but this may be complicated by loss/reactivity post-sampling (iMOST 4D). Investigation of the airfall dust will help to address questions regarding the potential technical and health hazards posed by this phase that remains in suspension in the atmosphere for long periods of time. A laboratory-based thorough characterization of this material will enable production of accurate simulants that can be used for spacecraft and equipment testing and toxicological assessments (iMOST Objective 6). Observations of returned regolith may indicate its potential utility for In Situ Resource Utilization (iMOST obj 7).

Habitability and Biosignature potential: Laboratory-based, high resolution measurements of the mineral and organic distribution in the samples may provide more detailed information on the potential organic signals observed by SHERLOC, and any associations with specific solid phases. Analyses that characterize

the compositional, structural, and isotopic diversity of organic compounds in the regolith samples can also help constrain their origin.

References

Allwood, A.C., Wade, L.A., Foote, M.C., Elam, W.T., Hurowitz, J.A., Battel, S., Dawson, D.E., Denise, R.W., Ek, E.M., Gilbert, M.S. and King, M.E., 2020. PIXL: Planetary instrument for X-ray lithochemistry. *Space Science Reviews*, *216*, pp.1-132.

Berger, J.A., Schmidt, M.E., Gellert, R., Campbell, J.L., King, P.L., Flemming, R.L., Ming, D.W., Clark, B.C., Pradler, I., VanBommel, S.J. and Minitti, M.E., 2016. A global Mars dust composition refined by the Alpha-Particle X-ray Spectrometer in Gale Crater. *Geophysical Research Letters*, *43*, pp.67-75.

Brückner, J., Dreibus, G., Gellert, R., Squyres, S. W., Wanke, H., Yen, A., and Zipfel, J. (2008) Mars Exploration Rovers: chemical composition by the APXS, chapter 4, 58-101, *The Martian Surface: Composition, Mineralogy, and Physical Properties*, ed. J. F. Bell III., Cambridge University Press.

Clark, B. C., Baird, A. K., Weldon, R. J., Tsusaki, D. M., Schnabel, L., and Candelaria, M. P. (1982) Chemical composition of martian fines, *Journal of Geophysical Research*, *87*, B12, 10059-10067,

Cousin, A., Dehouck, E., Meslin, P.-Y., Forni, O., Williams, A. J., Stein, N., Gasnault, O., Bridges, N., Ehlmann, B., Schröder, S., Payré, V., Rapin, W., Pinet, P., Sautter, V., Lanza, N., Lasue, J., Maurice, S., and Wiens, R. C. (2017) Geochemistry of the Bagnold dune field as observed by ChemCam and comparison with other aeolian deposits at Gale crater, *Journal of Geophysical Research: Planets*, *122*, 2144-2162,

Farley, K. A., Williford, K. H., Stack, K. M., Bhartia, R., Chen, A., de la Torre, M., Hand, K., Goreva, Y., Herd, C. K. K., Hueso, R., Liu, Y., Maki, J. N., Martinez, G., Moeller, R. C., Nelessen, A., Newman, C. E., Nunes, D., Ponce, A., Spanovich, N., Willis, P. A., Beegle, L. W., Bell III, J. F., Brown, A. J., Hamran, S.-E., Hurowitz, J. A., Maurice, S., Paige, D. A., Rodriguez-Manfredi, J. A., Schulte, M., and Wiens, R. C. (2020) Mars 2020 mission overview, *Space Science Reviews*, *216*, 142.

Farley, K. A., et al. (2022) Aqueously altered igneous rocks sampled on the floor of Jezero crater, Mars, *Science*, *377*, 6614.

Goudge, T. A., Mustard, J. F., Head, J. W., Fassett, C. I., and Wiseman, S. M. (2015) Assessing the mineralogy of the watershed and fan deposits of the Jezero crater paleolake system, Mars, *Journal of Geophysical Research: Planets*, *120*, 775-808.

Mangold, N., Schmidt, M.E., Fisk, M.R., Forni, O., McLennan, S.M., Ming, D.W., Sautter, V., Sumner, D., Williams, A.J., Clegg, S.M. and Cousin, A., 2017. Classification scheme for sedimentary and igneous rocks in Gale crater, Mars. *Icarus*, *284*, pp.1-17.

Moore, H. J., Hutton, R. E., Clow, G. D., and Spitzer, C. R. (1987), *Physical Properties of the Surface Materials at the Viking Landing Sites on Mars*, 222 pp., U. S. Geol. Survey Prof. Pap. 1389, U. S. Government Printing Office, Washington.

Rieder, R., Economou, T., Wänke, H., Turkevich, A., Crisp, J., Brückner, J., Dreibus, G., and McSween, H. Y. (1997) The chemical composition of Martian soil and rocks returned by the mobile alpha proton X-ray spectrometer: preliminary results from the X-ray mode, *Science*, *278*, 1771–4.

Sullivan, R., Anderson, R., Biesiadecki, J., Bond, T., and Stewart, H. (2011) Cohesions, friction angles, and other physical properties of Martian regolith from Mars Exploration Rover wheel trenches and wheel scuffs, *Journal of Geophysical Research, 116*, E2, E02006.

Tice, M.M., Hurowitz, J.A., Allwood, A.C., Jones, M.W., Orenstein, B.J., Davidoff, S., Wright, A.P., Pedersen, D.A., Henneke, J., Tosca, N.J. and Moore, K.R., 2022. Alteration history of Séítah formation rocks inferred by PIXL x-ray fluorescence, x-ray diffraction, and multispectral imaging on Mars. *Science Advances*, *8*, p.9084.

Yen, A. S., Gellert, R., Schröder, C., Morris, R. V., Bell III, J. F., Knudson, A. T., Clark, B. C., Ming, D. W., Crisp, J. A., Arvidson, R. E., Blaney, D., Brückner, J., Christensen, P. R., DesMarais, D. J., de Souza Jr., P. A., Economou, T. E., Ghosh, A., Hahn, B. C., Herkenhoff, K. E., Haskin, L. A., Hurowitz, J. A., Joliff, B. L., Johnson, J. R., Klingelhöfer, G., Madsen, M. B., McLennan, S. M., McSween, H. Y., Richter, L., Rieder, R., Rodionov, D., Soderblom, L., Squyres, S. W., Tosca, N. J., Wang, A., Wyatt, M., and Zipfel, J. (2005) An integrated view of the chemistry and mineralogy of martian soils, *Nature*, *436*, 49-54.

INITIAL REPORT

M2020-639-21 *Crosswind Lake*

Sample Designation: M2020-639-21 *Crosswind Lake*

Date of Coring: 06-Dec-2022

Mars Time of Sample Core Sealing: 21:30 LMST, Sol 639, Ls 350.49

Latitude (N), Longitude (E), Elevation: 18.45132238, 77.40121614, -2524.977556 m

Campaign: Delta Front

Region of Interest: *Observation Mountain*

Lithology: Regolith sample consists of a mixture of coarse grains up to ~ 5 mm diameter, finer sand of various grades, silt, and likely (not directly resolved) atmospheric dust. Primary (igneous) minerals include variably altered olivine, pyroxene, Fe- and Ti-oxides, and possibly quartz. Secondary phases include sulfates and carbonates and possibly Fe-Mg phyllosilicates. Phosphates and aluminosilicates may be primary or secondary or both.

Estimated Volume Recovered: 7.47 cm^3

Coring Bit Number: Regolith

Core Orientation: NA

Sample Serial Numbers: Tube SN173; Seal SN191; Ferrule SN106

ACA Temperature at Time of Sealing: 313K

Estimated Rover-Ambient Pressure and Temperature at Time of Sealing: 727 Pa, 211 K

Estimated Amount of Martian Atmosphere Headspace Gas: 1.88x10-6 mol

Subsurface Regolith Targets: *Topographers Peak* (wheel scuff tailings pile), *Geographers Harbor* (wheel scuff tailings pile), *Fultons Falls* (wheel scuff wall), *Funnel Creek* (wheel scuff cavity floor)

Anomalous Behavior: Regolith assessment and sampling occurred in two separate phases (sols 593-606, and sols 632-641).

February 7, 2023

E.M. Hausrath, K.A. Farley, R. Sullivan, Y. Goreva, T. V. Kizovski, A. O. Shumway, A.H. Treiman, M.M. Tice, S. VanBommel, S. Siljeström, S. Sharma, E. Cardarelli, L. Mandon, A. Udry, A. Cousin, T. Bosak, R. Wiens, A. Vaughan, H. Amundsen, S-E. Hamran, A. Czaja, M-P. Zorzano, G. Martinez, C.T. Adcock, J. Simon, C. Herd, L. Mayhew, J.M. Madariaga, K. Williford, J. Johnson, D. Shuster, F. Calef, the PIXL team, the RSSWG, the Regolith WG, and the Mars 2020 Team

This sample is paired with M2020-634-20 *Atmo_Mountain*. See Initial Report for M2020-634-20 *Atmo Mountain* for details of this sample.